

19th
ABAF

BRNO 2018

Advanced Batteries, Accumulators
and Fuel Cells

INTERNATIONAL CONFERENCE

August 26th - August 29th 2018

Organised by:

Department of Electrical and Electronic Technology,
Faculty of Electrical Engineering and Communication,
Brno University of Technology

Organizing committee:

Jiří Vondrák
Marie Sedlaříková

co-sponsored by



Centre for Research
and Utilization
of Renewable Energy



Shmuel De-Leon
Energy Ltd

Honourary Scientific Committee:

- Petr Vanýsek, *Northern Illinois University, DeKalb, Illinois, USA*
- Jaroslav Cihlář, *FME BUT, Brno, Czech Republic*
- Arnaldo Visintin, *INIFTA, La Plata, Argentina*
- Günter Fafilek, *TU Wien, Vienna, Austria*
- Tatjana Kulova, *IPCE RAS, Moscow, Russia*
- Vito Di Noto, *University of Padova, Padova, Italy*
- Alexei Kornyshev, *Imperial College, London, UK*
- Boris Markovsky, *Bar-Ilan University, Tel Aviv, Israel*
- Philipp Adelhelm, *Friedrich Schiller University, Jena, Germany*
- Laurence Hardwick, *University of Liverpool, Liverpool, UK*
- Renata Oriňáková, *UPJŠ, Košice, Slovakia*
- Grzegorz Lota, *Poznan University of Technology, Poznan, Poland*
- Mariusz Walkowiak, *Institute of Non-Ferrous Metals, Poznan, Poland*

Organisation Committee:

- Jiří Vondrák, *FEEC BUT, Brno, Czech Republic*
- Marie Sedlaříková, *FEEC BUT, Brno, Czech Republic*
- Vítězslav Novák, *FEEC BUT, Brno, Czech Republic*
- Miroslav Zatloukal, *FEEC BUT, Brno, Czech Republic*
- Tomáš Kazda, *FEEC BUT, Brno, Czech Republic*
- Lucie Šimonová, *FEEC BUT, Brno, Czech Republic*
- Jiří Libich, *FEEC BUT, Brno, Czech Republic*
- Josef Máca, *FEEC BUT, Brno, Czech Republic*
- Tomáš Binar, *University of Defence, Brno, Czech Republic*
- Jiří Švarc, *University of Defence, Brno, Czech Republic*
- František Klein, *Brno, Czech Republic*

Program Committee:

- Jiří Vondrák, *FEEC BUT, Brno, Czech Republic*
- Marie Sedlaříková, *FEEC BUT, Brno, Czech Republic*
- Mariusz Walkowiak, *Institute of Non-Ferrous Metals, Poznan, Poland*
- Arnaldo Visintin, *INIFTA, La Plata, Argentina*
- Petr Vanýsek, *Northern Illinois University, DeKalb, Illinois, USA*
- Günter Fafilek, *TU Wien, Vienna, Austria*
- Boris Markovsky, *Bar-Ilan University, Tel Aviv, Israel*
- Tatjana Kulova, *IPCE RAS, Moscow, Russia*
- Alexei Kornyshev, *Imperial College, London, UK*
- Philipp Adelhelm, *Friedrich Schiller University, Jena, Germany*
- Laurence Hardwick, *University of Liverpool, Liverpool, UK*
- Josef Máca, *FEEC BUT, Brno, Czech Republic*
- Vítězslav Novák, *FEEC BUT, Brno, Czech Republic*
- Petr Bača, *FEEC BUT, Brno, Czech Republic*
- Tomáš Kazda, *FEEC BUT, Brno, Czech Republic*
- Helena Polsterová, *FEEC BUT, Brno, Czech Republic*
- Miroslav Zatloukal, *FEEC BUT, Brno, Czech Republic*
- Andrea Fedorková-Straková, *UPJŠ, Košice, Slovakia*
- Michal Jahn, *FEEC BUT, Brno, Czech Republic*
- Jiří Libich, *FEEC BUT, Brno, Czech Republic*
- Lucie Šimonová, *FEEC BUT, Brno, Czech Republic*
- Tomáš Binar, *University of Defence, Brno, Czech Republic*
- Jiří Švarc, *University of Defence, Brno, Czech Republic*

ISBN 978-80-214-5651-8

Contents

Lithium batteries and related systems

M. Zúkalová, J. Procházka and B. Pitňa Lásková

Layered $\text{LiNi}_{1/3}\text{Mn}_{1/3}\text{Co}_{1/3}\text{O}_2$ (NMC) with optimized morphology for Li-ion batteries.....8

V. Redko, E. Shembel, T. Pastushkin, A. Markevych, A. Straková Fedorková, O. Girin, O. Kolomoiets, Y. Polishchuk

Synergistic Effect of Innovating Electrode Technology and Eddy-Current Electromagnetic Impedance for Non-Destructive Testing are Resulting in Increasing Battery Power9

T. Kazda, K. Jaššo

Lithium-sulfur batteries and the methods of their stabilization12

O. V. Markevych, E. M. Shembel

Innovating methods production high energy sulfur based electrode for stable and safer Lithium-Sulfur Batteries15

Yulin Ma, Zhenxin Zhou, Changjin Li, Long Wang, Yang Wang, Xinqun Cheng, Pengjian Zuo, Chunyu Du, Hua Huo, Yunzhi Gao, Geping Yin

Enabling Reliable Lithium Metal Batteries by a Bifunctional Anionic Electrolyte Additive.....18

E. Legotin, K. Fröhlich, R. Hamid, N. Zhang, C. Täubert and F. Winter

Improved Electrochemical Performance of NMC Cathode Material Produced via Spray-Roasting Route.....19

Mohammad Ayub Ansari, Pramod Yallappa Kumbhar and Narasimhan Swaminathan

A Computational Study on the Effect of Stress Concentrations on Stress-Electrochemistry Interactions in Li-ion Battery Electrode Particle21

J. Vondrák, M. Sedlaříková, J. Máca

Contribution to chemistry of EMIM.BF₄ ionic liquid24

K. Banov, D. Ivanova, L. Fachikov, B. Banov

NMC cathode material for large scale application in EV28

K. Gavalierová, D. Capková, A. Straková Fedorková, R. Oriňáková, M. Strečková

Cathode Material Based on S/C Composite for Li-S Batteries31

M. Jahn, I. Veselkova, M. Sedlaříková, J. Vondrák, K. Bartušek

Gel Polymer Electrolytes Modified Nanoparticles and Polymerized in Magnetic and Electric Fields.....33

K. Jaššo, T. Kazda

Carrageenan as the Binder for the Lithium-Sulfur Batterie.....37

H. Kim, T. Hwang and M. Cho

Structure Instability of Cathode Active Materials in Lithium Ion Battery Induced by Lattice Distortion: Phase Field Analysis40

<i>Seyed Saeed Madani, Erik Schaltz, Søren Knudsen Kær</i> A Comprehensive study of Working Temperature and Entropy Impacts on a Lithium-Ion Battery Thermal Behaviour by Employing Isothermal Calorimeter	43
<i>Seyed Saeed Madani, Erik Schaltz, Søren Knudsen Kær</i> Investigation of Reversible and Irreversible Heat Sources and Entropic Coefficient in a Lithium-Ion Battery by Employing Isothermal Calorimeter	47
<i>Seyed Saeed Madani, Erik Schaltz, Søren Knudsen Kær</i> Investigation of the Effect of State of Charge, C-rates and on the Heat Generation, Internal Resistance and Efficiency of a Lithium-ion Battery by Using Isothermal Calorimeter.....	50
<i>Seyed Saeed Madani, Erik Schaltz, Søren Knudsen Kær</i> A Review of Different Electric Equivalent Circuit Models and Parameter Identification of Lithium-ion Batteries	54
<i>A. V. Potapenko, S. A. Kirillov</i> Improving high-rate properties of electrode materials: prevention of aggregation and surface modification.....	59
<i>Francis Amalraj Susai, Hadar Sclar, Raman Ravikumar, Sandippan, Saphir Giladi, Yehonatan Levartovsky, Judith Grinblat, Michael Talianker, Arup Chakraborty, Dan T. Major, Boris Markovsky, Doron Aurbach</i> Recent Advances and Challenges on Ni-Rich Cathode Materials for Lithium-Ion Batteries	62
<i>I. Veselkova, M. Jahn, M. Sedlaříková and J. Vondrák</i> Flame Retardants as Solvent in Gel Polymer Electrolytes	63
<i>P. Vorel, D. Cervinka, M. Toman, J. Martis</i> Durability of a Li-ion battery pack	66
<i>Sangkoan Yi, Kyeongjae Cho and Meanghyo Cho</i> Ab-initio Calculation of New Poly-oxyanion Cathode Materials of Li-ion Battery.....	69
<i>L. Chladil, D. Kunický and O. Čech</i> In-situ X-ray study of Electrodes for Li-ion Battery in Different State of Charge.....	71
Supercapacitors	
<i>K. Lota, I. Acznik, A. Sierczynska, G. Lota</i> The Activated Carbon From Biopolymers as the Electrode Material for Electrochemical Capacitors	75
<i>G. Lota, A. Bund, Ł. Kolanowski, M. Graś, J. Wojciechowski</i> The Influence of Electrolyte on the Performance of Electrochemical Capacitors.....	78
<i>Ł. Kolanowski, M. Graś, J. Wojciechowski, G. Lota</i> Heteroatom-doped Carbon for Energy Storage	80

Fuel Cells

L. Kolanowski, M. Graś, J. Wojciechowski, K. Lota, G. Lota

Carbon-supported AB₅-type Hydrogen Storage Alloy for DBFC Application.....82

Ali Muneer Hadi, Hassan A.Z.Al-Fetlawi

Performance Enhancement of a Single-Chamber Membraneless Microbial Fuel Cell84

I. O. Chikunova, V. S. Semeykina, P. N. Kalinkin, E. N. Gribov and E. V. Parkhomchuk

Macroporous SnO₂ As A Stable Cathode Catalyst Support For PEMFCs.....85

J. Mališ, M. Paidar, K. Bouzek, M. Šmíd

Development of PEM FC based auxiliary power unit.....88

Aqueous Batteries

P. Křivík, S. Vaculík, P. Bača, J. Kazelle

In situ measurement of PEIS of lead acid battery cell90

G. Lota, K. Kopczyński, A. Gabryelczyk, M. Baraniak, J. Pernak, E. Jankowska, P. Kędzior

The Lead - Acid Battery Modified By Ionic Liquid93

New systems of Batteries

I. Maksyuta, E. Shembel, A. Markevych, D. Bondar

Electrodes Based on Magnesium Alloys for Innovative Magnesium Batteries with Non-Aqueous Electrolytes.....95

P. Mazúr, J. Mrlík, J. Charvát, J. Vrána, J. Pociď, J. Dundálek, J. Kosek

High-performance long-lasting vanadium redox flow batteries for stationary energy storage applications98

E. V. Alekseeva, M. V. Novogilova, V. A. Ershov, A.S. Konev and O.V. Levin

Effect of Structure of Polymeric Nickel Complexes with Salen-Type Ligands on The Stability in Solutions of Water-Containing Electrolytes and The Charge Transfer Parameters99

R.D. Apostolova, A.V. Markevich, I.V. Kirsanova

Electrochemical Properties Electrodes Based on Mn₃O₄, Mn₂O₃ in Non-Aqueous Electrolyte with Magnesium or Lithium Perchlorate.....102

T. Hwang, H. Kim and M. Cho

First -Principles Study On Mechanism Of Graphite Oxide As Anode material in Na-Ion Battery System.....105

J. Libich, M. Sedlářková, J. Vondrák, J. Máca, P. Čudek, A. Chekannikov, W. Artner and G. Fafilek

Performance of Graphite Negative Electrode In Lithium-Ion Battery Depending Upon The Electrode Thickness.....108

O. V. Markevych, E. M. Shembel

Electrochemical properties of magnesium electrodes in lithium non-aqueous electrolytes. Perspective of high-energy hybrid magnesium batteries111

V. Rojas, N. Briones, E. Navarrete, J. Román, G. Cáceres, E. Muñoz, F. Herrera

Chemometric approach to study the influence of synthesis parameters on the structural and electrical responses of metal polycyanometalates (MPCMs) for optimizing their use as cathodes in metal(M) ion batteries (M = Li⁺, K⁺, Na⁺)114

Photovoltaics

E. Shembel, V. Redko, T. Pastushkin, L. Yashchenko, N. Yarova

Nanostructured Transparent Polymer Provides Innovation Design for Solar Cells. Increasing Energy and Improving Performance116

I. A. Rusetskyi, L. G. Shcherbakova, M. O. Danilov, I. A. Slobodyanyuk

Accumulation of "Solar" Hydrogen in the Photoelectrochemical System Based on CdSe Photoanode and MH Cathode119

T. Dvořák, V. Novák

Changes in Properties of Perovskite Solar Cells During Their Lifetime122

J. Hylský, D. Strachala, P. Čudek, J. Vaněk

Protection Against PID Degradation at Photovoltaic Cell Level125

J. Hylský, E. K. Ovando, D. Strachala, J. Vaněk and P. Vyroubal

Possibilities of Regeneration of a PID Degraded PV Cell129

K. Jandova, M. Janda

Simulation Of Effects Of Wind In The Installation PV Power Plants132

D. Strachala, M. Kratochvíl, J. Hylský, L. Chladil, A. Gajdoš and J. Vaněk

Changes of the Active Perovskite Solar Cell Layer Caused By External Influences135

D. Strachala, M. Kratochvíl, J. Hylský, A. Gajdoš, P. Čudek and J. Vaněk

Perovskite Solar Cells with Increased Resistance to Moisture138

Other technology, applications and simulations

B. Polnik

An innovative power supply system dedicate for Roadheading mining machines141

R. Bayer

Static pressure measurement within a flow measurement and mapping chamber145

M. Bílek, P. Hlavatá, J. Maxa

Analysis of the Impact of the Baffle Placement in the Supersonic Flow in the Differentially Pumped Chamber148

R. Cipin, M. Toman, P. Prochazka, and I. Pazdera

High-Frequency Model of Alkaline Battery in Form of Transfer Function153

<i>D. Dobrocký, Z. Pokorný, Z. Studený</i> Change of surface texture parameters of grinded surfaces after application of hard and abrasion resistant layers	156
<i>P. Faltejsek, D. Kusmič</i> Corrosion Resistance of High Temperature Plasma Nitrided X12CrMoWVNbN10-1-1 martensitic stainless steel	157
<i>J. Martis, P. Vorel and D. Cervinka</i> Battery-powered Soldering Gun	160
<i>Falah K. Matloub, Muataz Mohammed Sulaiman, Zaid Nidhal Shareef</i> Separation of Chromium from Tanning Wastewater by Electrochemical Method	163
<i>P. Hlavatá, J. Maxa, P. Vyrubal</i> Design of the conic static probe tip of the Pitot's tube in experimental chamber	164
<i>J. Maxa, P. Hlavatá, P. Vyrubal</i> Comparative analysis of ideal and real gas in pumping of the experimental chamber	168
<i>Z. Pokorný, D. Dobrocký, P. Faltejsek</i> The influence of alloying elements on surface hardness of ferritic nitrocarburizing layers of ball screws.....	172
<i>P. Procházka, I. Pazdera, R. Cipin, P. Vorel, J. Knobloch</i> Battery powered mini-excavator	173
<i>T. Reichl, P. Hrzina</i> Study of the Current Value Influence on the Internal Resistance Value	176
<i>M. Sedlaříková, J. Vondrák, A. Košíček and M. Hávová</i> Preparation and corrosion of biodegradable iron based porous materials.....	179
<i>M. Sedlaříková, J. Vondrák, Z. Galanova, P. Čudek, T. Binar</i> Chemical corrosion of porous iron alloys prepared pyrolytically.....	183
<i>M. Toman, R. Cipin, P. Vorel</i> Thermal Model of Cylindrical Battery Cell	187
<i>J. Vanek and R. Mach</i> Electrical conductivities of reduced graphene oxide thin-film layers	190
<i>P. Vyrubal, T. Kazda</i> FEA Methods for Lithium Ion Battery Simulation	194
<i>P. Vyrubal, T. Kazda</i> FEM Analysis of LiIon Battery Nail Test.....	198
<i>P. Vyrubal, L. Šimonová</i> Thermal Simulation of Thermo-photovoltaic Emitter	200

We would like to express our thanks to the Brno University of Technology, Faculty of Electrical Engineering and Communication for support and help with organising 19th ABAF conference.

Layered $\text{LiNi}_{1/3}\text{Mn}_{1/3}\text{Co}_{1/3}\text{O}_2$ (NMC) with optimized morphology for Li-ion batteries

M. Zukalová¹, J. Procházka² and B. Pitňa Lásková¹

¹J. Heyrovský Institute of Physical Chemistry, v.v.i., AS CR, Dolejškova 3, CZ-18223 Prague 8, Czech Republic

²HE3DA, s.r.o., Beranových 130, 199 05 Praha 18

While LiCoO_2 , a commercial widely used cathode material, still raises some concerns about the cost, abundance of cobalt, and potential safety limitations at elevated temperatures, layered $\text{LiNi}_{1/3}\text{Mn}_{1/3}\text{Co}_{1/3}\text{O}_2$ is a promising cathode material from all points of view¹. Its Co content is only 1/3 of that of LiCoO_2 , it exhibits impressive stability upon cycling, reasonable specific capacity (150 mA h g^{-1}), good high rate capability, and good safety features¹. It is iso-structural to layered LiCoO_2 and in fact seems to integrate the features of LiCoO_2 , LiNiO_2 and LiMnO_2 . The electrochemical performance of $\text{LiNi}_{1/3}\text{Mn}_{1/3}\text{Co}_{1/3}\text{O}_2$ depends on the particle size, crystallinity, surface morphology, porosity and potential range of cycling. This material exhibits reasonable cycling stability in a potential window 2.5 V/4.2V, however, when it is cycled to the higher potentials above 4.4 V, capacity fading and a shift of the average discharge voltage to lower values occur as a consequence of a formation of a spinel-like phase¹.

In our work commercial NMC material was treated in appropriate way to provide cathode material with reasonable charge capacity and high cycling stability upon C/2, 1C, and 2C charging/discharging rate. Electrochemical performance of tested materials was studied by cyclic voltammetry of Li insertion and galvanostatic chronopotentiometry. An influence of mechanical treatment, surface area and carbon content on the charge capacity and cycling stability was evaluated and the parameters of the optimized sample providing charge capacity of 141 mA h g^{-1} (cyclic voltammetry) and 135 and 131 mA h g^{-1} (galvanostatic chronopotentiometry) at 1 and 2C, respectively, represent a platform for scale up during the next period of the research.

Acknowledgement

This work was supported by the Ministry of Industry and Trade of the Czech Republic (contract TRIO FV20471).

References

1. Nayak, P. K.; Grinblat, J.; Levi, M.; Wu, Y.; Powell, B.; Aurbach, D. *J Electroanal Chem* **2014**, 733, 6-19.

Synergistic Effect of Innovating Electrode Technology and Eddy-Current Electromagnetic Impedance for Non-Destructive Testing are Resulting in Increasing Battery Power

Vlad Redko^a, Elena Shembel^{a,b}, Timothy Pastushkin^a, Alexander Markevych^b,
Andrea. Straková Fedorková^c, Oleg Girin^b, Olga Kolomoiets^b, Yuliya Polishchuk^b

^a Enerize Corporation, Coral Springs, FL, 33067, USA Oleg Girin

^b Scientific-Research Laboratory of Chemical Power Sources, Ukrainian State University of
Chemical Technology, Dnipro, 49005, Ukraine

^c Pavol Jozef Safarik University, Kocice, SK-04154, Slovak Republic

Introduction

During discharge process of batteries the resistance the interface between electrode mass layer & the current collector influences on the battery voltage. The surface of the aluminum foil, which used as a current collector for positive electrodes in lithium and lithium-ion batteries is passivated by Al₂O₃ thin film that has a low electric conductivity. As result the energy and power battery characteristics are decreased. Our presentation is connected with technology for Li electrode production that insures the low interface resistance between electrode collector and electrode mass, the increasing the power of the batteries and stability the cycling. This technology is based on the electro erosion treatment of the current collector using a graphite electrode that fused in Al. For non-contact non- destructive testing the interface resistance during electrode production we developed method of eddy-current electromagnetic impedance [1]. For electrochemical investigation the VoltaLab PGZ 301 has been used

Modification of Al current collector

On Fig.1 the photo of samples of current collectors from Al with different level of the modification are presented.



Figure 1. Samples of aluminum foil, the surface of which is modified by spectral purity graphite. Diameter of the modified surface is 16 mm. The aluminum current collectors have the different degree of modification. 1. Ten graphitized lines (lines intersect at an angle of 90°; 2. Sixteen graphitized lines; 3. Fully modified surface

From the Figure 2 we can see that the Al foil after modification has also the evenly expanded surface. This is also promising for good adhesion between modified current collector and cathode mass based on sulfur

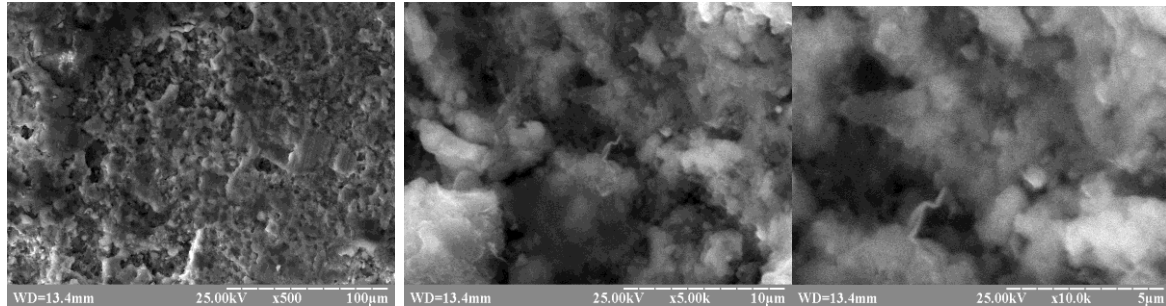


Figure 2. Electronic scanning microscopy of surface of Al that modified using the method of electroerosion, fusing the carbon into Al

Eddy- current electromagnetic impedance method for non-destructive non-contact testing the interface resistance

Fig.3 illustrates arrangement of the first eddy current probe relative to the current lead stripe with a coating 1) the figure above is a view in the movement direction of the current lead stripe with a coating, 2) the figure below is a view in the direction that is perpendicular to the movement direction of the current lead stripe with a coating

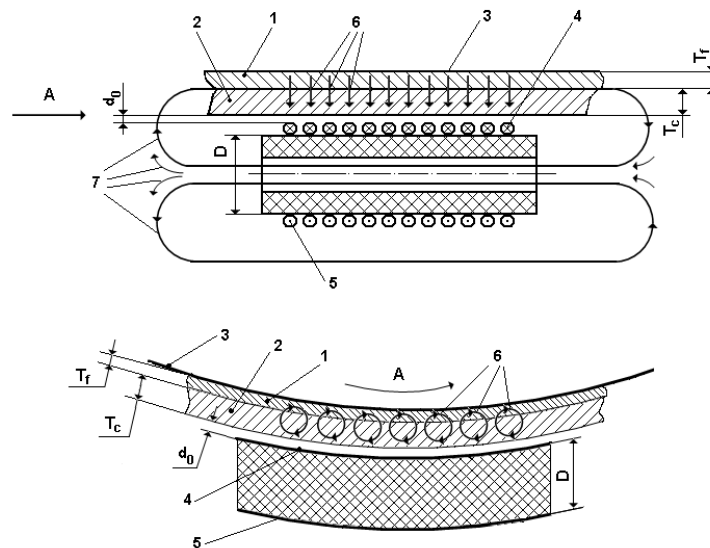


Fig. 5.

Figure 3. Eddy-current electromagnetic probe

As follows from Fig.3, the trajectories of the eddy currents being induced in the sample by the field of the first probe, cross the boundary between the foil and the coating. In such case the eddy current flows in succession through the region of the foil, the boundary and the coating region. The electrical conductance of the metallic foil is a stable value. Therefore the value of the eddy current and the shape of each of its trajectory will depend on the contact resistance between the foil and the coating and on the specific electrical conductance of the coating. 1 – the stripe (foil) of the current

lead, 2 – the coating, 3 – the surface of the shaft guiding the movement of the current lead stripe, 4 – current lines on the operating surface of the probe shell, 5 – current lines on the opposite surface of the probe shell, 6 – eddy currents in the foil with a coating, 7 – intensity lines of the probe magnetic field, T_f – foil thickness, T_c – coating thickness, d_0 – the installation gap value of the probes relative to the top surface of the coating, D – width of the probe shell.

Impedance of sulfur electrode with and without the modified Al current collector.

Electrodes with modified current collector have three layers: 1) current collector; 2) layer of highly conductive carbon material, which is fused into the current collector; 3) electrode mass based on sulfur. The electrode mass includes: 1) powder of sulfur, or polymer sulfur – 75%; 2) carbon black- 10%; Graphite EUZM- 10%, PVdF (6020/1001, Solef) - 5%. For electrochemical investigation the universal instrument VoltaLab PGZ 301 has been used

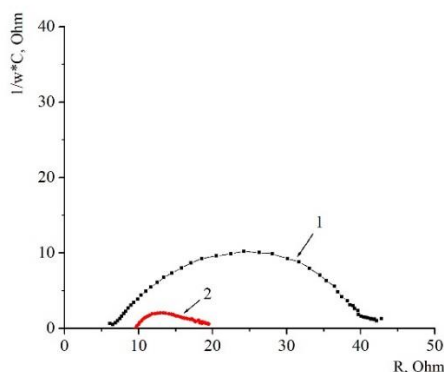


Fig. 4A

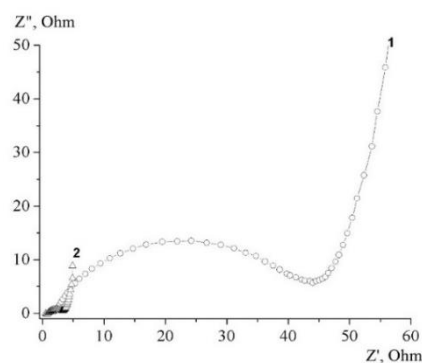


Fig.4B

Figure 4. Comparison impedance parameters of Li-S batteries with different current collectors, S 4A.

Cathode based on sulfur powder. 4B. Cathode based on polymer sulfur. 1. Current collector: non modified Al; 2 Current collector: modified Al. The sulfur based cathodes with modified current collector illustrate the dramatically decreased the electrochemical impedance, and low polarization

Aknowledgment

The work was carried out according to the project based on framework of NATO SPS 985148 "Development of New Cathodes for Stable and Safer Lithium-Sulfur Batteries". Company Enerize Corporation is an industrial partner of this project. Ukrainian State University of Chemical Technology participates in this project

References

1. V. Redko, V. Khandersky, E. Shembel, etc. *US Patent* No.7,982,457.(2011)

Lithium-sulfur batteries and the methods of their stabilization

T. Kazda^a, K. Jaššo^a

^a Department of Electrical and Electronic Technology, Faculty of Electrical Engineering and Communication, BUT, Technická 10, 616 00 Brno, Czech Republic

Lithium Sulfur batteries are one of the most promising battery technology nowadays. This technology meets several most important parameters for battery applications such as low cost, high energy density, safety and environmental compatibility. However, several major drawbacks such as low cycle life, high self-discharging and structural instability are still not fully resolved. In this article advantages, disadvantages of lithium sulfur batteries and possible methods of its solution are discussed.

Introduction

Lithium sulfur batteries are electrochemical power sources that use for energy storage conversion reaction of S_8 to higher and lower polysulfide to form lithium sulfide (Li_2S). [1] Thanks to average cell voltage 2.15 V vs. Li and high theoretical capacity 1672 mAh/g can lithium sulfur batteries reach gravimetric energy density greater than 3000 Wh/kg. [2] [3] This energy density is approximately five times higher than gravimetric energy density of the Li-ion batteries. The biggest advantage of this system (the conversion reaction) is also the biggest drawback of this system because conversion reaction is connected with a volume expansion of 80%. [4] This volumetric expansion of the sulfur increases the internal pressure in the electrode layer, which leads to the cracking and disintegration of electrode layer. Another problem is the fact that sulfur and lithium sulfide are insulators. [5] Addition of conductive additives in to the electrode is then necessary which dramatically decrease amount of active material (sulfur) in electrode composition. In addition, formation of to higher and lower polysulfides during charging and discharging is complicated process and some of polysulfide are soluble in the electrolyte. The dissolved polysulfides subsequently migrate to the side of the negative electrode on which the passivation layer is formed (shuttle effect). [1] This process leads to fast decreasing of the cell capacity and increasing of internal resistance of the cell during cycling. [6] All of these problems are obstacles that block the commercial use of lithium sulfur batteries. The last problem connected with this system is the use of metallic lithium on the anode side, which leads to the dendrites formation during cycling and brings questions about system safety. [7] Several areas are being developed to address these challenges. A more detailed description of these methods is given in the next chapter.

Methods of the blocking of polysulfide shuttle mechanism

At recent years, researchers have been working on about four major ways to improve the properties of the lithium sulfur batteries. The first of these methods is using of carbon sulphur composite materials. In this case, the porous carbon structures are used. [8] These structures works like protective layer on the surface of sulfur particles or sulfur is impregnated in to the pore in carbon structure and last possibility of its use is sulfur encapsulation in carbon hollow structure or carbon nanofibers. [9] [10] The second method is use of the graphene sulfur composite materials. This method is widely used in last few years and is derived from the use of porous carbon structures.

Graphene, graphene oxide or reduced graphene oxide are used as the functional material. [2] [11] Other method is use of polymer composite materials such as PEDOT, PAN, PPy in combination with sulfur as an ordered structure in which sulfur is encapsulated. [12] [13] The last widely used method is using of porous 3D current collector. These 3D structures are made from carbon, graphene, metal or are based on biological 3D structures (Figure. 1). [14] [15] [16] The advantage of this method is that it allows high sulfur loading. All these methods seek to improve cycling performance by immobilizing the active material by trapping of dissolved polysulfide and by accelerating charge transfer.

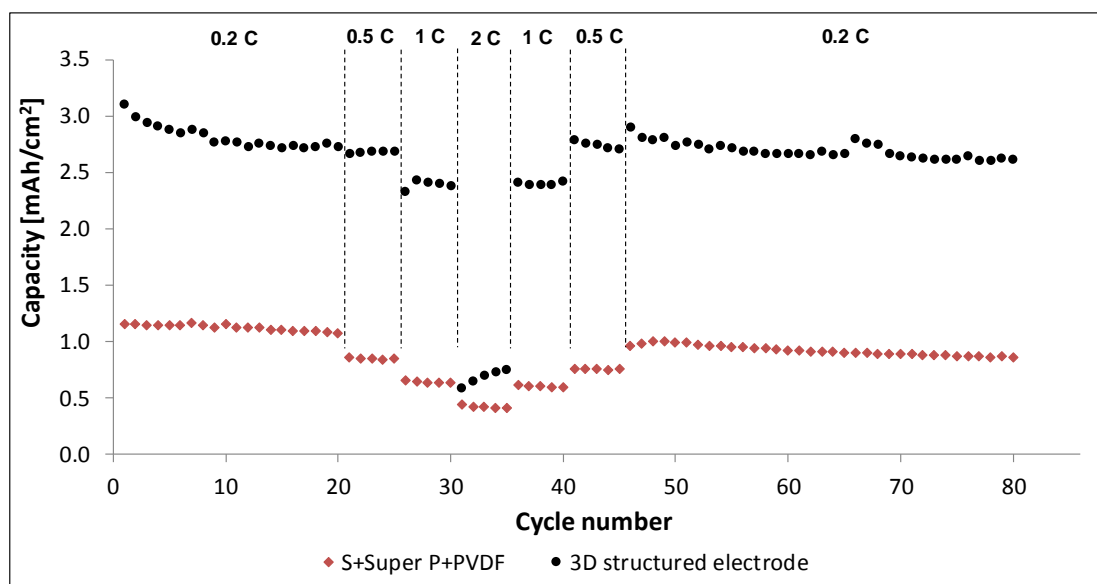


Figure 1. The Comparison of capacity per square centimetre changes during cycling of *Spongia officinalis* 3D structured electrode and S + Super P +PVDF electrode [16]

Acknowledgments

This research has been carried out in the Centre for Research and Utilization of Renewable Energy (CVVOZE). Authors gratefully acknowledge the financial support from the Ministry of Education, Youth and Sports of the Czech Republic under NPU I programme (project No. LO1210), BUT specific research programme (project No. FEKT-S-17-4595).

References

1. Y. Yin, S. Xin, Y. Guo and L. Wan, *Angewandte Chemie International Edition*, **vol. 52**, 13186-13200 (2013).
2. A. Manthiram, Y. Fu, S. Chung, C. Zu and Y. Su, *Chemical Reviews*, **114**, 11751-11787 (2014).
3. H. Yoo, E. Markevich, G. Salitra, D. Sharon and D. Aurbach, *Materials Today*, **vol. 17**, 110-121 (2014)..
4. J. Kim, D. Lee, H. Jung, Y. Sun, J. Hassoun and B. Scrosati, *Advanced Functional Materials*, **vol. 23**, 1076-1080 (2013).
5. Y. Choi, K. Kim, H. Ahn and J. Ahn, *Journal of Alloys and Compounds*, **449**, 313-316 (2008).

6. A. Fedorková, R. Oriňáková, O. Čech and M. Sedlaříková, *INTERNATIONAL JOURNAL OF ELECTROCHEMICAL SCIENCE*, **8** (2013).
7. S. Xiong, K. Xie, Y. Diao and X. Hong, *Electrochimica Acta*, 78-86 (2012).
8. S. Evers and L. Nazar, *Accounts of Chemical Research*, **vol. 46**, 1135-1143 (2013).
9. X. Li, Y. Cao, W. Qi, L. Saraf, J. Xiao, Z. Nie, J. Mietek, J. Zhang, B. Schwenzer and J. Liu, *Journal of Materials Chemistry*, **21**, 16603-16610 (2011).
10. N. Nitta, F. Wu, J. Lee and G. Yushin, *Materials Today*, **vol. 18**, 252-264 (2015).
11. X. Zhao, J. Tu, Y. Lu, J. Cai, Y. Zhang, X. Wang and C. Gu, *Electrochimica Acta*, **vol. 113**, 256-262 (2013).
12. F. Wu, J. Chen, R. Chen, S. Wu, L. Li, S. Chen and T. Zhao, *The Journal of Physical Chemistry C*, **vol. 115**, 6057-6063 (2011).
13. H. Cheng and S. Wang, *Journal of Materials Chemistry A*, **vol. 2**, 13783- (2014).
14. G. Babu, K. Ababtain, K. Ng and L. Arava, *Scientific Reports*, **vol. 5**, 8763- (2015).
15. L. Mi, W. Xiao, S. Cui, H. Hou and W. Chen, *Dalton Transactions*, **2016**, 3305-3309 (2016).
16. T. Kazda, P. Čudek, J. Vondrák, M. Sedlaříková, J. Tichý, M. Slávik, G. Fafilek and O. Čech, *Journal of Solid State Electrochemistry*, **22**, 537–546 (2018).

Innovating methods production high energy sulfur based electrode for stable and safer Lithium-Sulfur Batteries

O. V. Markevych ^a, E. M. Shembel^{a,b}

^a Ukrainian State University of Chemical Technology, Dnipro, 08540, Ukraine

^b Enerize Corporation, Coral Springs, FL, 33067, USA

Advantages of innovating method production the sulfur based cathode

Stability of the parameters and safety of high energy Li – S batteries are depended on many factors, included composition of active cathode mass, composition of electrolytes, nature of anode materials. Among these factors the technology of production of sulfur based cathode is also very important. Main current technologies production of sulfur based cathodes are using various types of binder, including PVdF and F4-D. During production of cathodes the high temperature using for treatment the binder and evaporation the solvent. Problem is connected with evaporation of sulfur that begin under temperature higher than 60 °C. As result not only decreases the quantity of the sulfur in cathode, but also impossible to correctly determine the amount of sulfur in the cathode mass. The innovative method of manufacturing sulfur electrodes that described in this presentation allows to optimize the macrostructure of cathode, to reduce the binder content to 3% without loss of strength of the electrode layer, and to treatment the electrodes at a temperature below 60 °C, which excludes evaporation of sulfur from the cathode structure.

Description of innovating method production the sulfur based cathode

The developed method of electrode manufacturing includes the following basic steps: 1) formation of a porous carbon matrix on the surface of a metal current lead; 2) dissolution of sulfur in a low boiling organic solvent; 3) impregnation with a sulfur solution of the porous carbon matrix; 4) evaporation of the low-boiling solvent under vacuum at a temperature below 60 °C; 5) formation of a layer of solid sulfur in the pores of the carbon matrix.

The macrostructure of the porous carbon matrix determines the macrostructure of the sulfur electrode. The change in the macrostructure of the porous carbon matrix is an effective way of optimizing the macrostructure of the sulfur electrode.

The high solubility of sulfur in an organic solvent makes it possible to saturate the porous carbon matrix with the necessary amount of sulfur; and the low boiling point of the solvent allows the cathodes to be dried under vacuum at a temperature below 60 °C.

A porous carbon matrix is formed on a stainless steel mesh. The mesh thickness is 80 μm, the cell size is 40 μm. The carbon matrix includes 90% acetylene black and 10% binder F-4D. The carbon matrix is dried at a temperature of 250 °C to reflow the binder for 4 hours. After this, the porous carbon structure is saturated with a solution of sulfur in a low boiling solvent at a temperature of 40-45 °C under vacuum: 10-20 mm Hg, as shown in Fig. 1. Impregnation and evacuation of solvent are repeated 4-5 times to achieve a 70 % sulfur content and higher in the cathode. After that, the cathodes are dried at a temperature of 40-60 °C for 6 hours until the remnants of the low boiling solvent are completely removed from the cathode structure.

Schematically this method is shown in Fig. 1.

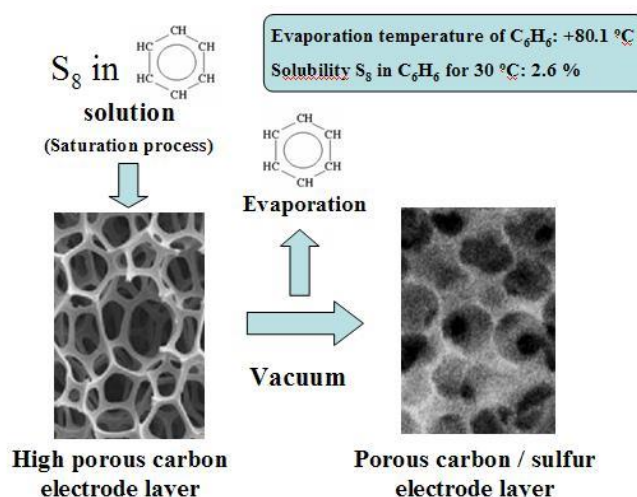


Figure 1. The schematic diagram of manufacturing high-energy sulfur electrodes by an innovative method of saturation of a porous carbon matrix with sulfur.

Manufactured electrodes, the characteristics of which are presented below, have the following composition: 70% sulfur, 27% carbon (soot), 3% binder (fluoroplastic). The weight of sulfur per unit geometric surface of the cathode was 3.0-3.5 mg/cm². This meets the requirements of commercial applicability for the content of active material for sulfur electrodes of lithium-sulfur batteries [1].

For subsequent testing, sulfur electrodes were manufactured in casings of prismatic elements or disk elements. In Fig. 2A shows the photos electrodes before and after saturation of the gray porous carbon matrix in the housings of elements of size 2016. Figure 2.B shows the optical microscopy of the finished sulfur electrode.

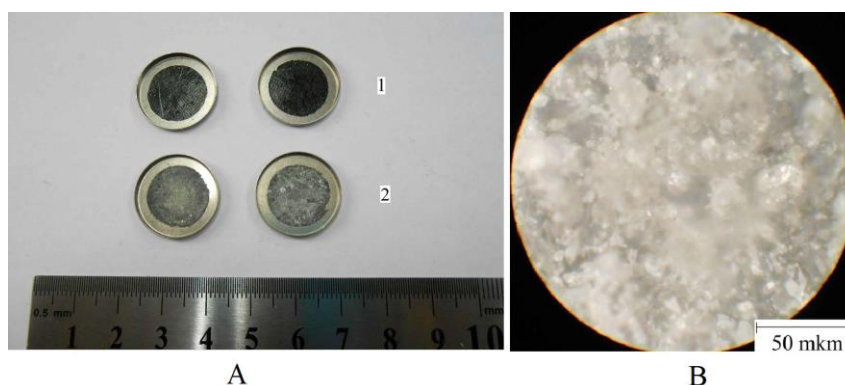


Figure 2. Sulfur electrodes made by saturation with a gray porous carbon matrix. A: 1 - porous carbon matrix before saturation with sulfur; 2 - porous carbon matrix field of saturation with sulfur. B - optical microscopy of sulfur electrode.

Electrochemical characteristics of sulfur electrodes produced by the saturation method

Electrochemical cells were manufactured in disk housings of size 2016. Metal lithium was used as the negative electrode. Composition of electrolyte: DME, DOL, (1:1), 1 M $LiN(CF_3SO_2)_2$. Separator – Celgard 2300. In Fig. 3 shows the comparative discharge characteristics of sulfur electrodes that have been made by saturation with a gray porous carbon matrix.

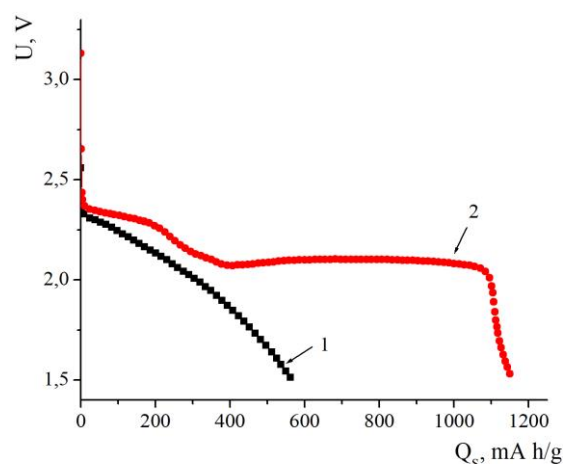


Figure 3. Discharge characteristics of sulfur electrodes that have been made by the saturation method. The discharge current is 0.1 C. Curve 1 is an electrochemical cell with a cathode that does not have an optimized macrostructure. Curve 2 is an electrochemical cell with a cathode having an optimized macrostructure

From Fig. 3 shown that the sulfur electrode made using the developed innovative method and having an optimized macrostructure has a high specific discharge capacity of 1150 mAh/g, which is 70% of the theoretical capacity. Thus, the method is effective and promising for the commercial manufacture of high-energy sulfur electrodes of lithium-sulfur batteries.

Acknowledgment

The work was carried out according to the project based on framework of NATO SPS 985148 project "Development of New Cathodes for Stable and Safer Lithium-Sulfur Batteries". Ukrainian State University of Chemical Technology participate in this project.

Company Enerize Corporation is and industrial partner of this project.

References

1. Patrick Bonnick, Erika Nagai, John Muldoon, *J. Electrochem. Soc.*, **165**(1), p. A6005 (2018).

Enabling Reliable Lithium Metal Batteries by a Bifunctional Anionic Electrolyte Additive

Yulin Ma^{a,b,*}, Zhenxin Zhou^{a,b}, Changjin Li^{a,b}, Long Wang^{a,b}, Yang Wang^{a,b}, Xinqun Cheng^{a,b}, Pengjian Zuo^{a,b}, Chunyu Du^{a,b}, Hua Huo^{a,b}, Yunzhi Gao^{a,b}, Geping Yin^{a,b}

School of Chemistry and Chemical Engineering, Harbin Institute of Technology No. 92, West Dazhi Street, Harbin, China mayulin@hit.edu.cn

Lithium metal has been considered as an attractive anode for high energy density lithium battery because of high specific capacity and the lowest redox potential [1]. However, the growth of Li dendrites during cycling has hindered the practical application of Li metal battery (LMB) [2]. Herein, TTFEB is adopted as a bifunctional electrolyte additive to improve the performance of Li metal anode, which is beneficial for the surface chemistry of anode and the property of the electrolyte. A LiF-rich SEI layer and enhanced Li^+ migration in electrolyte can be achieved with 2% TTFEB, which result in uniform Li deposition without uncontrollable Li dendrites. With controlled Li deposition in TTFEB-containing electrolyte, a significantly improved Coulombic efficiency ($\sim 96\%$) in Li|Cu cell, long lifetime (over 1000 h), and weak polarization in Li|Li cell can be obtained. Moreover, excellent cycling performance and rate capability of Li|LiFePO₄ cells with TTFEB are also presented in this work. Our strategy provides new insights on the diverse function of electrolyte additives for rechargeable LMB.

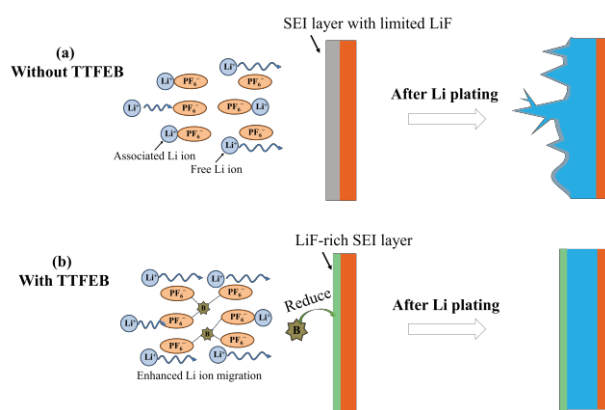


Figure 1. Schematic illustration of the structural changes of Li metal anodes and property of electrolyte: (a) without TTFEB; (b) with TTFEB.

Reference

1. Xu, W., Wang, J., Ding, F., Chen, X., Nasybulin, E., Zhang, Y., & Zhang, J. G. (2014). Lithium metal anodes for rechargeable batteries. *Energy & Environmental Science*, 7(2), 513-537.
2. Lin, D., Liu, Y., & Cui, Y. (2017). Reviving the lithium metal anode for high-energy batteries. *Nature nanotechnology*, 12(3), 194.

Improved Electrochemical Performance of NMC Cathode Material Produced via Spray-Roasting Route

E. Legotin^{a,b}, K. Fröhlich^a, R. Hamid^a, N. Zhang^a, C. Täubert^a, and F. Winter^b

^a AIT Austrian Institute of Technology GmbH, Center for Low-Emission Transport, Giefinggasse 2, 1210 Vienna, Austria

^b TU Wien, Institute of Chemical, Environmental and Bioscience Engineering, Getreidemarkt 9, 1060 Vienna, Austria

Corresponding author: evgeny.legotin@ait.ac.at

Lithium nickel cobalt manganese oxide ($\text{LiNi}_{1/3}\text{Co}_{1/3}\text{Mn}_{1/3}\text{O}_2$), also known as NMC111, is one of the most widely used cathode materials for lithium-ion batteries. Due to their high power and energy density as well as good thermal and cycling stability, NMC materials easily meet major requirements for automotive applications. NMC is already employed in a variety of electric vehicles, both in pure form (e.g. in Daimler Smart EV) and as a blend with lithium manganese oxide (LMO) [1]. However, the high cost of NMC materials remains one of the negative factors regarding their application in commercial batteries. The market prices of conventional NMC materials are now around 21-31 \$/kg, being higher than those of lithium iron phosphate and lithium manganese oxide (about 16 \$/kg and 7 \$/kg, respectively) [2]. The prices are affected by both the costs of the respective metals and production expenses.

Recently, we reported on a new large-scale production route of NMC111 cathode material [3]. NMC111 was produced by spray roasting of an aqueous solution of nickel, cobalt and manganese chlorides and subsequent high-temperature treatment of the resulting mixed oxide with lithium precursor. Spray roasting is known as an established industrial technology to produce fine metal oxide powders. However, to the best of our knowledge, no work on large-scale spray-roasting production of electrode materials had been published until recently. Due to the continuous manufacturing process, reduced processing times as well as lower power inputs are expected.

The feasibility of the manufacturing process was proven and the effect of treatment conditions on material characteristics was examined [3,4]. In the current study, the formation reaction of NMC111 was additionally investigated by means of simultaneous thermal analysis. The results of latest electrochemical tests are presented. The electrochemical performance of the material has been improved by adjusting the slurry formulation.

The particle morphologies were studied by both scanning electron microscopy and laser diffraction particle size analysis. It was shown that the final NMC material represents a well-crystallized powder with primary grain size of about 0.4 μm . The phase purity of the material was verified by X-ray diffraction measurements. The control of the material stoichiometry as well as impurities level was performed by means of X-ray fluorescence analysis.

Electrochemical tests were performed in coin 2032-type half cells and included long-term cycling, rate capability test, cyclic voltammetry and pulse tests at different state-of-charge levels. The synthesized material shows a discharge capacity of 137 mAh/g after 100 cycles at a C-rate of C/10 in the potential range 3.0-4.2 V, good average coulombic efficiency of 99.6%, and capacity retention of 93% after 100 cycles.

The obtained material reveals characteristics comparable to those of market-available NMC111 materials. Further adjustment of the material production route as well as electrochemical testing in a full-cell configuration vs. graphite anode is ongoing.

Acknowledgments

We are grateful to the Austrian Research Promotion Agency (FFG) for financial support of this work (project PyroBat, grant application No. 848603).

References

1. D. Andre, et al., *J. Mater. Chem. A*, **3**, 6709–6732 (2015).
2. C. Pillot, *The Rechargeable Battery Market and Main Trends. 2016 – 2025*. Presented at the BATTERIES conference in 2017 in Nice, France.
3. K. Fröhlich, et al., *J. Solid State Electrochem.*, **21**(12), 3403–3410 (2017).
4. E. Legotin, et al., in *E-MRS 2017 Fall Meeting/2017*, A.P1.45 (online access), Warsaw (2017).

A Computational Study on the Effect of Stress Concentrations on Stress-Electrochemistry Interactions in Li-ion Battery Electrode Particle

Mohammad Ayub Ansari^a, Pramod Yallappa Kumbhar^a, and Narasimhan Swaminathan^a

^a Department of Mechanical Engineering, Indian Institute of Technology Madras, Chennai 600036, India

Abstract

A Li-ion battery (LIB) anode particle made of graphite is studied to analyze the role of stress concentrations due to voids on the interaction between electrochemistry and mechanics. First, charge-discharge (CD) voltammetry experiment is simulated; following which the particle is first discharged and then charged (DC). These experiments are conducted for various ratios of hole radius to particle radius $\left(\frac{r}{R}\right)$. Our results show that for DC case the effects of stresses on the electrochemical response decreases with the increase in $\left(\frac{r}{R}\right)$ ratio, while for CD voltammetry the effects may increase or decrease depending on $\left(\frac{r}{R}\right)$ ratio and particle size. Specifically, for particle size less than 5 μm the effect of stress reduces with increase in $\left(\frac{r}{R}\right)$ ratio and for particle sizes between 5 and 25 μm the effect of stress may increase or decrease depending on $\left(\frac{r}{R}\right)$ ratio. The simulations are used to observe the phenomenon and explain the underlying physics.

Introduction

The effects of intercalation induced stresses in LIB are well explored and modeled through the thermo-elasticity framework [1-3], where concentration gradients are treated in a manner analogous to temperature gradients. Stresses developed can cause failure of the particles. Furthermore, various phenomena associated with electrochemical behavior [4] are also affected. In addition to the diffusion-induced stresses (DIS), stress-induced diffusion (SID) affects the concentration distribution, which in turn impacts the electrode's response to the externally applied-voltages. For example, it was shown in [5] that stress generation in particle not only could lead to mechanical degradation and failure but also affect its electrochemical response. Electrode particles have voids or other geometric discontinuities which create stress concentrations. To understand the physics of these additional driving forces on the electrochemical response, particles with a geometrical discontinuity like a hole is studied. To this end, various particle sizes (radius R) with different hole sizes (radius r), positioned at the center of the particle is subjected to electrochemical loads and the physics of the response is understood.

Equation and boundary conditions

Two-way interaction between stress and diffusion is modeled by including stress-dependent chemical potential (μ) (Eq.1). Young's modulus ($E(c)$) is assumed to be concentration (c) dependent.

$$\mu = \mu_o + \bar{R}T \ln C - \alpha \left(\Omega \sigma_h + \frac{1}{2E^2} \frac{dE}{dc} (v \sigma_{ii} \sigma_{kk} - (1 + v) \sigma_{kj} \sigma_{kj}) \right) \quad (1)$$

Where, \bar{R} is the universal gas constant, T is the absolute temperature, v is Poisson's ratio, σ_{ii} is the Cauchy stress and σ_h is the hydrostatic component of the stress. α determines whether the effects of stresses are included. $\alpha=0$ is for no role of stress, while $\alpha=1$ includes the effects of stresses. Nonlinear coupled, equations are then solved in order to obtain the evolution of stress distributions (Eq.(2)) and the concentrations (Eq.(3)) with the applied voltage.

$$\sigma_{ij,j} = 0 \quad (2)$$

$$\frac{\partial c}{\partial t} + \nabla \cdot (-Mc \nabla \mu) = 0 \quad (3)$$

M is mobility of Li ion in graphite. Potentiodynamic flux is specified using Butler-Volmer expression at the outer boundary (See Eq(4)), where F is the Faraday's constant, η is the overpotential and λ is 0.5. The current density was monitored as a function of the applied voltage for $\alpha=0$ and $\alpha=1$ for various $\left(\frac{r}{R}\right)$ ratios. The difference between the peak current densities for $\alpha=0$ and $\alpha=1$ was used as a measure of the effect of stress on the electrochemical response.

$$J(R, t) = \left[k_{re} c_l^{(1-\lambda)} (c_m - c)^{(1-\lambda)} c^\lambda \right] \left[\exp \left(\frac{F\eta(1-\lambda)}{\bar{R}T} \right) - \exp \left(-\frac{\lambda F\eta}{\bar{R}T} \right) \right] \quad (4)$$

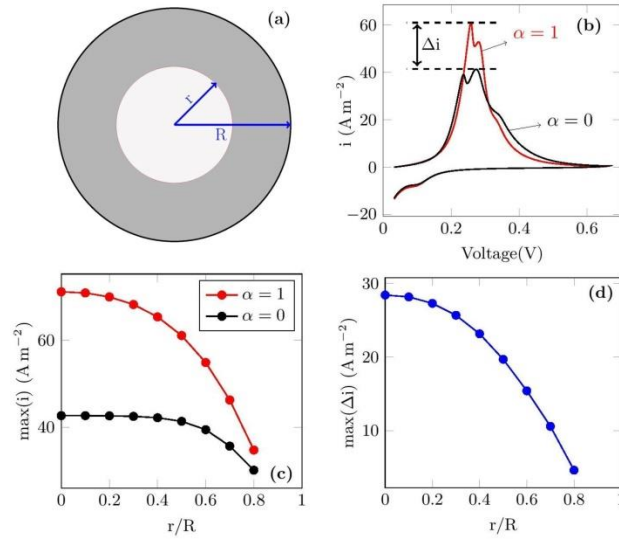


Figure 1. (a) Particle with $\left(\frac{r}{R}\right)=0.5$, (b) DC voltammetry plot for 10μm particle with $\left(\frac{r}{R}\right) = 0.5$, (c) Variation of peak current with increase in $\left(\frac{r}{R}\right)$ ratio for DC voltammetry, (d) Represents effect of stresses with increasing $\left(\frac{r}{R}\right)$ ratio for DC voltammetry.

Results and Discussion

Figure 1(b) shows the DC voltammogram for particle $R=10\mu\text{m}$ and $r=5\mu\text{m}$ at the center of particle (i.e. $\left(\frac{r}{R}\right) = 0.5$). It is clear that the peak current is different for $\alpha=0$ and $\alpha=1$. Hence the difference in peak current $\max(\Delta i)$ can be used to quantify the influence of stress on electrochemical response. Figure 1(c) shows the variation of $\max(i)$ with increasing $\left(\frac{r}{R}\right)$ ratio for 10μm particle and Figure 1(d) shows the variation of $\max(\Delta i)$ with the increase in $\left(\frac{r}{R}\right)$ ratio. As

observed from figure, the effect of stresses reduces with increase in $\left(\frac{r}{R}\right)$ ratio because the maximum hydrostatic stresses in the particle reduce in the presence of hole. Figure 2 below shows the effects of stress for various particle sizes with increasing $\left(\frac{r}{R}\right)$ ratio for both CD (Figure 2(a)) and DC (Figure 2(b)) voltammetry. It can be observed from figure 2(a) that in case of CD voltammetry, the effect of stress reduces with increase in r/R ratio for particle size less than $5\mu\text{m}$ and for particle size $5\mu\text{m}$ - $25\mu\text{m}$ effect of stress is high and irregular. For particle size greater than $25\mu\text{m}$ there is increase in effect of stress with increase in $\left(\frac{r}{R}\right)$ ratio. For particle size greater than $70\mu\text{m}$ there are no effect of hole and the effect of stresses remain constant. Figure 2(b) represents effect of stress for DC voltammetry; it can be observed that the effect of stress reduces with the increase in radii of hole and the behavior is same for all the particles.

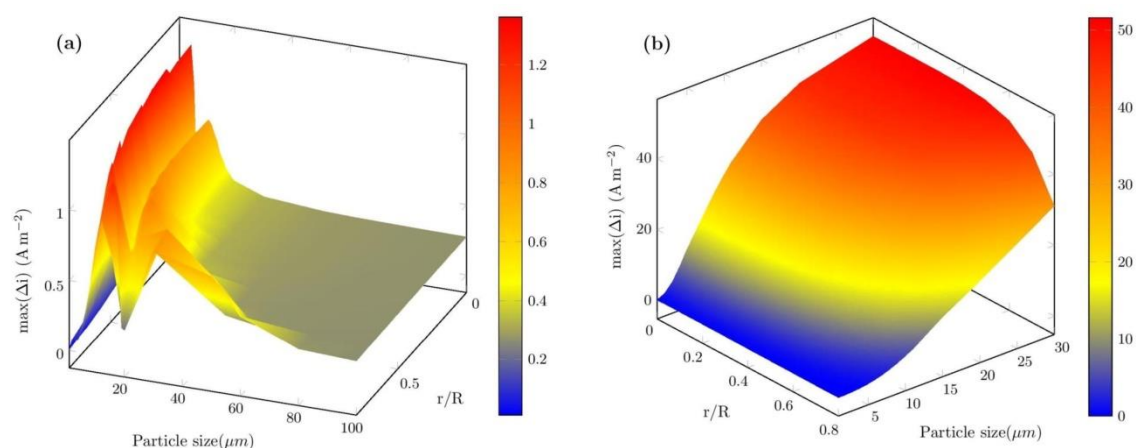


Figure 2. (a) Effect of stress for CD voltammetry, (b) Effect of stress for CD voltammetry.

References

1. X. Zhang, W. Shyy, and A. M. Sastry, *J. Electrochem. Soc.*, **154**, A910 (2007).
2. S. Golmon, K. Maute, S.-H. Lee, and M. L. Dunn, *Appl. Phys. Lett.*, **97**, 033111 (2010).
3. R. Deshpande, Y. Qi, and Y.-T. Cheng, *J. Electrochem. Soc.*, **157**, A967 (2010).
4. A. Mukhopadhyay and B. W. Sheldon, *Prog. Mater. Sci.*, **63**, 58 (2014).
5. N. Swaminathan, S. Balakrishnan and K. George, *J. Electrochem. Soc.*, **163**, A488-A498 (2016).
6. M. Alnæs, J. Blechta, J. Hake, A. Johansson, B. Kehlet, A. logg, C. Richardson, J. Ring, M. Rognes and G. Wells, *Arch. Numerical Software.*, **3**, 100 (2015).

Contribution to chemistry of EMIM.BF₄ ionic liquid

J. Vondrák^a, M. Sedlaříková^a, J. Máca^a

^a Department of Electrical and Electronic Technology, Brno University of Technology, Technická 10, 616 00 Brno, Czech Republic

Ionic liquid EMIM.BF₄ with LiBF₄ was compared with EMIM.BF₄ with sulfolane. The viscosity, conductivity and specific volume are depressed by the presence of Li BF₄, which undergoes dissociation to anions and cations. The freezing point is lowered markedly due to high cryoscopic constant (42 K/mol) correspondingly to very low heat of crystallization. Moreover, the fluidity of LiBF₄ is that of a non-newtonian liquid. Potential widow close to 3V makes the usage as electrolyte in lithium batteries possible.

Introduction

Ionic liquids (further, IL) based on substituted heterocyclic core cations and Li salts; their specific conductivity close to 10 – 20 mS/cm, excellent resistivity against incineration and good stability in wide range of potentials (called “potential window” sometimes) are their benefit. Therefore, their usage in lithium ion batterie’s is od much interest now ‘for example [1], [2]. On the other hand, the cationic IL does not contain lithium ions intrinsically and these ions must be delivered in any suitable way; one of them is based on the solubility of lithium salts in IL. The ethyl methyl imidazolium fluoroborate (further, EMIM ot EMIM.BF₄) and lithium fluoroborate LiBF₄ were taken for described experiments.

Dissolution of LiBF₄ in EMIM is due to high viscosity slow, but possible. We have prepared solutions up to 0.5 M which is certainly not the solubility limit.

Principle of comparative method

For the first description of system EMIM.LiBF₄ + additive LiBF₄ a comparative method was chosen. It consisted in comparison of those systems with system containing EMIM + sulfolane (SL) in corresponding range of concentrations. Sulfolane was taken as a polar but not dissociated substance of not much different molecular mass. The influence of ionic nature of LiBF₄ added should be observed in that way.

Density of the systems with LiBF₄ and/or sulfolane

The changes od density caused by addition LiBF₄ or SL was investigated. Apparently, the sulfolane as additive decreases the density on contrary to LiBF₄ who causes increase of that quantity. It can be considered that SL as an organic compound with lower density than EMIM is connected to increase of specific volume, while the LiBF₄ can be ascribed to the generation of forces causing contraction of the liquid phase. This effect must be considered in computation of thermodynamic parameters of the EMIM-LiBF₄ systems.

Cryoscopy

The status of the systems containing EMIM and other substances was evaluated by cryoscopy. The freezing point of EMIM+ LiBF₄ was lowered so that this corresponded to cryoscopic constant 42 K/mol in comparison to the same value for EMIM + SL, which reached 16 K/mol only. Hence, complete dissociation of Li salt in EMIM + LiBF₄ must be expected and high cryoscopic constant of EMIM-LiBF₄ corresponds to formation of two ionic particles and the system can be described as a solution of strong univalent electrolyte, on contrary to sulfolane where any dissociation can be hardly expected.

Transport properties

The solution of EMIM.BF₄ with LiBF₄ is very viscous and its conductivity is decreased almost from 10.cm⁻² several times. This is rather anomalous, as the conductivity is decreased enhancing of ion concentration. The viscosity of system containing Li salt is increased on similar way and it shows typical non-newtonian behaviour. In the case of system ENIM + sulfolane, the diffusion coefficient smoothly decreases, and the standard properties of such systems are maintained. (see Fig. 1 for system EMI + SL and Fig. 2 for system EMIM + LiBF₄)

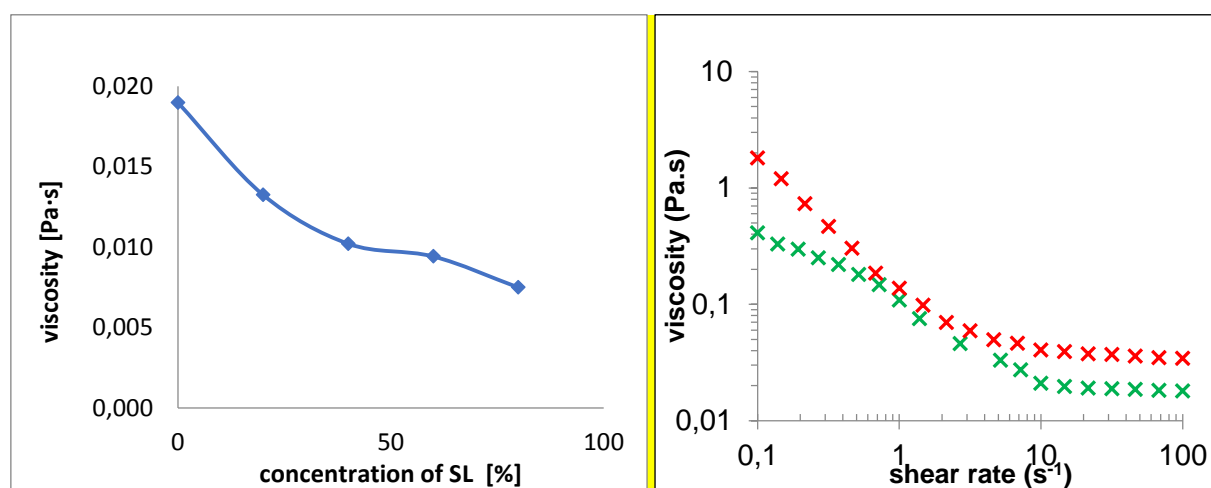


Figure 1. (left) Dynamic viscosity of the system EMIM + SL

Figure 2. (right) Dynamic viscosity if pure EMIM (green) and EMIM with added LiBF₄ (red)

Therefore, the system of EMIM ; ionic compound cannot be considered as a system containing EMIM as solvent and LiBF₄ as solute and it would be worth of deeper theoretical treatment. On the other hand, the system of EMIM.BF₄ + sulfolane behaves as a mixture of two miscible substances without formation of any temporary intermediate compounds which should be governed by Walden Rule at least approximately.

Walden Rule

In a very simplified way, the movement of ions in liquid can be described as result of electrostatic force impeding to fluidity. This was verified on the system EMIM-SL (see Table 1)

Test of Walden Rule validity (symbol W is the product of viscosity and molar concentration of IL.) The quantity denotes as symbol W is product of viscosity η and molar conductivity, i.e.,

fraction of specific conductivity σ and molar concentration x . For the system, EMIM-SL its value is approximately constant which indicates the behaviour of the system as a solution of EMIM in nonpolar SL. Contrary to this, such computation was considered not adequate due to non-newtonian viscosity of the system and such a correlation should be hardly possible.

Table 1. Validity test of Walden rule for EMIM + sulfolane; symbols: $W = \eta \cdot \sigma / x$ (cPa.s, S/cm, mole /dm³)

% SL	W
0	9.50E+2
20	1.06E+3
40	1.18E+3
60	1.06E+3
80	9.89E+2

The quantity denoted as symbol W is product of viscosity and molar conductivity, i.e., fraction of specific conductivity and molar concentration x . For the system, EMIM-SL its value is approximately constant which indicates the behaviour of the system as a solution of EMIM in nonpolar SL. Contrary to this, such computation was considered not adequate due to non-newtonian viscosity of the system and such a correlation should be hardly possible.

Potential window

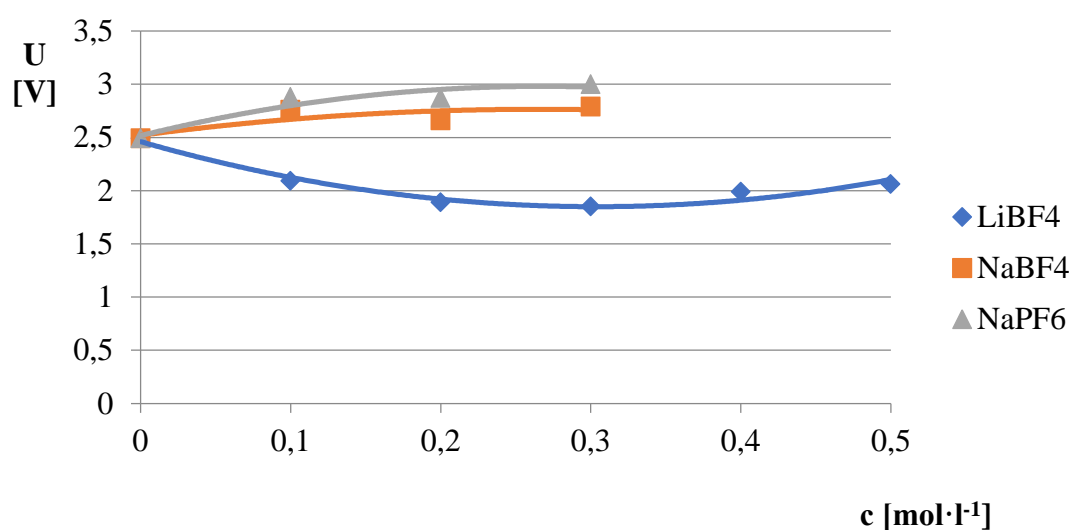


Figure 3. Potential window of lithium and/or sodium salts in EMM

Preliminary results of potential window for lithium or sodium salt containing EMIM.BF₄ was investigated from viewpoint of possible application. The width of the window is in vicinity of 3 volts, which would be sufficient for lithium batteries of lower voltage (see Fig. 3). Improvement in this direction would be welcomed. It could be reached either by use other anions for both EMIM and Li salt, or by choosing a more stable core replacing that one used in EMIM. The potential window is sufficient for application in lithium or sodium intercalation cells of voltage not exceeding 3 V.

Conclusion

By comparison of systems EMIM-SL and EMIM-LiBF₄, some conclusions can be drawn. First, the latter exhibits lower conductivity despite higher concentration of ions. Further, also the densification by LiBF₄ indicates the existence of electrostatic attractive forces which inhibit the ionic movement and fluidity in general. For the use in electrochemical power sources, the lowering of conductivity must be taken in concentration. Another until now not discussed problems are high solubility of many materials and unknown health issue of ionic liquids in general.

Acknowledgement

This work was supported by project the Centre for Research and Utilization of Renewable Energy (CVVOZE) at financial support of MŠMT under project No. LO1210 – “Energy for Sustainable Development (EN-PUR).

References

1. B. Scrosati et al, *Angew. Chem, Ind. Edit*, 55,500 (2016).
2. Jin Xiang, F. Wu and Y. Huigen,, *J.Power Sources* 233, 115(2013)

NMC cathode material for large scale application in EV

K. Banov^{1,2}, D. Ivanova², L. Fachikov², B. Banov^{1,3}

¹⁾ Institute of Electrochemistry and Energy Systems, IEES-BAS, Bl.10, 1113 Sofia

²⁾ University of Chemical Technology and Metallurgy, UCTM, “K. Ohridski” 1756 Sofia

³⁾ European Polytechnical University, 23, “St. St. Cyril and Methodius” str., 2300 Pernik

To meet the requirements of electric and hybrid vehicles (EV HEVs) and due to the rising prices of raw materials as nickel and cobalt, manganese rich materials attract more attention. In this work was made an initially research for estimation the most suitable stoichiometry of components for this materials. The following materials $\text{LiMn}_y\text{Co}_{1-y}\text{O}_2$ and $\text{LiNi}_y\text{Co}_{1-y}\text{O}_2$ ($y = 0.1, 0.3, 0.5$) have been synthesized, by Solid State Reaction SSR within temperature range from 650-750°C in an oxygen atmosphere. Electrochemical measurements have been performed in CC mode within 3.0-4.75V vs Li reference electrode. The test cells consist of tested cathode material, assembled in 2032-type coin test cell with lithium metal as an anode and 1.0M LiPF_6 in EC:DMC as electrolyte. For a better understanding of the difference between the materials, their structures were examined by scanning electron microscopy (SEM) and X-ray Powder Diffraction (XRD).

The main objectives in the research of lithium ion batteries (LIBs) are the increase of the energy density and the cost reduction of materials used. The material characteristics related to specific energy, power density, cycle life and safety play basic role. Main segment of battery market in the world of portable lithium ion batteries is occupied by the lithium cobaltite, because of its easy synthesis way, stable electrochemical characteristics, high discharge voltage and good energy density. On the other hand lithium phosphate is the cathode material for large scale applications nevertheless at the expense of discharge voltage, low electronic conductivity of active electrode material (AEM) and low specific capacity resulting in overall modest energy density. The cathode material is cheap, environmentally friendly, nontoxic and even more environmentally compliant. It is not necessary to be recycled because it can be used directly as phosphate artificial manure. Lithium manganese dioxide spinel is another candidate as high voltage, environmentally friendly cathode material, but it also suffers of low stability and cyclability. An overlithiation or partial replacement of manganese ions with cobalt [1, 2], nickel or aluminum improve enough cycleability and stabilize crystal structure suppressing the Jan Teller Effect of manganese dioxide. The last candidate is NMC offering high discharge capacity up to 276 mAh g⁻¹ in the voltage window from 2.0V to 4.8V, high discharge voltage, good stability, acceptable cycleability and perfect power density [3]. The usual ratio between different metals is 1:1:1 thus obtaining AEM with 33% of cobalt, nickel and the same percentage of manganese [4].

In our study we are focusing on investigating and developing NMC cathode material with high manganese content, higher than 50% thus reducing the price of obtained AEM but preserving, in big part, all its advantages as high discharge voltage, discharge capacity and overall energy and power density. Electrochemical performances of lithium spinel, lithium cobalt and NMC 1:1:1 are used as base line for comparison and internal reference. The AEM are synthesized by the same

R&D group thus eliminating differences appearing from application of other preparation techniques [1, 2, 5]. All electrochemical testes are realized in the same laboratory and staff.

We have started our investigation with preparing and characterizing two AEM compositions $\text{LiNi}_x\text{Co}_{1-x}\text{O}_2$ (NMC 109, 307, 505) and $\text{LiMn}_x\text{Co}_{1-x}\text{O}_2$ (NMC 019, 037, 091). Both types of materials are used as “pilot tests” for the preparation of investigated NMC compounds. All cited samples are successfully synthesized by solid state reaction SSR in the temperature ranged between 650 and 750°C and physicochemical characterized by XRD, Scanning Electron Microscopy (SEM), and Energy-Dispersive X-ray Spectroscopy (EDS) and electrochemically tested.

Figure 1 shows the XR diagram of $\text{LiMn}_{0.1}\text{Co}_{0.9}\text{O}_2$ (NMC 019). Active electrode material is well crystallized and present pure phase with negligible content of impurities, of Co_3O_4 and MnO_2 , obtained during the synthesis way. Nevertheless the AEM is indexed as pure phase. The used synthesis way is optimised for preparation of investigated AEM, as two or three components compounds.

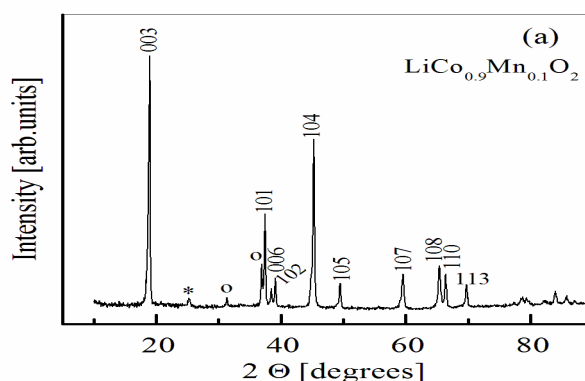


Figure 1. XRD pattern of $\text{LiMn}_{0.1}\text{Co}_{0.9}\text{O}_2$ (NMC 019) prepared by SSR. Present impurities are indexed to Co_3O_4 (°) and MnO_2 (*).

The Figure 2 presents the SEM picture of same AEM $\text{LiMn}_{0.1}\text{Co}_{0.9}\text{O}_2$ (NMC 019). It can be seen from the picture that obtained AEM is more or less with spherical shape and particle size ranged from 50 up to about 200 nm.

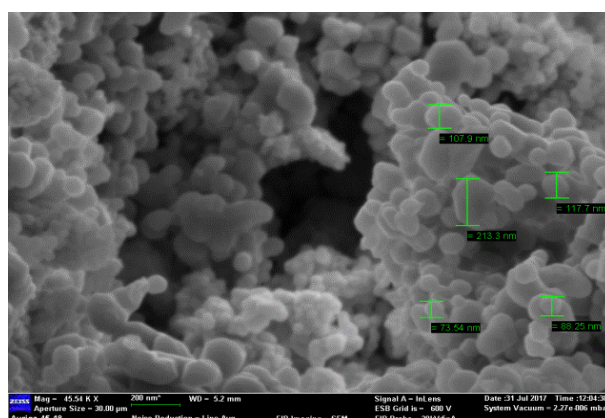


Figure 2. SEM picture of $\text{LiMn}_{0.1}\text{Co}_{0.9}\text{O}_2$ (NMC 019) giving information about particle size and overall granulometry of sample.

The specific surface area SSA of thus prepared samples are ranged from 7 to 12 m² g⁻¹ and porosity realised by micro and macro pores is 1:2 by ratio. The picture shows also that the AEM obtained is very uniform and with necessary particles size distribution. For designing cell for EV&HEV you need special electrode design based on uniform particles with dimensions less than the characteristic length of the diffusion coefficient. In our case we successfully realize this requirement.

Performed electrochemical testes are shown on Fig. 3. Small amount of manganese increase discharge potential of cell up to over 4 Volts. The middle discharge voltage we obtain is 4.05V for the AEM tested LiMn_{0.1}Co_{0.9}O₂, which is higher than the discharge voltage of LiCoO₂ 3.6 -3.8V depending of the applied discharge load. And this increase of voltage is due to very small amount of manganese in the structure of AEM, 10 % mol.

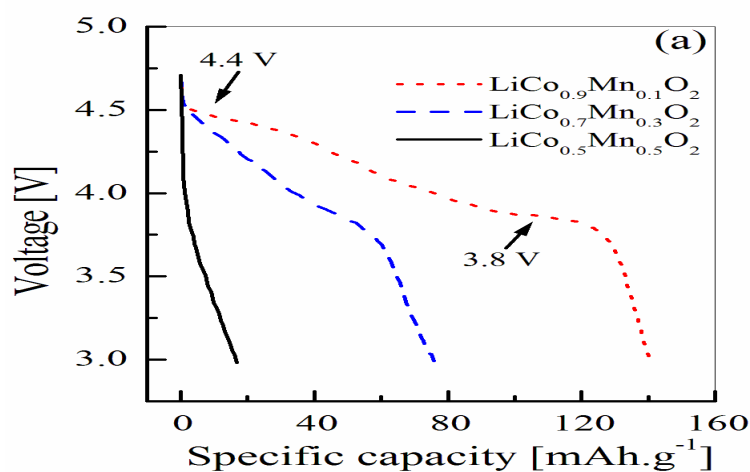


Figure 3. Charge discharge profile of LiMn_{0.1}Co_{0.9}O₂ (NMC 019, 037, 055).

Increasing the manganese percentage in the AEM the electrochemical characteristics decrease drastically. The results are shown on Fig. 3. This result demonstrates that increasing the manganese content is not the right way to increase the discharge voltage of tested AEM.

Acknowledgments

The author of the paper Dipl. Chem. Eng. Krum Banov is thank full for the financial support to the Operational Program "Science and education for smart growth" 2014-2020 of the European Union cofounded by the European Social Fund through the Project BG05M2OP001-2.009-0015 "Support for the development of capacity of doctoral students and young researchers in the field of engineering, natural and mathematical sciences".

References

1. V. Manev et. al., *Journal of Power Sources* **57**, 99-103 (1995)
2. B. Banov et. al., *Journal of Power Sources* **68**, 578-581 (1997)
3. Y. Todorov et. al., *ISE Annual Meeting 97-18*, 176, France, Ext. Abstr. 1997
4. H. J. Noh et. al., *Journal of Power Sources*, **121**, 233, (2013)
5. B. Banov et. al., *Journal of Power Sources*, **54** (2), 268-270, 1995

Cathode Material Based on S/C Composite for Li-S Batteries

K. Gavalierová^a, D. Capková^a, A. Straková Fedorková^a, R. Oriňaková^a,
M. Strečková^b

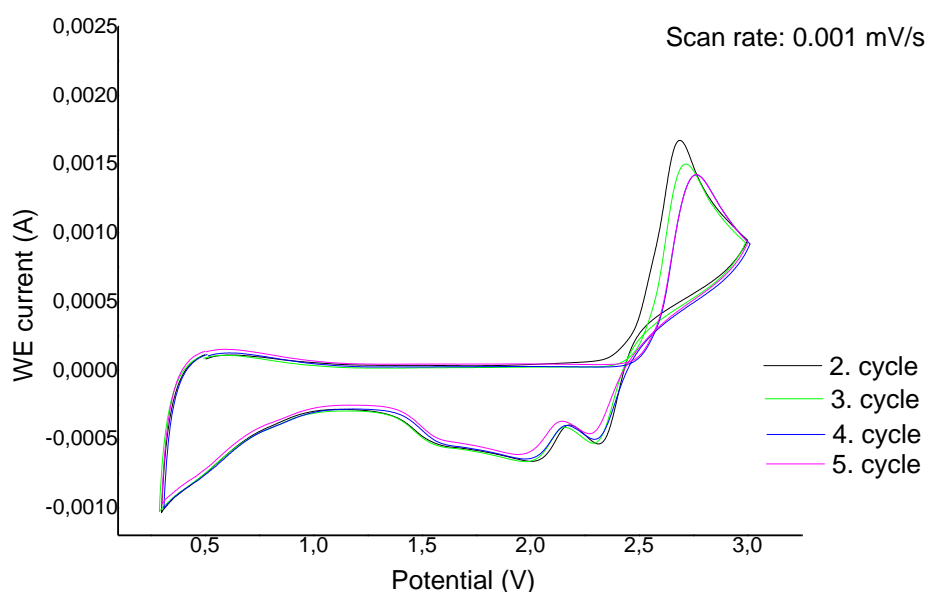
^a Department of Physical Chemistry, Pavol Jozef Šafárik University, Moyzesova 11, 040 01 Košice, Slovakia

^b Institute of Material Research, Slovak Academy of Sciences, Watsonova 47, 040 01 Košice, Slovakia

Nowadays, there is a huge demand for energy due to the population growth and technological progress. The researchers pay an intensive attention to the devices able to produce and store energy. Lithium-sulfur batteries represent this kind of device.

Li-S batteries play a significant role in a development of rechargeable batteries. They are attractive adept due to their high theoretical capacity of sulfur (1672 mAh g^{-1}), abundance and non-toxicity of sulfur and low cost of sulfur. Li-S battery belongs to the conversion type of battery; it means new chemical compounds during electrochemical reactions. However, it is needed to solve some scientific problems, such as non-conductivity of sulfur and its volume increase during charge and discharge process [1, 2]. To solve these problems, composite materials based on sulfur are investigated. This abstract deals with sulfur/carbon composite as a cathode material for lithium-sulfur batteries. There are more forms of carbon which can be mixed with sulfur to improve the battery performance. Herein we report carbon nanofibers added to sulfur/ CS_2 solution as a composite cathode material.

Cyclic voltammetry, electrochemical impedance spectroscopy and galvanostatic charge/discharge process were used to study electrochemical behaviour of the battery. Fig. 1 shows the cyclic voltamperogram of the sample S/CS_2 + PAN PVP 1.5 carbon nanofibers recorded at the scan rate 0.001 mV/s . As seen there are two cathodic peaks owing to the two-step reduction of sulfur and the anodic peak. This indicates the electrochemical activation in the sample.



Acknowledgments

This research was sponsored by the NATO Science for Peace and Security Programme under grant 985148 and by the project VEGA 1/0074/17.

References

1. Yin Y., Xin S., Guo Y., Wan L.: *Angewandte Chemie* 52, 13186 (2013).
2. Strakova Fedorkova A., Kazda T., Gavalierova K., Gomez-Romero P., Shembel E.: *Int. J. Electrochem. Sci.* 13, 551 (2018).

Gel Polymer Electrolytes Modified Nanoparticles and Polymerized in Magnetic and Electric Fields

M. Jahn^a, I. Veselkova^a, M. Sedlaříková^a, J. Vondrák^a, K. Bartušek^b

^a Department of Electrical and Electronic Technology, The Faculty of Electrical Engineering and Communication Brno University of Technology, Technická 10, Brno 612 00, Czech Republic

^b Department of Theoretical and Experimental Electrical Engineering, The Faculty of Electrical Engineering and Communication Brno University of Technology, Technická 10, Brno 612 00, Czech Republic

Gel polymer electrolytes are perspective electrolytes for new types of Li-ion batteries today. The properties respectively advantages of these gels can be used also in other fields of electrochemistry. The gel polymer electrolyte is composed of a conductive component (liquid electrolyte) and the polymer component (methacrylate-based polymer). In this paper, I present fundamental characteristics of gel polymer electrolytes modified nanoparticles and preparation of these gel polymer materials with nanoparticles polymerized in electric and magnetic fields.

Introduction

Gel polymer electrolyte materials separate anode and cathode and play the significant role of transmitting lithium ions during charging and discharging processes. Also, electrolyte is one of the key components that define the battery's performance: charging/discharging capacity, safety, cycling performance, and current density. The main advantages these electrolytes are the elimination leakage of electrolyte, better resistance to vibration and mechanical damage, or better resistance to volume changes of the electrodes. Another advantage is the adhesion of the gel to the electrode surface, this effect reduces the formation of aggregates on the surface and thus provides protection against internal short circuit and reduction capacity. Advanced gel polymer electrolytes having the same ionic conductivity as liquid electrolytes (3,5,6,7,8). Subsequent research has focused on improving electrical, electrochemical and mechanical properties of these electrolytes with selected nanoparticles, which are influenced by magnetic and electric fields during polymerization (2,4).

Nanoparticles are characterized in sizes from about 1 nm to about 100 nm in at least one direction (1×10^{-7} to 10^{-9}) and in a certain spatial arrangement. Nanoparticles can form nanowires, nanotubes, nanocomposites, ceramic or other thin films or layers. Characterization of nanoparticles is a huge increase in the ratio of surface area to volume nanomaterial particles. This ratio strongly affects most of the chemical and physical bonds at the grain boundaries in the material. The behavior of nanoparticles is governed by quantum physics, and quantum phenomena lead to totally new possibilities (2).

Chemical composition

The gel polymer electrolyte is composed of a conductive component and the polymer component. This conductive part forms a salt LiPF_6 and a solvent EC/DEC (1:1 weight ratio). The polymeric part forms methyl methacrylate as a monomer, 2,2'-Azobis(2-methylpropionitrile) as a polymerization initiator (thermal polymerization) and ethylene glycol dimethacrylate as a networking agent (3,5). The molar proportion of monomer to the conductive component (0.5 mol/l LiPF_6 in EC/DEC) is 20 mol%. The molar proportion of polymerization initiator and networking agent to the monomer is for the polymerization initiator 1.0 mol% and for the networking agent 3.5 mol% (3,5,6,7,8). Nanoparticles were added to improve the electrical, electrochemical and mechanical properties of gel polymeric electrolytes. For all samples, the effect of physical fields on these properties was monitored (2,4). The specific conductivity of these electrolytes without added additives ranges in mS/cm (1 to 4 mS/cm) and the electrochemical stability is usually high, the usable potential window is 3.5 and 4.5 V (3,5,6). Selected nanoparticles of metal oxides used in the experimental part: alumina (Al_2O_3), tungsten oxide (WO_3), zirconia (ZrO_2), lanthanum oxide (La_2O_3), nickel oxide (NiO) and sodium titanate (NaTiO_3).

Sample resp. gel polymer electrolyte is disc with a diameter 16 mm and thickness 0,9 mm, which is cut out from the total area of formed (polymerized) gel. All handling of the gel is performed in a glove box with argon atmosphere. All chemicals are mixed in a vial with a magnetic stirrer in glove box. The time required for complete dissolution of all chemicals is about 20 minutes and time of polymerization in thermal chamber is 2 hours at 70 °C. Samples are measured in metallic El-Cells using the potentiostat Bio-Logic (potentiostatic impedance and linear sweep voltammetry) (3,5).

Experimental Results

In the experimental part four series of samples with different nanoparticles and parameters of polymerization. The amount (weight) of the nanoparticles was added in a percentage ratio to the conductive component (salt and solvent) of gel polymer electrolyte. The amount of nanoparticles used was 0.1 and 1 %. The conductivity component (salt and solvent) of the base gel without nanoparticles was 100% by weight. The conductivity component consisted of salt and solvent (100 %) + nanoparticles (0.1% or 1%). Measurement range of potentiostatic impedance is from 1 MHz to 0,1 Hz, steps per decade is 6 and amplitude sinusoidal signal is 10 mV. The measured results shown in Table 1, 2, 3 and 4. Measurement range of linear sweep voltammetry is from 0,1 V to 5,1 V and sweep speed 0,5 mV/s. Parameters and conditions for all series of samples were as follows:

- 1 series – test samples with 1% nanoparticles (the amount of nanoparticles to the polymer component is neglected) to verify the influence of magnetic and electric fields during polymerization, 1.2 kV electric field (Table 1);
- 2 series – is based on the first series of samples, for comparison of the polymerization even without the physical field (Table 2);
- 3 series – content of nanoparticles 1% and change in electric field of 5.6 kV (Table 3);
- 4 series – based on a third series of samples, the change amount of nanoparticles 0.1% (Table 4).

TABLE I. Conductivity of gel polymer electrolytes – series 1

Nanoparticles [type]	Conductivity [mS/cm]	
	<i>Magnetic field</i>	<i>Electric field</i>
free	2.96	3.67
Al₂O₃	2.12	0.97
NaTiO₃	4.35	3.69

TABLE II. Conductivity of gel polymer electrolytes – series 2

Nanoparticles [type]	Conductivity [mS/cm]		
	<i>Without field</i>	<i>Magnetic field</i>	<i>Electric field</i>
free	1.18	2.11	1.65
Al₂O₃	1.09	1.82	0.75
NaTiO₃	1.33	1.43	0.23
WO₃	1.92	2.07	0.79
La₂O₃	1.18	2.44	1.83

TABLE III. Conductivity of gel polymer electrolytes – series 3

Nanoparticles [type]	Conductivity [mS/cm]		
	<i>Without field</i>	<i>Magnetic field</i>	<i>Electric field</i>
free	1.18	2.66	1.93
Al₂O₃	1.05	2.28	1.66
La₂O₃	0.66	1.70	0.26
NaTiO₃	1.16	2.16	2.34
NiO₂	0.77	2.36	1.54
WO₃	0.54	2.17	1.76
ZrO₂	---	2.47	2.01

TABLE IV. Conductivity of gel polymer electrolytes – series 4

Nanoparticles [type]	Conductivity [mS/cm]		
	<i>Without field</i>	<i>Magnetic field</i>	<i>Electric field</i>
free	1.18	2.66	1.92
Al₂O₃	---	2.24	2.15
La₂O₃	0.67	2.64	2.69
NaTiO₃	2.19	2.61	3.30
NiO₂	0.92	1.89	2.40
WO₃	0.96	---	3.07
ZrO₂	0.06	0.65	3.05

From the measured values of gel polymer electrolytes is evident that the specific conductivity value is dependent on the nanoparticles used. Further results and potential windows of the samples will be published elsewhere.

Conclusion

These experimental results serve as an initial study. The measured and evaluated results show that nanoparticles affect ionic conductivity, electrochemical stability (potential window) and mechanical properties of gel polymer electrolytes. Measured quantities are influenced by physical fields during polymerization. There may be changes in the polymer network of the entire polymer system. The differences in the measured quantities range from tens percent to hundreds percent of the gel without added nanoparticles and without physical field effects, as shown in the tables 1-4.

Current development is focused on improving the parameters of polymer electrolytes: increase ion conductivity, extension in potential window and improvement of mechanical properties. Further research in this area will focus on the specific mechanisms and reactions during polymerization that are generated by the action of physical fields and the next series of measured samples will be prepared. Research will also focus on combining different types of monomers/copolymers. The main objective of this research is to explain the mechanisms during polymerization due to the action of physical fields

Acknowledgments

This work was supported by the grant FEKT-S-17-4595 "Materiály a technologie pro elektrotechniku III" and Centre for Research and Utilization of Renewable Energy under project No. LO1210 - "Energy for Sustainable Development (EN-PUR)".

References

1. Y. Kambe, CH. G. Agres, S. Patel, M. P. Stoykovish and P. F. Nealey, Ion Conduction in Microphase-Separated Block Copolymer Electrolytes. The Electrochemical Society Interface, **61-67**, vol. 26, no. 1, (2017).
2. Krajská hygienická stanice, Nanotechnologie a nanomateriály (2009), https://www.khsova.cz/01_aktuality/nanotechnologie.php?datum=2009-03-18.
3. O. Krejza, Gel polymer electrolytes for electrochromic device, p. 117, Brno: Vysoké učení technické v Brně, Fakulta elektrotechniky a komunikačních technologií, (2009).
4. B. Sedlák and I. Štoll, Elektřina a Magnetismus, p. 632, Academica, Praha (2002)
5. M. Sedlaříková, Polymerní gelové elektrolyty a jejich využití v elektrotechnice, p. 83, Brno: Vysoké učení technické v Brně, Fakulta elektrotechniky a komunikačních technologií, (2003).
6. A. M. Stephan, Review on gel polymer electrolytes for lithium batteries. European Polymer Journal, **21-42**, vol. 42, (2006).
7. C. A. Vincent, Polymer electrolytes. Progress in Solid State Chemistry, **145-261**, vol. 17, no. 3, (1987).
8. R. Zhang, Advanced gel polymer electrolyte for lithium-ion polymer batteries, p. 98, Iowa: Iowa State University, (2013).

Carrageenan as the Binder for the Lithium-Sulfur Batteries

K. Jaššo^a, T. Kazda^a

^a Department of Electrical and Electronic Technology, Brno University of Technology, Technická 10, 616 00 Brno, Czech Republic

With the technology growth of mobile devices and electric vehicles, demands for batteries capable of meeting their high energy requirements increased. Lithium-sulfur battery system have a potential to meet these requirements and to replace Li-ion batteries in various applications due to its higher theoretical capacity and potentially low price. However, it is necessary to solve several deficiencies of this technology prior to deployment in the commercial sphere. Some of them could be solved or at least suppressed using a suitable binder in the production of positive electrodes of these batteries. Due to the environmental protection, research is mainly focused on non-toxic types of binders. The non-toxic, water-soluble binders used in the food and cosmetics industry are of interest. This article deals with the use of carrageenan as a binder for lithium-sulfur batteries.

Introduction

Lithium-sulfur batteries (Li-S or LSB) have a potential to overcome the limits of current Li-ion technology and meet the demand for high energy density and low-cost energy sources. Sulfur is particularly promising thanks to its high theoretical capacity of 1672 mAh g⁻¹, high availability and low cost. However, lithium-sulfur battery system has some drawbacks, that need to be resolved before it could be deployed into commercial production. The most notable is the negative shuttle effect, when the active material is lost due to the dissolution of polysulphides generated during cell cycling, which results in significant capacity fading. Next drawback is the low conductivity of the sulfur; therefore, the positive electrode of Li-S battery must contain conductive material (commonly amorphous carbon), which reduces the content of active material in the volume of positive electrode. Another drawback is the volume change through which the electrode passes during cell cycling. This volume change causes mechanical stress in electrode material that may negatively affect its coherence and internal electrical conductivity. From the above statements, it is clear that the binder connecting the sulfur and conducting material have a significant effect on the resulting physical and electrochemical properties of the electrode.[1]

The most commonly used binder in the Li-S battery research is PVDF¹ that exhibits good properties in combination with other cell materials. However, to form a positive electrode slurry, it is necessary to dissolve PVDF in the NMP² solvent, which is according to the WHO³ slightly toxic.[2] Although PVDF works well with other cell materials and can keep electrode materials together during cycling, it has no positive effect on cell chemistry and brings health risk step into the manufacturing process. Interesting PVDF substitution could be organic water-soluble binders used in the food, pharmaceutical or cosmetics industry, such as carrageenans. Carrageenans are

¹ PVDF – Polyvinylidene fluoride

² NMP – N-methyl-2-pyrrolidone

³ WHO – World Health Organization

linear sulfated polysaccharides that are extracted from seaweeds belonging to red algae (class: Rhodophyceae). Depending on the type of seaweed and extraction method there are several types of carrageenans. Carrageenans are roughly classified into three main types: Kappa, Iota and Lambda that differ in the number and position of the ester sulfate groups on the repeating galactose units. Carrageenans contain sulfate leaving groups that should be able to capture polysulphides and hydroxyl groups that form stable conductive networks with carbon conductive additives.[3]

Experiment

In the first phase of the experiment, which is part of this article, 2 types of carrageenan differing in sulfate groups content from CP Kelco were examined: Sulfat 21.42% “Genuine” and Sulfat 31.4% “Lambda-like”.

The electrode samples were assembled into an electrochemical cell (El-Cell[®]) in argon glove box. The electrochemical cells thus prepared were subjected to electrochemical analyzes on the potentiostat (Biologic VMP3).

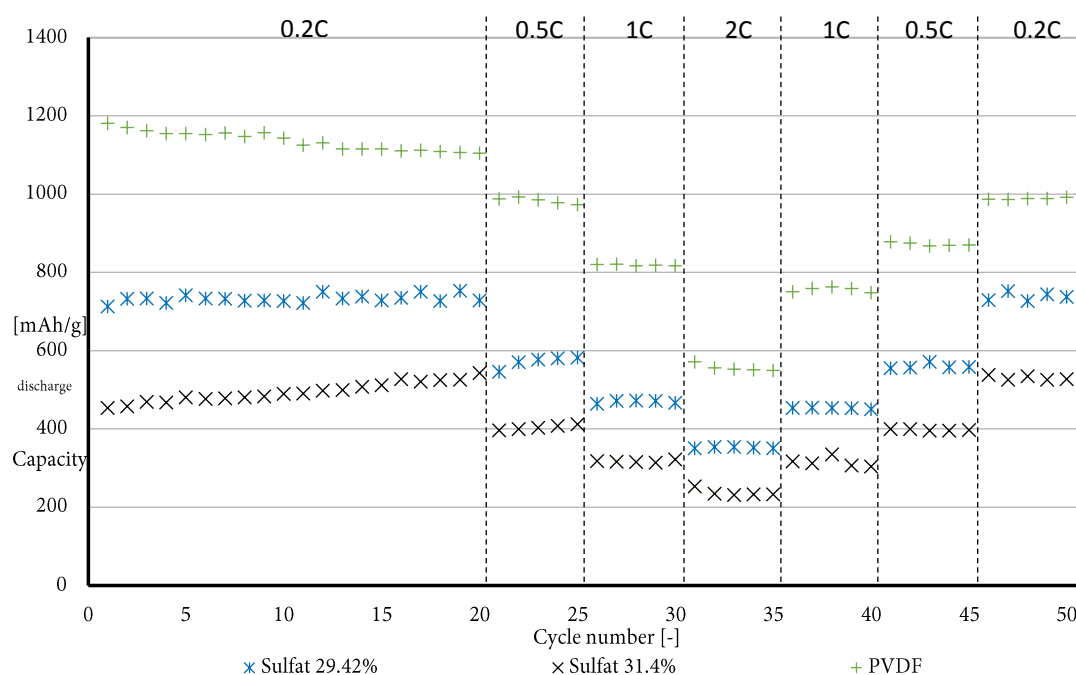


Figure 1. Comparison of discharge capacities of the electrode samples

For all samples, 50 cycles of GCPL⁴ at different currents were performed (Figure 1). The selected GCPL values were plotted in the table (TABLE I.). Measured results (Figure 1. and TABLE I.) shows, that the highest capacities are reached by an electrochemical cell containing the PVDF binder electrode, while the capacity decreases during cell cycling. In the case of electrodes containing carrageenan, overall capacities achieved are lower than that of PVDF, wherein an electrode containing a smaller amount of sulfate groups reaches higher capacities. In the case of electrodes containing carrageenan, there was an increase in capacity during cell cycling, with the percentage increase being higher in the case of an electrode containing a higher amount of sulfate groups.

⁴ GCPL – Galvanostatic Cycling with Potential Limitation

TABLE I. Comparison of selected values from the GCPL chart (Figure 1.)

Sample	Capacity in 1 st cycle [mAh g ⁻¹]	Capacity in 20 th cycle [mAh g ⁻¹]	Capacity in 50 th cycle [mAh g ⁻¹]	1 st – 20 th cycle percentage change [%]	1 st – 50 th cycle percentage change [%]
PVDF	1180	1104	992	-6.44	-15.98
Sulfat 29.42%	712	728	736	2.27	3.44
Sulfat 31.4%	453	543	527	19.85	16.37

Conclusion

From the results measured so far, it is clear that the use of carrageenans as a binders of electrode materials of a Li-S battery is possible and, in addition, there is no loss of capacity for 50 cycles of GCPL. An increasing content of sulphate groups apparently prevents capacity fading, but at the expense of total capacities achieved. The probable cause of total capacity reduction is the decrease in hydroxyl groups that form conductive bonds with carbon and hence an increase in the internal resistance of the cell. In order to make a clear conclusion, more experiments need to be done. In the following research, the plan is to focus on other types of carrageenans and other similar binders. After determining the most suitable binder, it will be subjected to long-term cycling.

Acknowledgments

This research work has been carried out in the Centre for Research and Utilization of Renewable Energy (CVVOZE). Author gratefully acknowledge financial support from the Ministry of Education, Youth and Sports of the Czech Republic under NPU I programme (project No. LO1210). This research was also sponsored by the NATO Science for Peace and Security Programme under grant 985148.

References

1. A. Manthiram, S. Chung, and C. Zu, *Adv. Mater.*, **27**, 1980–2006 (2015).
2. P. D. Howe, M. Wood, and U. Kingdom, *N-METHYL-2-PYRROLIDONE*, p. 39, (2001).
3. M. Ling et al., *Nano Energy*, **38**, 82–90 (2017).

Structure Instability of Cathode Active Materials in Lithium Ion Battery Induced by Lattice Distortion: Phase Field Analysis

H. Kim^a, T. Hwang^a and M. Cho^{a,b}

^a Department of Mechanical and Aerospace Engineering, Seoul National University, Gwanak-gu, Seoul 08826, Republic of Korea

^b Institute of Advanced Machines and Design, Seoul National University, Gwanak-gu, Seoul 08826, Republic of Korea

Active materials in lithium ion batteries operate through an electrochemical redox reaction accompanying phase separation that can affect that of cyclic performance and structural stability. During (de)intercalation process, the active material in the electrode is separated into Li-rich and Li-poor regions inducing misfit stress inside the bulk region due to lattice misfit. Moreover, the regions where induced stress is concentrated could initiate crack inside the bulk of active material leading to capacity fading. Therefore, it is significant to analyze the active material from a mechanical point of view to improve stability and performance. With phase field analysis, it could unveil the phase separation phenomena of the active material, especially LiFePO₄, leading to misfit stress. As a result, this study elucidates the origin of structure instability of the active materials in lithium ion batteries by mechanical approach.

Introduction

Nowadays, the demand for high-performance energy storage devices has been increasing as interest in the electric vehicles (EVs) has increased. Among them, many efforts have been made to develop EVs using lithium ion batteries having high energy density and long cyclic performance. Lithium ion batteries used in EVs should be able to satisfy both safety and longevity at the same time, while maintaining high electrochemical performance. Therefore, the importance of research of improving the performance of a lithium ion battery is higher than ever.⁽¹⁾

Among the various commercialized cathode active materials, LiFePO₄ guarantees durability, but has a low capacity of 170 mAh g⁻¹ problematic for a long time usage such as EVs. To overcome a lack of capacity, many studies are conducted on high energy density materials like Ni-rich LiNi_{1-2x}Co_xMn_xO₂ (NCM). However, because of the characteristics of nickel, the cathode active material of the NCM types is degraded and the lifetime is unstable, which is not usual in the LFP. In order to ensure the stable cyclic performance of high capacity cathode active materials, materials must be designed with an understanding of the stable performance of LFP. Up to date, studies on the cause of cyclic degradation have been largely attributed to phase transformation.⁽²⁾ However, there is little research on how such a phase transformation affects cyclic degradation.

In this study, we examine the origin of structure instability by presenting the phase separation and the mechanical behavior of the lithium ion battery cathode active material, LFP, during charging and discharging with phase field model. Using the material properties obtained on the atomic analysis⁽³⁾ and experimental data⁽⁴⁾, we simulate the phase separation in mesoscale and confirm the progress of the stress distribution induced by lattice misfit.

Numerical Model

In this study, phase separation of ex-situ LFP was performed using the phase field model, and the analysis of the elastic stress caused by the mismatching of the interface, which are separated into two phases with different crystal constants, was also conducted. Total free energy density G_{free} of the LFP consisting of homogeneous free energy density and elastic energy density is given as follows:⁽⁵⁾

$$G_{free} = \int_{\Omega} \rho_n \left(f_{hom} + \frac{\kappa}{2} |\nabla c|^2 \right) + \frac{1}{2} C_{ijkl} \varepsilon_{ij}^e \varepsilon_{kl}^e d\Omega \quad (1)$$

$$f_{hom} = \Omega c(1-c) + 2k_B T \{c \ln c + (1-c) \ln(1-c)\} \quad (2)$$

Among the various numerical analysis methods, this study was accomplished with finite element analysis that can deal with various shapes and boundary conditions. However, since the Cahn-Hilliard governing equation is the 4th order PDE, it is difficult to interpret it with a C0 finite element. Therefore, a mixed formulation strategy was used to handle the equation with the C0 element.⁽⁶⁾ Eq. (1) is decomposed into two coupled equations as below:

$$\begin{aligned} \frac{\partial c}{\partial t} &= \nabla \cdot (M \nabla \mu) \\ \mu &= \frac{\partial f_{hom}}{\partial c} - \frac{\kappa}{2} \nabla^2 c + \frac{1}{\rho_n} \frac{\partial f_{elastic}}{\partial c} \end{aligned} \quad (3)$$

Results and Discussions

It is important to understand the cathode active material phase separation because it affects the cyclic stability of battery system. Fig. 1 shows that LFP having a solid solution state, uniform lithium ion concentration, is separated into Li-rich (red region) and Li-poor (blue region) phases. It was found that it is thermodynamically stable to form a phase having two different lattice constants due to a non-uniform distribution of lithium ions in the LFP single particle after (de)intercalation.

Furthermore, the induced stress due to lattice misfit between Li-rich and Li-poor phases can be calculated. The Li-poor region with a relatively small crystal constant was subjected to a force in the direction of shrinkage due to the influence of the Li-rich region, and a tensile stress was induced in the Li-poor region.

Phase field analysis combined with First-principles calculation and experimental results simulated LFP phase separation, which is difficult to observe experimentally. In addition, by analyzing the mechanical phenomena caused by structural instabilities affects from phase separation, we have identified the factors that should be considered in designing materials with improved performance.

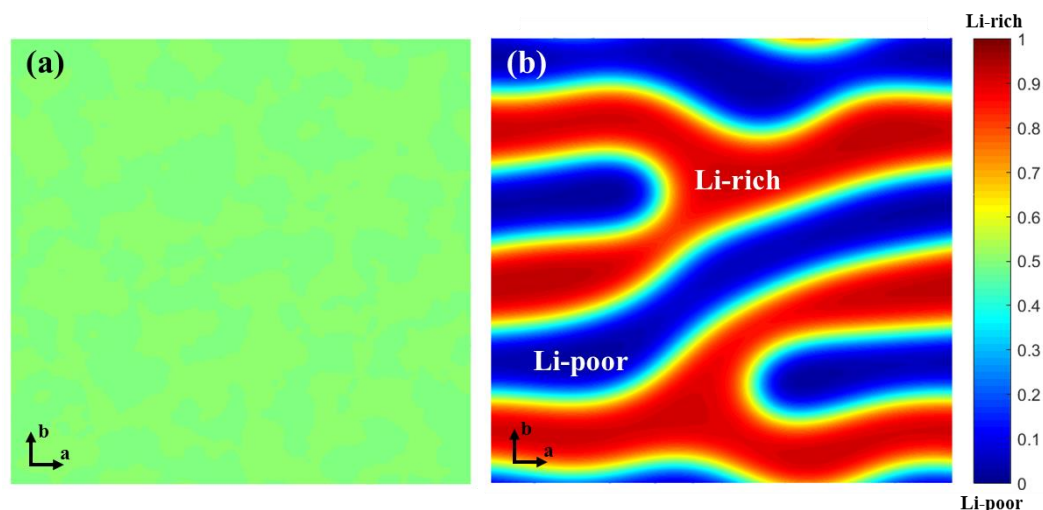


Figure 1. (a) Solid solution state of LFP with initial concentration of Li-ion ($c=0.5$). (b) Phase separated in to Li-rich and Li-poor phases in equilibrium state.

Acknowledgments

The National Research Foundation of Korea (NRF) grant funded by the Korea government (MEST) (No. 2012R1A3A2048841) and the Technology Innovation Program of the Korea Institute of Energy Technology Evaluation and Planning (KETEP) granted financial resource from the Ministry of Trade, Industry & Energy, Republic of Korea (No. 20152020105420)

References

1. Y. Sun, S. Myung, B. Park, J. Prakash, I. Belharouak and K. Amine, *Nature Materials*, **8**, 4 (2009).
2. M. Z. Bazant, *Accounts of chemical research*, **46**, 5 (2013).
3. T. Maxisch, F. Zhou and G. Ceder, *Physical Review B*, **73**, 17 (2006).
4. A. Yamada, H. Koizumi, S. Nishimura, N. Sonoyama, R. Kanno, M. Yonemura, T. Nakamura and Y. Kobayashi, *Nature Materials*, **5**, 5 (2006).
5. T. Ichitsubo, K. Tokuda, S. Yagi, M. Kawamori, T. Kawaguchi, T. Doi, M. Oishi, and E. Matubara, *J. Mater. Chem. A*, **1**, 7 (2013).
6. C. M. Elliott, D. A. French and F. A. Milner, *Numerische Mathematik*, **54**, 5 (1989).

A Comprehensive study of Working Temperature and Entropy Impacts on a Lithium-Ion Battery Thermal Behaviour by Employing Isothermal Calorimeter

Seyed Saeed Madani, Erik Schaltz, Søren Knudsen Kær

Aalborg University, Department of Energy Technology, Aalborg, DK-9220, Denmark

Email: ssm@et.aau.dk, esc@et.aau.dk, skk@et.aau.dk

Present research explores the impact of working temperature and entropy of a 13 Ah Lithium Titanate Oxid battery cell on its thermal behaviour, heat generation, efficiency and maximum temperature. To accomplish this, different loading patterns were applied to the battery. The experiments were accomplished at several charge and discharge cycles with different C-rates and state of charge levels. Temperature is one of the most important parameters, which have considerable impacts on the dynamic performance, cycle lifetime, safety and heat generation of lithium-ion batteries. Notwithstanding, the comprehensive and detail effects of temperature on the heat generation of lithium-ion batteries is necessary to be found. The findings allow us to have a better understanding of the effect of temperature on different aspect of the battery.

Introduction

The development of battery electric vehicles (BEVs), plug-in hybrid electric vehicles (PHEVs), and hybrid electric vehicles (HEVs) is accompanied with substantial design and technological challenges. Because lithium-ion battery with high energy density is the essential part for next-generation electrical vehicles, a complete comprehending of its thermal behaviours at various charge and discharge rates and temperature is absolutely necessary for the thermal management and design of lithium-ion batteries pack. One of the considerable drawbacks of lithium-ion batteries is their sensitivity to the temperature. When the operation temperature is beyond the limits specified by the manufacture, the performance and endurance of lithium-ion batteries is greatly affected. Hence, battery thermal management is the most important in accommodating lithium-ion batteries in EVs and HEVs.

In the last few years, there has been a growing interest in the thermal behaviour of lithium-ion batteries. However, to the author's best knowledge, very few publications can be found in the literature that discuss the issue of different aspect of lithium-ion batteries thermal behaviour which are related to the thermal modelling and management. Impact of cycle aging of lithium-ion battery cells on their thermal behaviour were investigated (1). It demonstrated complicated relationship between thermal behaviour and aging parameters. Lengthened cycling which causes approximately half of capacity loss enhances the heat generation for the time being discharged (1). This is reflected in remarkably decreased energy efficiency. In the case of fifty-fifty decayed cells, those with maximal number of cycles likewise represent lowermost discharge energy efficiency and maximal heat generation rates during discharge (1). In addition, raised heat generation increases safety risks of massively aged cells that might be heated up overhead the highest safe temperature even meanwhile carried out within the normal situations (1).

A 25 Ah pouch type lithium-ion battery were designed (2) to study its thermal behaviours. Heat transfer coefficient with environment, heat capacity, heat generation rate, and temperature distribution were investigated in that study. Outcomes demonstrated that the temperature growth of the charged pouch batteries greatly depends on the depth of discharge and discharge rate (2). In addition, prognostication model with lumped parameters was employed to approximate the temperature evolution at varied discharge rates of Lithium-ion battery (2). The anticipated outcomes was in good accordance with the experimental outcomes at all discharge rates. Hence, it was concluded that the thermal model was appropriate to anticipate the average temperature for the large-scale batteries under normal functioning situations (2).

Reference (3) applied the differential scanning calorimeter for quantifying the reactive hazards or thermal of the organic solvents. Enthalpy changes and exothermic beginning temperatures were analysed and measured (3). It was concluded that the thermal behaviours of these organic carbonates released less enthalpy variations. Notwithstanding, severe exothermic reactions were discovered between the lithium metal and linear or cyclic carbonates (3).

An analytical and numerical model for the thermal management of lithium ion battery stacks were developed (4) in order to study the thermal behaviours of cylindrical stacks and flat-plate during discharging. It was concluded that for the identical volume ratio of battery and cooling channel in flat-plate arrangement, changing the number of channels and channel size brought about identical average battery temperatures (4).

The temperature increase of a small lithium-ion secondary battery at the same time as fast discharging and charging cycles were calculated (5). The heat-source factors were measured as well as battery heat capacity, which was measured by a twin-type heat conduction calorimeter. In addition, the heat transfer coefficient was measured accurately (5). It was considered as a function of ambient and cell temperatures (5). It was concluded that the temperature, which was, computed by battery thermal behaviour model was almost the same as the cell temperature, which was measured by thermocouple during fast discharge and charge cycles (5).

With the intention of evaluating the heat, which is because of the electrochemical side-reaction, calorimetry was accomplished (6) for a lithium ion battery during high-rate cycling experiment. Insufficiency electric energy loss compared with the heat generation was seen (6). This paper has clearly shown that it was related to the impedance enlargement of the battery, which was caused by side-reactions (6).

However, most of the previous studies did not take into account the effect of working temperature and entropy on lithium-ion batteries thermal behaviour by using isothermal battery calorimeter (IBC).

Experimental setup

The experiments were accomplished by employing isothermal battery calorimeter (IBC284) which was manufactured by NETZSCH. The IBC 284 is not comprehensively automatic. Approximately all of the functions are controlled manually through the front panel. All of the experimentation parameters and data acquisition are set up with the user-friendly control program. The IBC 284 is an isothermal calorimeter capable of operating from minus thirty to sixty degree Celsius. The IBC 284 can measure heat generated by any kind of batteries functioning between 100 mW and 50 W. Main diagram of the IBC 284 is illustrated in Figure 1. As can be seen from the figure, it consist of a tank, cooling plate, heating element and isothermal bath. To control the fluids flow four solenoid valve and one manual valve and motorized ball valve are employed.

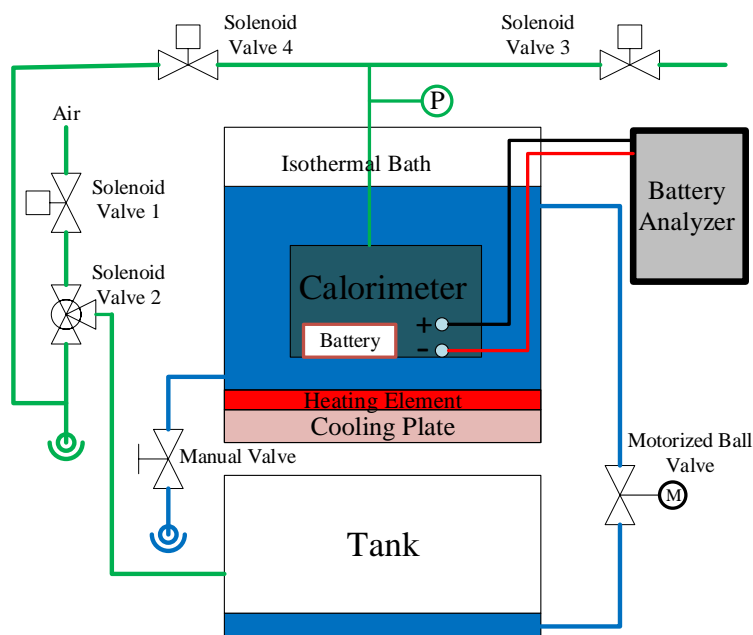


Figure 1. Main diagram of the IBC 284

Experimental procedure

At the beginning, the isothermal bath was drained to gain access to the calorimeter chamber. The liquid was transferred from the isothermal bath to the bottom tank until the level reached beneath the calorimeter lid.

A fixture was designed for the battery to avoid expansion during operation. After placing the battery inside the calorimeter chamber, it was connected electrically. For this purpose, two wires for powering and two wires for sensing were attached to the existing connections.

To be operated by the Maccor automated test system, the battery was connected to the two bus bars. Following that, the calorimeter lid was fastened by placing it on the box and closing all the latches. Once the experiment was established, the bath was filled out with liquid.

Filling the isothermal bath operates the reverse draining way. The calorimeter chamber pressure was increased until it reached two psi. When the pressure reaches greater than three psi owing to a temperature increase in the instrument, it will release pressure to protect the rupture disk from bursting. When the pressure reaches under two psi owing to a temperature decline in the instrument, it will open a solenoid valve so the calorimeter can be filled with inert gas.

The temperature set point was defined. To achieve very good temperature homogeneity inside the isothermal bath stirring motors were turned on. Two different ranges exist for heating. The high power range was used to move quickly from one temperature to a higher one in order to save time. The low power range was used during measurement in order to assure very good and stable temperature control of the isothermal bath. In order to measure the temperature distribution of the battery during charging and discharging cycles, four thermocouples were used which were located onto four different locations on the battery. A complete analysis of the battery cell temperature by using isothermal calorimeter is shown in Figure 2.

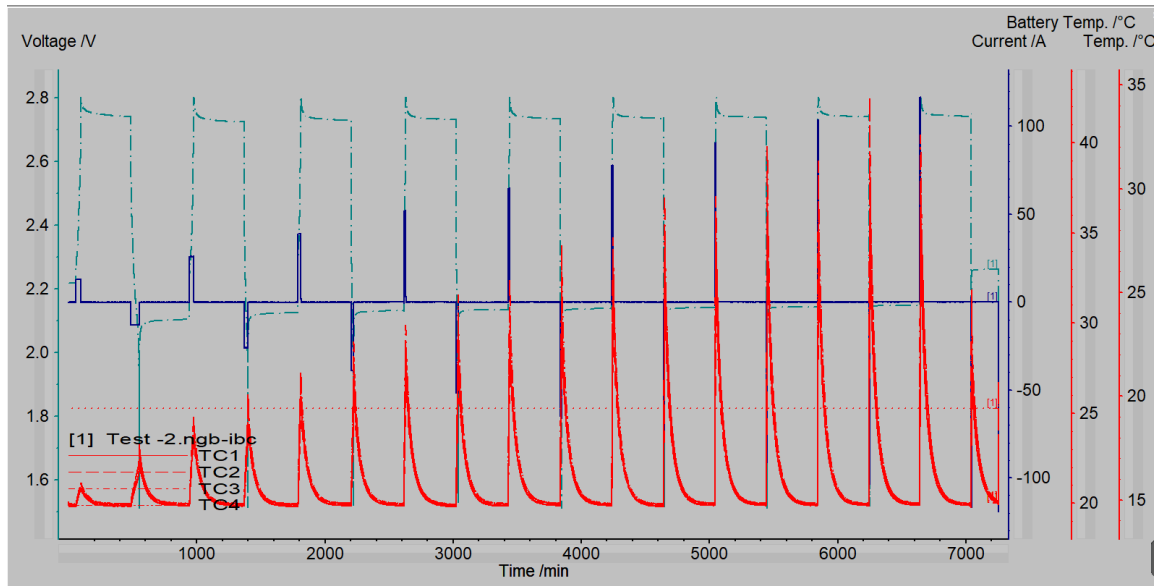


Figure 2. Analysis of the battery cell temperature.

References

1. J. Geder, R. Arunachala, S. Jairam, and A. Jossen, *2015 IEEE Green Energy Syst. Conf. IGESC 2015*, pp. 24–29, 2015.
2. F. L. Yun, L. Tang, W. C. Li, W. R. Jin, J. Pang, and S. G. Lu, *Rare Met.*, vol. 35, no. 4, pp. 309–319, 2016.
3. Y. Y. Sun, T. Y. Hsieh, Y. S. Duh, and C. S. Kao, *J. Therm. Anal. Calorim.*, vol. 116, no. 3, pp. 1175–1179, 2014.
4. J. Xun, R. Liu, and K. Jiao, *J. Power Sources*, vol. 233, pp. 47–61, 2013.
5. T. Ohshima, M. Nakayama, K. Fukuda, T. Araki, and K. Onda, *Electr. Eng. Japan (English Transl. Denki Gakkai Ronbunshi)*, vol. 157, no. 3, pp. 17–25, 2006.
6. Y. Saito, *J. Power Sources*, vol. 146, no. 1–2, pp. 770–774, 2005.

Investigation of Reversible and Irreversible Heat Sources and Entropic Coefficient in a Lithium-Ion Battery by Employing Isothermal Calorimeter

Seyed Saeed Madani, Erik Schaltz, Søren Knudsen Kær

Aalborg University, Department of Energy Technology, Aalborg, DK-9220, Denmark

Email: ssm@et.aau.dk, esc@et.aau.dk, skk@et.aau.dk

The main objective of the paper is to quantify the reversible and irreversible heat sources in a 13 Ah pouch type commercial Lithium Titanate Oxid battery by using isothermal calorimeter. Lithium-ion batteries are the most appropriate technology for electrified vehicles applications. Isothermal battery calorimeters are precise devices, which are used to determine the heat generated by the batteries. The heat generation in a functioning lithium-ion battery during the discharge and charge process is usually estimated by the aggregate of two fundamental sources, which are the irreversible and reversible heat. The reversible heat generation rate could be determined from the entropy variation. The irreversible heat is a complicated parameters to be determined and is characterized in dissimilar procedures in various heat analysing models. The results will assists on a precise thermal model of the battery.

Introduction

A battery is an energy storage device. The most prevalent battery chemistry on the market for automotive usages is the lithium ion battery. Lithium-ion batteries have been extensively employed in many electric appliances, but derisive accidents have been happened occasionally.

Lithium-ion batteries are extensively used for various applications such as, laptops, cameras, mobile phones, automotive and telecommunication. Low self-discharge rate, long cycle life, high open circuit voltage, high specific energy, no memory effect are some of the advantages of lithium-ion batteries.

System safety, cycle life, and cell performance are influenced by temperature distribution in the cell. Consecutively, it depends on heat dissipation rate at surface of the cell and heat generation rate within the cell.

Although lithium-ion batteries are susceptible to extreme heat load under severe or abnormal functional conditions, thermal management has been one of the considerable issues in developing a lithium-ion batteries in hybrid electric vehicle (HEV) battery system applications.

With the intention of reaching out to safety requirements of the lithium-ion batteries on electronic device applications, researchers are resuming to do supplementary investigations on the essential issues in relation to the lithium-ion batteries.

In recent years, research on lithium-ion batteries heat sources has become very popular. However, most of the previous studies did not quantify the reversible and irreversible heat sources in lithium-ion batteries.

A simple modelling methodology characterizing thermal behaviour of an air-cooled Li-ion battery system was suggested [1] with the intention of designing a suitable thermal management system.

In addition, a suggested mathematical model was formulated based on the battery's mechanical and electrical properties [1]. Outcomes demonstrated that the model could offer good approximations for simulating convective heat transfer cooling during battery functioning. The improved thermal model was beneficial in constructing the flow system and specifying the suitable cooling capacity for a battery system [1].

An enhanced single particle (ESP) model were developed [2] to understand the thermal behaviour of lithium-ion secondary batteries. It was concluded that temperature estimation on the cell wall and of the electrode interior, which was obtained through the ESP model, were in good agreement with actual experimental measurements. [2]

A thermal model was established for a battery module [3] by using channelled liquid cooling thermal management system. Simulation results demonstrated that enhancing the charge and discharge C-rate aggravates the temperature uniformity and causes bigger temperature in the battery module. In addition, enhancing the liquid flow rate could considerably improve the temperature uniformity and reduce the temperature in the battery module [3].

Background

Lithium-ion batteries heat generation and performance are extremely dependent on temperature. Temperature evolution in electrical power storages systems plays a considerable function for the aging behaviour of lithium-ion battery cells [4, 5]. Heat generation inside lithium-ion batteries is a complex procedure. Concentration, activation and ohmic are three fundamental sources which generate heat in lithium-ion batteries [6].

Bernardi et al. [7] developed a formulation (1) for battery heat generation by employing a thermodynamic energy balance. An expression were determined for heat generation inside the battery [6, 7].

$$q = -IV - \sum_l I_l T^2 \frac{d \frac{U_{l,avg}}{T}}{dT} + \sum_j \frac{d}{dt} \left[\int_{v_j} \sum_i 8.314 * c_{i,j} T^2 \frac{\partial}{\partial T} \ln \left(\frac{\gamma_{i,j}}{\gamma_{i,j}^{avg}} \right) dv_j \right] + \sum_{j,j \neq m} \sum_i \left[\left(\Delta H_{i,j \rightarrow m}^o - 8.314 * T^2 \frac{d}{dT} \ln \frac{\gamma_{i,m}^{avg}}{\gamma_{i,j}^{avg}} \right) \frac{dn_{i,j}}{dt} \right] \quad (1)$$

where

$\Delta H_{i,j \rightarrow m}^o$: Molar enthalpy phase change , $\gamma_{i,j}$: Activity coefficient , $n_{i,j}$: Moles

Where I represents total cell current, V and U are overall cell and open circuit potentials and j, l, m are reaction and phase indexes. The heat generation of lithium cells during the discharging and charging process can be divided to the irreversible heat and reversible heat sources. A simplified form of equation (2) was proposed by Bernardi et al. [8].

$$q = I(U - V) - I(T \frac{\partial U}{\partial T}) \quad (2)$$

This form has been introduced and reported formerly [6-10]. The first term represents the irreversible heat contribution which corresponds to the cell over potential owing to ohmic losses. The second term is the entropy changes and reflects entropic heat, which is corresponding to reversible sources. The term $\frac{\partial U}{\partial T}$ corresponds to entropic heat coefficient and defines as the potential derivative with respect to temperature which is usually considered as the entropic factor. Analysis of the heat generation to find the heat efficiency and other parameters is illustrated in Figure 1.

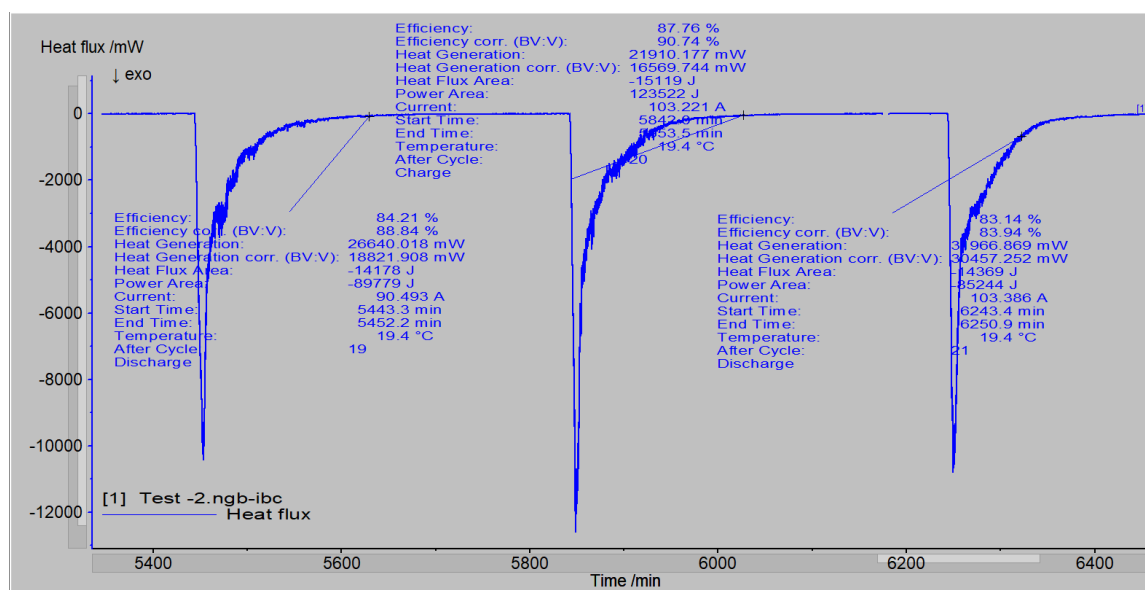


Figure 1. Analysis of the heat generation to find the heat efficiency.

References

1. Y. S. Choi and D. M. Kang, *J. Power Sources*, vol. 270, pp. 273–280, 2014.
2. N. Baba, H. Yoshida, M. Nagaoka, C. Okuda, and S. Kawauchi, *J. Power Sources*, vol. 252, pp. 214–228, 2014.
3. C. Zhao, W. Cao, T. Dong, and F. Jiang, *Int. J. Heat Mass Transf.*, vol. 120, pp. 751–762, 2018.
4. I. Bloom et.al., *Journal of Power sources*, 101(2001), 238 - 247.
5. E.V. Thomas et.al., *Journal of Power sources*, 184(2008), 312-319.
6. T. M. Bandhauer, S. Garimella, and T. F. Fuller, *J. Electrochem. Soc.*, vol. 158, no. 3, p. R1, 2011.
7. D. Bernardi, E. Pawlowski, J. Newmann, Vol. 132, University of California - Berkeley (1985).
8. W. B. Gu and C. Y. Wang, vol. 147, no. 8, p. 2910, 2000.
9. J. M. Sherfey and A. Brenner, “Electrochemical Calorimetry,” *J. Electrochem. Soc.*, vol. 105, no. 11, p. 665, 1958.
10. L. Millet, M. Bruch, P. Raab, S. Lux, and M. Vetter, *2017 12th Int. Conf. Ecol. Veh. Renew. Energies, EVER 2017*, no. 2, 2017.
11. (11) N. Nieto et al., *J. Electrochem. Soc.*, vol. 160, no. 2, pp. A212–A217, 2012.

Investigation of the Effect of State of Charge, C-rates and on the Heat Generation, Internal Resistance and Efficiency of a Lithium-ion Battery by Using Isothermal Calorimeter

Sayed Saeed Madani, Erik Schaltz, Søren Knudsen Kær

Aalborg University, Department of Energy Technology, Aalborg, DK-9220, Denmark

Email: ssm@et.aau.dk, esc@et.aau.dk, skk@et.aau.dk

To comprehend the thermal behaviour, performance and the dependency of the affecting parameters such as state of charge and C-rates on the heat generation, efficiency, heat flux and maximum temperature of a commercial pouch type Lithium-ion battery under various working conditions, different loading were applied to the battery. The capacity of the battery is 13 Ah, which has a lithium titanate oxide based anode from Altairnano. Surface temperatures and heat flux of the Lithium-ion battery cell were measured by means of isothermal battery calorimeter. Different charge and discharge current pulses at nineteen state of charge (SOC) levels from 5% to 95% SOC were applied to the battery by using maccor automated test system.

Introduction

Emissions from vehicles, which consume fossil fuels, has become an environmental issue because of greenhouse effect and air pollution. Governments from various countries are struggling to diminish the quantity of greenhouse gases and pollutant. The demand for vehicles is increasingly therefore electric and hybrid electric vehicles are of the best alternative for fossil fuels vehicles [1]. Electricity consumed could be generated from extensive sources of energy containing nuclear power, fossil fuels, wind power and solar energy. Consequently, electric vehicles (EVs) could be replaced by fossil-fuel powertrain or internal combustion engine [2].

Lithium-ion batteries have many advantages such as high energy densities and high cell voltages. Consequently; they are appealing energy sources for electric vehicles (EVs) and hybrid electric vehicles (HEVs) [3]. However, these batteries are encountered with some restrictions for high energy consumption applications because of their thermal problems.

Temperature has a significant effect on the battery performance and battery life. It is essential to control the battery temperature during operation in electric vehicles (EVs) and hybrid electric vehicles (HEVs). Maximum battery allowable temperature and the amount of heat, which should be taken from each battery to provide suitable operating range, are of important factors to determine thermal behaviour of lithium-ion batteries. Battery life and the costs associated with the production and warranty of the electric vehicles are tied up with these issues. In recent years, an increasing attention has been paid to the battery thermal management issues. An appropriate modelling to predict the thermal behaviour of the battery can be helpful in decision making and to improve the design of the heat management system.

The battery pack thermal management system is able to minimize irregular temperature distribution between the modules with the intention of minimizing the electrical imbalance in order

to attain anticipated performance. By the same token, operating in favourable temperature scope will bring about optimized battery life and performance [4].

Various lithium-ion cells were cycled to appraise their performance and heat dissipation rates at several discharge and charge rates [5]. It was concluded that the heat dissipation rate for all cells were function of the rate of discharge. In addition, it enhanced remarkably toward the end of discharge. This was because of the increased polarization at the end of discharge. Heat effects for all cells were exothermic and endothermic during discharging and charging correspondingly [5].

Thermodynamic experiment were performed on lithium-ion batteries [6]. It was concluded that input and output heat depend on charging and discharging correspondingly. Heat generation factors were divided to three parts namely joule, polarization, and reaction heat values. The involvement of each factors was expressed quantitatively [6].

The importance of reversible heat to the thermal behaviour of lithium ion battery was investigated through simulations [7]. A great relevance was seen among the battery cell characteristics and the battery temperature. The importance investigation of reversible heat is essential when accurate information about the heat distribution and the heat generation across a battery cell is needed. It was concluded that decreasing in active material particle size and electrode thickness would result in battery temperature reduction during operation. Consequently, the safety of lithium-ion battery, reliability and performance were improved [7].

Instrument and test procedure

The Isothermal Battery Calorimeter (IBC) 284 is a robust instrument, which is constructed and designed for the precise measurement of heat, which is generated by batteries at the same time as being discharged or charged under isothermal conditions. The IBC operates between -30°C to +60°C and can measure heat, which is generated by batteries ranging from 100 mW to 50 W. External system components of the IBC 284 is illustrated in Figure 1a. The IBC 284 was connected to two different gas networks, which is illustrated in Figure 1b. The first one is nitrogen gas, which is used for the calorimeter chamber. The inlet pressure of nitrogen gas should be less than 15psi. This gas is used for over pressurizing (up to uttermost three psi) the calorimeter chamber so the liquid cannot pass through the calorimeter lid and get inside the chamber in the case of sealing failure. There is a lever switch and pressure controller, which automatically controls the inert gas pressure inside the calorimeter chamber. The process meter holds the pressure between 2 and 3psi inside the chamber.

The second gas network is dry and clean compressed air, which is used for liquid level management. The air inlet pressure should be less than 30 psi. The compressed air is used to push the liquid from the buffer tank, which is placed on the bottom of the instrument to the calorimeter bath. Liquid high level and liquid tube are illustrated in Figure 2.

After closing the calorimeter, the liquid was transferred from the bottom tank to the isothermal bath until the calorimeter lid was entirely covered (liquid high level position). Liquid level sensor will automatically cut off the filling of the isothermal bath when the level is distinguished as too high. Thermal fluid, which was used, composed of approximately 33 gallons of deionized water mixed with dynalene ethylene glycol with equal ratio.

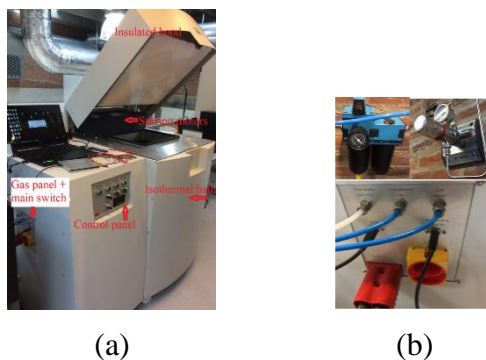


Figure 1. (a) External system components of IBC 284, (b) gas networks.

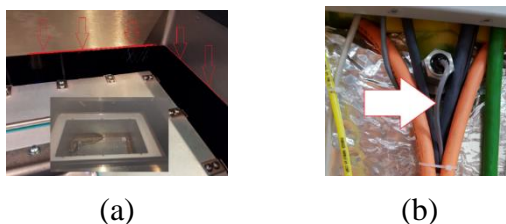


Figure 2. (a) Liquid high level, (b) Liquid tube.

Two fans, which are positioned behind the stirring motors, provide air cooling for motors. Heat measurement system is situated in the calorimeter chamber. Silicone/Rubber heating element was employed for controlling the temperature. Cooling plate, which is placed at the bottom of the bath, is straight connected to the refrigerating system. Two stirring motors drive the stirring to provide temperature homogeneity inside the isothermal bath. Heating is performed through a silicone rubber heater, which is placed beneath the isothermal bath. Cooling is carried out by a powerful refrigeration system, which is situated on left side of the instrument.

A line connection for safety exhaust were connected to the laboratory flexible vent duct. A rupture disk was provided for the IBC 284, which will burst inside the calorimeter chamber if the pressure reaches too high as a consequence of battery thermal runaway. Safety exhaust of the calorimeter, stirring motors, laboratory flexible vent duct and fans are illustrated in Figures 3a,b. Buffer tank is used for maintaining the thermal fluid coming from the bath during set up or maintenance operations. Maccor automated test system, which was selected as external battery analyser is illustrated in Figure 3c. The external battery analyser was connected to the IBC 284 by two cables.

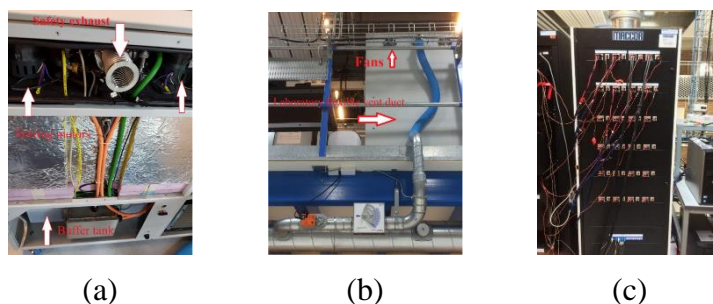


Figure 3. (a) Safety exhaust of the calorimeter and stirring motors, (b) Laboratory flexible vent duct and fans (c) Maccor automated test system.

Results

In order to investigate the influence of different parameters such as state of charge, on the heat generation, an experiment was designed through Maccor automated test system. The current profile, which was applied to the battery, is illustrated in Figure 4. In addition, heat flux, voltage, power and temperature variations are shown in this figure. It can be seen that heat generation rates during charging is excessively different from discharging and heat generation rises during charging process, approaching high SOC, and approaching low SOC during discharging process. This consequently could be appertaining to diffusion limitations.

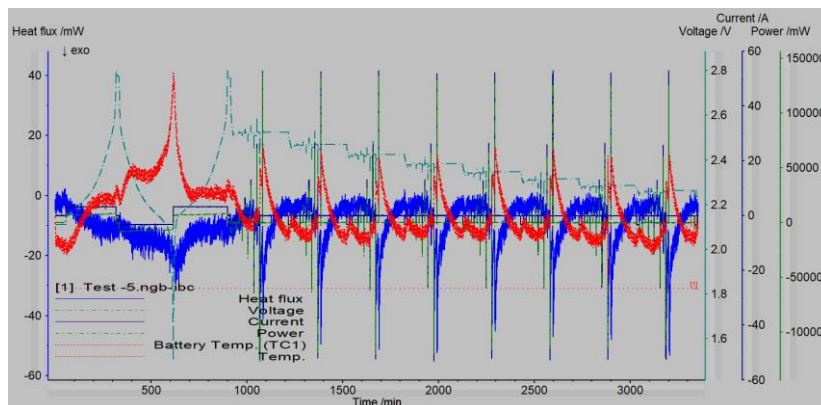


Figure 4. 13 Ah altairnano lithium-ion battery cell analysis by means of isothermal battery calorimeter.

Reference

1. J. Xun, R. Liu, and K. Jiao, *J. Power Sources*, vol. 233, pp. 47–61, 2013.
2. R. Liu, J. Chen, J. Xun, K. Jiao, and Q. Du, *Appl. Energy*, vol. 132, pp. 288–297, 2014.
3. N. Baba, H. Yoshida, M. Nagaoka, C. Okuda, and S. Kawauchi, *J. Power Sources*, vol. 252, pp. 214–228, 2014.
4. A. A. Pesaran, S. Burch, and M. Keyser, *Proc. 4th Veh. Therm. Manag. Syst.*, no. January, pp. 24–27, 1999.
5. S. Al Hallaj, J. Prakash, and J. R. Selman, *J. Power Sources*, pp. 186–194, 2000.
6. N. Sato, *J. Power Sources*, vol. 99, no. 1–2, pp. 70–77, 2001.
7. R. Zhao, J. Gu, and J. Liu, *J. Power Sources*, vol. 266, pp. 422–432, 2014.

A Review of Different Electric Equivalent Circuit Models and Parameter Identification of Lithium-ion Batteries

Seyed Saeed Madani, Erik Schaltz, Søren Knudsen Kær

Aalborg University, Department of Energy Technology, Aalborg, DK-9220, Denmark

Email: ssm@et.aau.dk, esc@et.aau.dk, skk@et.aau.dk

Lithium-ion batteries have many advantages in compare to other conventional batteries. Because of that, they have many applications in different sectors such as portable electronic devices, electric vehicles and other fields. To assure that the operation and performance of lithium-ion batteries are reliable, safe and economic, the approximation of state of charge, cycle life and other parameters for lithium-ion batteries are necessary. Equivalent circuit models are one of the most important research topic in the field of lithium-ion batteries. Several researcher have suggested a variety of equivalent circuit models. Some of these models are simple whereas some others are complicated. This paper presents a review of different equivalent circuit models and parameters identification in lithium-ion batteries for energy storage applications. These models include the internal resistance model, one time constant model, two time constants model, Thévenin model, PNGV (partnership for a new generation of vehicles) model, DP (dual polarization) model, Improved PNGV model, three seeds algorithm, electrochemical impedance spectroscopy method, and Randles' model.

Introduction

There has been a global alteration in the direction of battery electric vehicles (BEVs), plug-in hybrid electric vehicles (PHEVs) and hybrid electric vehicles (HEVs) owing to increasing trend in the emissions of greenhouse gasses. Therefore, considerable developments on the battery management systems (BMSs) and battery technologies is necessary to ensure safe, reliable and efficient operations of the lithium-ion batteries under demanding driving conditions.

Long cycle life, low memory effect, large operating temperature range, high operating voltage, lightweight, small volume, low self-discharge rate are some of the advantages of the lithium-ion batteries. Lithium-ion batteries have been extensively used in portable consumer electronics such as digital cameras, mobile phones, laptops. In addition, they have many applications in military, aerospace, renewable energy storage electric power and other demanding fields.

Parameters such as State-of-Health (SOH) and State of Charge (SOC) are not measurable directly by sensors, usually model-based estimation algorithms are needed for determination of these parameters [1]. An essential purpose of the BMS (battery management system) is to monitor the conditions of these parameters. For this reason, precise battery models are of uttermost importance [1]. Moreover, a balance between accuracy and model complexity is needed to provide precise estimations. In other words, it is essential to have models, which are precise enough and not unessentially complex [1]. Usually simple models are not capable of simulating the dynamic characteristics of lithium-ion batteries; notwithstanding, it is challenging to exert a complicated model to a real-time system. Electrochemical models, which consider all important behaviors of

battery cells [2–4] generally, can achieve high precision. Notwithstanding, partial differential equations with a large number of unknown variables are usually employed. The complicatedness frequently leads to considerable requirement for memory and computation [5].

Equivalent circuit battery models have been investigated specifically for the applications such as battery management system development and vehicle power management control [5]. The dynamic characteristics of the lithium ion batteries were investigated over various current profiles [6]. A dynamic equivalent circuit model was suggested to characterize the dynamic characteristics of the batteries. Simulation outcomes demonstrated that dynamic equivalent circuit model could indicate the output characteristic of the batteries precisely [6]. Two equivalent circuit models for a lithium-ion battery were investigated [7]. The Gauss-Newton (G-N) least square was employed to determine the two model parameters. Outcomes demonstrated that the second-order RC model offers better estimation for the real battery terminal voltage than the first-order [7]. Reference [8] presented an enhanced equivalent circuit model (EECM) appertaining to electrochemical investigation, in which the surface SOC (SOC_{surf}) demonstrated the lithium concentration at the particle surface and was employed to specify the terminal voltage. The outcomes demonstrated that the EECMs, which consider SOC_{surf} , produces better precision than the conventional ECMs in low-SOC area [8]. A procedure were suggested [9] for parameter estimation and dynamic model identification of LiFePO_4 cells based on electrochemical impedance spectroscopy (EIS) and current pulse measurements. They concluded that root-mean-square deviations remained within 28 mV at all C-rates and temperatures [9]. An adaptive algorithm were developed [10]. The proposed algorithm approximated six electrical parameters for lithium-ion batteries. A reliable SOC were produced based on one of the approximated battery parameters. Vehicle validation and simulation outcomes demonstrated acceptable robustness and conformity of the algorithm with high computational effectiveness and low implementation expenses [10]. Battery model parameters were estimated by employing a layered method [11]. They concluded that layered procedure was successful in fitting an equivalent circuit model (ECM) to a lithium iron phosphate cell data. In this review, various lithium-ion battery equivalent circuit models are presented. Furthermore, a number of parameter identification procedures, which were used in the models, are explained and analyzed.

1. OTC Model (one time constant model)

Reference [13] introduced internal resistance model (IR), one time constant model (OTC), and finally the two-time constants model (TTC) for the state of charge (SOC) determination of lithium-ion batteries. The parameters were identified by characteristic measurements [13]. The IR model is not appropriate for the precise approximation of SOC during any non-constant load or dynamical operation because this model does not demonstrate the transient behavior of lithium-ion cells [13]. The difference between OTC model and IR model is a parallel RC network, which was added in series to the internal resistance R_0 of the IR model, with the intention of approximating the dynamic behavior of the lithium-ion batteries [13]. In this method R_{OTC} , C_{OTC} , describes the battery transient response, V_{OC} is open-circuit voltage (OCV), and τ is time constant [13].

It was seen that the battery demonstrates a large discrepancy between the long time and the short time transient behavior in no-load condition. Consequently, the OTC model is not able to demonstrate the dynamic characteristics very precisely [13]. For the OTC model parameters identification an exponential function $f(t) = A + Be^{-\alpha t}$ was used for nonlinear data fitting [13].

2. TTC Model (two-time constants model)

The difference between the TTC and OTC model is a RC network, which was added in series to the OTC circuit in order to increase the flexibility of the OTC model [13]. R_{TTC1} , C_{TTC1} and R_{TTC2} , C_{TTC2} are to describe the short-term and long-term characteristics correspondingly [13]. For the TTC model parameters identification an exponential function $f(t) = A + Be^{-\alpha t} + Ce^{-\beta t}$ was used for nonlinear data fitting.

3. The Thevenin Model

The Rint, RC, Thevenin , PNGV and dual polarization (DP) models were studied [14]. To detect the optimum time constant of the model a genetic algorithm method was employed for the model parameters identification [14]. The experimental data was obtained from a Hybrid Pulse Power Characterization (HPPC) test. The Dynamic Stress Test (DST) was employed for the determination of the dynamic performances of the models. Federal Urban Driving Schedules (FUDS) experiment was used for the precision of SOC approximation with the Robust Extended Kalman Filter (REKF) method [14]. It was concluded that the DP model has the best dynamic performance and provides the most accurate SOC estimation [14]. To explain the dynamic characteristics of the lithium-ion batteries a parallel RC network in series was added to the Rint model [14].

4. The PNGV (partnership for a new generation of vehicles) Model

Capacitor $(1/V'_{oc}) = V_d$ is to explain the variation of the open circuit voltage, which is generated in the time accumulation of load current [14].

5. The DP Model

The Thevenin model is able to simulate the polarization characteristic to some extent. Notwithstanding, the discrepancy between electrochemical polarization and concentration polarization causes an incorrect simulation at the end of discharge or charge [14]. U_{OC} is Open-circuit voltage and R_O is Ohmic resistance. A dual polarization (DP) model by appending an additional RC circuit to the Thevenin model is able to simulating the concentration polarization and electrochemical polarization independently [14]. R_{D1} and R_{D2} are for characterizing electrochemical polarization correspondingly. C_{D1} and C_{D2} are to characterize the transient response during transfer of power correspondingly [14].

5.1 Method 1:

An investigation of the conventional lithium-ion battery equivalent circuit models named Thevenin, PNGV, dual polarization (DP) was done by reference [14]. Results showed that both the Thevenin model and the DP model have more desirable dynamic simulation outcomes, which demonstrates that these two models are more appropriate for the modeling of lithium-ion batteries [14]. The PNGV model in comparison with the Thevenin model has an extra capacitor, which gives an explanation for the impact of the open circuit voltage. Notwithstanding, it demonstrates an oscillation in the battery model, and produces a big error [14].

Based on the experimental data the terminal voltage, which, was approximated by the Thevenin model, produced a more appropriate dynamic performance [14]. The dynamic characteristics of the battery could be simulated better by The DP model. In addition, it produces the lowest error in comparison with other models. Consequently, the DP model is reasonable and accurate [14].

5.2 Method 2: TSA Method

Reference [16] employed advanced tree seeds algorithm for parameter identification of equivalent circuit models for lithium-ion batteries. Experimental verifications by employing various profiles showed that the proposed procedure could bring about a better outcome with more precision and robustness and lower complicatedness. The advantages of this method are [16]:

- No need for gradient information and initial values.
- Less time consume and higher precision.
- Preponderant in multiple mode functions.

Reference [17] explained three types of equivalent circuit model (ECM) of lithium-ion batteries. These models were Thevenin, PNGV, Improved PNGV. Among them improved PNGV model will be described in the following part. Least square procedure by HPPC test was employed for the model parameters identification. The improved PNGV model voltage response is more precise than PNGV model voltage response at the start of zero-input state. In comparison with the other methods, improved PNGV model had higher precision [17]. To specify the discharge and charge characteristics of lithium-ion batteries an RC circuit (R_2, C_2) should be added to the PNGV model (17).

6. Improved PNGV Model

Reference [18] employed the PNGV model for simulating the external characteristic of LiFePO_4 lithium-ion battery.

7. The Randles Model

Reference [19] reviewed different lithium-ion battery models such as equivalent electrical-circuit based models, empirical or data-based models and electrochemical or physics-based models. Gould et al. [20] developed a new battery model through the star-delta transformation of the original Randles circuit.

The modified Randles model, contains the similar number of parameters as the Randles model. Notwithstanding, there is a small modification in the transient states for the modified Randles model. Both the modified Randles and the Randles models contain two capacitors to comprise the OCV and the transients accompanied with the diffusion effects correspondingly [19].

Reference [21] analyzed electrochemical impedance spectroscopy for lithium-ion battery modeling. Elements, which were specified from the measured impedance spectra, were the parameters for the equivalent circuit. Curve sketching was employed to approximate the parameters of the components [21]. The approximated parameters are the primary values for the minimization

function, which is based upon the least-squares procedure, which is shown in the following equation [21]: The parameters for these equivalent circuits were calculated by the Levenberg–Marquardt and trust-region algorithm and least-squares method. The relative deviation of the impedances was computed [21]:

Reference

1. X. Hu, S. Li, and H. Peng, vol. 198, pp. 359–367, 2012.
2. C. Y. Wang, C. Y. Wang, V. Srinivasan, and V. Srinivasan, *J. Power Sources*, vol. 110, pp. 364–376, 2002.
3. V.R. Subramanian, V. Boovaragavan, V. Ramadesigan, M. Arabandi, *J. Electrochem.Soc.* 156 (2009) A260–A271.
4. A.P. Schmidt, M. Bitzer, A.W. Imre, L. Guzzella, *J. Power Sources* 195 (2010)5071–5080.
5. X. Hu, S. Li, and H. Peng, *J. Power Sources*, vol. 198, pp. 359–367, 2012.
6. L. Chenglin, L. Huiju, and W. Lifang, pp. 1662–1665, 2009.
7. S. Li and X. Cheng, pp. 1–4, 2014.
8. G. Liu et al., pp. 1–6, 2014.
9. C. R. Birkl and D. A. Howey, 1st Catapult Conf. Energy Storage Technol., pp. 1–6, 2013.
10. X. Tang, X. Mao, J. Lin, and B. Koch, *Am. Control Conf. (ACC)*, 2011, pp. 941–946, 2011.
11. R. Jackey, M. Saginaw, P. Sanghvi, J. Gazzarri, T. Huria, and M. Ceraolo 2013.
12. Hongwen He, Rui Xiong, and Jinxin Fan, *J. Energies*, vol. 4, pp 582-598, ISSN 1996-1073, March 2011.
13. A. Rahmoun and H. Biechl, vol. 2, no. 7, pp. 152–156, 2012.
14. H. He, R. Xiong, and J. Fan, no. December, 2011.
15. Kiran M S TSA: 2015 *Expert Syst Appl* 426686-98.
16. E. Science, 2017.
17. F. Jin, H. Yongling, and W. Guofu, vol. 6, no. 20, pp. 3756–3759, 2013.
18. Wengen Gao, Ming Jiang, Youming Hou, 2011 6th IEEE Conference on Industrial Electronics and Applications.
19. “A Systematic Review of Lumped-Parameter Equivalent Circuit Models for Real-Time Estimation of Lithium-ion Battery States,” pp. 183–196, 2016.
20. C. R. Gould, C. M. Bingham, D. A. Stone, and P. Bentley, *IEEE Trans. Veh. Technol.*, vol. 58, no. 8, pp. 3905-3916, October 2009.
21. U. Westerhoff, K. Kurbach, F. Lienesch, and M. Kurrat, pp. 1620–1630, 2016.

Improving high-rate properties of electrode materials: prevention of aggregation and surface modification

Anna V. Potapenko^{a,b}, Sviatoslav A. Kirillov^b

^a University of Electronic Science and Technology, Chengdu, 610054, P.R. China

^b Joint Department of Electrochemical Energy Systems, Kyiv, 03042, Ukraine

A modified citric acid route has been applied for obtaining materials prospective for using in lithium ion batteries of new generation. These have twice smaller particle size compared with commercial ones and endure high current loads ($\geq 100\text{C}$). The morphology of these samples has been studied by SEM and TEM. It has been indicated that perfectly shaped crystals with the average particle size of 150-200 nm are obtained. This is in line with our conclusion that a balance between high rate properties and capacities should be determined not only by the size of crystals but also by their perfectness and ability to aggregation.

It is known that an ideal electrode material should consist of nonaggregated, nanosized, perfect single crystals. The absence of aggregation would provide an access to the whole surface and whole volume of the crystals for easier lithium ion transportation from the bulk of an electrolyte solution to the electrode and diffusing inside the electrode. Nanodimensionality would be necessary for achieving the minimal possible times of diffusion in the solid material. In the spirit of Aricó et al. [1], one can formulate the following requirements to electrode materials from the point of view of the accessibility of theoretical capacities and high rate of discharge of lithium batteries [2]: The perfectness of the crystals would guarantee the absence of defect regions inaccessible to the lithium ions, i.e. would ensure the attaining of theoretical capacity. Therefore a balance between high rate properties and capacities should be determined not only by the size of crystals but also by their perfectness and ability to aggregation.

In this presentation, continuing our efforts directed towards obtaining electrode materials by means of a modified citric acid aided route [3-5], we demonstrate several approaches to improving high-rate properties, namely (i) prevention of aggregation performing the pyrolysis of precursors in an inert atmosphere and (b) surface modification.

Citrate precursors have been obtained by following way [6-7]. Solutions of metal nitrates and citric acid have been evaporated up to a resin state ($80\text{ }^{\circ}\text{C}$). The resins have been dried at $120\text{ }^{\circ}\text{C}$ giving the precursors for all further operations.

According to the ‘standard’ scheme, the LiMn_2O_4 precursors have been pyrolyzed and annealed in air. By the proposed scheme, pyrolysis has been performed in the argon atmosphere and after that, pyrolyzed samples have been annealed in air. The temperature of pyrolysis has been equal to $400\text{ }^{\circ}\text{C}$; the duration of pyrolysis has been taken equal to 1 h. Subsequent operations with the samples pretreated in air have been made according to Ref. [7] and consisted of 24 h annealing in air at $700\text{ }^{\circ}\text{C}$ with heating and cooling rates taken equal to 5 and $2\text{ }^{\circ}\text{C}/\text{min}^{-1}$, respectively.

Surface modification of LiMn_2O_4 has been performed with $\text{LiNi}_{0.5}\text{Mn}_{1.5}\text{O}_4$ (the so-called gradient sample) [6,7] and with a conductive polymer. Details of the preparation of the latter sample will be published elsewhere.

Electrochemical tests have been made on a M-Tech workstation (Ukraine). Working electrodes consisted of 81 wt. % of the active material, 10 wt. % of a conductive additive (soot) and 8 wt. % of a binder (poly (vinyliden) difluoride). For LiMn_2O_4 surface modified with a conductive polymer, 5% of a polymer has been added to the electrode composition instead of soot. A 20-30 μm layer of the slurry has been casted onto an aluminum foil with a doctor blade and then dried at 120 $^\circ\text{C}$ for 18-21 h under an IR radiator. The quantity of active material in a dried remainder has been of 3–8 $\text{mg}\cdot\text{cm}^{-2}$. Cells have been assembled in coin-type 2016 cases with a Celgard 2400 separator and an electrolyte containing the 1 M solution of LiPF_6 in a mixture of ethylene carbonate and dimethyl carbonate taken in the 1:1 mass ratio. The reference and counter electrode has been made of lithium metal.

SEM (a, b) and TEM (c, d) images of the samples obtained by the modified citric acid route are shown in Fig. 1. It can be observed that the morphology of the particles is different. Agglomeration occurs for the air-fired sample, influencing the electrochemical properties of the electrode materials (Fig. 1, a). In the case of argon-fired samples (Fig. 1, b) we have smaller, perfect 150 nm particles compared with those obtained in air. For the gradient composition, due to similarity in crystal structures of LiMn_2O_4 and $\text{LiNi}_{0.5}\text{Mn}_{1.5}\text{O}_4$, it is very difficult to distinguish between the core and the shell (Fig. 1, c). However, for the polymer modified material we have well separated, perfect core crystals with thin polymeric shells (Fig. 1, d).

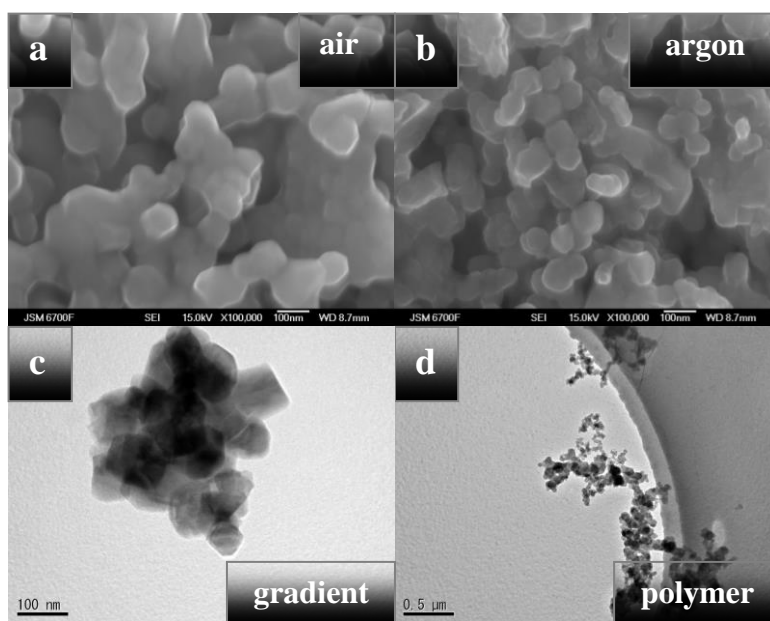


Figure 1. SEM (a, b) and TEM (c, d) images of the samples.

All these peculiarities are reflected on unique electrochemical properties of the electrode materials (Fig. 2). As could be seen, for the argon-fired samples, the current loads are higher than for air-fired materials (100C against 45-65C). The most powerful are the electrodes consisting of particles mixed with a polymer additive and enduring more than 130C.

So, one can conclude that prevention of aggregation and surface modification significantly improve the high-rate properties of electrode materials and can be much effective for making them applicable for hybrid vehicles where an initial start impulse is a must.

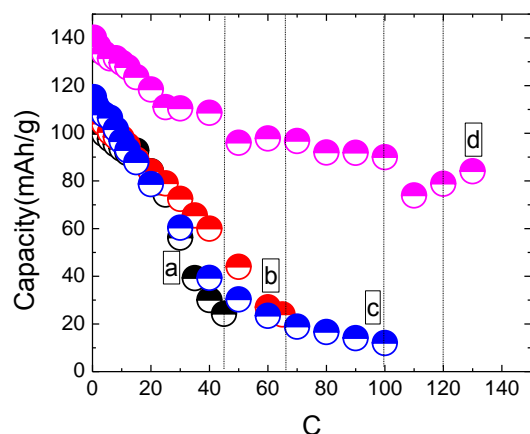


Figure 2. Dependence the capacity on the current rate (C units) for various samples. a – air-fired material, b – argon-fired material, c – gradient material, d – polymer-covered material.

References

1. A. S. Aricó, P. Bruce, B. Scrosati, J.M. Tarascon, W. Schalkwijk. *Nat. Mater*, **4** (1) 366 (2005).
2. A. V. Potapenko, S. A. Kirillov. *J. Energy Chem.*, **23** (1) 543 (2014).
3. S. A. Kirillov, I. V. Romanova, I. A. Farbun. *NATO Science Series II: Mathematics, Physics and Chemistry*, **229** (1) 495 (2006).
4. I. A. Farbun , I. V. Romanova, S. A. Kirillov. *J. Sol-Gel Sci.Technol.*, **68** (3) (2013) 411.
5. I. Romanova, S. Kirillov, *J. Therm. Anal. Calorimetry*, **132** (1) 503 (2018).
6. A. V. Potapenko, S. I. Chernukhin, I. V. Romanova, K. Sh. Rabadanov, M. M. Gafurov, S. A. Kirillov. *Electrochim. Acta*, **134** (1) 449 (2014).
7. A. V. Potapenko, S. A. Kirillov. *Electrochim. Acta*, **258** (1) 9 (2017).

Recent Advances and Challenges on Ni-Rich Cathode Materials for Lithium-Ion Batteries

Francis Amalraj Susai ^a, Hadar Sclar ^a, Raman Ravikumar ^a, Sandippan ^a, Saphir Giladi^a, Yehonatan Levartovsky^a, Judith Grinblat ^a, Michael Talianker ^b, Arup Chakraborty ^a, Dan T. Major ^a, Boris Markovsky ^a, Doron Aurbach ^a

^a*Department of Chemistry, Bar-Ilan University, Ramat-Gan 52900, Israel*

^b*Department of Materials Engineering, Ben-Gurion University of the Negev,
Beer-Sheva, Israel*

One of the cathode materials of Li-ion batteries (LIB), utilized in electric vehicles (EV) nowadays is $\text{LiNi}_{0.85}\text{Co}_{0.10}\text{Al}_{0.05}\text{O}_2$, which belongs to a family of layered Ni-rich ($\text{Ni} \geq 80$ at. %) transition metals oxides $\text{Li}(\text{Ni-Co-Mn})\text{O}_2$. Although these materials provide a combination of high reversible capacity (200-250 mAhg^{-1}) and high operating voltage (~ 3.8 V vs. Li/Li^+) which are very essential for the EV application, they in turn have severe drawbacks like synthesizing the material in exact stoichiometry, long-term cyclability, and thermal runaway. These issues are to be critically addressed to realize full potential of Ni-rich oxides as next-generation cathodes for LIBs.

By keeping the above issues, we aimed in the present investigation to reduce the cationic disorder in $\text{Li}(\text{Ni-Co-Mn})\text{O}_2$ by partial metal ion substitution (doping) in the layered structure. This not only enhances the reversible capacity of the electrode but also stabilizes the structure. The main questions studied were lattice doping by Al^{3+} , Zr^{4+} and Mo^{6+} of the above materials in relation to the electrode behavior, structural stability, and thermal reactions [1-3]. For these materials, using density functional theory calculations, we have shown that doping by the above cations is preferred at Ni sites. It was established that the interfacial resistance of the doped samples is much lower compared to that of undoped measured by impedance spectroscopy at several potentials during charge. For these electrodes, the interfacial resistance increases rapidly with cycling, while Zr and Mo-doped electrodes exhibit stability of this parameter even at high electrode potentials, >4.0 V, upon cycling. This implies therefore more stable modified electrode/solution interface of doped electrodes developed on these samples. We discuss also the following issues: *ab-initio* calculations of the preferential substitution of Al^{3+} , Zr^{4+} and Mo^{6+} on the Li or transition metal sites; influence of dopant ions on the $\text{Li}^+/\text{Ni}^{2+}$ mixing and on charge distribution, changes of the lattice constants, voltage profiles, and of the dopant segregation at the surface studied by TOF-SIMS.

References:

1. D. Aurbach, O. Srur-Lavi, C. Ghanty, B. Markovsky et al. J. Electrochem. Soc. 162 (2015) A1014.
2. F. Schipper, M. Dixit, D. Kovacheva, M. Talianker, O. Haik, J. Grinblat, E. M. Erickson, C. Ghanty, D. T. Major, B. Markovsky, and D. Aurbach, J. Mater. Chem. A, 4 (2016) 16073.
3. F. Schipper, H. Bouzaglo, M. Dixit, E. M. Erickson, T. Weigel, M. Talianker, J. Grinblat, L. Burstein, M. Schmidt, J. Lampert, C. Erk, B. Markovsky, D. T. Major, D. Aurbach, *Adv. Energy Mater.* **2017**, 1701682.

Flame Retardants as Solvent in Gel Polymer Electrolytes

I. Veselkova^a, M. Jahn^a, M. Sedlářiková^a and J. Vondrák^a

^a Department of Electrical and Electronic Technology, Brno University of Technology, Technická 10, 616 00 Brno, Czech Republic

This paper deals with a method of preparation of gel polymer electrolyte without a solvent. As a solvent used one type of flame retardant, other components of chemical composition didn't change. This work is focused on estimation electrical conductivity and potential window of gel electrolyte. Electrical properties were measured by linear voltammetry and impedance spectroscopy.

Introduction

Gel polymer electrolytes (GPE) have received significant attention in recent years for application in lithium-ion batteries and other energy sources due to fact that they combine the properties of both a solid electrolyte and a liquid electrolyte. GPE have the acceptable values of electrical conductivity and can avoid the leakage from the battery. Thus, they are good alternatives to all the rest (1) (2).

Electrolyte flammability is one of the most important safety issues, not only in liquid electrolyte systems, but in most gel polymer systems too. The flammability of an electrolyte may cause side-accidents when a lithium battery is broken or heats up by another accident, for example by improperly chemical reaction. To solve this important problem different flame retardants can be used as additives to the main chemical composition of electrolyte (3).

Flame retardant is a material that does not itself maintain combustion without an external heat source and therefore retards the spread of fire. These materials can act in the condensed or vapor phase, and can thus interfere with the combustion process during heating, pyrolysis, ignition, or flame propagation.

Chemical composition

Initial sample of gel polymer electrolyte contained salt lithium hexafluorophosphate (LiPF_6) in concentration 0.5 mol/l in solvent, monomer methyl methacrylate (MMA) in concentration 20 mol% to conductive component, a cross-linking agent ethylene glycol dimethacrylate (EDMA) 3.5 mol% in monomer and UV-polymerization initiator benzoin ethyl ether (BEE) in concentration 1 mol% in monomer. As solvent five types of flame retardants were used in concentrations 0.25 mol/l, 0.5 mol/l, 0.75 mol/l, 1 mol/l, 1.25 mol/l and 1.5 mol/l. Selected retardants were triethylene phosphate (TEP), trimethyl phosphate (TMP), tributyl phosphate (TBP), triphenyl phosphate (TPP) and the last one dimethyl methylphosphonate (DMMP). Figure 1 represents chemical formulas of selected flame retardants.

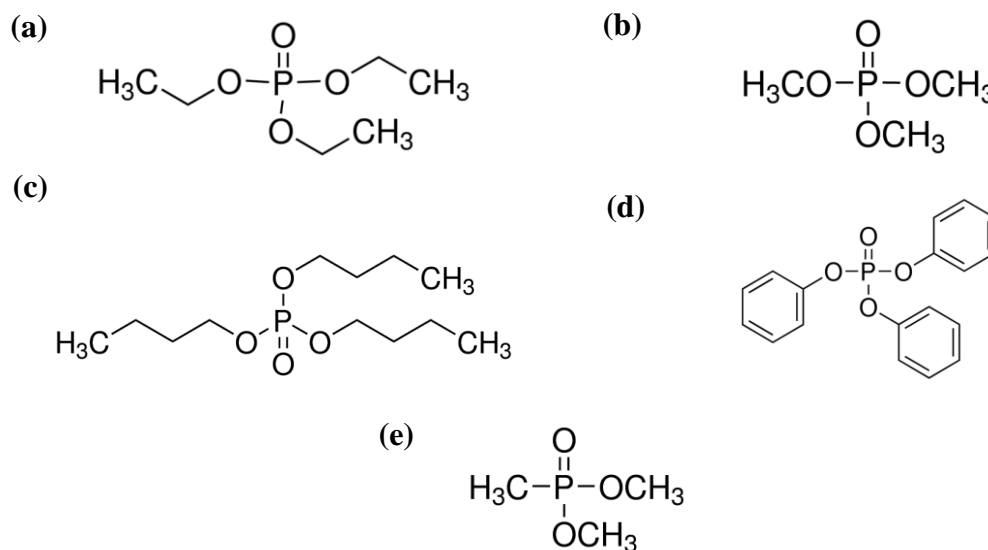


Figure 1. Chemical formulas of flame retardants: (a) TEP; (b) TMP; (c) TBP; (d) TPP; (e) DMPP

Experimental results

In experimental part five series of samples with selected flame retardants were prepared in glove box with argon atmosphere JACOMEX. Polymerization process took place in chamber with UV-light for a period of time 60 min. Thickness of the samples 0.9 mm was determined by thickness of Teflon in glass form. Electrical conductivity and potential window of each sample of GPE were measured. Measurements were carried out on the potentiostat BioLogic. Figure 2 shown values of conductivity that were measured during the experiment.

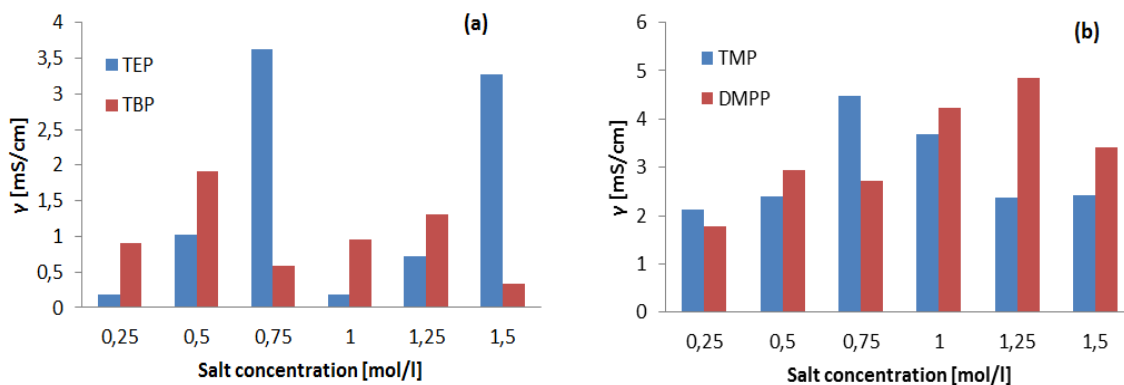


Figure 2. Comparison values of conductivity of gel polymer electrolytes with selected flame retardants: (a) comparison of TEP with TBP; (b) comparison of TMP with DMPP

The results from Figure 2 indicate that gel with TMP or DMPP have conductivity much more than TEP or TBP. All gel electrolyte samples with flame retardant TPP didn't polymerize and their electrochemical properties could not be measured. With increasing concentration of salt, the solution crystallized too fast, this causes the impossibility of filling the solution into the glass form, and its subsequent polymerization.

Conclusion

The main goal of this experiment was focused on increasing ionic conductivity and electrochemical stability of the polymer. Comparison the results show that TMP and DMMP flame retardants have much higher conductivity than TEP and TBP. The highest value of conductivity had gel electrolyte with DMMP in salt concentration 1.25 mol/l. The smallest value of conductivity had gel electrolyte with TEP in salt concentration 0.2 mol/l.

Further study will be focused on improvement flammability with high conductivity and electrochemical stability and to validate the use in Li-ion batteries.

Acknowledgments

This research work has been carried out in the Centre for Research and Utilization of Renewable Energy (CVVOZE). Author gratefully acknowledge financial support from the Ministry of Education, Youth and Sports of the Czech Republic under NPU I programme (project No. LO1210). This research was also sponsored by the NATO Science for Peace and Security Programme under grant 985148.

References

1. Q. Lu, J. Yang, W. Lu, J. Wang and Y. Nuli, Advanced semi-interpenetrating polymer network gel electrolyte for rechargeable lithium batteries. *Electrochimica Acta*, **152**, (2015).
2. W. Li, Y. Xing, Y. Wu and J. Wang, Study the effect of ion-complex on the properties of composite gel polymer electrolyte based on Electrospun PVdF nanofibrous membrane. *Electrochimica Acta*, **151**, (2015).
3. H. Akashi and K. Sekai, A novel fire-retardant polyacrylonitrile-based gel electrolyte for lithium batteries. *Electrochimica Acta*, **43**, (1998).

Durability of a Li-ion battery pack

P. Vorel^a, D. Cervinka^a, M. Toman^a, J. Martis^a

^a Department of Power Electrical and Electronic Engineering, Brno University of Technology, Brno, Czech Republic

Introduction

Capacity and internal resistance of a Li-ion battery pack were measured periodically during a period of 13 years. This battery pack was completed in 2005 by the author together with an electric bike (1 kW) with an induction motor. The problems of battery pack life time, reliability and possibility to predict the lifetime are discussed very often in the field of electric vehicles (2), (3).

From 2005 to 2013 the electric bike was used quite often and a distance of ca. 14000 km was ridden with this battery pack. Last 5 years (from 2013 till 2018) the bike was used rarely. However the aging process of the battery pack can be further observed and documented with the measurements. The maximum current taken from the battery with the traction inverter of the bike is ca. 50A. The charger developed for this bike provides the maximum charging current of 20 A (a slow charging with 5 A can be switched if required). The bike enables regenerative braking providing max. approx. 40 A charging current (mostly short time intervals of several seconds or tens of seconds). Parameters of the battery are in Tab. I.

TABLE I. Cell and battery pack parameters (new battery pack in year 2005).

	Single Cell	Battery Pack
Nominal voltage	3.6 V	25.2 V
Discharge cut-off voltage	3.1 V	21.7 V
Final charging voltage	4.1 V	28.7 V
Maximum discharging current	2.38 A	50 A
Used maximum charger current	0.95 A	20 A
Available capacity	1.9 Ah	40 Ah
DC internal resistance	120 mΩ	40 mΩ

Battery pack design and way of performance

The battery pack consists of 7 blocks connected in series. Each block contains 21 cells Panasonic CGR18650C (1) connected in parallel. The total number of cells is 147. The minimum allowed voltage per 1 cell (deepest discharging) was set to 3.1 V (not 2.5 V like usually). The allowed maximum voltage was set to 4.1 V (not 4.2 V like usually). Only ca. 90% of the full achievable capacity (from 2.5 V to 4.2 V) is available in this operation regime (from 3.1 V to 4.1 V). However the author expected to achieve a longer durability of the battery pack using these stronger limits.

The battery was re-charged at any occasion, not only when it was fully discharged. The action radius of the bike is ca. 60 – 70 km and mostly it was re-charged after ca. 30 km. The author expected a positive influence on the life time again. On the other hand the battery was stored in fully charged state (e.g. in winter when the bike was not used) what could have a negative influence on the lifetime. The storage temperature was mostly ca. 25°C. The maximum operation temperature of the cells was not measured exactly but it can be guessed about ca 60°C (riding or charging in hot sunny summer days).

Battery management system and charging strategy

Simple reliable BMS electronic circuits were constructed. Comparator blocks monitoring the over-voltage and under-voltage of each cell are continuously supplied from corresponding cells. Each of the 7 comparator blocks (7 serial blocks of the battery pack) provides 2 individual logical signals (overvoltage 0=YES/1=NOT, under-voltage 0=YES/1=NOT). These signals are galvanically separated from the monitored cells. Then one common over-voltage signal and one common under-voltage signal are created from these individual output signals using logical gates “AND”. If an over-voltage appears at any cell (at least 1) then the common over-voltage signal is set to 0. If an under-voltage appears at any cell (at least one) then the common under-voltage signal is set to 0. The logical zero of the common under-voltage signal turns off the power terminal of the battery using a relay (no further discharging is possible). The common over-voltage signal leads to the traction inverter of the bike in order to limit the regenerative braking. Moreover this signal leads to the charger as the control feedback, see Fig. 1.

A cascade control strategy is used in the charger control circuitry in principle. A slave current loop is used. The demanded current value is obtained from a non-traditional master voltage controller which ensures that no cell can be over-charged. The control structure is in Fig. 1. The common over-voltage logic signal from the management system is filtered by a low-pass filter with a high time constant. If any cell is already near to the full voltage then the over-voltage signal oscillates between 0 and 1. Then the average value of this pulse signal serves as the demanded current.

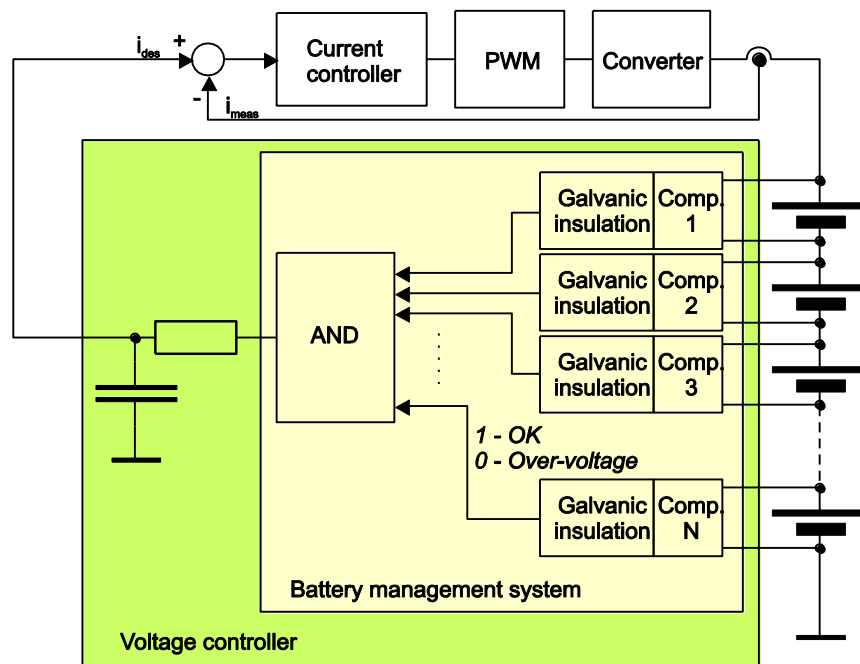


Figure 1. Charger control strategy

Periodical measurements

The capacity was measured at a constant discharging current of 20 A. The discharging started from fully charged battery and stopped when the common under-voltage signal cut-off the battery terminals. The internal resistance was measured at SOC ca. 50%, after a discharging process. The steady open-circuit voltage was measured and then the voltage at a current of 20 A (after ca 15 second of discharging to let the voltage stabilize). The obtained results are in Table II.

TABLE II. Periodical measurements of capacity and internal resistance (whole pack)

Date	Total distance	Capacity [Ah]	DC internal res. [$m\Omega$]
10.8.2005	540 km	39.2	40
26.7.2006	1666 km	37.7	40
30.1.2008	4667 km	35.0	40
21.10.2008	9192 km	35.0	40
7.7.2009	10847 km	34.3	40
7.5.2010	12074 km	33.0	40
4.3.2011	13865 km	33.0	40
10.12.2013	Ca. 14000 km	32.7	44.5
18.7.2018	Ca. 14000 km	30.7	52

Conclusions

The durability of the pack is surprisingly high. During 13 years the internal resistance increased only about 30% and the capacity decreased about 22%. The performance of the battery pack during 13 years confirmed the relevance of the used control strategy and BMS conception. Regular cell voltage distribution (always the same pack maximum voltage of 28,6 V and cut-off voltage of ca 22 V) was achieved during the whole time with no additional balancing! The connection of 21 parallel cells in each block improves statistically the regularity of the capacity and internal leakage of the blocks each other. The charging strategy together with existence of some non-zero consumption of comparator circuits from each cell ensures the regularity of charge distribution to the cells during a long time.

Acknowledgment

This research work has been carried out in the Centre for Research and Utilization of Renewable Energy (CVVOZE). Authors gratefully acknowledge financial support from the Ministry of Education, Youth and Sports of the Czech Republic under NPU I programme (project No. LO1210).

References

1. Panasonic CGR18650C Cell Datasheet.
<http://www.rosebatteries.com/pdfs/Panasonic%20CGR18650C.pdf>
2. Ying Shi, Kandler Smith, Regan Zane, Dyche Anderson, "Life prediction of large lithium-ion battery packs with active and passive balancing", *American Control Conference (ACC) 2017*, 2017.
3. N. Lotfi, J. Li, R. G. Landers, J. Park, "Li-ion Battery State of Health Estimation based on an improved Single Particle model", *American Control Conference (ACC) 2017*, pp. 86-91, 2017.

Ab-initio Calculation of New Poly-oxyanion Cathode Materials of Li-ion Battery

Sangkoan Yi^a, Kyeongjae Cho^b, and Meanghyo Cho^a

^a School of Mechanical and Aerospace Engineering, Seoul National University, Gwanka-gu, Seoul 08826, Korea

^b Department of Materials Science and Engineering and Department of Physic, University of Texas at Dallas, Richardson, USA

Poly-oxyanion cathode materials are recent found materials that higher capacity, higher stability and longer cyclic life than existing materials. LiFePO_4 is one of attractive cathode materials as mentioned before. But this material has limitations for using commercial batteries, low voltage and low ionic diffusivity. The anion P and O strong bonding is effected properties of LiFePO_4 . In this study, we suggest that substituted from P to other anion As and Sb, and confirm the different properties and the properties are suitable for using Li-ion battery.

Today, electrochemical energy storage devices are the focus of many research efforts for solve the growing environmental and sustainability problems associated to fossil fuel devices. Above all things, lithium ion batteries are used in various electronic devices because of their higher specific capacity, higher energy density, and can used repeatedly compared to existing batteries. However, they are limited to use for HEV (Hybrid Electronic Vehicle), EV (Electronic Vehicle) and other energy storage devices because most commonly used battery cathode material like the LiCoO_2 (LCO) has insufficient performance. Thus, need to research continue to be directed finding new cathode materials for use large-scale electronic devices.

Until now, several different materials have been investigated for alternative cathode materials in order to improve the performance of Li-ion batteries. Among several cathode materials, poly-oxyanion compounds with strong binding with oxygen have excellent thermal stability than other cathode materials. Phosphate (LiTMPO_4 (TM=Fe, Mn, Co and so on)) is interested in many researchers because this material is show the higher capacity (~170mAh/g) than existing material like LCO (~120mAh/g), and has very safety. And this cathode material has stable structure and was show almost theoretical capacity because phosphate has octahedral structure that six oxygen atoms are formed octahedron with transition metal (TM). The octahedral structure is very stable, so cannot occur structural problems when Li ion is extracted. However, phosphate has poor electronic and ionic conductivity, and phosphate's crystal structure olivine has only one dimensional Li diffusion path so if this path is blocked, diffusivity is many decreased. And iron phosphate LiFePO_4 has lower voltage (~3.4V), hence has low energy density and power density.

Recently, silicates materials ($\text{Li}_2\text{TMSiO}_4$ (TM=Fe, Mn, Co and so on)) receive huge interest because have higher capacity (~330mAh/g) than other cathode materials and safer than commercialized cathode material. However in previous studies, silicate cannot show theoretical capacity and has poor electrochemical properties. For example, $\text{Li}_2\text{FeSiO}_4$ (LFS) only show more than 160mAh/g with reversible capacities of 120-140mAh/g cannot show theoretical capacity 330mAh/g. Silicates are polymorphism through synthesis method, so have many space groups like Pmn21, P21n, Pmnb and so on. These structures are all tetrahedral structures that four oxygen atoms are formed tetrahedron with transition metal (TM). The tetrahedral structure has structural

problems when Li ion is extracted because relatively few oxygen atoms are formed. Therefore, polyhedrons are changed when Li ion is extracted, so this change is occurred structural problems and cannot shows theoretical capacity.

If transition metal of phosphate and silicate is Fe, the materials have strong point at price because Fe is cheaper than other transition metals and the Fe is very safer than other transition metals.

Likewise, if poly-oxyanion structures have different anion, the structures have different electrochemical properties and kinetic properties. Hence we motivate that design the new poly-oxyanion cathode materials for overcome the limitation of battery performance. And we calculated the materials are that substituted from phosphorus (P) to other anions step by step based on olivine crystal structure based on density functional theory. Among the various anion elements, Arsenic (As) and Antimony (Sb) are belong to carbon group in periodic table same with phosphorus, so they have all same valence electrons. In addition, their atomic radius's values are 1.10 Å, 1.21 Å and 1.41 Å at P, As and Sb. In other words, the values have very similar, hence will not distort if substituted from P position to As or Sb position. However structure's electrochemical and kinetic properties are different if substituted from P position to As or Sb position. So we calculated most optimized structure when substituted from P position to As or Sb position, and calculated electrochemical and kinetic properties related to battery's performance.

This research of the new poly-oxyanion compound cathode material that used ab-initio study show the new promising cathode material compared with existing cathode material. Furthermore, the research provides the different directions that can develop the Li ion battery, so advanced for using HEV (Hybrid Electronic Vehicle), EV (Electronic Vehicle) and other electronic devices.

Acknowledgments

The National Research Foundation of Korea (NRF) grant funded by the Korea government (MEST) (2012R1A3A2048841) and the Technology Innovation Program of the Korea Institute of Energy Technology Evaluation and Planning (KETEP) granted financial resource from the Ministry of Trade, Industry & Energy, Republic of Korea (No. 20152020105420)

References

1. A.K. Padhi et al, *J. Electrochem. Soc.*, **144**, 1188 (1997).
2. A. Yamada et al, *J. Electrochem. Soc.*, **148(3)**, A224 (2001).
3. Fei Zhou, *Electrochem. Commun.*, **6**, 1144 (2004).
4. P.Zhang et al, *Phys.Chem.Chem.Phys.*, **14**, 7346 (2012).
5. Motoaki Nishijima et al, *Nature communications*, **5**, 4553 (2014).

In-situ X-ray study of Electrodes for Li-ion Battery in Different State of Charge

L. Chladil^{a,b}, D. Kunický^a and O. Čech^{a,b}

^a Department of Electrical and Electronic Technology, Brno University of Technology, Technická 10, 616 00 Brno, Czech Republic

^b Centre for Research and Utilization of Renewable Energy, Faculty of Electrical Engineering and Communication, BUT, Technická 10, 616 00 Brno, Czech Republic

This paper is focused on the structural characterization of commercially exploited cathode material LiFePO_4 in different state of charge. The material was measured inside of modified ECC-Opto-Std cell and X-ray characterization were performed using Rigaku Miniflex 600 HR diffractometer. State of charge were set potentiostatically and lattice parameters and volume changes were evaluated. Measured data and obtained results were discussed with conclusions of other researchers and as a result we found the full agreement that among other confirms validity of the used instrumentation.

Introduction

Internal crystallographic structure is changing during charging and discharging of any active materials for Li-ion batteries. Charging of cathodes is associated with changes in relation to decrease of overall amount of lithium ions and take place so far as the lithium ions leaves the structure. From structural point of view slight decrease of lithium concentration lead to decrease of ion occupancy that could change the lattice constant only to a small extent. As the process of delithiation continues, gradual loss of lithium planes leads to complete transfer of structure in certain cases of cathode materials. As example, in case of Li_xCoO_2 the hexagonal unit cell is transforming to monoclinic structure lithium poor phase. The transition is gradual process and therefore the transitional area around $x = 1/2$ where both structural phases are present has appeared [1]. Phase transition is also accompanied by significant changes in lattice dimensions that results in volume changes of materials during charging. It is also known that volume changes directly influenced long-term stability of the materials and therefore knowledge of these structural parameters in different state of charge (different state of lithiation) is essential for assessing the assumptions for long-term usability.

Whereas LiCoO_2 , LiMnO or LiNiMnO exhibit large changes in volume of unit cell during de-lithiation, LiFePO_4 is stable material where only small changes in lattice dimension were detected [2]. Upon extracting lithium from LiFePO_4 , the olivine structure is preserved, and orthorhombic FePO_4 is obtained. It results in the volume changes below 6 %, which guarantees excellent stability of matter during Li intercalation/de-intercalation.

Present work brings the short study of crystallography of LiFePO_4 in different state of charge using affordable powder diffractometer Rigaku Miniflex 600 HR equipped with modified ECC-opto std cell.

Experimental

LFP powder was mixed with Super-P and polyvinilidene fluoride (PVDF) in ration 80:10:10. N-Methyl-2-Pyrrolidone (NMP) has been added to create a dense paste The paste was stirred with a magnetic stirrer for at least 24 hours and then coated onto aluminum foil stamped in the shape of the cell and dried at 50 °C for 1 hour. A second layer of active substance was then applied, followed by drying at 50 °C for 1 hour followed by drying at 105 °C for at least 24 hours. After thorough drying, the sample was pressed with a laboratory press CARVER 3851 by pressure 25 kN/cm². Final load of active material was 7.39 g/cm².

Electrode was then put into opto-std cell by El-Cell[®] that has been adapted for direct insertion into the chamber of powder diffractometer Rigaku Miniflex 600 HR (Figure 1). Separator made from glass fibers was used and cell were filled by electrolyte EC/DMC (1:1) with 1 mol/L LiPF₆. Metal lithium was used as both reference and counter electrode.

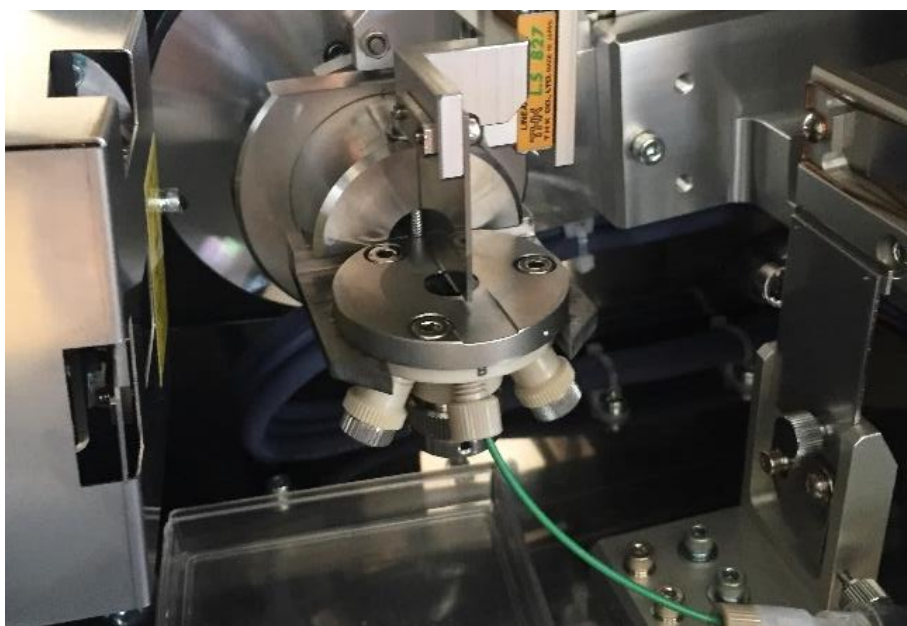


Figure 1. Modified opto-std cell by El-Cell mounted in chamber of powder diffractometer Rigaku Miniflex 600 HR ready to measurement.

Charging and discharging proceeds inside of the diffractometer chamber and state of charge were set in two steps. LiFePO₄ was galvanostatically charged to $V_c=3.7$ V, 4.0 V and 4.3 V at 2 C rate first, then kept at this voltage until the current was less than 0.2 C. X-Ray characterization was performed after hour brake that was used for reaching of equilibrium state of the electrode.

Results and Discussion

Obtained diffraction patterns in different state of charge are shown in Figure 1. From comparison of patterns is obvious, that a major change of crystallographic structure has already occurred in the first phase of charging. In this first step the material was hold at 3.6 V vs. Li/Li⁺ until current reached the 0.2 C value. In this step LiFePO₄ active matter were almost fully transformed to FePO₄. In this state of charge electrode has received 82,7 % of total capacity. Complete transition of structure to FePO₄ has to be discussed in spite of speed of discharging. Chang et al. studied the dynamics of structural transformation and their results revealed that during fast (1 C) delithiation LFP material remained as the LiFePO₄-structure until near the end of charge,

and then transformed abruptly to the FePO_4 -structure upon reaching another rest period [3]. This correspond to our measurement where more than hour brake before measurement was applied. This time delay helps to transformation of LiFePO_4 -phase to FePO_4 .

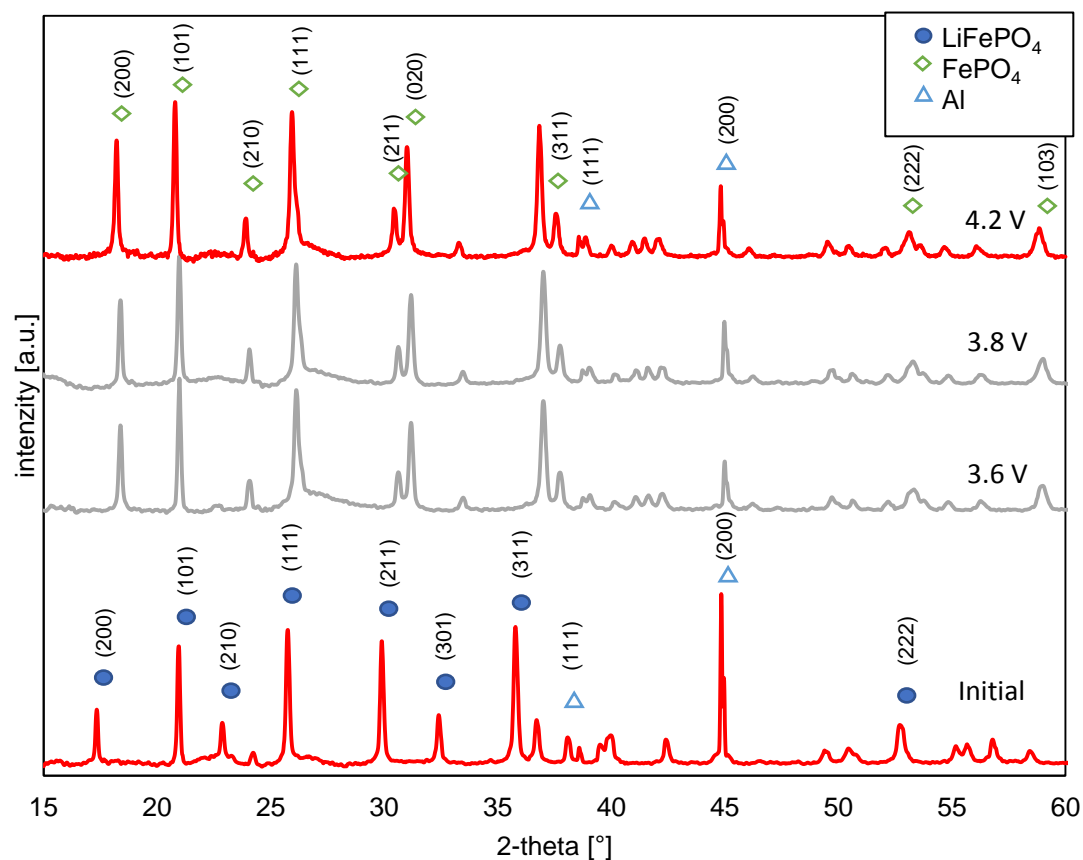


Figure 2. Diffraction spectra of LFP in different state of charge

Andersson et al. performed slow discharging of LFP at approx. 0.016 C and they observed linear changes of $\text{LiFePO}_4/\text{FePO}_4$ ratio during the cycling and after full charging the materials exhibits still 17 mol% of remained LiFePO_4 phase. One possible explanation is that in our case we use the working electrode of 14 mm in diameter whereas lithium counter electrode was only 8 mm. Therefore, especially at higher C rate, delithiation may occur preferentially at the central part of electrode where also the X-ray characterization took place while the overlapping parts was still discharged. Therefore, we were able to perform other charging of seemingly fully charged matter. In this case we recommended the use of smaller working electrode (WE) of the same dimension as counter electrode (WE without overlapping).

Finally, we perform the Rietveld analysis of initial (only LiFePO_4 phase) and fully delithiated electrode (only FePO_4 phase) and the results of lattice parameters are summarized in Table 1. We obtain the almost identical cell parameters for both identified phases as was reported by Strelsov et al. [4] and Eventoff et al. [5]. From comparison of unit cell volumes of lithiated and delithiated phase we easily calculated volume changes 6,92 % in respect to discharged (LiFePO_4) state.

Table 1. Summary of lattice parameters for LPF cathode material in fully lithiated (LiFePO_4) and de-lithiated (FePO_4) state obtained by Rietveld refinement.

Parameter	Measured		Results of [4] and [5]	
	LiFePO_4	FePO_4	LiFePO_4	FePO_4
Lattice parameter a [\AA]	10,33	9,81	10.3290	9.8142
Lattice parameter b [\AA]	6,01	5,79	6.0065	5.7893
Lattice parameter c cell [\AA]	4,69	4,77	4.6908	4.7820
Volume of unit cell [\AA^3]	291,28	271,11	291,02	271,70

Conclusion

Characterization of LiFePO_4 by affordable Rigaku Miniflex 600 HR system equipped by ECC-opto std. cell was performed. Potentiostatic approach is not appropriate for precious setting of certain state of charge which is in relation to small potential change of voltage plateau during charging. For precious setting of state of charge, we recommend using of galvanostatic mode rather. In order to homogeneous reaction across the whole working electrode the active mass should be deposit only on the same area which is in close contact with counter-electrode or charge/discharge rate should be significantly reduce. The parameters we fitted by Rietveld are in agreement with the previously published ones which confirm the ability of our system to acquire valid structure information.

References

1. J. N. Reimers, *J. Electrochem. Soc.*, 139 (8), 2091-2097 (1992)
2. A. Ait-SalaH, J. Dodd, A. Mauger et al., *Z Anorg Allg Chem.*, 632(8-9), 1598-1605 (2006)
3. H.H. Chang, Ch. Ch. CHANG, H. Ch. Wu et al., *Eletrochem Commun.*, 10 (2), 335-339 (2008)
4. V. A. Strelsov, E. L. Belokoneva, V.G. Tsirelson et al., *Acta Crystallogr., Sect. B: Struct. Sci.*, 49 (2), 147-153 (1993)
5. W. Eventoff, W. R. Martin and D. R. Peacor, *Am. Mineral.*, 57, 45-51 (1972)

The Activated Carbon From Biopolymers as the Electrode Material for Electrochemical Capacitors

K. Lota^a, I. Acznik^a, A. Sierczynska^a, G. Lota^b

^a Institute of Non-Ferrous Metals Division in Poznan, Central Laboratory of Batteries and Cells,
Forteczna 12, 61-362 Poznan, Poland

^b Poznan University of Technology, Institute of Chemistry and Technical Electrochemistry,
Berdychowo 4, 60-965 Poznan, Poland

Introduction

Electric double layer capacitors mainly use activated carbons with a high specific surface area as electrode materials, which enhances efficiency use of the electrode surface [1]. Efforts are being made to develop new materials for capacitor electrodes and suitable electrolytes which should be characterized by a large capacitance, cyclic stability and lowcost [2-4]. One of the most popular methods of preparing carbon electrodes is the chemical method of KOH activation [5].

The aim of the study was to determine the effect of carbon precursor, from biopolymers such as chitosan, starch, cellulose or pectin, on capacitance properties of prepared electrodes and choose the most suitable electrolyte for prepared carbon materials.

Experimental

The active carbons based on carbonized chitosan, cellulose and pectin from citrus peel and three types of starch were prepared. Chemical activations of the carbonized biopolymers were carried out in the ambient atmosphere in the temperature range of 600–850°C, with the C:KOH ratio of 1:4. The structure, morphology and physicochemical properties of active carbons were estimated using: Scanning Electron Microscopy (SEM EVO®40 ZEISS), nitrogen adsorption/desorption measurements (ASAP 2010 M (Micromeritics)) and elemental analysis (Vario MICRO CUBE Elementar Analysen Systeme GmbH).

The capacitor electrodes were formed into pellets consisting of 85% active material, 10% binder and 5% acetylene black. The activated carbons were tested in three aqueous electrolytes: 1M H₂SO₄, 6M KOH and 1M Na₂SO₄, using two-electrode Swagelok system. The specific capacitances of electrode materials were obtained using three techniques: cycling voltammetry, galvanostatic charge/discharge and electrochemical impedance spectroscopy using potentiostat-galvanostat VMP3/Z (Biologic, France).

All supercapacitors were subjected to cycling galvanostatic charging/discharging with current regime 2 Ag⁻¹.

Results and discussion

The morphology of the activated carbons was observed with SEM. Carbons prepared by carbonization of materials demonstrate similar morphology with visible fragmentation, while in activated carbons images particles with a destroyed, irregular shape are observed. The porosity and surface area strongly depend on the temperature of activation. Applying different polysaccharides

as precursors of activated carbons gives possibility to obtain carbons with well-developed surface area, which provide high capacitances probably as a result of suitable porosity and electrolyte ion dimensions. The activated carbons had a surface area more than $2000 \text{ m}^2\text{g}^{-1}$, with predominant contribution of micropores, where mainly the charging process of the electrical double layer took place.

Figure 1 presents dependence of capacitance values on current load for activated carbon from pectin in various electrolytes. The largest values of capacitance are observed in the acidic medium. Lower but very stable values of capacitance during cyclability measurements were obtained for carbons operating in $1 \text{ M Na}_2\text{SO}_4$. All carbon electrode materials in alkaline electrolyte show decrease in capacitance as the current regime was increased. The activated carbon prepared from chitosan with the temperature of activation standing at 750°C exhibits the largest specific surface area and capacitance of 295 Fg^{-1} at current density of 0.1 Ag^{-1} in the acidic medium. Moreover, the activated carbon from chitosan shows excellent cycling stability (almost 99% capacitance retention over 5000 cycles). The results showed that the activated carbon prepared from cellulose with the temperature of activation standing at 700°C exhibits the highest capacitance values using high current regimes in the acidic medium.

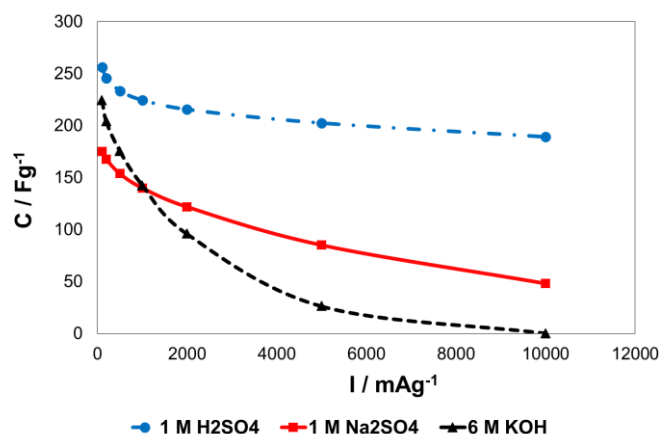


Figure 1. Capacitance versus current load dependence for activated carbon from pectin

Conclusion

The porosity and surface area strongly depend on the temperature of activation. High specific surface area enhances the efficient use of the electrode surface and influences on capacitance properties of material. The activated carbons have a surface area with predominant contribution of micropores, where mainly the charging process of the electric double layer takes place.

Applying the polysaccharide-based activated carbons as electrode materials for electrochemical capacitors gives high capacitances in acidic medium, probably as a result of suitable porosity and electrolyte ion dimensions. Moreover, the polysaccharide-based activated carbons showed good charge propagation and excellent cycling stability.

Acknowledgements

The authors acknowledge the financial support from the Ministry of Science and Education (Poland) – Grant no 3787/E-138/S/2016 and 3787/E-138/S/2018

References

1. P. Sharma, T.S. Bhatti, *Energy Convers.Manag.***51**, 2901 (2010).
2. K. Lota, I. Acznik, A. Sierczynska, G. Lota *Mat. Lett.* **173**, **72** (2016).
3. K. Lota, A. Sierczynska, I. Acznik, G. Lota *Chemik* **67** (11), 1138 (2013).
4. M. Mirzaeian, Q. Abbas, A. Ogwu, P. Hall, M. Goldin, M. Mirzaeian, H. F. Jirandehi, *Int. J. Hydrogen Energy* **42**, 25565 (2017)
5. T. Pagketanang, A. Artnaseaw, P. Wongwicha, M. Thabuot *Energy Procedia* **79**, 651 (2015).

The Influence of Electrolyte on The Performance of Electrochemical Capacitors

G. Lota^a, A. Bund^b, Ł. Kolanowski^a, M. Graś^a, J. Wojciechowski^a

^aInstitute of Chemistry and Technical Electrochemistry, Poznan University of Technology,
Berdychowo 4, Poznan 60-965, POLAND

^bTechnische Universität Ilmenau, Electrochemistry and Electroplating Group, Gustav-Kirchhoff-
Straße 6, 98693 Ilmenau, GERMANY

grzegorz.lota@put.poznan.pl

This study discusses the influence of electrolyte on the performance of electrochemical capacitors. The appropriate modification of current collectors or electrolyte could increase the performance of electrochemical capacitors. All electrochemical measurements have been performed in a two- and three-electrode Swagelok[®] type system in aqueous electrolyte. Based on the obtained results the electrolyte affects strongly the operating voltage of the system, the presence of pseudocapacitive effect and the corrosion of current collectors as well.

Introduction

Electrochemical capacitors (supercapacitors or ultracapacitors) are able to store the energy due to the formation of the electrical double layer at the electrode/electrolyte interface. Supercapacitors are characterized by high power density, quick charge/discharge and excellent cycling stability. The main goal of supercapacitor development is to increase the energy density. The energy density could be improved by increasing the capacitance or operating voltage of the system. The increase of capacitance could be realized by the so-called pseudocapacitance effect. The pseudocapacitance effects can originate from the quick faradaic reactions at the electrode/electrolyte interface. Quick faradaic reactions can be induced by the appropriate modification of electrode. The novel approach is to modify the electrolyte in order to enforce the pseudocapacitive effect [1-10].

Electrochemical capacitors are composed of two electrodes separated by a separator and soaked in electrolyte. Electrode material (activated carbon) is applied on the surface of metal/steel current collectors. In such a case, current collectors are exposed to corrosive electrolytes and can be subjected to corrosion processes. The corrosion phenomena are very often neglected in research by many authors.

Experimental

Electrochemical measurements were performed in two- and three-electrode Swagelok[®] cells in 1 M H₂SO₄, 1 M Na₂SO₄, 1 M KI, 1 M KOH and 6 M KOH. The Swagelok[®] system was assembled with reference electrode and two stainless steel 316L current collectors. The electrode was composed of 85 wt% activated carbon, 10 wt% polyvinylidene fluoride (Kynar Flex 2801) as a binder and 5 wt% acetylene black. The electrochemical measurements were carried out by using

cyclic voltammetry, galvanostatic charge/discharge and electrochemical impedance spectroscopy [11].

Summary and Conclusions

Based on the obtained results it can be concluded that electrolytes have significant impact on the performance of electrochemical capacitors (capacitance, energy and power density, operating voltage, self-discharge, internal resistance and cycling stability). Moreover, electrolytes affect the current collector corrosion. Corrosion potentials increase with decreasing pH value of electrolyte. This phenomenon can be assigned to the formation of passive oxide layer on the stainless steel current collectors (Table 1) [11].

TABLE I. Corrosion potentials and corrosion current densities of stainless steel 316L, calculated by the Tafel method using EC-Lab Software® [11].

Electrolyte	E_{corr} (mV vs NHE)	j_{corr} ($\mu\text{A cm}^{-2}$)
1 M H_2SO_4	280	0.385
1 M Na_2SO_4	93	0.361
1 M KI	-1	0.055
1 M KOH	-93	0.195
6 M KOH	-146	0.125

Acknowledgments

The authors acknowledge the financial support from the National Science Centre (Poland) - Grant no DEC-2013/10/E/ST5/00719.

References

1. F. Béguin and E. Frackowiak (Ed.), *Supercapacitors: Materials, Systems and Applications*, Wiley-VCH, Weinheim (2013).
2. F. Béguin, V. Presser, A. Balducci, E. Frackowiak, *Adv. Mater.*, **26**, 2219 (2014).
3. B.E. Conway, *Electrochemical Supercapacitors – Scientific Fundamentals and Technological Applications*, Kluwer Academic, New York (1999).
4. G. Lota, P. Krawczyk, K. Lota, A. Sierczyńska, Ł. Kolanowski, M. Baraniak, T. Buchwald, *J. Solid State Electrochem.*, **20**, 2857 (2016).
5. G. Lota, K. Lota, R. Kapica, J. Tyczkowski, K. Fic, E. Frackowiak, *Int. J. Electrochem. Sci.*, **10**, 4860 (2015).
6. K. Kopczyński, G. Milczarek, G. Lota, *Electrochem. Commun.*, **68**, 28 (2016).
7. E. Frackowiak, F. Béguin, *Carbon*, **39**, 937 (2001).
8. R. Kötz, M. Carlen, *Electrochim. Acta* **45**, 2843 (2000).
9. T. Brousse, D. Bélanger, J.W. Long, *J. Electrochem. Soc.*, **162**, A5185 (2015).
10. M. Inagaki, H. Konno, O. Tanaike, *J. Power Sources*, **195**, 7880 (2010).
11. J. Wojciechowski, Ł. Kolanowski, A. Bund, G. Lota, *J. Power Sources*, **368**, 18 (2017).

Heteroatom-doped Carbon for Energy Storage

Ł. Kolanowski, M. Graś, J. Wojciechowski, G. Lota

Institute of Chemistry and Technical Electrochemistry, Poznan University of Technology,
Berdychowo 4, Poznan 60-965, POLAND

lukasz.m.kolanowski@doctorate.put.poznan.pl

The purpose of this research is to obtain the new carbon materials rich in heteroatoms for electrochemical application. This study discusses the relationship between physicochemical and electrochemical properties of modified and unmodified carbon materials. In this work, the novel approach to modify the activated carbon surface by ozone has been performed. The utilization of ozone treatment enables the production of new carbon materials for electrochemical capacitors as well as electrodes for oxygen reduction reaction.

Introduction

Carbon material are widely used in industry, environmental protection, for energy storage and conversion. Due to the different hybridization of carbon atom orbitals, this element occurs in many allotropic forms. Carbon materials are used as adsorbents, catalysts and their carriers as well as electrode materials. Considering the variety of carbon materials (powders, granulates, fibers, fabrics and felts), particular attention is given to electrochemical applications (1-2).

Strong demand for portable electronic devices has led to significant progress in the field of chemical power sources. The huge market demand for efficient power sources led to the rapid development of lithium-ion batteries, photovoltaic cells, fuel cells and electrochemical capacitors. Therefore, it is desirable to design and produce new electrode materials capable to store and convert the energy (1-2).

Electrochemical capacitors, despite their many advantages, are characterized by low energy density. The increase in energy can be obtained by increasing the capacitance of or the operating voltage of the system. The increase in capacitance could be realized by appropriate modification of the electrode material in order to incorporate the heteroatoms into the carbon structure (3-4).

Considering the cost of the fuel cells (due to the presence of platinum as catalyst) and the possibility of poisoning the platinum with carbon monoxide, it is desirable to find other efficient electrode materials. In this case, carbon materials can catalyze the cathodic oxygen reduction process (ORR) (5-6).

Experimental

The modified and unmodified activated carbons by ozone treatment were used as electrode materials of an electrochemical capacitor. In order to estimate the performance of the electrochemical capacitor, all measurements were carried out with two- and three-electrode cells assembled in a Swagelok[®] system in aqueous electrolytes. The capacitance properties were

examined by galvanostatic charge/discharge, cyclic voltammetry and electrochemical impedance spectroscopy.

The reduction processes of oxygen have been investigated by means of cyclic voltammetry (CV) and linear sweep voltammetry (LSV) with rotating disc electrode measurements (RDE). The glassy carbon as well as modified glassy carbon were used as the working electrodes (0.07 cm^2), platinum wire and saturated calomel electrode were used as counter and reference electrode, respectively. The working electrode was polished with a suspension of Al_2O_3 and diamond in water and rinsed in water and ethanol before experiments. Glassy carbon has been modified by commercial carbon materials. Carbon material has been modified also by ozone treatment in order to increase the surface oxygen functional groups. The slurry of carbon materials was spread (5mL) on the glassy carbon surface. The slurry was obtained by mixing and sonication the 1ml of ethanol, 5 mg of carbon material and 5mL solution of Nafion[®].

Summary and Conclusions

Electrochemical measurements proved that ozone-treated carbon is desirable as an electrode material for electrochemical capacitors. It should be noted that pseudocapacitive effect is responsible for the increase the capacitance. Moreover, all measurements show that negative electrode is characterized by the higher capacitance in the comparison with positive one. It can be assigned to the process of electrosorption of hydrogen in carbon materials during negative polarization.

Based on the obtained results it can be concluded also that carbon materials rich in oxygen functional groups could catalyze the ORR reactions. The calculated numbers of electrons is less than 4 indicating many intermediates during this reaction. It is well known that quinone-like groups have shown catalytic activity towards oxygen reduction reaction for hydrogen peroxide production.

Acknowledgments

The authors acknowledge the financial support from the National Science Centre (Poland) - Grant no DEC-2013/10/E/ST5/00719.

References

1. F. Béguin and E. Frackowiak (Ed.), *Supercapacitors: Materials, Systems and Applications*, Wiley-VCH, Weinheim (2013).
2. B.E. Conway, *Electrochemical Supercapacitors – Scientific Fundamentals and Technological Applications*, Kluwer Academic, New York (1999).
3. G. Lota, P. Krawczyk, K. Lota, A. Sierczyńska, Ł. Kolanowski, M. Baraniak, T. Buchwald, *J. Solid State Electrochem.*, **20**, 2857 (2016).
4. G. Lota, K. Lota, R. Kapica, J. Tyczkowski, K. Fic, E. Frackowiak, *Int. J. Electrochem. Sci.*, **10**, 4860 (2015).
5. K. Lee, L. Zhang, H. Lui, R. Hui, Z. Shi, J. Zhang, *Electrochim. Acta*, **54**, 4704 (2009).
6. K. Mohanraju, V. Sreejith, R. Ananth, L. Cindrella, *J. Power Sources*, **284**, 383 (2015).

Carbon-supported AB₅-type Hydrogen Storage Alloy for DBFC Application

Ł. Kolanowski^a, M. Graś^a, J. Wojciechowski^a, K. Lota^b, G. Lota^a

^aInstitute of Chemistry and Technical Electrochemistry, Poznan University of Technology,
Berdychowo 4, 60-965 Poznan, POLAND

^bInstitute of Non-Ferrous Metals Division in Poznan Central Laboratory of Batteries and Cells,
Forteczna 12, Poznan 61-362, POLAND

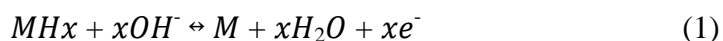
lukasz.m.kolanowski@doctorate.put.poznan.pl

Fuel cells are quiet, efficient and environmentally safe energy devices that directly convert chemical energy into electricity. Borohydride as a solid fuel is more convenient to store and transport than hydrogen, moreover, it is chemically stable and non-flammable. It is important to develop the best composition of the anode material in order to improve the efficiency of oxidation reaction. Multicomponent hydrogen storage alloys such as AB₅ and AB₂ type are a special group of anode materials also employed in direct borohydride fuel cells, because they can absorb atomic hydrogen associated with a decreased evolution of the gas and can be used instead of the noble metals.

Introduction

The direct borohydride fuel cell seems to be an optimistic alternative to the existing and well-known fuel cells. The chemical energy stored in the borohydride ion (BH₄⁻) and oxidant is directly converted into electricity, as a result of electrochemical conversion [1-2]. Fuel is an alkaline solution of metal borohydride. Unfortunately, a significant amount of it is lost, as a result of hydrolysis reaction, causing the hydrogen evolution which makes also structural problems [3-4]. The most commonly used anodic materials are expensive noble metals. It is therefore necessary to find solutions that will reduce the cost of fuel cell production, as well as improve its efficiency [5-6].

Multicomponent hydrogen storage alloys such as AB₅ and AB₂ can be used instead of the noble metals. These rare earth metal-based alloys have a good catalytic activity toward the borohydride oxidation reaction. Moreover, these compounds can also absorb atomic hydrogen causing a safe reduction of gas evolution [7]. Gas storage takes place in three stages. In the first one, the hydrogen is adsorbed on the surface of multi-component hydrogen storage alloy. The next step is related to the transfer of hydrogen atoms adsorbed on the surface to inside of the electrode. Finally, the gas diffuses into interior of the crystalline lattice (as in nickel-metal hydride battery) in order to be electrochemically oxidized by the following reaction [8]:



Experimental

In order to prepare the working electrode, the commercial AB₅ – type alloy of formula LaMnNi_{3.55}Al_{0.30}Mn_{0.40}Co_{0.75} was used. The alloy was mixed with nickel carbonyl and carbon materials. A three-electrode measurement system was built of the working electrode, the counter

electrode made of the nickel foam and the Hg/HgO electrode as the reference one, immersed in fuel solution.

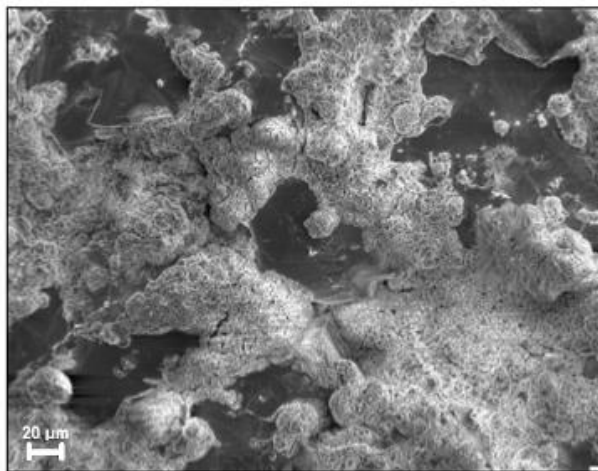


Figure 1. The morphology of graphite electrode after testing.

Results and discussion

The greatest stability of polarization potential for the anode consisted of hydrogen storage alloy with nickel carbonyl was obtained for 0.5 M NaBH₄ + 6 M KOH electrolyte, therefore it was chosen for further measurements. Graphite is an inexpensive carbon material, but its hydrogen absorbing performance has attracted little attention (Figure 1). This type of carbon material improved the conductivity of anode composites. Such an additive enhances the utilization of borohydride fuel. The addition of 3% of graphite to composite with AB₅-storage alloy would be a promising supplement for half cell of DBFC application.

Acknowledgments

The authors are grateful to financial support from the Ministry of Science and Higher Education, grant no 03/31/DSPB/0356.

References

1. C. Ponce de León, F.C. Walsh, D. Pletcher, D. J. Browning, J.B. Lakeman, *J. Power Sources*, **155**, 172 (2006).
2. Merino-Jiménez, C. Ponce de León, A.A. Shah, F.C. Walsh, *J. Power Sources*, **219**, 339 (2012).
3. R. Valiollahi, R. Ojani, J.B. Raoof, *Electrochim.Acta*, **191**, 230 (2016).
4. J. Liu, L. Yi, X. Wang, Q. Zhao, Y. Zhang, J. Gao, W. Wei, *Int. J. Hydrogen Ener.*, **40**, 7301 (2015).
5. D.M.F. Santos, C.A.C. Sequeira, *Renew.Sust.Ener.Rev.*, **15**, 3980 (2011).
6. G. Lota, A. Sierczyńska, I. Acznik, K. Lota, *Int. J. Electrochem. Sci.*, **9**, 659 (2014).
7. M. Graś, A. Sierczyńska, K. Lota, G. Lota, *Ionics*, **22**, 2539 (2016).
8. L. Wang, C. Ma, Y. Sun, S. Suda, *J. Alloy. Compd.*, **39**, 318 (2005).

Performance Enhancement of a Single-Chamber Membraneless Microbial Fuel Cell

Ali Muneer Hadi¹, Hassan A.Z.Al-Fetlawi²

¹Electrochemical Engineering Department, College of Engineering, University of Babylon ,Iraq
ali.zaun2014@gmail.com

²Electrochemical Engineering Department, College of Engineering , University of Babylon ,Iraq
fetlawi@uobabylon.edu.iq

Abstract

A single chamber membraneless microbial fuel cell is designed to operate at an operating temperature of 30 °C and pH =7±0.4 using wastewater as inoculum and fuel collected from the Al-Delmaj marsh site in Iraq at an initial chemical oxygen demand concentration of 862 mg/l and pH of 7.8 (reduced to 7±0.4 in all experiments by adding HCL acid). Rectangular sheets of graphite and smooth surface carbon fiber of 42 cm² surface area used for anode and cathode electrodes. The obtained results indicated that the cell performance for the cell using graphite for anode and cathode electrodes is better than that using the carbon fiber of smooth surface. The open circuit voltage and power per unit surface area for the cell using graphite for anode and cathode electrodes are 190 mV and 5.95 mW/m², respectively. Adding 300µM methylene blue as a mediator to the wastewater increased the open cell voltage to 311 mV and elevated its power density production to 1458.3 mW/m². The open cell voltage and power density improved to 310 mV and 1071 mW/m², respectively by using 400 µM of potassium permanganate as an oxidizing agent with the wastewater.

Macroporous SnO₂ As A Stable Cathode Catalyst Support For PEMFCs

I. O. Chikunova^a, V. S. Semeykina^{a,b}, P. N. Kalinkin^{a,b}, E. N. Gribov^{a,b} and E. V. Parkhomchuk^{a,b}

^a Boreskov Institute of Catalysis, Siberian Branch, Russian Academy of Sciences, Novosibirsk 630090, Russia

^b Faculty of Natural Sciences, Novosibirsk State University, Novosibirsk 630090, Russia

Introduction

Polymer electrolyte membrane fuel cells (PEMFCs) are the promising, environmentally friendly devices, in which carbon blacks (CB) are conventionally used as a cathode supports for Pt catalysts. However using CB as a support material ultimately leads to rapid corrosion of the Pt/CB catalyst, mainly caused by carbon oxidation at elevated potentials up to 1.5 V RHE [1]. Against this background, SnO₂ has attracted attention due to its high corrosion resistance compared to CBs and other metal oxides that are thermodynamically stable in PEMFC environment [2,3]. The hierarchically porous structure of SnO₂ as the Pt catalyst support is preferable because it would ensure efficient transport of the reactants and products through the catalyst layer and at the same time provide sufficient specific surface area for active component deposition. Here, we suggested the use of template technique for the synthesis of SnO₂ with hierarchical macroporous structure and bimodal pore distribution.

Experimental

PS microspheres with average diameter of ~ 250 nm were used as a template for synthesis of tin dioxides. They were prepared using 4,4'-azobis(4-cyanovaleric acid) as an initiator in accordance with the following work [4]. The first series of SnO₂ (named TC1, TC2, TC3) was synthesized by aging of sols from SnCl₄ in the presence of PS microspheres suspension in water-ethanol solution. The PS was removed from SnO₂ samples by annealing at 450°C in O₂ atmosphere. The final powders were yellow. The second series of tin dioxide (named TO1, TO2) was synthesized from SnC₂O₄. At first, SnCl₂ was precipitated by (NH₄)₂C₂O₄ in the presence of PS suspension while stirring. Then PS was extracted from SnC₂O₄ by toluene. The samples of SnC₂O₄ were heat treated at 450°C to provide thermal decomposition. The synthesis conditions are given in Table I.

Corrosion resistance of the SnO₂ samples, Ketjen Black EC-300J (AkzoNobel) and Vulcan XC-72R (Cabot Corp.) CBs was studied by using accelerated "Start/Stop cycling" protocol in 1–1.5 V RHE of the potential range in 0.1 M HClO₄ electrolyte with a 0.5 V/s of sweep rate. The cyclic voltammograms (CVs) were recorded in the range 0.05–1.2 V RHE with a sweep rate of 0.05 V/s before the "Start/Stop cycling" protocol and every 2000 cycles. Since the corrosion resistance criterion of the oxide supports has not been reported in the literature, we have suggested considering as a stability criterion the change of the specific surface charge of the samples (Q_{sp}), calculated from the CV curves. It was found that cycling the potential in the range of 1.0–1.5 V RHE ultimately led to a decrease in the specific charge resulted from the material degradation, as it had been observed before for the carbon supports [5]. The specific surface charge Q_{sp} (C/g) was calculated according to the equation (1):

$$Q_{sp} = \frac{\int IdE}{v \times m} \quad (1),$$

where I is the measured current (A), dE is the adjusted change in the potential (V), v is the sweep rate (V/s), m is the mass of the support (g).

Results and discussion

According to the X-ray diffraction (XRD), the TC1, TC2, TC3 and TO2 samples contained the only tetragonal phase. In contrast, TO1 represented 2 phases: tetragonal and orthorhombic with the last being metastable. CHNS elemental analysis was carried out to investigate if SnO_2 contained carbon or nitrogen impurities resulted from incomplete removal of PS. The analysis showed that only TC2 (0.17 ± 0.01 wt. %) and TO2 (0.23 ± 0.04 wt. %) samples contained carbon. No sulfur and nitrogen impurities were detected for the SnO_2 samples.

The scanning electron microscopy (SEM) data indicated the presence of spherical macropores for TC1, TC2, TC3 and TO1 samples with the average size in the range of 100-180 nm. To show an example of this macroporous structure, the SEM image of TC1 is given in Fig. 1a). TO2 had no distinct spherical macropores and represented rod-like particles with the length comparable to 10 μm . The mercury intrusion porosimetry (MIP) data of TC1, TC2, TC3 samples showed the maxima of pore size distribution in the range of meso- and macropores (Fig. 1b)). The TO1, TO2 samples possessed mesopores and had no macropores (>50 nm). TO2 sample was characterized by a bimodal pore size distribution with the maxima at 6 and 24 nm, while the TO1 sample had a wide peak at 11 nm, where a shoulder at 24 nm could be due to the presence of small amount of pores. All the samples had a reasonable surface area (Table I). The MIP pore volumes (V_{MIP}) of TC1, TC2, TC3 were greater the BET pore volumes (V_{BET}) because of higher quantity of macropores in the samples. The V_{MIP} and V_{BET} of TO1, TO2 were the same due to higher quantity of mesopores which can be formed because of the evolution of a large amount of CO, CO_2 during the SnC_2O_4 decomposition (Table I).

TABLE I. Synthesis Parameters And Textural Properties Of The Samples.

Precursor	Name	Aging Time, Days	Mass ratio of precursor to PS	S_{BET} , m^2/g	V_{BET} , cm^3/g	V_{MIP} , cm^3/g
SnCl_4	TC1	1	1:2.7	45	0.18	0.26
	TC2	60	1:2.7	31	0.09	0.20
	TC3	14	1:4.7	38	0.15	0.29
SnC_2O_4	TO1	-	1:0.5	32	0.15	0.15
	TO2	-	1:3	42	0.16	0.16

The testing of the SnO_2 samples by “Start/Stop cycling” protocol revealed that the most stable samples were TC3 and TO2 synthesized with the biggest mass ratio of precursor to PS (Fig. 2b)). Increasing the sol aging time resulted in increasing in the corrosion resistance of the SnO_2 (Compare TC1 and TC2 in Fig. 2a)). Comparing corrosion resistance of TC3, TO2 and CBs, it was found that TC3, TO2 were more stable than Ketjen Black EC-300J. Furthermore, TC3, TO2 showed comparable corrosion resistance with Vulcan XC-72R CB.

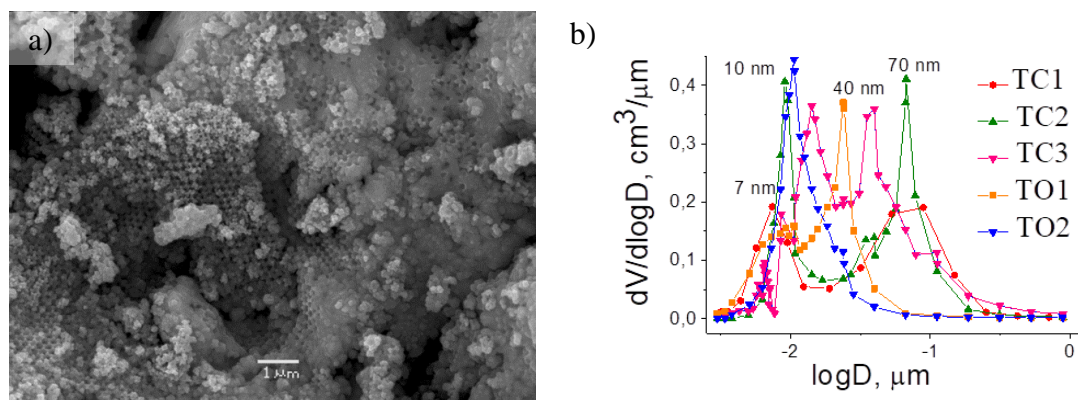


Figure 1. a) The SEM image of TC1, b) the pore size distributions for the SnO₂ samples.

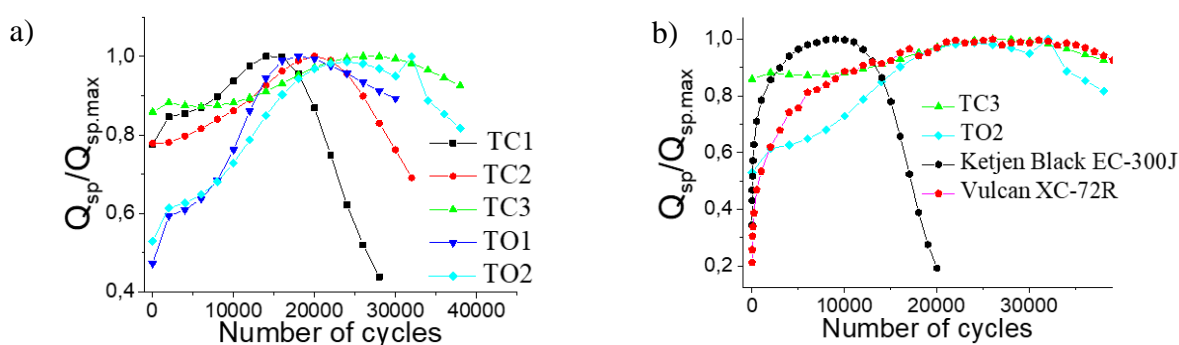


Figure 2. Comparison of stabilities of a) the SnO₂ samples, b) the most stable samples – TC3 and TO2 – with commercial CBs – Ketjen Black EC-300J and Vulcan XC-72R.

Conclusions

The template techniques of synthesis of macroporous SnO₂ from SnCl₄ and SnC₂O₄ had been developed. The SnO₂ samples obtained proved to be promising supports for PEMFC cathode catalysts in terms of their corrosion resistance.

Acknowledgments

The work was financially supported by the Ministry of Education and Science of the Russian Federation (RFMEFI60417X0159, title of the agreement: "Development of methods for hydrotreating of vacuum residue into high-quality marine fuels on macroporous catalysts"). The participation in the conference was financed by Gazpromneft and The Moscow refinery.

References

1. Y. Shao, G. Yin, Y. Gao, *J. Power Sources*, **171**, 558 (2007).
2. Y. Takabatake, Z. Noda, S. M. Lyth et. al., *Int. J. Hydr. Energy*, **39**, 5074 (2014).
3. K. Sasaki, F. Takasaki, Z. Noda et. al. *ECS Trans.*, **33**, 473 (2010).
4. E. V. Parkhomchuk, V. S. Semeykina, et. al., *Top. Catal.*, **60**, 180 (2017).
5. E. N. Gribov, N. V. Maltseva, V. A. Golovin, A. G. Okunev, *Int. J. Hydr. Energy*, **41**, 18207 (2016).

Development of PEM FC based auxiliary power unit.

J. Mališ, M. Paidar, K. Bouzek, M. Šmíd

University of Chemistry and Technology, Prague
Technická 5, Praha 6 Dejvice, 166 28, The Czech Republic
paidarm@vscht.cz

Modern rescue and military units require for their efficient work numerous electronic devices. Number of devices used rapidly grows. For such services long-lasting and reliable energy supply for outdoor activities, represents an important issue. Typical long-time communication and necessary equipment in outdoor operations comprises 100-200 W of base load and up-to 300 W of peak consumption. Auxiliary power units (APU) are often used for longtime operation.

PEM fuel cells represent proven technology for efficient conversion of chemical energy of fuel into electrical energy. They have several important advantages as high efficiency, flexibility, process intensity, nontoxic reaction products and silent operation. This fact allows application of fuel cells also in areas sensitive to exhalations, e.g. mobile medical beds or closed rooms. PEM fuel cell based mobile APU thus represents promising solution to ensure required power. Its main advantages are high flexibility and efficiency, high process intensity, instantaneous refueling and absence of moving parts. APU weight should not exceed 15 kg limit. It represent upper weight limit of the entire system, excluding pressurized gas cylinders. Logical solution is to use ambient air as an oxidant in order to reduce complexity of the system. Present work deals with development of PEM fuel cell base APU unit.

Typical electric consumption of connected devices is not constant in time and varies significantly. It is in contradiction to the preferred PEM fuel cell operation regime. Also as peroxide radicals are generated during PEM fuel cell operation on electrodes, these radicals can attack membrane and catalyst support. Used solution to reduce this phenomenon is periodic short circuiting of fuel cell for couple of milliseconds. Mentioned specific operation needs of PEM fuel cell must be accomplished by suitable energy management and combination with correspondingly sized accumulators. Li-ion accumulators represent suitable option to solve this task. It is due to their low weight and high charging/discharging currents. Another option is the use of supercapacitor instead accumulator. The main task for power management of APU is to minimize variation in output voltage with respect to the PEMFC operation and also with varying load of connected devices. All components have to be able to operate with high flexibility in the broad range of temperatures, including low ones. Selection of components was limited due to the set requirement on the weight of the system. The best ration between desired stability and weight were determined for system consist of PEM fuel cell, supercapacitor with small capacitance and accumulator able to work with high currents.

Another issue of PEMFC based APU is requirement for air purification. Especially in the case of operation in polluted air e.g. near to the fire. Impurities presented in the air can reduce fuel cell lifetime. Solid impurities like dust can deposit on cathode surface and in combination with produced water form a sludge blocking distribution channels and gas distribution layers of the fuel cell. Also platinum nanoparticles used as a catalyst can be poisoned by the various pollutants often presented in the air in industrial agglomerations. Most dangerous is dihydrogen sulfide and other sulfur compounds, which are known as strong poisons for platinum catalysts. Carbon monoxide is dangerous only on the anodic (hydrogen) side, because on the cathodic side can be oxidized by incoming air. Nitrous oxides can oxidize of catalysts support typically based on carbon black. Last group of potentially dangerous air pollutants are organic compounds like benzene, toluene and other.

These compounds if adsorbed can block the catalyst surface. Filters for removal of mechanical particles with diameter down to 0.2 μm are commercially available today. The active carbon can absorb chemical impurities. Promising approach to air treatment represents use of filters with interlayer of active carbon. Another important parameter for application in APU is power demand of blowers and thus pressure drop over the filter. Commercial filters were tested with respect to absorption capacity and pressure drop. On the basis of these data filter suitable for operating fuel cell was selected. However, no one filter exhibits sufficient absorption capacity. Improving is possible by different ways as adding extra layer of active carbon to increase their capacity for individual pollutants removal, combination of filter with special sorbents in form of pellets or spherical, adding extra honeycomb filter with high specific selectivity. By this way it was possible to produce filters optimized for different environment, e.g. for industrial areas, highways, plantation, mines, sandpits and others.

As a final work the assembly of all required APU components to the limited space of standard suitcase was done. Also the design of air input and output, controlling buttons and power connectors were done.

Acknowledgment

This work was supported by Ministry of the Interior of the Czech Republic within the framework of the Project No. VI20152019018.

In situ measurement of PEIS of lead acid battery cell

Petr Křivík¹, Sebastian Vaculík¹, Petr Bača¹, Jiří Kazelle¹

¹ Department of Electrotechnology, Faculty of Electrical Engineering and Communication, Brno University of Technology, Technická 10, 616 00 Brno, Czech Republic

The paper explores change of important parameters of lead acid battery cell during discharge and charge by potential electrochemical impedance spectroscopy (PEIS) method. Nyquist diagrams measured in situ were used for determination of ohmic and charge transfer resistance of lead acid battery cell.

Introduction

Suitable method for study of the lead acid battery is impedance spectroscopy. In a wide range of frequencies, impedance of electrochemical cell is measured and the measurement results are shown by impedance diagrams.

The electrochemical impedance of a battery characterizes its dynamic behaviour - response to an excitation of small amplitude [1, 2, 3]. In principle, any type of excitation signal may be used, for example square waves [4]. However, in practice, sine waves are the most often used.

Impedance diagrams may be plot in the Bode diagram (modulus in log scale vs. frequency and phase angle vs. frequency) or in the Nyquist diagram (imaginary part vs. real part). In the Nyquist diagram, electrochemists are used to plot the opposite of the imaginary part on the y - axis, so that the capacitive loop appear in the upper quadrant [5].

The general shape of the Nyquist diagram of the complex electrochemical impedance of battery cell contains a high frequency resistance in the range of mΩ, which is the real part of the impedance at frequencies higher than 100 Hz (1 kHz), a capacitive loop for frequencies between 0.1 and 100 Hz, a second loop for frequencies lower than 0.1 Hz.

In Nyquist diagram of a battery cell is included the ohmic resistance due to the connections, the separator, the electrolyte resistivity and the surface coverage of the electrodes by crystallized lead sulphate. Size of capacitive loop, corresponds to charge transfer resistance. Charge-transfer reaction has a certain speed that depends on the temperature, the concentration of the reaction products, and the potential. For positive electrode during discharge this is the resistance of the electron transfer from crystal to electrolyte and resistance of the charge-transfer of reduction of Pb^{4+} to Pb^{2+} [6].

Second loop at low frequencies is controlled by mass transport of Pb^{2+} ions and depends on the sulphatation reaction on the electrodes.

Experiment

For the experiment exploring changes of impedance in the lead acid battery cell a sealed lead acid cell was used, with spiral construction, containing AGM separator with a capacity of 2.5 Ah, nominal voltage 2V and internal resistance 5 mΩ (see Fig. 1).



Figure 1. Scheme of measured lead acid battery cell [7].

The cell was inserted in temperature chamber with constant temperature of 34 °C and then subjected to discharge with current 0.4 A. End of discharge was set to 1.6 V. After attaining of limiting voltage, charging continued with a charge current 0.4 A with a 2.4 V voltage limitation. In the course of discharging and charging, the potential electrochemical impedance spectroscopy (PEIS) was measured. Amplitude of PEIS was 5 mV, frequency interval was from 6 kHz to 50 mHz, with 6 measured points per decade.

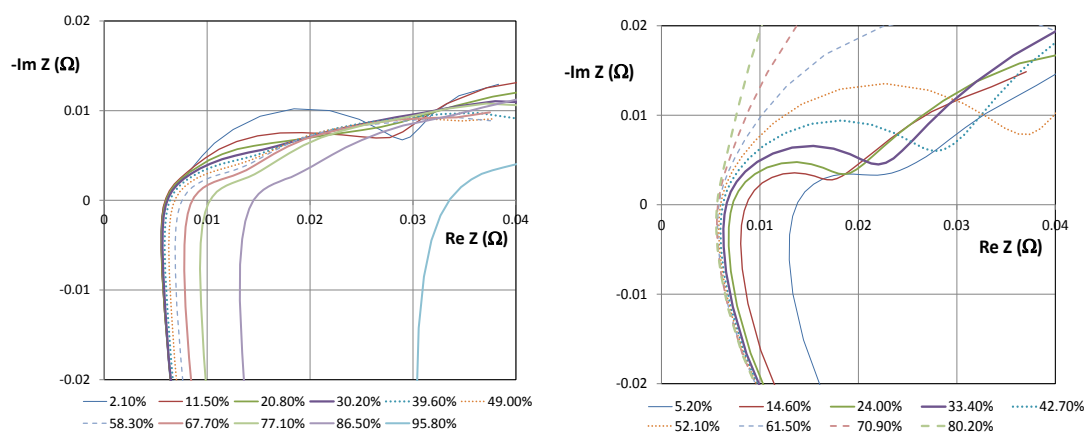


Figure 2. Nyquist diagram of the cell during discharge (DoD = 2.1% - 95.8%) – on the left and during charge (SoC = 5.2% - 80.2%) – on the right.

Figure 2 shows a comparison of Nyquist diagrams of the cell measured in situ during discharging and charging. From the dependencies, the difference in the shape of the two diagrams is obvious. During the discharge, there is a shift of dependencies towards the right, especially at the end of discharge. This is because of increase in internal resistance due to the formation of PbSO_4 crystals in the active mass of the electrodes.

Ohmic resistance, located at the intersection of the x-axis, corresponds to a frequency of about 1 kHz. This resistance increases during discharge, the highest increase is at the end of discharge. Size of capacitive loop (charge transfer resistance) decreases during discharge till 86% of DoD. Then, at the end of discharge, increases slightly.

Nyquist diagrams during charging of the cell shift to the left because of a drop in internal resistance, while the highest shift is at the beginning of charging as assumed. The size of the capacitive loop increases during charging as the charge transfer resistance increases.

Conclusions

Nyquist diagrams of the cell measured in situ during discharging and charging reflect the change of the important parameters of the lead acid battery cell, especially ohmic resistance and charge transfer resistance on the electrodes. Changes of these resistances cause change of the Nyquist diagrams and value of these resistances can be obtained from the diagrams.

Acknowledgements

This research work has been carried out in the Centre for Research and Utilization of Renewable Energy (CVVOZE). Authors gratefully acknowledge financial support from the Ministry of Education, Youth and Sports of the Czech Republic under NPU I programme (project No. LO1210).

References

1. C. Gabrielli, Identification of electrochemical processes by frequency response analysis, Solartron, Technical Report No 4183 (1983) 120.
2. N.A. Hampson, S.A.G.R. Karunathilaka, R. Leek, The impedance of electrical storage cells, J. Appl. Electrochem. 10 (1980) 3.
3. S. Rodrigues, N. Munichandraiah, A.K. Shukla, A review of state-of-charge indication of batteries by means of ac impedance measurements, J. Power Sources 87 (2000) 12.
4. T. Yokoshima et al., Application of electrochemical impedance spectroscopy to ferri/ferrocyanide redox couple and lithium ion battery systems using a square wave as signal input, Electrochimica Acta 180 (2015) 922.
5. H. Blanke et al., Impedance measurements on lead–acid batteries for state-of-charge, state-of-health and cranking capability prognosis in electric and hybrid electric vehicles, J. Power Sources 144 (2005) 418.
6. D. Pavlov, G. Petkova, Phenomena That Limit the Capacity of the Positive Lead Acid Battery Plates, Journal of The Electrochemical Society, 149 (2002) A654.
7. Cyclon Application manual. <http://www.produktinfo.conrad.com/index.php?bl=CS&q=254916>, 2008 (accessed 12 June 2018).

The Lead - Acid Battery Modified By Ionic Liquid

G. Lota^a, K. Kopczyński^a, A. Gabryelczyk^a, M. Baraniak^a, J. Pernak^b,
E. Jankowska^c, P. Kędzior^d

^a Poznań University of Technology, Institute of Chemistry and Technical Electrochemistry
Berdychowo 4, 60-965 Poznań, Poland.

^b Poznań University of Technology, Institute of Chemical Technology and Engineering,
Berdychowo 4, 60-965 Poznań, Poland.

^c Institute of Non-Ferrous Metals Division in Poznań, Central Laboratory of Batteries and Cells,
Forteczna 12, 61-362 Poznań, Poland.

^d PPUH Autopart Jacek Bąk sp. z o.o., Kwiatkowskiego 2a, 39-300 Mielec, Poland.

Hexadecyltrimethylammonium sulfate ionic liquid was used as an modifier for positive electrode in lead – acid battery. Influence of this compound on corrosion parameters, hydrogen and oxygen evolution potentials and capacity of positive electrode was examined. Studies showed inhibition of current collectors corrosion, increase of oxygen and hydrogen evolution reaction overpotentials as well as increase of positive active mass utilization.

Introduction

Lead – acid battery due to its properties such as reliability, safety of use and low cost of production connected with easy recycling are widely spread on the battery market (1). Despite the fact that lead – acid batteries were invented over hundred fifty years ago, they constantly suffer from several problems. Low utilization of active mass, high internal resistance, water decomposition during charging or corrosion of current collectors are the main problems that influence lead – acid battery working parameters (1, 2).

Materials used as additions to positive electrode mass in lead – acid battery must exhibit high stability in sulfuric acid, electrochemical stability in electrode potential range, high oxygen evolution overpotential, good adhesion to electroactive material, low toxicity and high conductivity. Additionally this compound should increase active mass utilization (1,3).

Nowadays various additives are used to enhance working parameters of lead – acid battery. Examples of such materials are:

- Carbon materials (4)
- Sodium sulfate(VI) (5)
- Mineral additives (6)

Ionic liquids due to its exceptional properties found a lot of applications in electrochemistry. Addition of ionic liquids enhanced efficiency of fuel cells, photovoltaic cells or lithium – polymer cells (7). This type of compounds was also investigated as addition to electrolyte in lead – acid battery (8). Ionic liquids influenced decomposition of water, corrosion of current collectors and increased lead sulfate to lead dioxide conversion rate.

Aim of this study was to enhance utilization of positive electrode in lead – acid cell as well as reduce corrosion of current collectors and influence the oxygen overpotential by using hexadecyltrimethylammonium sulfate ionic liquid.

Experimental

Influence of selected ionic liquid on corrosion parameters and hydrogen and oxygen evolution overpotentials were tested by linear sweep voltammetry and electrochemical impedance spectroscopy. Those parameters were tested on lead-calcium-tin alloy commonly used in lead – acid battery industry for current collector production.

Positive electrodes with addition of hexadecyltrimethylammonium sulfate ionic liquid were produced. Modified electrodes were used for manufacturing of lead – acid cells. They were subjected to electrochemical measurements. Influence of ionic liquid in positive electrode on formation process and utilization of active mass was tested using chronopotentiometry and electrochemical impedance spectroscopy measurements.

Results and discussion

Results showed excellent corrosion inhibition properties of hexadecyltrimethylammonium sulfate ionic liquid on lead-calcium-tin alloy. Overpotentials of both hydrogen and oxygen increased. Electrochemical impedance spectroscopy results showed lower internal resistance, lower charge transfer resistance and higher double layer capacitance of modified electrode than in case of unmodified one.

On the surface of electrode layer of particles formed that increased polarization resistance of electrode. This layer also influenced hydrogen and oxygen evolution reaction potentials. This layer of ionic liquid didn't stop the reactions ongoing on the electrode. Utilization of positive electrode active material was enhanced. Addition of stable ionic liquids to improve working parameters of lead – acid battery may be a way to solve some problems of this system.

Acknowledgments

The authors would like to acknowledge gratefully the financial support from the National Centre for Research and Development (Poland)- Grant no PBS3/A5/43/2015.

References

1. A. Bhattacharya, I.N. Basumallick, *J. Power Sources*, **113**, 382 (2003).
2. D.A.J. Rand, D.P. Boden, C.S. Lakshmi, R.F. Nelson, R.D. Prengaman, *J. Power Sources*, **107**, 280 (2002).
3. K. McGregor, *J. Power Sources*, **59**, 31 (1996).
4. Yu. Kamenev, N. Chunts, N. Yakovleva, V. Nikitin, A. Kiselevich, E. Ostapenko, *J. Power Sources*, **114**, 303 (2003).
5. J.-S. Chen, *J. Power Sources*, **90**, 125 (2000).
6. M. Foudia, M. Matrakova, L. Zerroual, *J. Power Sources*, **279**, 146 (2015).
7. M.A. Deyab, *J. Power Sources*, **390**, 176 (2018).
8. B. Rezaei, E. Havakeshian, A.R. Hajipour, *J. Solid State Electrochem.*, **15**, 421 (2011).

Electrodes Based on Magnesium Alloys for Innovative Magnesium Batteries with Non-Aqueous Electrolytes

I. Maksyuta, E. Shembel, A. Markevych, D. Bondar

Scientific Research Laboratory of Chemical Power Sources of Ukrainian State University of Chemical Technology (USUCT), Dnipro, 49005, Ukraine

Introduction.

The magnesium batteries are the potential competitors with lithium batteries in the important fields of application in particular, in electric vehicles. Special promising direction could be using magnesium electrodes for batteries with sulfur cathode for decreasing the self discharge the sulfur electrodes. For realizing the potential properties of magnesium batteries we use the idea that the modification of the interface between Mg electrode and electrolyte could be realizing using the magnesium alloys instead of pure magnesium.

Stability the magnesium in the gas atmosphere or in electrolyte solutions does not have a thermodynamic basis. In almost all cases, the magnesium surface is covered with a primary MgO film of a thickness of the order of 20-30 Å. The possibility of interaction the primary MgO film with the components of non-aqueous electrolytes results in formation of a secondary film on the magnesium surface. In the case of the magnesium alloys their electrochemical properties are dependent on the alloys composition.

Experimental

The electrochemical behavior of electrodes based on magnesium and magnesium alloy was studied in a 3-electrode cell of a prismatic structure made of aluminum foil that laminated by polymer. The working electrodes: Mg or Mg-alloy were the foils with 100 µm thick. The working surface size is 1 x 1 cm. The auxiliary and reference electrodes are made of magnesium foil. In this article presented results of investigation the following magnesium alloy AZ31: magnesium 96%, aluminum 3%, zinc 1%. As electrolytes, a 0.5 M salt solution of Mg ((ClO₄)₂ in diglyme (G2, dimethyl ether of diethylene glycol, C₆H₁₄O₃) was used. The electrolyte solutions were preliminarily maintained above the molecular sieves for 5 weeks. Methods of investigation: galvanostatic discharge, and impedance spectroscopy of electrode. For electrochemical investigation the universal instrument VoltaLab PGZ 301 has been used. The elements have been assembled and sealed in a glove box in an atmosphere of dry argon.

Results of galvanostatic discharge research and their discussion

Figures 1 and 2 show galvanostatic curves for magnesium based electrodes and magnesium alloy electrodes for the 120 seconds, and for 1200 seconds.

A comparative analysis of the results of galvanostatic studies shows that the anode based on the Mg alloy, compared to pure Mg, is characterized by a smaller and stable polarization during the anodic dissolution process.

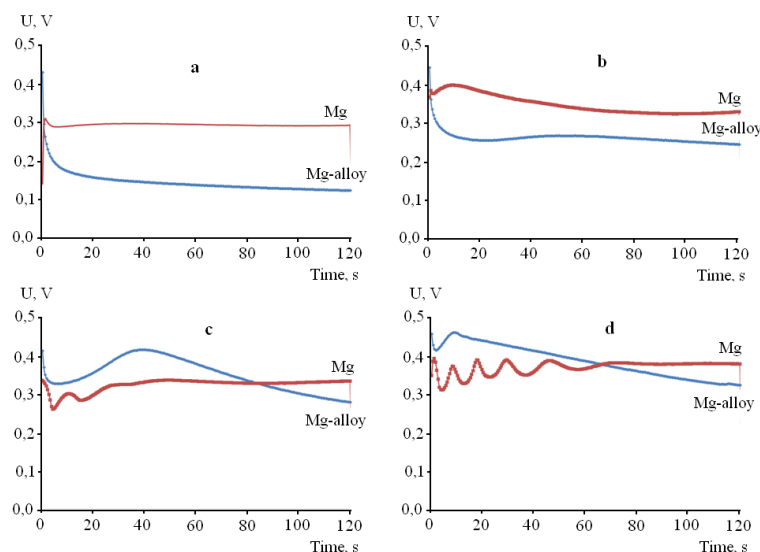


Figure 1. Galvanostatic discharge curves of electrodes based on metallic magnesium and magnesium alloy. Electrolyte - 0.5 M Mg (ClO₄)₂ + G2. Current density, mA/cm²: a – 20; b -50; c -100; d – 200

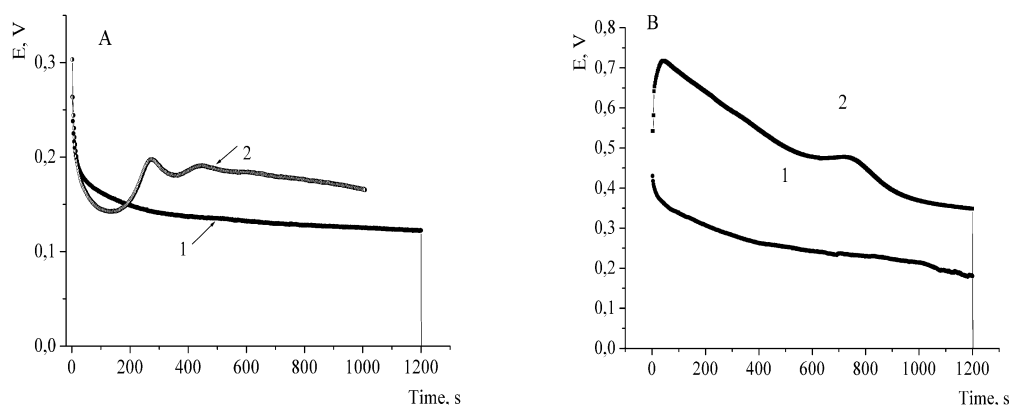


Figure 2. Galvanostatic discharge curves of electrodes based on metallic magnesium and magnesium alloy (1) and magnesium (2). Electrolyte - 0.5 M Mg (ClO₄)₂ + G2. Current density: A- 20 mA/cm²; B) - 50 mA/cm².

The results of impedance spectroscopy of electrode studies, and their discussion

Below (Fig. 3, and 4) presented the comparison the impedances characteristics of Mg and Mg alloy electrodes before and after galvanostatic discharge. After anodic dissolution of the electrodes in the passivation film on the surface of the Mg anode, a new component appears, which has a higher Mg ions conductivity. The resistance of the passivation film, determined from the high-frequency arc of the impedance spectrum, for electrode based on the magnesium alloy is lower, compared to electrode based on pure magnesium.

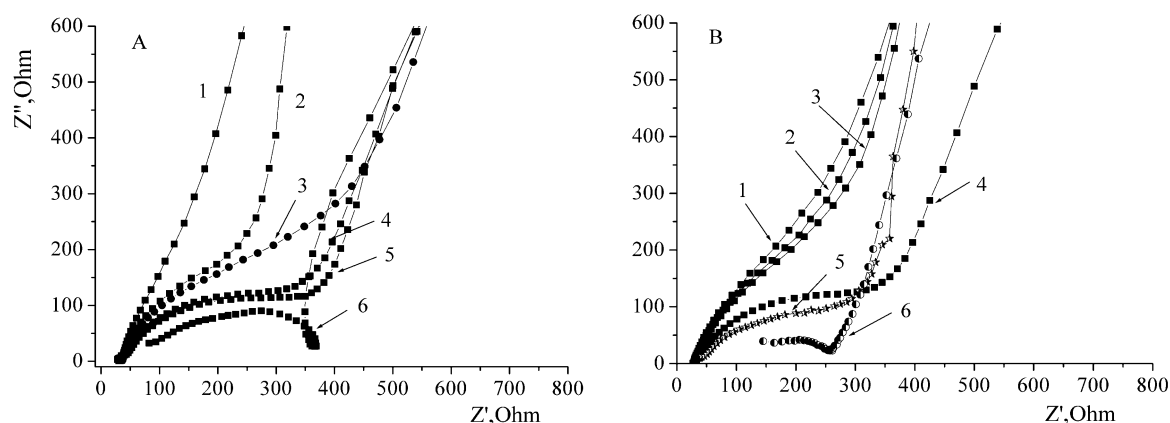


Figure 3. Comparison the impedances of electrode based on Mg alloy (A) and pure Mg (B) in electrolyte of 0.5 M Mg (ClO_4)₂, G2 for “fresh” electrodes and after discharge with different currents. 1- “fresh electrode”; Current of discharge, mA/cm^2 : 2- 10, 3-20, 4-50, 5-100. In Fig.3, A: 6-200 mA/cm^2 ; Fig. 3, B: 6 – 500 mA/cm^2

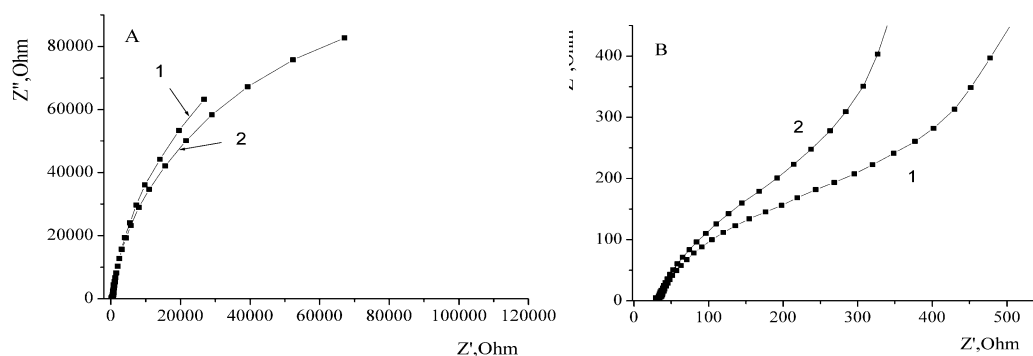


Figure 4. Comparison the impedances over a wide range of frequencies of electrodes based on Mg alloy (1) and pure Mg (2) after discharge under 20 μA . Electrolyte: 0.5 M Mg (ClO_4)₂, G2. Operating range of the frequency, A: 100 kHz -100 mHz; B: 100 kHz – 20 Hz

A comparison of the results the galvanostatic and impedance investigations for electrodes based on the pure magnesium and magnesium alloy shows that in the case of Mg alloy, better conditions are realizing for transferring magnesium ions through the interfaces the electrode / the passivation film, and the passivation film / electrolyte. This allows optimize the properties of magnesium batteries with non-aqueous electrolytes.

Acknowledgments

The work was carried out according to the project of the Ministry of Education and Science of Ukraine, project No. 42/170790 "Development of high energy power sources based on Ukrainian magnesium and manganese raw material for innovative instrumentation". Further development of the work is based on framework of NATO SPS 985148 project "Development of New Cathodes for Stable and Safer Lithium-Sulfur Batteries" USUCT participates in this project. Prof. E. Shembel is the Head of Scientific research laboratory of chemical power sources of Ukrainian state university of chemical technology and Partner country-Ukraine Director of this NATO project.

High-performance long-lasting vanadium redox flow batteries for stationary energy storage applications

P. Mazúr^a, J. Mrlík^b, J. Charvát^b, J. Vrána^b, J. Pcedič^a, J. Dundálek^b, J. Kosek^b

^a New technologies – Research Centre, University of West Bohemia, Univerzitní 8, 306 14 Pilsen, Czech Republic

^b Department of Chemical Engineering, University of chemistry and technology Prague, Technická 5, 166 28 Prague, Czech Republic

The growing share of renewable energy sources within the energetics mix emphasizes the need for reliable, safe and scale-able energy storage technologies, such as vanadium redox flow batteries (VRFB). These have currently started to be installed in MWh scale systems all over the world[1] for load-levelling and peak-shaving applications. The broader commercialization of the system, however, is still retarded by high investment cost of the technology. Depending on the storage parameters, battery stacks can cause over 1/3 of the total battery price[2].

In our contribution, we overview the R&D work done on UCT Prague and UWB Pilsen focused on the development of high-performance and long-lasting VRFB stacks. The optimisation of the graphite felt electrode structure and activation procedure together with identification of optimal membrane material enabled us to reduce the internal resistance of single-cell bellow $0.5 \Omega \text{ cm}^2$ and to achieve DC-DC energy efficiency of the charge-discharge cycle over 80% at 0.25 A cm^2 . Further ways of process intensifications are under investigation to enhance the system peak power over 1 W cm^2 . The electrochemical stability of the battery cell is systematically studied under various operation conditions. For our optimised cell, no irreversible decrease of cell performance is observed within 2000 charge-discharge cycle experiment. Mathematical model of equivalent circuits was employed to optimise the design and geometry of distribution channels which resulted in successful scale-up from laboratory single-cell to kW-class battery stacks. The performance stability of these is currently under investigation in our laboratories.

Acknowledgments

The work was supported from European Regional development Fund-Project "Organic redox couple based batteries for energetics of traditional and renewable resources (ORGBAT)" No.CZ.02.1.01/0.0/0.0/16_025/0007445.



EVROPSKÁ UNIE
Evropské strukturální a investiční fondy
Operační program Výzkum, vývoj a vzdělávání



References

1. D.o.E.o. USA in, Sandia Corporation, 2015, DOE Global Energy Storage Database, <https://www.energystorageexchange.org/>, available 18.7.2018.
2. C. Minke, U. Kunz, T. Turek, *Journal of Power Sources*, **361** 105-114 (2017).

Effect of Structure of Polymeric Nickel Complexes with Salen-Type Ligands on The Stability in Solutions of Water-Containing Electrolytes and The Charge Transfer Parameters

E. V. Alekseeva^a, M. V. Novogilova^a, V. A. Ershov^a, A.S. Konev^a and O.V. Levin^a

^a Department of Chemistry, Saint-Petersburg State University, Saint-Petersburg, Russia

Polymeric transition metal complexes with salen-type Schiff base ligands are considered as promising materials for modification of electrical double layer capacitor electrodes. Electrochemical properties of these polymers, such as their capacity, charge transfer rate and stability are mainly influenced by the ligand structure. This article describes results of systematic investigation of capacitance, charge transfer rate and stability of polymeric nickel complexes with different salen-type ligands. Analysis of results obtained by different electroanalytical techniques shows that introduction of electron donating substituents into the phenyl rings and diamine bridge of the salen ligand causes noticeable changes in electrochemical properties of corresponding polymeric nickel complexes, leading to formation of more stable films with good energy storage properties.

Results and discussions

Due to good reversibility of charge/discharge processes, high power density, and long cycle life, electrical double layer capacitors (EDLC), or supercapacitors, represent one the most promising technologies for electrochemical energy storage. The amount of energy stored in a supercapacitor can be increased by applying an electroactive thin film on the surface of the positive electrode. In such hybrid systems, EDL charging is accompanied by fast and reversible faradaic processes on the electrode surface so that the total capacitance of the composite electrode is the sum of double-layer capacitance and redox capacitance, often referred to as pseudocapacitance (1,2). Conductive polymers have been most often used for such modification of electrodes of hybrid supercapacitors(3,4). Among the applied conductive polymers, complexes of transition metals with the derivatives of salen (N,N'-ethylenebis(salicylimine)) ligand exhibit a set of important features like reversible electrochemical oxidation over a wide range of the potential (5) and specific capacity up to 300 F/g (6,7). The results of supercapacitor electrode modification by polymer films of nickel complexes with salen-type ligands have been reported (3,8,9), however the influence of the ligand structure on the electrochemical properties of these polymers that define their performance in the energy storage applications have not been systematically investigated. important parameters that define performance of electroactive polymers in energy storage devices are:

- (1) Effective charge diffusion coefficient;
- (2) Specific capacitance;
- (3) Cycling stability.

Despite the fact that many metal-salen type polymers have been synthesized and described (10-12), it is difficult to select the polymer most suitable for EDLC electrodes modification based on the available literature data due to lack of information on one more of abovementioned parameters. Therefore, this work focuses on the comparative study of polymeric nickel complexes

with salen-type ligands of different structure, as pertains to their potential energy storage application. The choice of the polymers for this comparative study is based on the expected effect of the substituents in the ligand on the polymer properties relevant to energy storage application. The graphical representation of a [Ni(Schiff)] complex, which is a structural unit of the polymers investigated in this work, is shown in Figure 1.

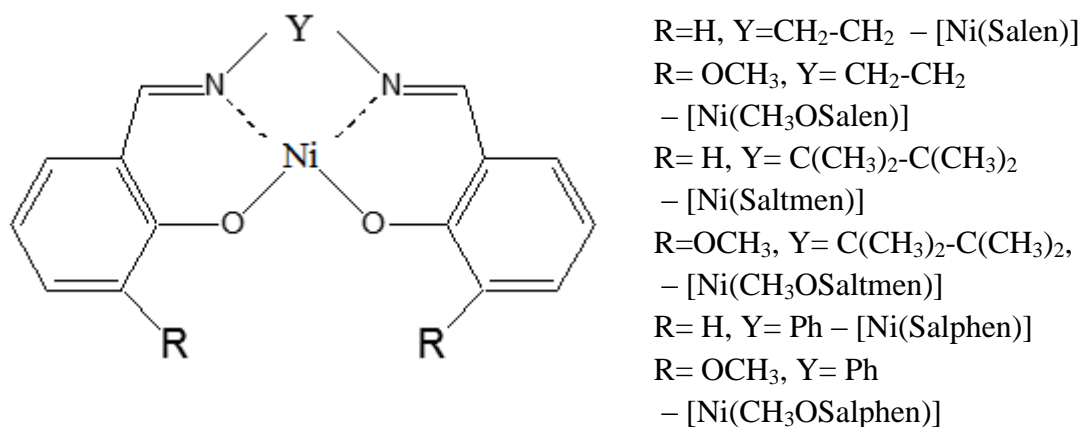


Figure 1. Structural representation of [Ni(Schiff)] monomers

Introduction of electron donating methoxy and methyl substituents into the phenyl rings of salen-type ligands should lead to an increase in electron density in the conjugated system, the methyl substituents in the diamine bridge of the ligand are not strong electron donors but their presence creates steric hindrance to processes, involving interaction of metal with electrolyte components. Using several electroanalytical, spectroscopic and physical-chemical methods we have evaluated the important performance parameters of polymers, formed from these complexes. Comparing charge transfer and storage characteristics together with long-term electrochemical stability of the polymers, we have found the superiority of methyl-substituted complexes over non-substituted or methoxy-substituted analogues. Possible mechanisms of the loss of electroactivity of the nickel complexes with the Schiff's bases were revealed, involving the oxidation in the presence of water traces, and the ways to increase the stability of [Ni(salen)]-type polymer modified electrodes were suggested.

Acknowledgments

This research was supported by the Russian Foundation for Basic Research (project no. 18-33-00682)

References

1. B. Ming, J. Li, F. Kang, G. Pang, Y. Zhang, L. Chen, J. Xu and X. Wang, *J. of Power Sources*, **198**, 428-431 (2012).
2. X. Lang, L. Zhang, T. Fujita, Y. Ding and M. Chen, *J. of Power Sources*, **197**, 325-329 (2012).
3. J. Luo, S. S. Jiang, R. Liu, Y. J. Zhang and X. Y. Liu, *Electrochim. Acta*, **96**, 103-109 (2013).
4. Y. Hu, J. Wang, X. H. Jiang, Y. F. Zheng and Z. X. Chen, *Applied Surface Science*, **271**, 193-201 (2013).

5. I. A. Chepurnaya, P. V. Gaman'kov, T. Yu. Rodyagina, S. V. Vasil'eva and A. M. Timonov, *Russ. J. Elchem.*, **39**, 314-317 (2003).
6. O. V. Levin, M. P. Karushev, A. M. Timonov, E. V. Alekseeva, S. Zhang and V. V. Malev, *Electrochim. Acta*, **109**, 153-161 (2013).
7. E. V. Alekseeva, I. A. Chepurnaya, V. V. Malev, A. M. Timonov and O. V. Levin, *Electrochim. Acta*, **225**, 378-391 (2017).
8. C. C. Hu, Y. H. Huang and K. H. Chang, *J. Power Sources*, 2002, **108**, 117-127.
9. X. Wang, T. M. Wang, C. Yang, H. D. Li and P. Liu, *Applied Surface Science*, **287**, 242-251 (2013).
10. A. C. W. Leung and M. J. MacLachlan, *J. of Inorganic and Organometallic Polymers and Materials*, **17**, 57-89 (2007).
11. J. Tedim, F. Gonçalves, M. F. R. Pereira, J. L. Figueiredo, C. Moura, C. Freire and A. R. Hillman, *Electrochim. Acta*, **53**, 6722-6731 (2008).
12. J. Tedim, C. Freire and A. R. Hillman, *Soft Matter.*, **5**, 2603-2613 (2009).

Electrochemical Properties Electrodes Based on Mn_3O_4 , Mn_2O_3 in Non-Aqueous Electrolyte with Magnesium or Lithium Perchlorate

R.D. Apostolova, A.V. Markevich, I.V. Kirsanova

Scientific Research Laboratory of Chemical Power Sources of Ukrainian State University of Chemical Technology, Dnipro, 49005, Ukraine

Magnesium battery (MB) attracts an attention of the developers above two ten years due theoretic specific volume magnesium energy, its wide prevalence in a nature, low price, lack of dendrites during electrodepositing. Magnesium battery is considered as an alternative to more expensive and environmentally unsafe lithium battery (LB) [1, 2].

Oxide film on magnesium that is impermeable for magnesium ions in majority of magnesium electrolytes, and delayed diffusion-migration of bivalent ions of Mg in cathode materials must be solved to the production of high energy MB.

The alternative strategy proposes for practical high energy magnesium system in accordance to which the high energy and the current density are achieved with the participation of surface redox reactions and capacitive non-Faraday processes. It was used in nanomaterials for lithium battery [3]. This strategy was also successful in nanometer anode material Mn_3O_4 in magnesium electrolyte [4].

However, there is the problem of using Mn_3O_4 in a magnesium high-energy battery capable of replacing a lithium battery that requires a solution. Mn_3O_4 has been successfully used in Aluminum-Phenyl-Chloride (APC) electrolyte with the low-voltage cathode material Mo_6S_8 Chevrel phase [4]. The electrochemical stability window of (APC) electrolyte is lower than it is necessary for its use with high-voltage cathode materials (V_2O_5 , MnO_2 , MoO_3 , MgFeSiO_4 and others) in a magnesium battery. Thus, a magnesium electrolyte with a wide window of electrochemical stability is necessary for Mn_3O_4 , compatible with high voltage cathode materials.

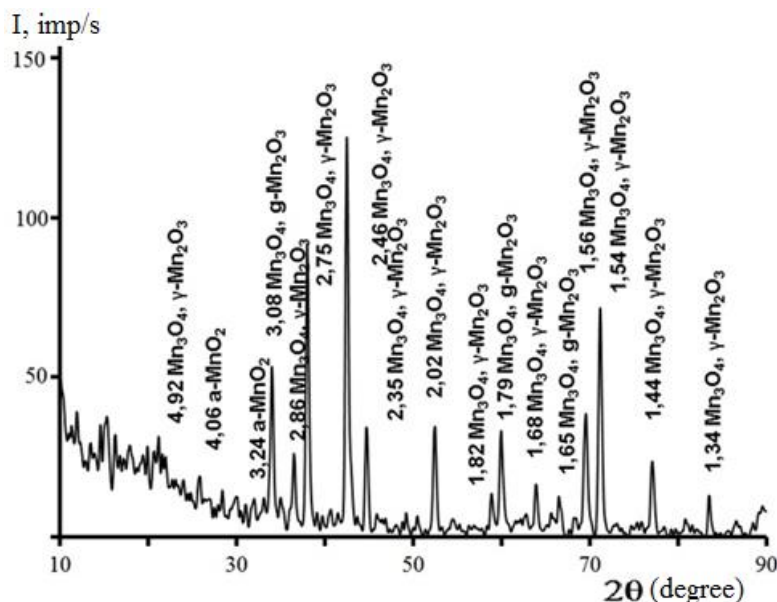


Figure 1. XRD pattern of Mn_3O_4 (90%), Mn_2O_3 (10%).

In this paper, the electrode material (Mn_3O_4 , Mn_2O_3) was synthesized and studied in magnesium perchlorate electrolyte based on glyme-solvents with magnesium counter electrode. The

study was carried out to investigate the Mn_3O_4 , Mn_2O_3 material as anode for magnesium-ion system. (Mn_3O_4 , Mn_2O_3) material with a crystalline size of 87 nm (Fig. 1) is obtained by thermal decomposition process of MnO_2 and is considered as less dangerous to mankind than the same nanometer material.

(Mn_3O_4 , Mn_2O_3) oxides used in a composition with Norit A SUPRA USP 30 carbon filler with surface area of $1900 \text{ m}^2 \text{ g}^{-1}$ as an electrically conductive additive, showed positive effect on LiMn_2O_4 spinel reformation in a lithium prototyping accumulator [5].

A comparison of (Mn_3O_4 , Mn_2O_3 , Norit) characteristics is performed in electrochemical cells with magnesium and lithium perchlorate electrolytes based on tetraglyme and dimethoxyethane (DME) solvents. (Mn_3O_4 , Mn_2O_3 , Norit) electrodes were investigated in magnesium electrolyte with a magnesium counter electrode and based on the magnesium alloy AZ61.

After slow voltage change, magnesiation voltage of (Mn_3O_4 , Mn_2O_3 , Norit)/ $0.25 \text{ mole} \cdot \text{l}^{-1}$ $\text{Mg}(\text{ClO}_4)_2 + \text{G4} + \text{DME} / \text{Mg}$ system is within the voltage limits that were determined in the studied nanometer Mn_3O_4 , Mn_2O_3 oxides, which are promising for the anodes of the magnesium-ion system (0.4-0.2 V). The possibility was shown and the electrochemical reformation conditions are determinate in magnesium electrolyte to obtain a capacity of Mn_3O_4 , Mn_2O_3 , Norit by the order of $200 \text{ mAh} \cdot \text{g}^{-1}$ at current density of $50 \mu\text{A} \cdot \text{cm}^{-2}$.

The magnesiation curve profile of (Mn_3O_4 , Mn_2O_3 , Norit)-electrode with magnesium counter electrode differs from that with magnesium alloy AZ61 counter electrode. The difference is in the duration of voltage delay. It is shown in Fig. 2 in the beginning of magnesiation curves of (Mn_3O_4 , Mn_2O_3 , Norit) on dependence time scale of the beginning stage: a) AZ61 (long time scale, insertion – short time scale), b) magnesium (long time scale).

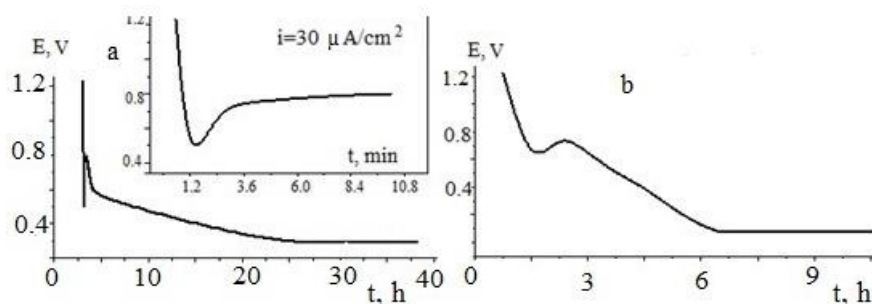


Figure 2. Beginning stages of magnesiation of (Mn_3O_4 , Mn_2O_3 , Norit) / $0.25 \text{ mole} \cdot \text{l}^{-1}$ $\text{Mg}(\text{ClO}_4)_2$, G4, DME with counter electrode: a) 1 – AZ61; b) – Mg.

The voltage delay in the system with AZ61 disappears within 2-3 minutes (Fig. 2a, insertion), whereas in the case of magnesium it is counted in hours (Fig. 2b).

The start lithiation capacity of (Mn_3O_4 , Mn_2O_3 , Norit)-electrode in electrochemical cells reaches to 980 mAh g^{-1} at current density of $305 \mu\text{A} \cdot \text{cm}^{-2}$ (Fig. 3). The values of such order were obtained with nanometer Mn_3O_4 , Mn_2O_3 [3].

The capacity of delithiation is reduced to $250\text{-}300 \text{ mAh g}^{-1}$ when the current is reduced by an order of the magnitude.

The Norit carbon material is not only an electrically conductive additive, but it exhibits electrochemical activity in a magnesium electrolyte with a magnesium counter electrode. Its magnesiation capacity reaches to 80 mAh g^{-1} in the first cycle.

The obtained capacity and rate of (Mn_3O_4 , Mn_2O_3 , Norit) reformation are lower than those of Mn_3O_4 , Mn_2O_3 oxides presented in literature springs where high characteristics of nanometer oxides were obtained only in composition with nanometer carbon fillers. As it is clear, the thermal synthesized Mn_3O_4 , Mn_2O_3 material is difficult to compete with nanometer analogues. The horizontal part of magnesiation and lithiation curves (Fig. 3, for example) at voltage of 0.4-0.2 V is determined in considerable degree by solid state diffusion processes. The part of curves in demagnesiation and delithiation of (Mn_3O_4 , Mn_2O_3 , Norit) is essentially smaller that is the evidence of diffusion limitations in electrode material.

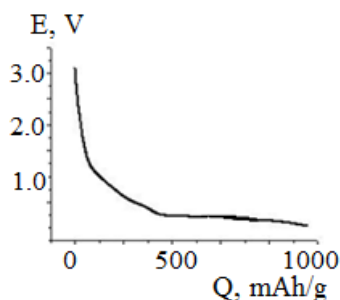


Figure 3. Start lithiation curve of (Mn_3O_4 , Mn_2O_3 , Norit)/ 0.5 mole l^{-1} LiClO_4 , G4, DME/ Li system.

Magnesium complex-formation plays essential role in effective magnesium electrolytes. Success of Mn_3O_4 in APC- electrolyte is much obliged to high chelating ability of Cl^- [4]. Evidently, further it is needed draw attention ClO_4^- chelating ability to complex formation with magnesium ions and glymes to improve the efficiency of reform of synthesized Mn_3O_4 , Mn_2O_3 oxides.

In the paper, the electrodes used with mass of $7\text{-}20 \text{ mg}\cdot\text{cm}^{-2}$ whereas mass of nanometer material on in literature data equals to 1 mg cm^{-2} . Specific electrochemical characteristics of Mn_3O_4 , Mn_2O_3 , Norit may be improved at the mass decrease.

Acknowledgments

The current presentation has been prepared in the framework of Ministry of Education and Science of Ukraine, project № 42/170790 “Development of high energy power sources based on Ukrainian magnesium and manganese raw materials for innovative instrument making”. Head of the project is Chief of the NILHIT prof. E.M. Shembel'.

References

1. Yoo, H.D., Shterenberg I., Gofer Y., Gershinsky G., Pour Nir, Aurbach D. // *Energy Environ. Sci.* 6, 2265 (2013).
2. Muldoon J., Bucur C.B., Gregory T. // *Chem. Rev.* 114, 11683 (2014).
3. Augustyn V., Come J., Lowe M.A., Kim J.W., Taberna P.L., Tolbert S. H., Abruña H.D., Simon P., Dunn, B. // *Nat. Mater.* 12, 518 (2013).
4. Wang L., Wang Z., Vullum P.E., Selbach S., Svensson A.M., Vullum-Bruer F. // *Nano Lett.*, Just Accepted Manuscript • DOI: 10.1021/acs.nanolett.7b03978
5. Apostolova R., Peskov R., Shembel' E. // *Surf. Engineer. Appl. Electrochem.* 51, 296 (2015).

First -Principles Study On Mechanism Of Graphite Oxide As Anode material in Na-Ion Battery System

T. Hwang^a, H. Kim^a and M. Cho^a

^aDepartment of Mechanical and Aerospace Engineering, Seoul National University, Republic of Korea

Graphite oxide has been considered a promising material as a practical Na-ion anode due to good capacity and inexpensiveness comparing with other Na-ion anode materials. In spite of great attention, there are lack of theoretical research on graphite oxide. Through first-principle calculations, this study examines structural, electronic and thermodynamically properties of graphite oxide. Graphite oxide retain enlarged interlayer spacing comparing with other conventional graphite anodes. Band structure and density of states of graphite oxide show reasonable electronic conductivity. However, bulk section of graphite oxide indicates thermodynamically unstable. Therefore, almost the whole electrochemical reactions is arisen on the surface section of graphite oxide.

Introduction

Recently, demand for devices and equipments of energy storage because of increases in usage of electric vehicles, mobile phone and developments of new regeneration energy like solar, wind and tidal power. Particularly, huge scales' energy storage systems(ESSs) receive great attention to store electrical energy generated by these new regenerations energy. Li-ion battery system is used as leading system because of good energy density and long life cycle.⁽¹⁾

However, Li-ion battery system has disadvantage in the view point of price because reserves of Li metal is stored in some countries and the price continuously increases. For these reasons, research on replacing Li-ion with inexpensive elements is under active discussion and also this alternative system must have good electrochemical properties. Na-ion battery system exhibit good electrochemical performance among candidates because this system has electrochemical redox reaction of mono-valence same as Li-ion battery property. This same redox system makes it possible for Na-ion system to be applicable for well developed and similar environments of Li-ion battery system. In addition to this good electrochemical property, price of Na metal is very inexpensive because of abundant reserves and this price-wise competitiveness is suitable for large scale's ESSs.⁽²⁾

Although Na-ion battery system has these advantages, there are some intrinsic difficulties to directly apply same electrode system of Li-battery system to Na-ion battery system. Particularly, graphite of superior anode material for Li-ion battery system indicates about capacity of 30 mAh/g, is under one of tenth comparing with capacity of graphite in Li-ion battery system. An atomic radius of Na-ion is 1.02 Å and is larger than radius of Li-ion(0.76 Å) and it makes difficult for Na-ion to intercalate into interlayer spacing of graphite(3.4 Å). To resolve this difficulty, research on enlarging interlayer spacing of graphite receive great interest by adopting oxygens between graphite layers known as graphite oxide.⁽³⁾

In spite of development of graphite oxide improving capacity, reaction mechanism has not been understood yet clearly. For this reason, this study carried out interlayer spacing, formation energy and electronic structures through first-principles calculation. Although interlayer spacing increase as oxygen ratio increases, formation energy also increase and this increase make it this graphite oxide thermodynamically unstable. For this reason, oxygen could be stabilized in surface area of graphite and also redox reaction is mainly possible near surface region. Therefore, this study might be guide for research on graphite oxide in the view point of capacity increase and mechanism understanding.

Computation details

The modeling of first-principles calculation is conducted by Vienna Ab Initio Simulation Package (VASP). The thermodynamical energy is calculated by using Generalized Gradient Approximation (GGA) and Density Functional Theory (DFT). K-point of 8x8x8 Monkhorst Pack, energy cut off of 450 eV and DFT-D2 considering van der Waals effect are set up in this simulation.⁽⁴⁾

Result and discussion

Na-ion's intercalation into pristine graphite is thermodynamically unstable (figure. 1). Interlayer spacing is rapidly increase as soon as Na-ion intercalated into graphite from 3.2 Å to 3.4 Å and formation energies indicates positive values all over the entire Na-ion concentration region. For this region, interlayer spacing is very important to reveal electrochemical reaction because of large ionic radius of Na-ion. Interlayer spacing of graphite increase as ratio of oxygen/carbon(O/C) increases. Interlayer spacing increases 0.88 Å from 3.2 Å to 4.08 Å as O/C ratio increases from 0% to 13.8%. This adopt oxygens bond with carbon elements of graphite. These bonds enlarge interlayer spacing and make Na-ion intercalation into enlarged interlayer of graphite oxide thermodynamically possible.

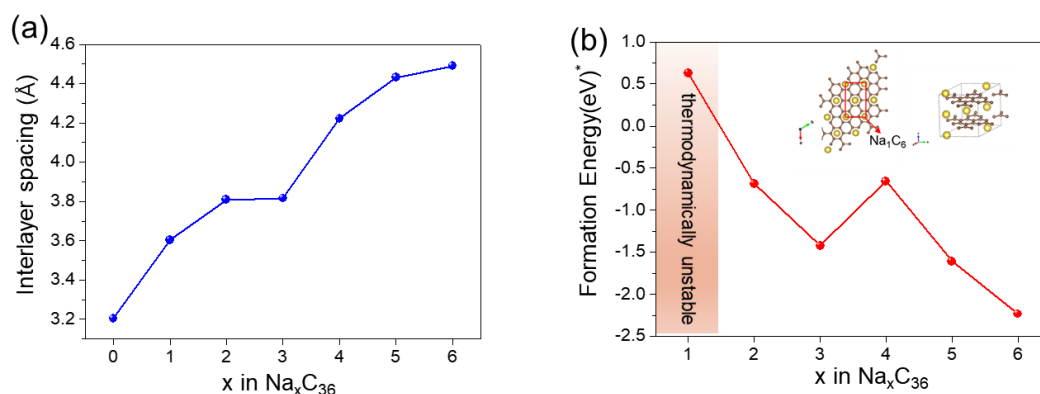


Figure 1. (a) Interlayer spacing and (b) formation energy of Na-ion intercalated graphite

In addition to structural properties, graphite electronic structure indicates electronic conductivity of graphite oxide is reasonable comparing with that of pristine graphite considering density of states of each material (figure 2). Density of states of pristine graphite indicates good electronic conductivity because of π bond states in vicinity of fermi level. Comparing with

graphite, graphite oxides retain similar π bond states. This similar electronic structures mean that graphite oxide is expected to reveal good electronic conductivity.

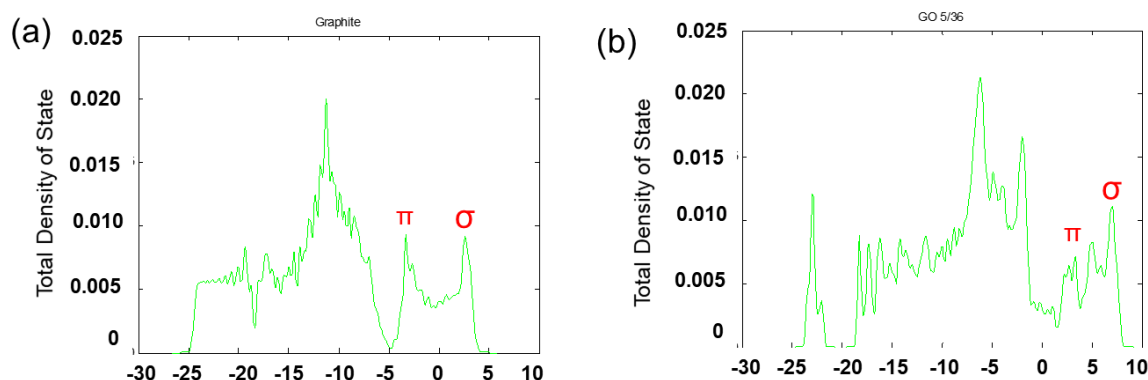


Figure 2. Density of states of (a) graphite and (b) graphite oxides

Although interlayer spacing of graphite oxide increases as O/C ratio increases and graphite has good electrochemical properties, formation energy of graphite oxide indicates bonding between oxygens and carbon in bulk graphite oxide is thermodynamically unstable. On the other hand, oxygen adoption on carbon defected graphite surface indicates that formation energy is negative value, which is thermodynamically stable. Therefore, electro chemical reaction of graphite oxide is expected to be mainly originated from surface region of graphite oxide and research on surface properties of graphite oxide is highly required.

Acknowledgments

The National Research Foundation of Korea(NRF) grant funded by the Korea government (MEST) (2012R1A3A2048841) and the Technology Innovation Program of the Korea Institute of Energy Technology Evaluation and Planning(KETEP) granted financial resource from the Ministry of Trade, Industry & Energy, Republic of Korea (No. 20152020105420)

References

1. V. Palomares, P. Serras, I. Villaluenga, K. B. Hueso, J. Carretero-Gonzalez and T. Rojo, *Energy Environ. Sci.*, **5**, (2012).
2. Y. Kang, S. Jung, J. Choi and Y. Han, *Chem. Mater.*, **27**, (2015)
3. Y. Wen, K. He, Y. Zhu, F. Han, Y. Xu, I. Matsuda, Y. Ishii, J. Cumings and C. Wang, *NATURE COMMUNICATIONS*, **5**, (2014)
4. S. Grimme, *J. Comput. Chem.*, **27**(15), (2006)

Performance of Graphite Negative Electrode In Lithium-Ion Battery Depending Upon The Electrode Thickness

J. Libich^a, M. Sedlaříková^a, J. Vondrák^a, J. Máca^a, P. Čudek^a, A. Chekannikov^b, W. Artner^c
and G. Fafilek^c

^aDepartment of Electrical and Electronic Technology, Faculty of Electrical Engineering and Communication, Brno University of Technology, 616 00 Brno, Czech Republic

^bSkolkovo Institute of Science and Technology, 143026 Moscow, Russian Federation

^cVienna University of Technology, Getreidemarkt 9, 1060 Vienna, Austria

Nowadays, the lithium-ion batteries are leading kind of secondary electrochemical power sources. The production along with demand for lithium-ion batteries increase annually. The manufactures mainly use common chemistry and material components. There is tend to increase volumetric and gravimetric energy density of the standardised cell formats like 18650 or 26650. The one of the key parameters is the capacity of the electrode and its thickness. The increasing or decreasing any of them has strong influence on capacity, stability, cyclability and rate-capability performance of the cell. This text describes the experiments dealing with manufacturing negative electrodes for lithium-ion batteries based on natural graphite. The electrodes were manufactured under various parameters of technology process, the optimum electrode thickness was evaluated with correlation to the electrode capacity and rate-capability parameter.

Introduction

The lithium-ion technology seems to be most promising electrochemical energy source for the future. From the release (1991) until now the lithium-ion batteries constantly develop and improve they parameters. Especially growing volumetric and gravimetric energy density, expanding operation temperature window, lowering price (approximately 8 % per year), low toxicity etc. all of these parameters make them leading type of battery. The application area of lithium-ion batteries changed from small portable devices over traction propulsion of electric vehicles to of off-grid energy power storage systems in MWhs range. Today, lithium-ion batteries take almost 40 % share of global batter market production followed by lead-acid batteries which take approx. 20 % share of the market. Both types of batteries vary in application area. Originally the lithium-ion batteries were used in portable devices, recent few years the lithium-ion batteries taking place in electric storage for traction propulsion of light electric vehicles and electric cars. The lead-acid batteries domain in area of starter batteries in conventional vehicles. It is very likely that global market share of lithium-ion batteries will continue in raising in the following 10 years. In the long term evolution the post lithium-ion batteries will take a part on battery market. As post lithium-ion battery can be considered lithium-air (Li-air) and lithium-sulphur (Li-S) technology. In respect to growing world population and the demand for cheap and environment friendly energy storage solutions, the sodium-ion aprotic system can be considered as solution. The main advantage of sodium-ion system compared to lithium-ion is an abundance of sodium in the Earth's crust, which lowering the price of

the battery. These technologies facing many issues and are still in early or advanced stage of research and development.

Current lithium-ion batteries use graphite as an active electrode material. Commercially available lithium-ion batteries are usually composed from cathode (positive electrode) material as LiCoO_2 (lithium cobalt oxide) or LiFePO_4 (Lithium iron phosphate) with polymer separator (depends on the type of lithium-ion cell) and natural or synthetic graphite anode (negative electrode) material. Electrolyte is made from mixture of DMC (dimethyl carbonate) a EC (Ethylene carbonate) in that is dissolved lithium salt, mostly LiPF_6 (lithium hexafluorophosphate). The operation scheme of lithium-ion battery is depicted in Fig. 1. Despite the fact, that lithium-ion batteries are under continuous development and many issues and problem are already solved, there are still many of them which remain. One of the important key points a do not relate with material components of the battery or operation principle, but relates with the technology of manufacturing process. There are many types of cells, prismatic, cylindrical, button or pouch cells, each of them have specific advantages and disadvantages connected with gravimetric and volumetric density.

Most spread type of lithium-ion cell reprints cell format 18650 see Fig. 2 below, this king of cell possess best gravimetric volume density. The capacity of the cell relates with the electrode thickness, material structure, morphology and mechanical properties. All these parameters have a close relationship and influence cell capacity, performance and stability along with lifespan. Our experimental work deals with experiments describe mutual relationship between negative electrode thickness and the electrode capacity, rate capability and cycle stability [1– 20].

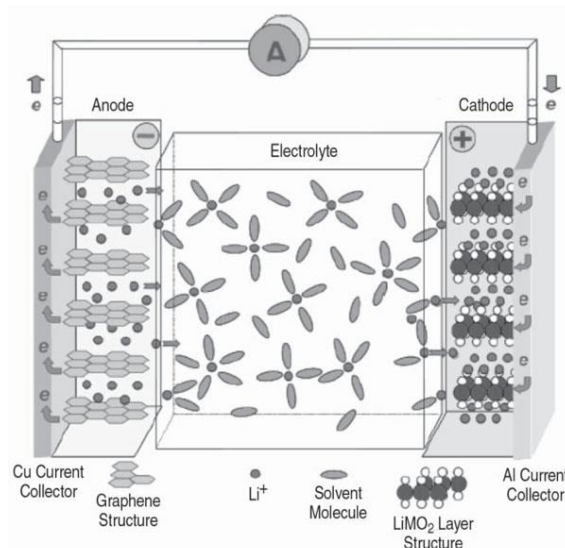


Figure 1. Operation principle of lithium-ion battery with convention material components [2].

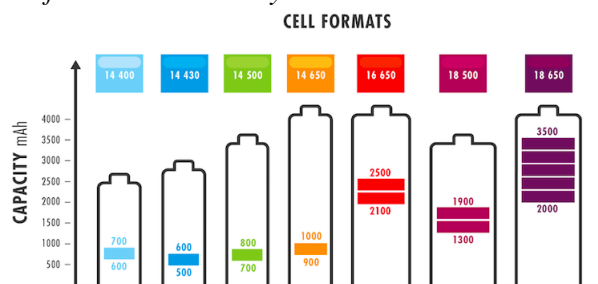


Figure 2. Most common cylindrical cell formats. The 18650 formats belong among most common in case of lithium-ion battery [3].

Acknowledgments

This work was supported by the project of the Centre for Research and Utilization of Renewable Energy under project No. LO1210 – "Energy for Sustainable Development (EN-PUR)" reg. No. 0398.

References

1. A. Hofmann, M. Schulz, S. Indris, R. Heinzmann, T.s Hanemann, *Electrochimica Acta*, 147(20), (2014).
2. J. Libich, J. Maca, M. Sedlarikova, J. Vondrak and O. Cech, *ECS Transaction*, 74(1), (2016).
3. Waldies Compound Ltd, (2017), Retrieved from URL: <http://www.waldies.com/2017/08/07/whats-future-ahead-lead-acid-batteries-lithium-ion-cells/>
4. M. L. Lee, Y. H. Li, S. Ch. Liao, J. M. Chen, J. W. Yeh, H. C. Shih, *Electrochimica Acta*, 112 (2013).
5. N. Takami, H. Inagaki, Y. Tatebayashi, H. Saruwatari, K. Honda, S. Egusa, *Journal of Power Sources*, 244 (2013).
6. G. Guigay, J. Eliasson, D. Gojkovic, L. G. Bengtsson, *Fire Technology*, 45 (2009).
7. H. Jin, G. Pan, S. J. Xue, and F. P. Wang, *ECS Transaction*, 58(48) (2014).
8. S. Suzuki, M.Yano, M. Miyayama, *ECS Transaction*, 16(29) (2009).
9. T. Oguni, at al., *ECS Transaction*, 50(26) (2013).
10. J. Zhang, B. Wu, J. Huang, *J. of Power Sources*, 259(1), (2014).
11. W. Jiang, T. Tran, X. Song, K. Kinoshita, *J. of Power Sources*, 85(2), (2000).
12. B. Kang, K. Honda, T. Aki, T. Omasa, H. Ohtake, D. Warren and J. M. Woodall, *Thermochimica Acta*, 517(12), (2011).
13. H. Jin, G. Pan, S. J. Xue, and F. P. Wang, *ECS Transaction*, 58(48) (2014).
14. S. Suzuki, M.Yano, M. Miyayama, *ECS Transaction*, 16(29) (2009).
15. J. Libich, J. Máca, M. Sedlaříková, J. Vondrák, A. Visintin, *ECS Transaction*, 63(1), (2014).
16. Ch. Li, Y. Zhao, H. Zhang, J. Liu, J.Jing, X. Cui, S. Li, *Electrochimica Acta*, 104(1), (2013).
17. L. Xing, W. Tu, J. Vatanmanu, Q. Liu, W. Huang, Y. Wang, H. Zhou, R. Zeng, W. Li, *Electrochimica Acta*, 133(1), (2014).
18. J. Libich, J. Máca, J. Vondrák, O. Čech, M. Sedlaříková, *Journal of Energy Storage*, 14 (3) (2017).
19. J. Libich, J. Vondrak, M. Sedlarikova, J. Maca and O. Cech, *Surface Engineering and Applied Electrochemistry* 53(6) (2017).
20. J. Libich, J. Vondrak, M. Sedlarikova, *Surface Engineering and Applied Electrochemistry*, 51(2) (2015).

Electrochemical properties of magnesium electrodes in lithium non-aqueous electrolytes. Perspective of high-energy hybrid magnesium batteries

O. V. Markevych ^a, E. M. Shembel^{a,b}

^a Ukrainian State University of Chemical Technology, Dnipro, 49005, Ukraine

^b Enerize Corporation, Coral Springs, FL, 33067, USA

Advantages of magnesium anode compared to lithium for batteries with non-aqueous electrolytes

Magnesium is a promising lithium alternative as a negative electrode in primary and rechargeable power sources with non-aqueous electrolytes. A more positive magnesium potential and a somewhat smaller value of the theoretical specific weight electrochemical capacitance can be compensated for by a higher specific volume capacity (3833 mAh/cm³ for magnesium and 2029 mAh/cm³ for lithium) [1]. In addition, magnesium is more common in the earth's crust (Mg ~ 2.35%, Li ~ 0.0065%) and 20 times cheaper than lithium. However, the main advantage of magnesium is the safety of cycling. Charge-discharge cycling on the surface of magnesium, unlike metallic lithium, does not form dendrites [2]. Consequently, there is no danger of short circuits in the inter electrode space and ignition of power sources. The magnesium electrode is a promising anode for various batteries, including batteries with a cathode based on sulfur. The Mg-S batteries will have a much lower self-discharge compared to Li-S batteries

Features of the properties of magnesium electrodes in lithium non-aqueous electrolytes

Similar to the lithium electrode, a passivation film is formed on the magnesium electrode in air and in a non-aqueous electrolyte medium. However, the resistance of a passivating film on magnesium is significantly higher than that of a passivating film on the lithium. As a result, a passivating film on the magnesium inhibits the transport of magnesium ions through the magnesium / electrolyte interface. [3]. This significantly reduces the allowable discharge current density, and consequently, the power of the magnesium battery.

The composition and properties of the passivation film on the magnesium surface depend on the composition of the non-aqueous electrolyte. To modify the passivation film on the surface of the magnesium anode, so-called hybrid electrolytes are promising. Hybrid electrolytes contain mixtures of magnesium and lithium salts. For a deeper understanding of the mechanism of formation of a passivation film on the surface of magnesium in hybrid electrolytes, we investigated the novel system: a magnesium electrode in a non-aqueous electrolyte based on lithium salt alone.

Magnesium foil 100 microns thick and working surface 1x1 cm was used as the working electrode. The purity of magnesium was 99.99%. Before assembling the electrochemical cell, the surface of the magnetic electrodes was mechanically cleaned from the surface film. As electrolytes, solutions LiCF₃SO₃ in organic solvents: tetrahydrofuran (THF), dimethoxyethane (DME) and tetraglyme (TG).

Galvanostatic and impedance studies of magnesium electrodes were carried out in electrochemical cells of a planar design using a 3-electrode scheme. As a secondary electrode and a reference electrode, lithium metal was taken. Electrochemical cells were assembled in a glove box in an atmosphere of dry argon.

The galvanostatic characteristics of magnesium electrodes in electrolytes based on various organic solvents with different dissolution current density were investigated. Impedance characteristics were investigated after the electrochemical discharge of the magnesium electrode at a certain current density, as well as during the storage of the magnesium electrode.

In Fig. 1 shows the galvanostatic curves of discharge of the magnesium electrode in the DME, 1 M LiCF_3SO_3 electrolyte at different current densities.

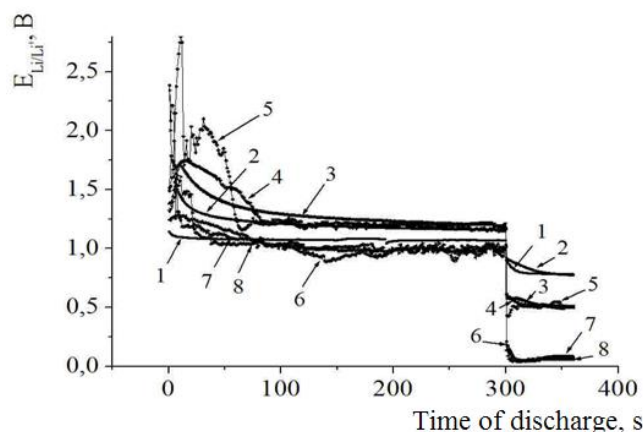


Figure 1. Galvanostatic characteristics of magnesium electrode dissolution at anodic polarization. Electrolyte: DME, 1 M LiCF_3SO_3 . Discharge current density: 1- $100 \mu\text{A}/\text{cm}^2$; 2- $200 \mu\text{A}/\text{cm}^2$; 3- $500 \mu\text{A}/\text{cm}^2$; 4- $1 \text{ mA}/\text{cm}^2$; 5- $2 \text{ mA}/\text{cm}^2$; 6- $5 \text{ mA}/\text{cm}^2$; 7- $10 \text{ mA}/\text{cm}^2$; 8- $20 \text{ mA}/\text{cm}^2$.

From Fig. 1 that the potential of galvanostatic dissolution of magnesium in the electrolyte DME, 1 M LiCF_3SO_3 relative to the lithium reference electrode was about 1 V. Considering that the potential of the magnesium electrode is 0.68 V positive than the lithium electrode, we can say that the potential of galvanostatic dissolution of magnesium relative to the magnesium reference electrode is 0.32-0.5 V depending of the discharge current density. In this case, the polarization of the magnesium electrode in the current range from 0.1 до $20 \text{ mA}/\text{cm}^2$ does not exceed 0.25 V. This indicates a high permeability Mg^{2+} through the electrode / electrolyte interface.

Galvanostatic studies had shown that maximum current density of galvanostatic dissolution of magnesium is reduced in the series of solvents $\text{DME} > \text{THF} > \text{TG}$. For the DME, maximum discharge current density was $20 \text{ mA}/\text{cm}^2$, for the THF - $10 \text{ mA}/\text{cm}^2$, for the TG - $2 \text{ mA}/\text{cm}^2$.

Impedance studies of the magnesium electrode after a galvanostatic discharge at different current densities had shown that the resistance of the electrode / electrolyte interface decreases with increasing discharge current. This means that when the magnesium electrode is discharged, activation of the electrode surface proceeds due to the destruction of the passivated film. The impedance spectra of the magnesium electrode are shown in Fig. 2.

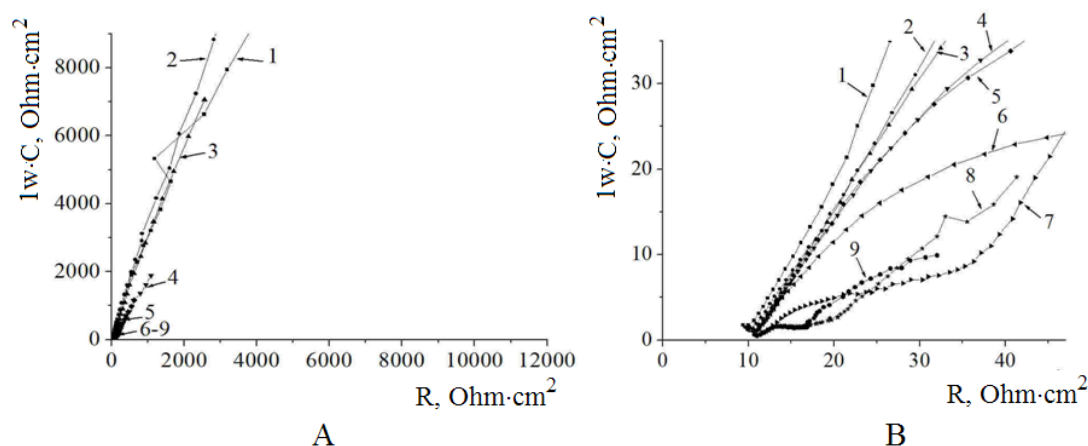


Figure 2. Impedance characteristics of magnesium electrode after anode polarization with different discharge current density. Electrolyte: *GI*, *LiTf*. *freshing assembly cell* (1) and *cell after discharge*: 2 – 100 $\mu\text{A}/\text{cm}^2$; 3 – 200 $\mu\text{A}/\text{cm}^2$; 4 – 500 $\mu\text{A}/\text{cm}^2$; 5 – 1 mA/cm^2 ; 6 – 2 mA/cm^2 ; 7 – 5 mA/cm^2 ; 8 – 10 mA/cm^2 ; 9 – 20 mA/cm^2 . A – general results. B – high frequency region.

As can be seen from the impedance spectra shown in Fig. 2, the interface resistance of the magnesium electrode / electrolyte decreases with increasing density of the discharge current. Obviously, this is due to the destruction of the initial passivating film on the magnesium surface, and the formation of a new film more permeable to Mg^{2+} .

The conducted studies showed the prospects of using non-aqueous electrolytes containing lithium salts to reduce the resistance of a passivating film on the surface of the magnesium anode in magnesium batteries.

Acknowledgments

The work was carried out according to the project of the Ministry of Education and Science of Ukraine, project No. 42/170790 "Development of high energy power sources based on ukrainian magnesium and manganese raw material for innovative instrumentation". Further development of the work is based on framework of NATO SPS 985148 project "Development of New Cathodes for Stable and Safer Lithium-Sulfur Batteries" Ukrainian State University of Chemical Technology participates in this project.

Company Enerize Corporation is an industrial partner of this project.

References

1. H.D. Yoo, I. Shterenberg, Y. Gofer, *J. Energy Environ. Sci*, Vol. 6 (8), p. A2265 (2013).
2. R. Mohtadi, F. Mizuno, *J. Nanotechnol.*, **5**, p. 1291–1311 (2014).
3. B.B. Claudiu; G. Thomas; O. G. Allen, *J. Phys. Chem. Lett.*, **6** (18), p. 3578–3591 (2015).

Chemometric approach to study the influence of synthesis parameters on the structural and electrical responses of metal polycyanometalates (MPCMs) for optimizing their use as cathodes in metal(M)-ion batteries ($M = \text{Li}^+, \text{K}^+, \text{Na}^+$).

V. Rojas^a, N. Briones^a, E. Navarrete^a, J. Román^a, G. Cáceres^a, E. Muñoz^a, F. Herrera^b.

^a Pontificia Universidad Católica de Valparaíso, Facultad de Ciencias, Instituto de Química, Av. Universidad 330, Valparaíso

^b Universidad de Santiago de Chile, Departamento de Química de los Materiales, Facultad de Química y Biología, Av. Libertador Bernardo O'higgins 3363 Estación Central, Santiago.

victormrojascontreras@gmail.com

In the last time, the growing demand for energy has led to the search for new technologies for the storage of energy. Electrochemical batteries have been seen as a good option, where the most known are the type Metal-ion batteries (MIBs), based on the electrochemical intercalation of the ions and being recognized as a promising alternative (1). The choice of cathode materials significantly affects the performance and cost of a M-ion battery. Therefore, is necessary to use inexpensive cathode materials could reduce the overall cost of MIBs and expand their application for energy storage (2). From this point of view, transition metal polycyanometometalates (MPCMs) could be considered as promising candidates. They possess an open framework where an intercalation process of ions presents in the electrolyte can occur (Figure 1). In this last process, a redox change of the central metal atom should happen simultaneously. Therefore, such compounds can be used as ionic host structures in the design of cathodes for M-ion batteries.

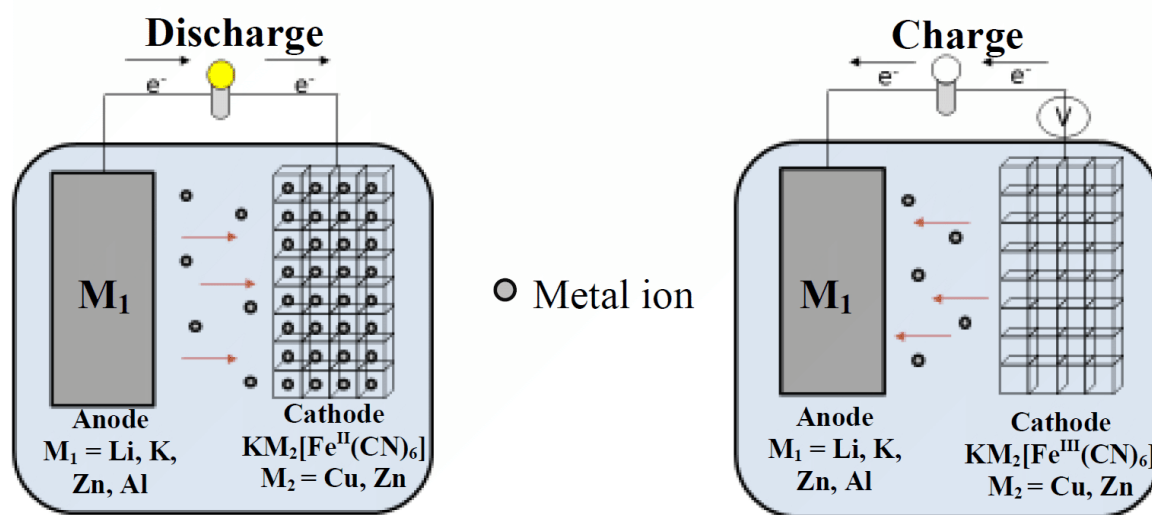


Figure 1. Intercalation process of ions presents in the electrolyte in the open framework structure of MPCMs, in this case the $KM_2[Fe(CN)_6]$.

In this work, the experimental variables for the synthesis of MPCMs ($KCu[Fe(CN)_6]$, $K_2Mo[Mo(CN)_8]$) by chemical procedures (hydrothermal synthesis) were optimized by chemometric approach allowing the adjustment of the microstructure and the parameters of the crystalline structure to improve the performance of these materials in the subsequent use as cathodes in M-ion batteries ($M_1 = \text{Li}^+, \text{K}^+, \text{Na}^+$) For the hydrothermal synthesis, 20 mL of aqueous

$\text{K}_3\text{Fe}(\text{CN})_6$ or $\text{K}_4\text{Mo}(\text{CN})_8$ solution was mixed with 20 mL of $\text{MCl}_2 \times 2\text{H}_2\text{O}$ ($\text{M}_2 = \text{Cu}, \text{Co}$). The mixed solutions were stirred for 10 min and were transferred to a Teflon-lined stainless steel autoclave and heated. After the reaction, the autoclave was cooled to room temperature and the resultant solid was washed with water and acetone three times and the resulting solid was washed with water and acetone three times and centrifuged at 4500 rpm for 5 min. Finally, the products were dried to 70°C. The variables for the synthesis for the chemometric approach were the precursors concentration, temperature and time of reaction.

The MPCMs obtained were characterized by XRD, SEM, EDX and electrochemical measurements such as cyclic voltammetry (electrochemical insertion of metal ion Li^+ , K^+ , Na^+) and charge/discharge curves were performed for obtaining the response variables.

Additionally, button-type batteries were assembled to study the performance of these materials as cathodes. Finally, a statistical relationship was obtained between the synthesis parameters and the responses analyzed, thus finding the optimal conditions of the synthesis process to obtain the best performance of the cathodic material. The chemometric strategy used in this work can be used for the optimization of cathode materials that are currently used in commercial lithium ion batteries.

Acknowledgments

The authors acknowledge the financial support from FONDECYT (Project No.1180784). V. Rojas and J. Román acknowledge to CONICYT for their National Doctoral Scholarships No. 21160733 and No. 21140218 respectively. E. Navarrete and G. Caceres acknowledge to Pontificia Universidad Católica de Valparaíso for their Postdoctoral project No. 37.0/2018 DI and Innovative thesis project No 037.728-29 respectively.

References:

1. L. Zhang y col., "Towards High-Voltage Aqueous Metal-Ion Batteries Beyond 1.5 V: The Zinc/Zinc Hexacyanoferrate System," *Adv. Energy Mater.*, 5, 1–5, 2015.
2. M. Omarova y col., "Nickel Hexacyanoferrate Nanoparticles as a Low Cost Cathode Material for Lithium-Ion Batteries", *Electrochimica Acta*, 184, 58-63, 2015.

Nanostructured Transparent Polymer Provides Innovation Design for Solar Cells. Increasing Energy and Improving Performance.

E. Shembel, V. Redko, T. Pastushkin, L. Yashchenko, N. Yarova.

Enerize Corporation. Coral Springs, FL, 33067, USA

Introduction

Nanostructured transparent polymer (NSTP) developed by Enerize Corporation for encapsulate solar cell / PV module allows to solve the problems of the traditional PV modules that laminated with glass. The traditional PV modules are complex, non-flexible, & expensive, requirement the antireflection coating and adhesive polymer between glass and semiconductor.

Additional benefit of using the NSTP includes: increasing the efficiency of solar cells by 20% relative, reducing price and weight by 30%; flexible solution but sufficient durability. New design for thin film flexible photovoltaic modules provide the possibility using single layer nanostructured high level transparency polymer for encapsulation, and protective coating of different type of thin film flexible solar cell.

Structure and properties of nanostructured transparent polymer

NSTP has a mosaic structure with the nanoscale domains. Micrograph of nanopolymer encapsulating on the surface of the solar cell includes a nanostructure in the form of prisms or lenses. This results in the concentration of light and increasing the efficiency of PV modules

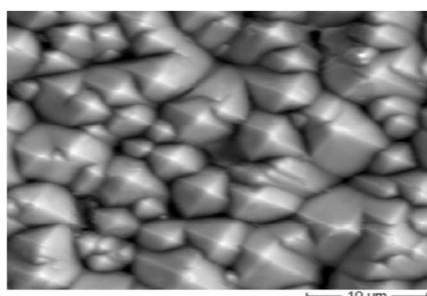


Figure 1. The RFM image of the surface distribution of the structures for optically transparent polymer composition that is formed on the surface of a silicon single crystal.

As shown from the results the test of NSTP this type of the structures leads to a significant increase in the absolute efficiency of solar cells & PV modules versus encapsulation with glass or other multiple-film polymers.

Below presented Figures that illustrate the properties of NSTP and benefit based on using the NSTP

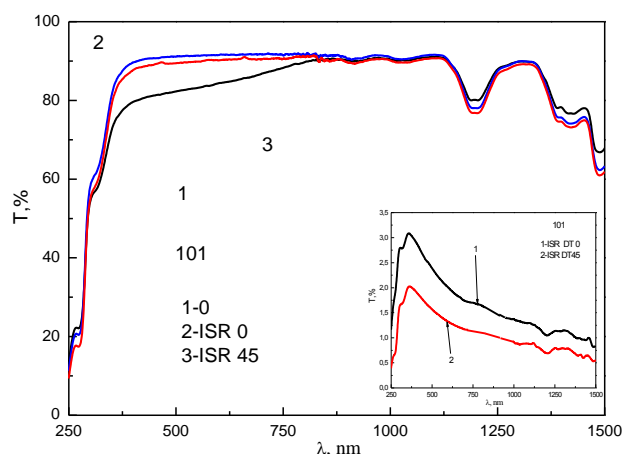


Fig. 2

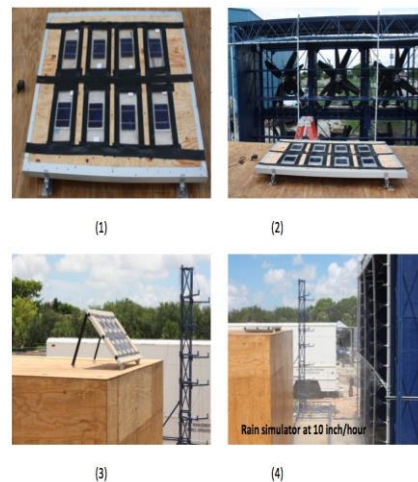


Fig. 3

Figure 2. The transmittance of NSTP under wavelengths of light. Nanostructured transparent polymer has high transparency, including UV area

Figure 3. Independent center for testing PV modules at Florida International University tested Enerize PV modules based on mono c-Si encapsulated with NSTP, and PV modules laminated with glass. During tests artificial hurricane conditions were modeled using a special test bench. Results of the test confirmed good stability of the properties of PV modules encapsulated with NSTP

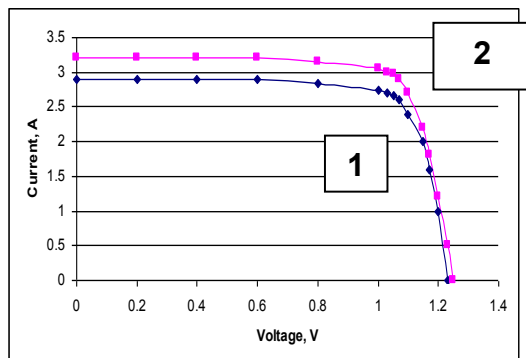


Fig. 4

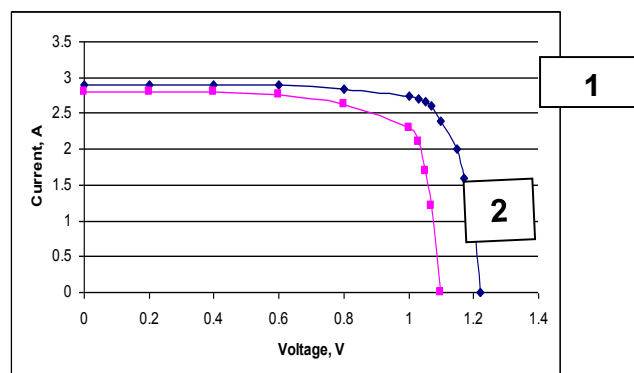


Fig. 5

Figure 4. Depicts characteristic of the solar cell before encapsulation with transparent polymer (1) and after (2) encapsulation with transparent polymer. After encapsulate with NSTP efficiency of solar cell increased.

Figure 5. Depicts characteristic of the solar cell before lamination with glass (1) and after (2) lamination with glass. After laminated with glass efficiency of solar cell decreased.

Market opportunity for nanostructured transparent polymer and solar cells encapsulated with NSTP

A single layer NSTP is enabling PV modules based on various types of solar cell to be cheaper, lighter and deliver higher efficiency via encapsulation vs. glass or multilayer polymer coating.

Non- active materials of PV modules account for 15% to 48% of module manufacturing costs. Demand for new NSTP has average anticipated growth rate of 48% per year.

NSTP is promising for encapsulation thin film flexible solar cells like CIGS, DSSC and organic solar cells.

Hybrid system of flexible PV modules and flexible Li-ion batteries has the great market opportunity. Some example is as followed: the next generation of EV that will be using the solar cell on the roof of car for powered the EV. This high-tech, solar-powered car may be the future for traveling.

Acknowledgements

This presentation is connected with the framework of NATO, Science for Peace and Security Programme Project SPS 985148 “Development of New Cathodes for Stable and Safer Lithium-Sulfur Batteries” in the light of the following development the hybrid system: flexible PV modules that encapsulated with Enerize nanostructured transparent polymer, and flexible high energy Lithium-Sulfur Batteries. Enerize Corporation is industrial partner of this NATO project

Accumulation of "Solar" Hydrogen in the Photoelectrochemical System Based on CdSe Photoanode and MH Cathode

I. A. Rusetskyi^a, L. G. Shcherbakova^b, M. O. Danilov^a, I. A. Slobodyanyuk^a,

G. Ya. Kolbasov^a, S. S. Fomanyuk^a, Yu. M. Solonin^b

^aVernadskii Institute of General and Inorganic Chemistry of the Ukrainian NAS, prospekt Palladina 32-34, 03680 Kyiv, Ukraine

^bFrantsevich Institute for Problems of Materials Science of the Ukrainian NAS, Krzhizhanovsky str., 3, 03680 Kyiv, Ukraine

The film photoanodes based on CdSe and NT-TiO₂/CdSe has been formed by the electrochemical and painting methods. It is shown that the introduction of graphene oxide into the structure of the semiconductor CdSe film promotes absorption of light and leads to improvement in their characteristics by 25-30 %. It is shown compatibility of the cathode based on composite of hydrogen-sorbing intermetallic alloys LaNi_{4.5}Mn_{0.5} + LaNi_{3.5}Al_{0.7}Mn_{0.8}, with current-conductive additives, in pair with the CdSe photoanode. It was found that 95 – 98 % of the total current generated under the influence of sunlight at the anodes was used on the formation and accumulation of hydrogen by cathodes.

Introduction

One of the promising ways for obtaining hydrogen is the photoelectrochemical (PEC) decomposition of water under the influence of sunlight. The hydrogen produced by the PEC method is very clean and does not require additional purification for its use. Photoelectrochemical systems in which it is possible to use semiconductor anodes sensitive to the visible spectrum of sunlight and cathodes that efficiently absorb hydrogen are one of the promising directions in creating systems for the production and accumulation of "solar" hydrogen.

A^{II}B^{VI} compounds based semiconductor electrodes were chosen as the object of research, nanocomposites and heterostructures were developed on their basis with the reduced graphene oxide as well as the AB₅ type (LaNi₅ based) hydrogen sorbing alloys with the PEC system for hydrogen production.

Experimental part

The TiO₂ (NT-TiO₂) nanotubes on the Ti substrate were obtained by the potentiostatic anodic polarization of titanium foil (1). CdSe films were obtained by the painting method on previously prepared Ti substrate. Depositions were following from suspension contained CdSe and CdCl₂ for the A1-A3 photoanodes. For the increasing the photocatalytic activity of semiconductor films, graphene oxide (A4 photoanode) was added to the CdSe suspension. Method of producing the GO was described in (2). The films of CdSe were applied in 2 layers. Each layer was annealed in an air atmosphere. According to the literature, at this temperature, it is also possible to partially reduce

graphene oxide by the decarboxylation (2). After that, the surface was activated in an aqueous solution of 0.5 M CrO₃.

The cathode (C1) was produced by pressing a mixture of powders of hydrogen sorbing alloy and copper onto a nickel. The capacity of the cathodes used in the process was about 23 mAh, which is enough for several hours of work in pair with the photoanode.

A polymethylmethacrylate cell with a cathode and anode space separated by the ion-exchange membrane MF-4SK used for the studies (3). Photoelectrodes were placed in an anode space filled with an alkaline solution of sulphide or sodium polysulphide. Sulfide electrolyte was used to exclude the effect of light absorption on the characteristics of photoelectrodes, while in the process of operating photoelectrodes this solution was enriched with polysulfide ions. The cathode space of a hydrogen sorbing electrode was filled with the 30 % KOH solution.

Results and discussion

It has been established that the incorporation of reduced graphene oxide into the NT-TiO₂/CdSe composite promotes the absorption of light and leads to an improvement of its characteristics by 25-30 % due to a larger separation of electron-hole pairs and, as a consequence, a decrease in the losses of photogenerated charge carriers for recombination. The optimal amount of graphene oxide as a modifier is 1.16 % by mass, at which the maximum V_{im} was about 0.6 V and I_{sc} was about 6 mA/cm² (4).

Tests of photoanodes were conducted by different methods of forming a photosensitive semiconductor layer, which operates in pair with the MH cathode.

In an open circuit in a sulfide solution, the potentials of the anodes A1 and A4 had values of -1.23 V and -1.24 V, for cathodes in a 30 % solution of KOH, the potentials were about -0.91 ÷ -0.93 V. Under conditions of stable solar illumination, the potentials of both electrodes reach relatively stable values. The difference between the potentials of the studied anode-cathode pairs under cell operating conditions was from 25 mV to 40 mV due to a drop in the potential on the ion-conducting membrane. The anode A4 containing the GO operates in pairs with the cathode in the region of the more negative potentials (-1.10 V) than the anode without the addition of GO ($E = -1.08$ V). When operating in pairs with the anode A4, the cathode is also charged in the region of more negative potentials.

When illuminated with solar light, photoanodes A1 - A3 generate currents that remain stable under the constant light flux does not change when works in a PEC cell. Despite the same composition of photoanodes and close values of the light flux intensity, the value of the photocurrents is somewhat different and is near 3 - 4 mA. At the photoanode A4 under identical conditions the currents are generated with larger by 25-30 % (from 3.7 mA to 5.0 mA) value. It has been established that with the increase in the number of painting layers of CdSe (3 layers), the magnitude of the photocurrents and the nature of their changes during the cell operation practically do not change.

The influence of the composition of the solution (sulfide and sodium polysulphide) on the characteristics of photoanodes A1 and A4 has been studied. From the obtained data it follows that the potentials of the anode with the addition of GO (A4) when operating in a PEC cell have the same values regardless of the composition of the solution. At the same time, when the A1 anode is operating in the polysulphide solution, its potential is shifted to the anode range.

During the operation of the photoanode A4 in a polysulfide solution, the photocurrent decreases from 4.8 mA to 2.93 mA. When the photoanode A1 is operating in a polysulfide solution,

stable photocurrents are generated, but are ~3 times less in value (~ 1 mA) than in a solution of sodium sulfide.

The discharge of the cathode by a current of 4 mA after a charge in the PEC cell has shown that from 90 % to 98 % of the current generated at the photoanode is used on the accumulation of hydrogen by the cathode. The overall efficiency of the PEC is limited only by the efficiency of the semiconductor photoanode. The results of the study of the PEC cell are given in Table 1.

Table 1. Test data of the PEC cell for the hydrogen accumulation.

Electrode Designations		The Ratio S _{an} /S _{cath}	Characteristics of the PEC Cell					Light Power**, mW / cm ²
Anode	Cathode		Photo-current*, mA	Current Density, mA / cm ²		Potential, V		
				Anode	Cathode	Anode	Cathode	
A1	C1	2.7	4.2	1.400	4.2	-1.060	-1.030	79.2
A2			3.7	1.233	3.7	-1.070	-1.040	76.0
A3			3.0	1.000	3.0	-1.080	-1.050	77.2
A4			5.0	1.667	5.0	-1.110	-1.070	75.8

*- maximum current value.

** - the intensity of the solar flux, which corresponds to the maximum value of the photocurrent.

Conclusions

It has been established that the introduction of graphene oxide into the structure of a semiconductor CdSe film leads to an improvement in their characteristics by 25-30 %.

It is shown that the composite cathode based on hydrogen-sorbing intermetallic alloy $LaNi_{4.5}Mn_{0.5}+LaNi_{3.5}Al_{0.7}Mn_{0.8}$ with the current-conducting additives was compatible in pair with the CdSe photoanode. It has been established that, on the cathode materials at currents $\leq 5 mA/cm^2$ negative potentials relative to the equilibrium potential of hydride formation occur. It was found that 95-98 % of the current generated by sunlight at the anodes is used on the formation and accumulation hydrogen on the cathodes.

References

1. J. M. Macak, H. Hildebrand, U. Marten-Jahns et. al., *J. Electroanal. Chem.*, **621**(2), 254 (2008).
2. M. O. Danilov, I. A. Slobodyanyuk, I. A. Rusetskii et. al., in *Graphene Science Handbook: Fabrication Methods*, M. Aliofkhazraei, N. Ali, W. I. Milne et. al., Editors, p. 205, CRC Press Taylor & Francis Group, New York (2016).
3. L. G. Shcherbakova, D. B. Dan`ko, V. B. Muratov et al., in *NATO Advanced Research Workshop on Hydrogen Materials Science and Chemistry of Carbon Nanomaterials*, p. 699, Proceedings, Springer, Dordrecht (2007).
4. I. A. Rusetskii, I. A. Slobodyanyuk, M. O. Danilov et. al., *Him. Fiz. Tehnol. Poverhni*, **7**(2), 195 (2016).

Changes in Properties of Perovskite Solar Cells During Their Lifetime

T. Dvořák^a, V. Novák^b

^a Department of Electrical and Electronic Technology, Brno University of Technology, Technická 10, 616 00 Brno, Czech Republic

This paper deals with the problematics of changes in electrical properties of perovskite solar cells, which can be the next generation of photovoltaic solar cells. For measurements of these changes were used various methods such as I-V characteristic or dependence of photocurrent on light intensity. Measurements indicate considerable changes of performance, which resulted from aging of perovskite solar cells.

Introduction

Since the first realization of photovoltaic cell many years have passed and developments in this sector are continuing. Photovoltaic cells belong to a group of renewable resources and this makes them more important these days, because of the ecology aspect.

Most of the photovoltaic solar cells are based on silicon semiconductors. However, the manufacturing of silicon of required quality is exacting and expensive. In addition, the silicon photovoltaic cells are getting to the limit of their efficiency. New materials can allow cheaper and easier manufacturing of photovoltaic cells.

Among such materials belongs perovskite. because of its simple preparation, the layer of perovskite necessary for same results as for silicon photovoltaic cells is one micrometre, when for silicon is this layer more than hundred times thicker.

The focus of this paper is to study changes in properties of perovskite solar cells in time.

Preparation of perovskite solar cells

Perovskite solar cells are composed of ITO (indium tin oxide) glass covered by layers of: PEDOT (transparent antistatic conductive layer), perovskite, PCBM and aluminium electrodes.

All steps of perovskite solar cells preparation were made in glovebox. This preparation include upcoming steps:

- Deposition of PEDOT on ITO glass.
- Heating of glasses on temperature 80 °C.
- Deposition of perovskite layer on spin coater.
- Annealing.
- Deposition of PCBM layer via spin coater and pipette.
- Cleaning of glass (place where cathode band belongs).
- Deposition of aluminium electrodes by vacuum evaporation.
- Application of epoxy resin.
- Epoxy resin is hardened by UV light.

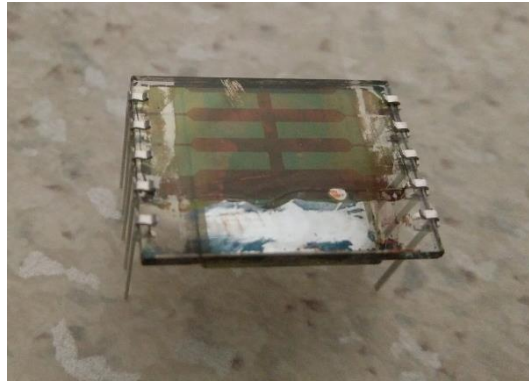


Figure 1. *Finished perovskite solar cell*

Method of solar cell measurements

Measurements were executed on CIMPS device with light source WLR02 s/n LS 1367 which have wide spectrum LED diode.



Figure 2. *Light source and solar cell holder with light sensitive sensor.*

I-V characteristic shows dependence of current on potential. From this characteristic is possible to gain MPP (Maximum Power Point), where the maximum output is gained. Light intensity of light source was set on 350 W/m^2 .

Experimental results

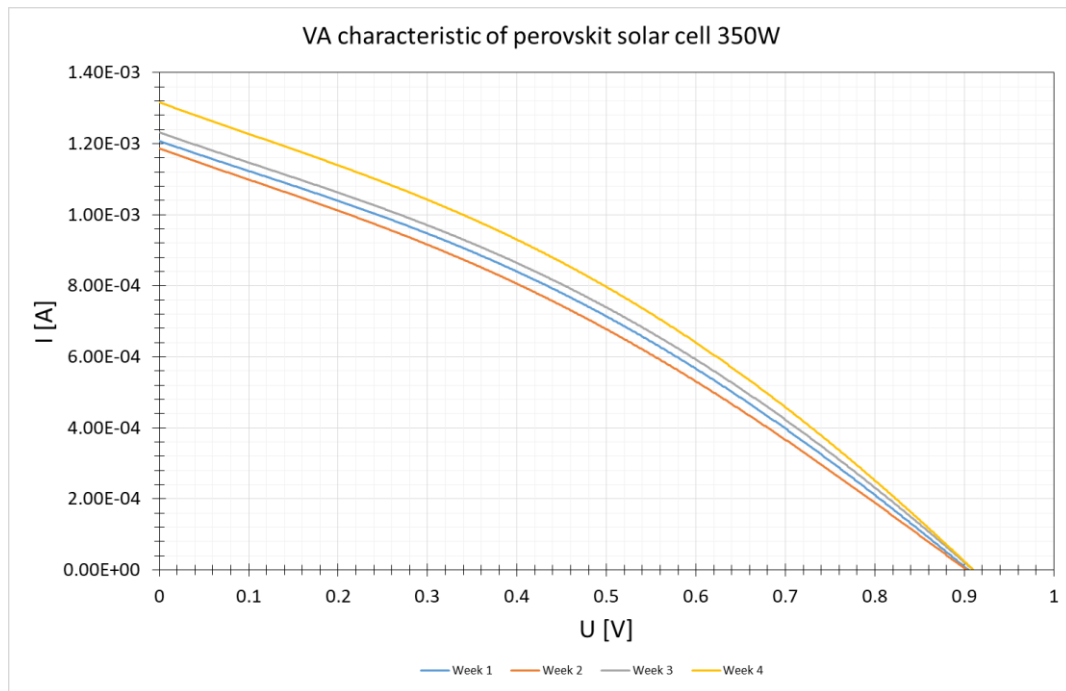


Figure 3. *I-V plots during 4 weeks*

From this I-V measurements can be observed visible increase of values of measured electrical properties after 4 weeks of perovskite solar cell lifetime. In next weeks it is expected perceptible decrease of these values.

Conclusion

The main goal of this paper was to measure changes in electrical properties of perovskite solar cells during their lifetime. After four weeks of perovskite solar cell lifetime, there was an increase of values of measured electrical properties, but a decrease of these values is expected in upcoming weeks.

Next study will be focused on making perovskite solar cells more stable and further study of its degradation.

Acknowledgments

This research work has been carried out in the Centre for Research and Utilization of Renewable Energy (CVVOZE). Author gratefully acknowledge financial support from the Ministry of Education, Youth and Sports of the Czech Republic under NPU I programme (project No. LO1210). This research was also sponsored by the NATO Science for Peace and Security Programme under grant 985148.

Protection Against PID Degradation at Photovoltaic Cell Level

J. Hylský, D. Strachala, P. Čudek, J. Vaněk

Department of Electrical and Electronic Technology, Brno University of Technology, Brno 616 00, Czech Republic

This paper deals with potential-induced degradation (PID), more specifically focuses on the PID resistive structure of a photovoltaic cell. In the article are compared the current – voltage characteristics of the reference and newly created PV cells, which are further supplemented by their external quantum efficiency. Finally, the PID resistive properties of the newly created photovoltaic cell are confirmed by an artificially created PID degradation.

Introduction

Degradation of photovoltaic power plants due to the PID (Potential Induced Degradation) is one of the main degradation mechanisms, which is responsible for a reduction of the photovoltaic systems efficiency. The problems with PID were already known in the 1980 and currently is this topic widely researched through many scientists (1). With the gradual increase of the production of photovoltaic modules and pressure to lowering the manufacturing costs began this undesirable phenomenon more frequent. The first company which warned about its negative effects was SOLON in 2010 and this has led to an increased awareness of PID (2). A detailed study about the PID in photovoltaic modules has released two years later the Fraunhofer Institute in Germany. Fraunhofer Institute identified PID in 46% of tested modules from 96 different manufacturers (3).

Potential Induced Degradation

The incidence of PID degradation is gradual and lasts for several years before it becomes fully observable - in extreme cases from 2 to 5 years. This degradation is accelerated by an environmental condition, such as humidity and heat. Therefore, the incubation time cannot be accurately determined and depends on the location and the conditions in which the photovoltaic modules operates.

The reason for the degradation process begins with the design of PV power plants with increasing performances, higher number of PV modules in series and higher potential between cells and grounded frame for security reasons. When using a floating potential (neither the positive or the negative pole of the string is grounded) a negative voltage potential arises at the negative pole, which causes the leakage currents from the PV cells passing through the sandwich structure of the PV module into the grounded frame. Conversely, the resulting neg-ative electric field between the aluminum frame and the PV cells accelerates the movement of the positive sodium ions contained in the cover glass of the PV module that travel across the sandwich structure to the PV cells.

If the PV module is created with PV cells susceptible to the PID (they contain stacking fault in their pn junction) sodium ions will reduce shunt resistance RSH and PV module performance will be lower. There are three levels in the protection against PID. The level of the whole photovoltaic system, the level of the photovoltaic module and the level of the photo-voltaic cell.

To understand the occurrence of PID, the level of the photovoltaic cell is the most important. If the sodium ions get through the sandwich structure of the PV module up to the surface of the cell, they will drift by an electric field through an anti-reflective layer of silicon nitride SiN_x, where they will accumulate in the silicon oxide SiO_x layer. The presence of stacking faults through the PN junction allows the sodium ion further penetrate into the PV cell result-ing in short-circuiting the PN junction. As a result of the above-described process, the value of the shunt resistance decreases and consequently the power of the whole PV cell is much lower.

Protection solution at this level is economically and technologically most acceptable because it does not interfere with the already functional PV system. It could be said that by modifying the technological process it is possible to modify the structure of the PV cell to be PID resis-tive.

PID protection and treatment at the levels of the PV module and the PV system is economi-cally disadvantageous due to higher intervention and changes in their structure. At the level of the PV module is needed to find an alternative to Ethylene vinyl acetate film (EVA film) in the PV module sandwich structure. Alternative material must protect PV cells from external influences, ensure light transmission to cells and its resistance must be high enough to prevent drifting of the sodium ions to the PV cells. Material with the above-described properties is, for example, Acit (partially neutralized polyethylene). This material would meet the require-ments, on the other hand its price is so high that the PV modules would be very expensive and it would reduce their competitiveness.

As described above, the best solution to protect against PID degradation is at the PV cell level. Therefore, this work is further focused on the solution of protection through structural modification of the PV cell.

Analysis of Photovoltaic Cells

As part of the serial production of standard 6-inch P-type PV cells, their structure was modified at half of one batch. Within this set, the parameters of the reference and newly created PV cells are compared in order to determine the effect of the modified structure of the newly created samples and then to determine their susceptibility to PID degradation. There is an emphasis on minimal interference with the current technological steps of the PV cells manufacturing process.

TABLE I. *Parameters of reference and new created PV cells.*

	P_{MPP} (W)	E_{ff} (%)	V_{MAX} (V)	I_{MAX} (A)	V_{OC} (V)	I_{SC} (A)
Ref. samples	4.215	17.63	0.522	8.081	0.626	8.238
New samples	4.244	17.76	0.525	8.084	0.625	8.233

When comparing the measured values of the newly created and referenced current – voltage characteristics of samples, it is clear that dependencies are identical, see Fig. 1. In particular, the value of the short-circuit ISC parameter in the newly created samples does not show a significant decrease, even for the other parameters such as the V_{OC} open-circuit voltage and the maximum power output P_{MAX} .

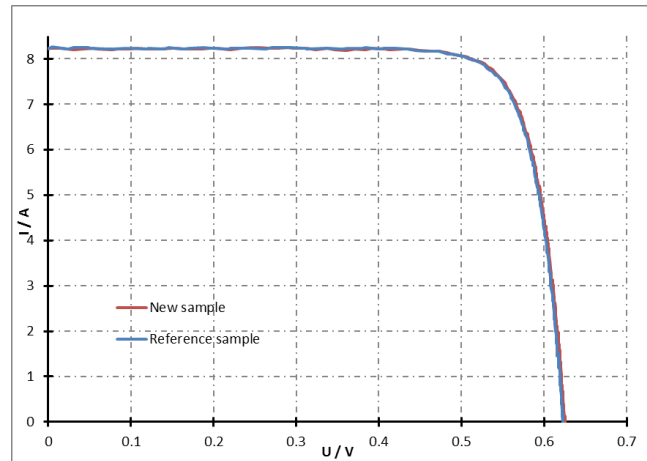


Figure 1. IV - characteristics of newly created and reference PV cells.

Fig. 2 illustrates the comparison of the external quantum efficiencies of the newly created samples and the reference without the PSG layer. From these, it is clear that the values of the newly created sample follows the measured values of the external quantum efficiency of the reference PV cell throughout the visible radiation region. This finding confirms the results of the IV characteristics, where the measured parameters of the samples are identical. From these results it can be stated that the newly prepared structure with its electrical parameters does not differ from the reference sample.

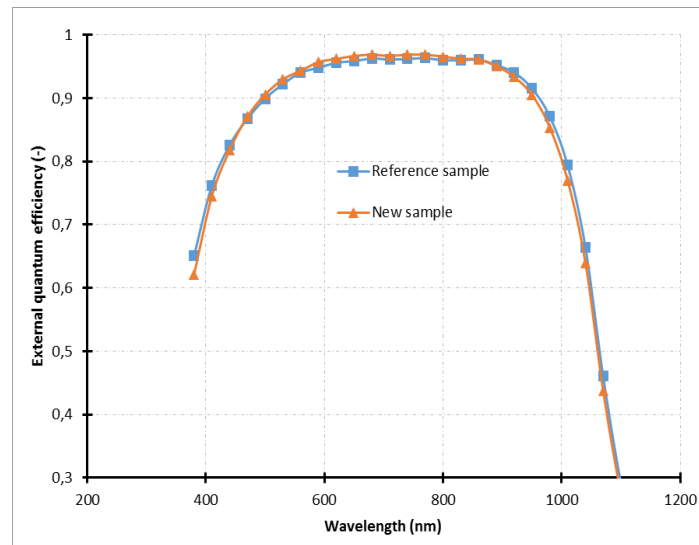


Figure 2. External quantum efficiency of newly created and reference PV cells.

Fig. 3 shows the behavior of both samples degraded by PID. As can be seen, the newly created sample of the PV cell has PID resistive properties over the entire time range of artificially generated degradation. On the other hand, the reference article shows a reduction in peak performance after four hours of degradation.

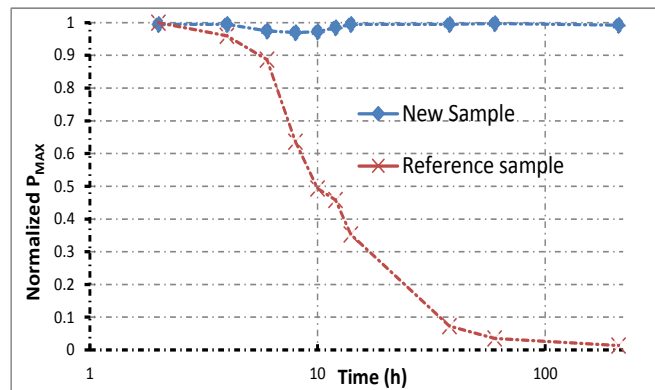


Figure 3. Dependence of the normalized maximum power output P_{MAX} on PID degradation time.

Conclusion

This article discussed the comparison of properties of newly created and reference PV cells. These samples exhibit the same properties as the reference samples, thus adjusting their structure does not reduce any of the major electrical parameters. Finally, the samples are subjected to artificially created degradation, which clearly shows the PID resistive properties of the newly created structure.

Acknowledgments

This research work has been carried out in the Centre for Research and Utilization of Renewable Energy (CVVOZE). Authors gratefully acknowledge financial support from the Ministry of Education, Youth and Sports of the Czech Republic under NPU I programme (project No. LO1210).

References

1. D. Lausch et al., *Energy Procedia*, **55**, 486-493 (2014)
2. V. Naumann, C. Brzuska, M. Werner, S. Großer, and C. Hagendorf, *Energy Procedia*, **92**, 569-575 (2016)
3. M. Barbato et al., *Solar Energy Materials and Solar Cells*, **168**, 51-61 (2017)

Possibilities of Regeneration of a PID Degraded PV Cell

J. Hylský^a, E. K. Ovando^b, D. Strachala^a, J. Vaněk^a and P. Vyroubal^a

^a Department of Electrical and Electronic Technology, Brno University of Technology, Brno 616 00, Czech Republic

^b Department of Industrial Engineering, University of São Paulo, São Carlos 13566-590, Brazil

This experiment was made with successive regenerations after degradation of PV cells, in order to measure the capacity of regeneration of a PID degraded silicon solar cell.

Introduction

Potential-induced degradation (PID) is one of the degradation mechanisms of crystalline silicon solar cell and has been widely studied since the first publications about this subject, in 2010 (1). Studying PID is relevant because of its high practical importance (2), once that the degradation determines the performance and the lifetime of PV cells. Therefore, the main goal of this experiment was to measure the capability of regeneration of one PID degraded silicon solar cell, to better understand its degradation process and foment the discussion about ways to increase a PV system's lifetime.

Experimental

In order to measure and analyze the capacity of regeneration of one solar cell, 20 hours of degradation stress followed by 20 hours of regeneration was performed successively in a solar cell sample. The stress was caused by 1000 V voltage in a thermic chamber with 70 °C. Every day the procedure started at the same time, to minimize external conditions.

The sample was made by a p-type monocrystalline solar cell with 5 cm x 5 cm dimensions covered by ethyl-vinyl acetate (EVA), both covered by soda lime glass, for simulating a standard PV panel.

This sample scheme is shown in Figure 1.

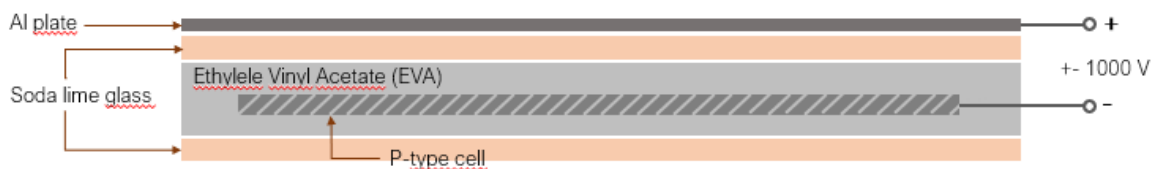


Figure 1. Scheme of the sample.

To degrade (or regenerate) the sample has been used Al flat wire, which were connected to the negative pole in the degradation, and to the positive pole in the regeneration process. The other pole is a Cu electrode that covers the cell and appears in Figure 2.

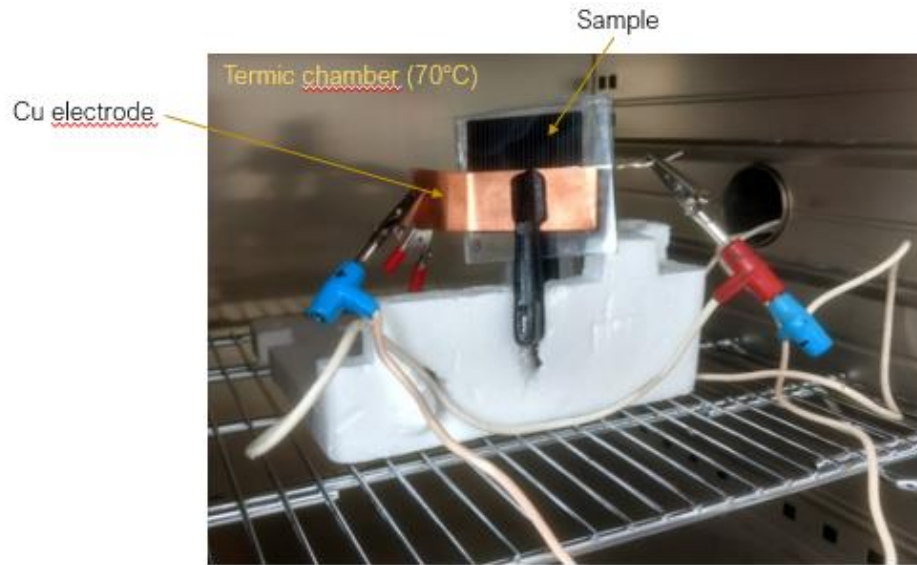


Figure 2. Procedure to degrade (or regenerate) the sample.

The sample was placed in the chamber to be exposed to the voltage and the temperature. The measurements were made by two methods: light test, using the PV tester PASAN SunSim 4C in STC (standard testing condition), and the dark test, using the SolarCell Tester active load without illumination.

The main results are shown in both Charts 1 and 2 below.

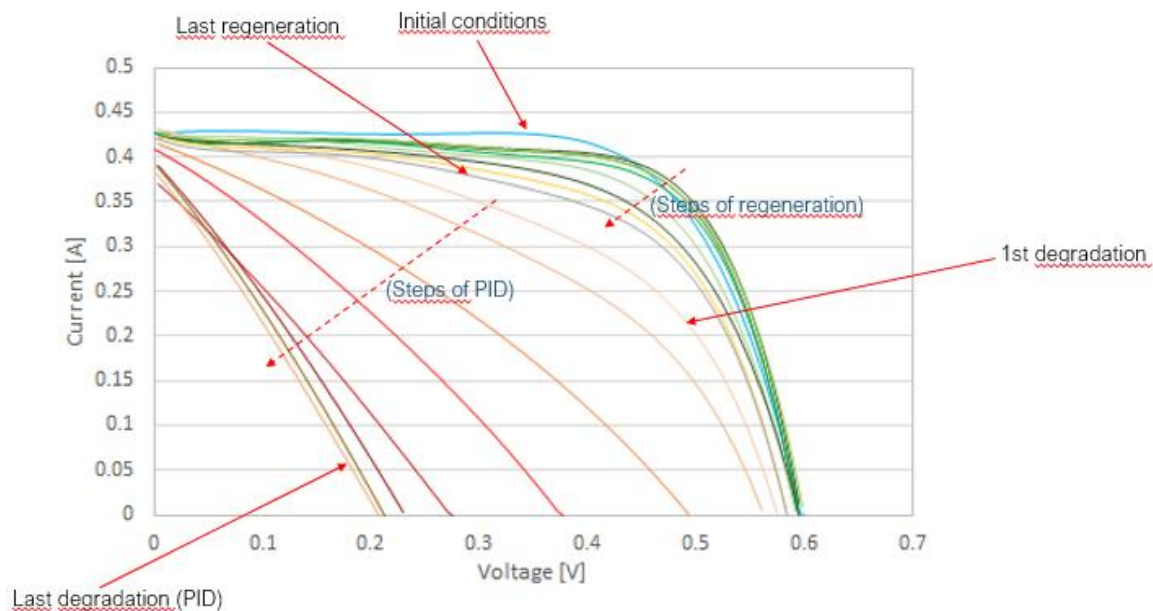


Figure 3. IV characteristics (light test) measured by PASAN SunSim 4C in STC.

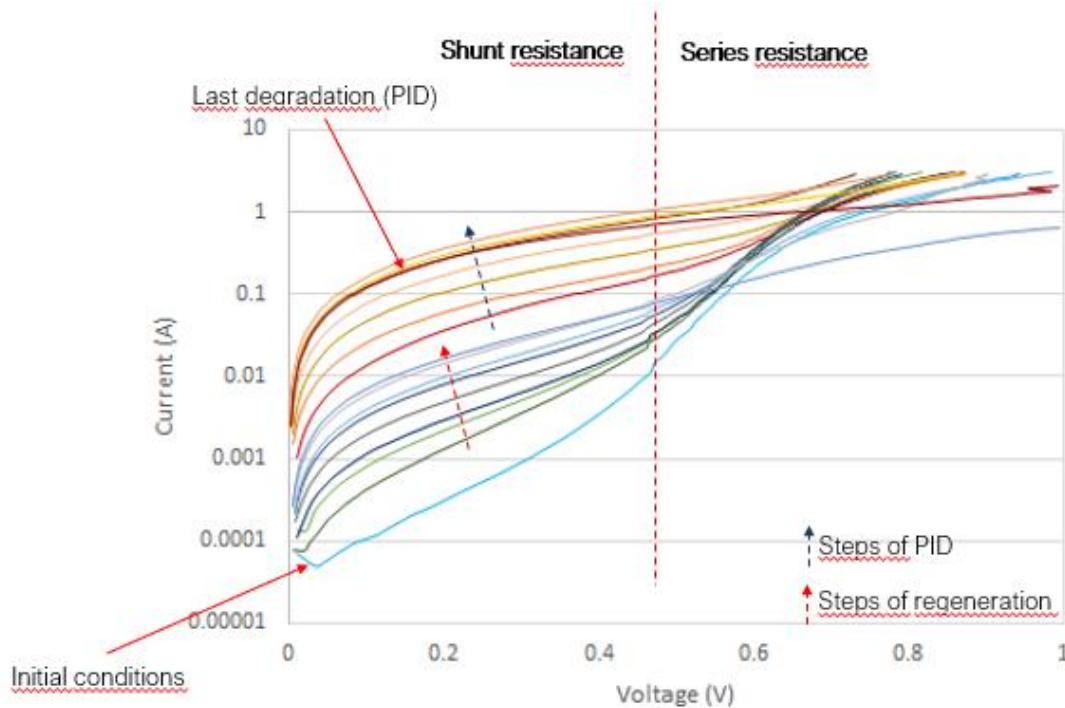


Figure 4. IV characteristics (dark test) measured by SolarCell tester active load.

Besides these behaviors (and to better understand it), some parameters of the cell were measured and analyzed: short circuit current, open circuit voltage, maximum power, efficiency and shunt resistance.

The charts of all the analysis and discussion about the results are presented in the full version of this article.

Acknowledgments

This research work has been carried out in the Centre for Research and Utilization of Renewable Energy (CVVOZE). Authors gratefully acknowledge financial support from the Ministry of Education, Youth and Sports of the Czech Republic under NPU I programe (project No. LO1210) and the UNIGOU Program, which provided the meeting of Brazilian and Czech researchers.

References

1. S. Pingel, et al., *Proceedings 35th IEEE PVSC*, 2817-2822 (2010).
2. V. Naumann, et al., *Solar Energy Materials & Solar Cells*, **120**, 383-389 (2014).

Simulation Of Effects Of Wind In The Installation PV Power Plants

K. Jandova^a, M. Janda^b

^a Department of Electrotechnology, Brno University of Technology, Faculty of Electrical Engineering and Communication Technologies, Technicka 10, 616 00 Brno, Czech Republic

^b Department of Power Electrical and Electronic Engineering, Brno University of Technology, Faculty of Electrical Engineering and Communication, Technicka 10, 616 00 Brno, Czech Republic

This article discusses the problem of flow calculation in the vicinity of ground installations of photovoltaic power plants, in particular due to the distance between individual panels of the panels to wind speed. The main aim of this work is to use the supporting structure to improve the airflow around the panels and thus to increase their cooling, respectively. effectiveness. As the simulations have shown, the greatest influence of the structure will be reflected at a distance of 3 m. In this case, it can be assumed that the modification of the supporting frames or their supplementation with simple current routers could mean an improvement in the temperature parameters of the photovoltaic panels. At large distances, the effect of the construction is not so great.

Introduction

At present, a large number of photovoltaic power plants are built, whether ground or roof installations. All modules are subject to various weather conditions. These include, for example, rain, snow or wind. These phenomena can significantly affect module performance. At higher outdoor temperatures, the photovoltaic module will naturally heat up and, at the same time, heat losses occur when solar radiation is converted into electricity. Wind and airflow play significant role in natural cooling.

The wind flow around the photovoltaic panels depends on many factors, such as the speed and wind direction and how the panels are installed, on the load-bearing structure. From the view of cooling, it is a very unstable and variable way of cooling. This article deals mainly with ground installations of PV power plants.

Simulation of flow near ground installation

The Ansys CFX program was used to simulate wind flow near the ground installation. As a computational geometry was used the model of two rows of photovoltaic panels placed on a simple construction. The main parameter that was changed during the calculation was the distance of the individual panels. The wind speed was selected at 5 m / s, which is the value determined from the average air flow rates. For simplicity, the direction of the action itself is determined perpendicular to the front of the model. The calculation itself took place for three installation cases, for a distance of 3m, 5m and 7m between the load-bearing structures.

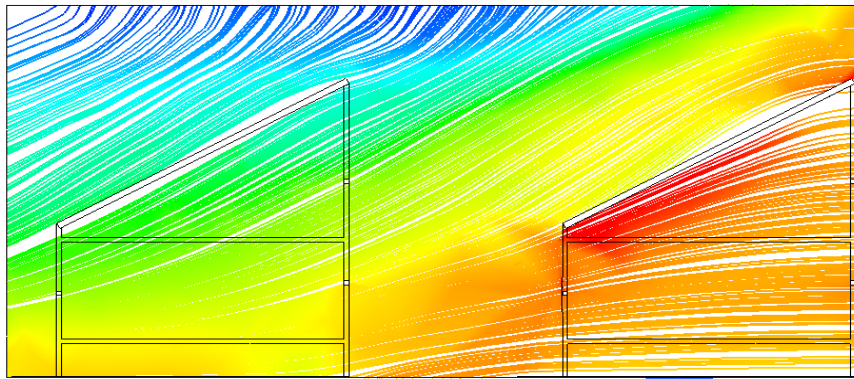


Figure 1. Flow around the ground installation – row distance 3m

Figure 1 shows the flow profile just for the installed distance of 3m. It can be seen that the close fitting of the panels causes the flow to be accelerated at the bottom of the panel in the second row, where the wind speed increases with the edge of the cutout to 6m / s. When selecting a greater distance between the rows (eg Figure 2) there is see a dampening effect of this phenomenon. Here is a noticeable decrease in wind speed in the space between installations.

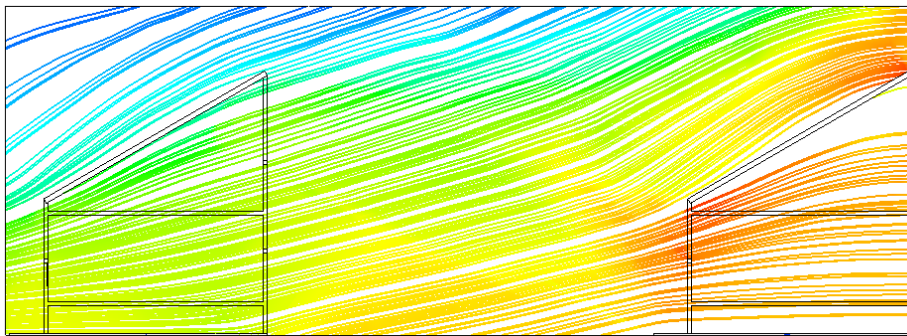


Figure 2. Flow around the ground installation – row distance 5m

A similar situation occurs with the installation of photovoltaic panels on structures that are 7 m apart (see Figure 3). As shown clearly, the flow profile for longer distances (see 5 and 7 m) is almost the same under constant climatic conditions.

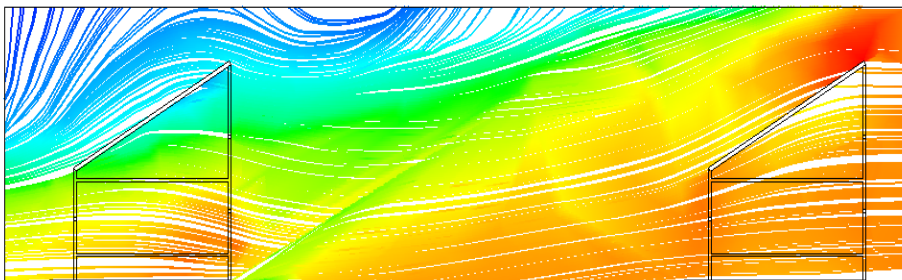


Figure 3. Flow around the ground installation – row distance 7m

The results of the simulations also show that the distribution of the supporting structures of the photovoltaic panels is manifested mainly in the case of smaller distances of the individual rows. At larger distances, the flow of individual jets is stabilized, so the effect of this design on speed is not so significant. Thanks to this, the amount of air witch flow around the panels is smaller. At

smaller distances, higher wind speeds can be achieved in the lower area of the panel to achieve better cooling of these parts.

Conclusion

Simulation results have shown that the distance between installations is mainly important due in cases with smaller lengths. The greatest influence on the flow velocity occurs at a distance of 3 m. From the flow profile, it results that at this distance the airflow at the bottom of the panels in the second row is the fastest. This phenomenon is due, among other things, to fracture edges. Higher air velocity means larger volumetric flow and hence a larger amount of cooling medium flowing around the ground constructions of the FV power plants. Due to the simplification that was made before the calculation with respect to the size of the model, it is not possible to fully monitor the flow in the vicinity of the backlit parts of the monitored part, in the boundary layer of that model. At a distance of 5 m and 7 m, the design is not so marked. At these distances, it would be advisable to incorporate an optimization algorithm in the other simulations, the parameters of which included several parameters, such as the angle of inclination of the PV panels, the height installation, the most frequent wind direction and force, the location of the power plants (with regard to the sunlight).

Acknowledgement

This research work has been carried out in the Centre for Research and Utilization of Renewable Energy (CVVOZE). Authors gratefully acknowledge financial support from the Ministry of Education, Youth and Sports of the Czech Republic under NPU I program (project No. LO1210).

References

1. J. Vaněk and K. Jandová, Possibilities of Usage LBIC Method for Characterisation of Solar Cells. In *Solar Cells - Silicon Wafer-Based Technologies*. Printed in India: InTech, Janeza Trdine 9, 51000 Rijeka, Croatia, 2011. s. 111-124. ISBN: 978-953-307-747- 5.
2. J. Strnadel, R. Gvritishvili and J. Vaněk, Comparison Between Visual And Thermovision Inspection of PV Field. In *Proceedings of 28th European Photovoltaic Solar Energy Conference and Exhibition*, Paris, France.: WIP, 2013. p. 3953-3956. ISBN: 3-936338-33- 7.
3. J. Vaněk and J. Strnadel, Long Time Monitoring of Heat Distribution in Photovoltaic Module by the Thermovision. In *ECS Transaction*. ECS Transactions. San Francisco, USA: ECS, 2014. p. 199-206. ISBN: 978-1-62332-031- 7. ISSN: 1938- 5862.

Changes of the Active Perovskite Solar Cell Layer Caused By External Influences

D. Strachala^a, M. Kratochvíl^b, J. Hylský^a, L. Chladil^a, A. Gajdoš^b, and J. Vaněk^a

^a Department of Electrical and Electronic Technology, Brno University of Technology, Brno 616 00, Czech Republic

^b Department of Physics, Brno University of Technology, Brno 616 00, Czech Republic

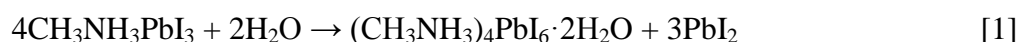
^c Institute of Physical and Applied Chemistry, Brno University of Technology, Brno 612 00, Czech Republic

This paper deals with the observation of the changes in the perovskite layer of $\text{CH}_3\text{NH}_3\text{PbI}_{3-x}\text{Cl}_x$ caused by external influences, especially humidity and oxygen. X-ray powder diffraction (XRD) measurement was used to monitor changes in the structure of perovskite solar cells. The measurement confirmed the increase in the amount of lead iodide over time.

Degradation Mechanism Influencing Perovskite Layer

Degradation of perovskite photovoltaic cells is not fully understood. Their main causes are known as the effects of humidity and impact of irradiance, but the physical and interlayer processes influencing the stability are not sufficiently explained. Degradation of perovskite can be generally divided into an extrinsic one with the external influences of oxygen, incident radiation, humidity, temperature and intrinsic degradation with the influence of temperature and electric field inside the structure.

Perovskite active layer - $\text{CH}_3\text{NH}_3\text{PbX}_3$ is very susceptible to the presence of oxygen and water and can be degraded within minutes, at most hours, during the ambient influence (1). One of the main reasons for reducing cell performance is the effect of moisture (1). There are several theories that H_2O molecules disturb perovskite causing its fading (due to the presence of ammonia and lead iodide formation after H_2O intrusion) (1). It is also assumed that a single molecule of water can cause material degradation. Moisture can decompose the hybrid organic-inorganic perovskite completely, see equation [1] (1).



XRD Measurement of Perovskite Layer

Moisture has significant impact on $\text{CH}_3\text{NH}_3\text{PbX}_3$ perovskite layers. Because of hygroscopic nature of the methylammonium it has a crucial influence during perovskite crystal formation. To examine the effect of moisture on the active part of the perovskite solar cells, two samples were placed in the climate chamber Climacell 111 with set humidity of 60% RH, $\vartheta = 25^\circ\text{C}$ for 48 hours. The active perovskite layer of sample 3-3 was then examined by X-ray diffraction measurement (XRD).

XRD measurements were performed using Rigaku miniflex 600 HR and obtained spectra was analyzed using PDXL software. Measured patterns were normalized to the maximum of the perovskite peak at 14.06° and displayed in logarithmic units for better observation of phases with a minor occurrence. Degradation of perovskite film was studied by XRD and measured diffraction spectra are depicted on Figure 1. Time interval between measurements was 24 hour and in measured patterns we identified three compounds – Indium tin oxide, perovskite structure and gradually increase amount of lead iodide. Prepared perovskite layer exhibit the cubic structure with space group symmetry $221:Pm3m$ that is the typical crystalline structure for the temperatures above 330 K for $\text{CH}_3\text{NH}_3\text{PbI}_3$ (2).

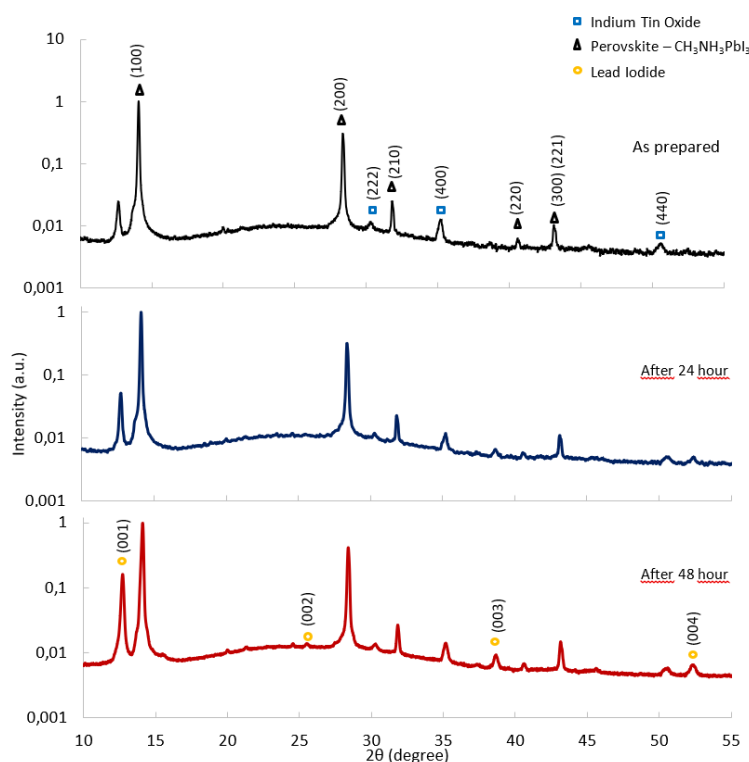


Figure 1. XRD patterns corresponding to the perovskite film during ageing in climatic chamber at 25°C and relative humidity 60 %

Quantitative results of perovskite and lead iodide content during ageing in the climatic chamber is listed in Table 1. Results of Rietveld analysis were done for better illustration how much molecules of perovskite degraded to lead iodide recalculated to the molar percentage. Results revealed that also in the case of as prepared sample the PbI_2 content was under 8 mol%. During the first 24 hour of ageing the perovskite structure loose more than other 5.5 mol% and during other 24 hour even more than 16 mol%. It seems that speed of perovskite degradation to lead iodide increased in time.

TABLE 1. Evolution of perovskite and lead iodide content in perovskite solar cells during ageing

	Prepared	24 hour	48 hour
PbI_2 [mol%]	8.34	14.0	30.3
$\text{CH}_3\text{NH}_3\text{PbI}_3$ [mol%]	91.7	86.0	69.7

Conclusion

XRD analysis confirmed the effect of moisture on the cells produced by decomposing of the perovskite layer with the increasing value of PbI_2 . The PbI_2 value has increased from 8.34 mol% to 30.3 mol% after moisture exposure (60% RH) for 48 hours. Interestingly, despite the declared composition of $\text{CH}_3\text{NH}_3\text{PbI}_{3-x}\text{Cl}_x$ perovskite, the absence of chlorine in the structure was confirmed by measurement. Chlorine during the manufacturing process probably contributes to the growth of perovskite grains without incorporating into the resulting structure.

The rest of the research will focus on other methods recording changes in perovskite active structure such as atomic force of microscopy and energy dispersive X-ray spectroscopy.

Acknowledgments

This research work has been carried out in the Centre for Research and Utilization of Renewable Energy (CVVOZE). Authors gratefully acknowledge financial support from the Ministry of Education, Youth and Sports of the Czech Republic under NPU I program (project No. LO1210) and specific research project No. FCH-S-18-5194. M. Kratochvíl was also supported by the FCH BUT by the Statutory City of Brno through the Brno PhD. talent program.

References

1. G. E. Eperon et al., *ACS Nano*, **9**, 9380-9393 (2015) <http://pubs.acs.org/doi/10.1021/acsnano.5b03626>.
2. K. P. Ong, T. W. Goh, Q. Xu, and A. Huan, *The Journal of Physical Chemistry*, **44**, 11033–11038 (2015) <http://pubs.acs.org/doi/10.1021/acs.jpca.5b09884>.

Perovskite Solar Cells with Increased Resistance to Moisture

D. Strachala^a, M. Kratochvíl^b, J. Hylský^a, A. Gajdoš^b, P. Čudek^a, and J. Vaněk^a

^a Department of Electrical and Electronic Technology, Brno University of Technology, Brno 616 00, Czech Republic

^b Department of Physics, Brno University of Technology, Brno 616 00, Czech Republic

^c Institute of Physical and Applied Chemistry, Brno University of Technology, Brno 612 00, Czech Republic

This article compares two methods of perovskite solar cells manufacturing process due to their resistance against moisture. Two sets of experimental perovskite samples were subjected to the study. Solar cells were exposed to increasing humidity in the climatic chamber. The results have shown that cells manufactured in a 15% relative humidity environment are more resistant to later external environmental influences.

Perovskite Solar Cells

The name was originally assigned to the calcium titanium oxide (CaTiO_3) mineral. The mineral was discovered by Gustav Rose in 1839 and is named after Russian mineralogist Lev Alekseyevich Perovski. All materials with the same crystal structure as CaTiO_3 are called perovskites (1).

Perovskite as an active layer of photovoltaic cells can be classified as hybrid organic - inorganic material. General composition of such solar cell is shown in Figure 1. a), along with the crystal structure in Figure 1. b). The most commonly studied perovskite absorber is methylammonium lead trihalide ($\text{CH}_3\text{NH}_3\text{PbX}_3$, where X is a halogen atom such as iodine, bromine or chlorine) with an optical bandgap between 1.5 and 2.3 eV depending on halide content (1).

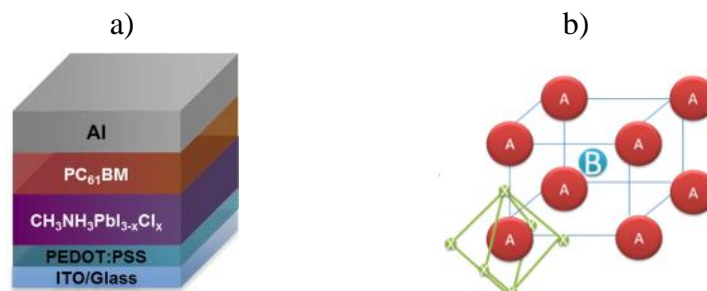


Figure 1. a) A generic composition of the perovskite photovoltaic cell (2): Glass + ITO; Electron Selective Contact – PC_{61}BM ([6,6]-Phenyl C61 butyric acid methyl ester.), Perovskite – $\text{CH}_3\text{NH}_3\text{PbX}_3$, Hole Transporting Layer (PEDOT:PSS (Poly3,4etylenedioxythiophen): polystyrenesulfonate) and metal contact: aluminium or silver b) A generic perovskite crystal structure (2).

The disadvantage of perovskite photovoltaic cells is in the content of lead in its active structure. Lead in its production and disposal increases the toxicity of the environment. Although current research focuses on lead replacements by tin. However, this solar cells do not achieve the properties of the lead structures - especially in the conversion efficiency parameters [6]. The main

problem of perovskite photovoltaic cells is their stability. The lifetime of silicon solar cells is between 20 and 30 years. The lifetime of perovskite solar cells is about a couple of months, especially due moisture influences.

Perovskite Solar Cells with Increased Resistance to Moisture

In order to analyze the effects causing degradation of perovskite photovoltaic cells, it was necessary to create the appropriate reference samples. Two series of perovskite solar cells were manufactured with the inverse planar structure ITO/PEDOT:PSS/CH₃NH₃PbI_{3-x}Cl_x/PC₆₁BM/Al.

The production of photovoltaic cell series differed in the environment in which they were manufactured. In the first series, nine samples were made in a glovebox with a nitrogen atmosphere with minimum moisture content. In the second series, six solar cells were made in a glove box filled with air. In this case, the humidity was controlled at 15% of relative humidity value (RH).

Perovskite photovoltaic cells of the first series had significantly better output parameters than the samples from series 2. To monitor their moisture resistance, samples from both series were stored for the same time in the climate chamber Climacell 111 in a pair of one cell of the first series and one from the second series. Their current voltage characteristic were measured after 24 hour interval with increasing relative humidity and constant temperature of 25 °C, see Figure 2. For simplicity, there are shown current-voltage characteristic of sample 2 of the first series and sample 4 of the second series. Other samples had similar characteristics, but they are not listed here for limited space.

The first series solar cells had a significant drop in performance after the relative humidity in the chamber has exceeded 50 % RH. When was the relative humidity higher than 55% RH, the parameters of the short-circuit current I_{SC} have been significantly reduced. At 70% RH, the open circuit voltage dropped, and the cells became almost inactive. From the results it can be concluded that perovskite cells produced in the first series are able to maintain their resistance against moisture only up to 50% RH.

Despite the significantly worse parameters visible from the current-voltage characteristics are solar cells from the second series more resistant against external moisture degradation. Above the 50% RH limit, they lost their performance, but not on such a scale as the former cells. The manufacturing process using 15% relative humidity has therefore proved to be more advantageous for perovskite solar cells.

The explanation may be that the perovskite structure produced in the 15% RH environment are more uniform with a smaller number of grain boundaries. Thus, water molecules are getting harder through the grain boundaries and do not interfere with the perovskite crystals.

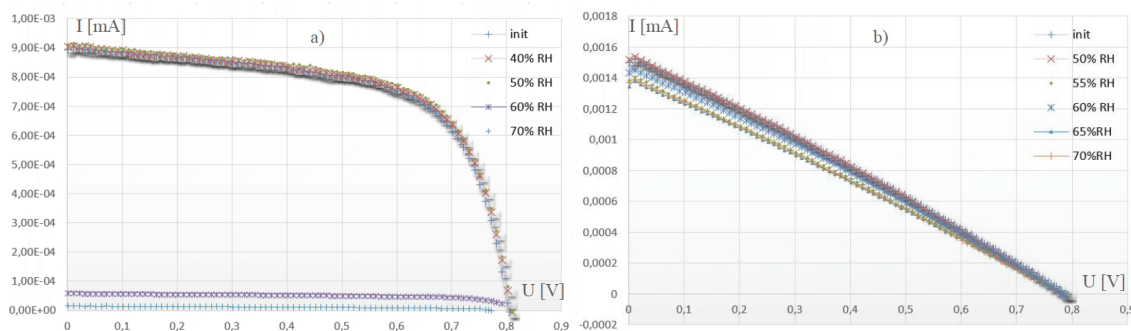


Figure 2. Current-voltage characteristics of a) sample 2_1 and b) sample 4_2

Conclusion

To investigate the stability of the perovskite cells, in particular against moisture as the most frequent degradation mechanism, two series of perovskite solar cells with $\text{CH}_3\text{NH}_3\text{PbI}_{3-x}\text{Cl}_x$ active layer were made. The first series of 9 samples was produced in the glovebox with an inert atmosphere. The second series with 6 cells, on the contrary, in the glove box with air environment with 15% RH.

The main finding of the research is that the perovskite cells from the second series, despite the worse output parameters, showed higher resistance against moisture. A low moisture presence during the perovskite solar cell production process probably contribute to increased resistance against later degradation effects of water molecules.

The follow-up research will deal with the modification of the manufacturing process of samples in order to reach the values of the first series and also will continue with observing the effects of moisture as an element of increased structural stability.

Acknowledgments

This research work has been carried out in the Centre for Research and Utilization of Renewable Energy (CVVOZE). Authors gratefully acknowledge financial support from the Ministry of Education, Youth and Sports of the Czech Republic under NPU I program (project No. LO1210) and specific research project No. FCH-S-18-5194. M. Kratochvíl was also supported by the FCH BUT by the Statutory City of Brno through the Brno PhD. talent program.

References

1. Ossila (2016) <https://www.ossila.com/pages/perovskites-and-perovskite-solar-cells-an-introduction>.
2. H. Dong et al., *Chemical Communication*, **43**, 8986-8989 (2015) <http://xlink.rsc.org/?DOI=C5CC01483B>.

An innovative power supply system dedicate for Roadheading mining machines

B. Polnik

Roadheading machines are commonly used in Polish coal mining, for works related to proper maintenance of the false floor in the corridor excavations. These are self-running machines on a tracked electro-hydraulic drive chassis. During drilling, a hydraulic pump driven by an electric motor, powered by a drop-down cable connected to the mine power network. The disadvantage of this solution is the limited mobility and exposure of the cable to the mechanical damage. In connection with the above, work was undertaken to develop a drive system powered by battery cells. This work was undertaken at the KOMAG Institute of Mining Technology, in cooperation with the mining machinery manufacturer HYDROTECH S.A.

This paper presents the results of research on the energy consumption of the Roadheading machine, based on which the technical and technological assumptions of the innovative solution were specified. The results of laboratory tests on the safe use of selected lithium cells are also presented together with stand tests of the innovative power supply system. All of the work was concluded with the prospects for the development of mining drives for small mechanization machines in the perspective of the coming years.

Energy consumption.

Energy consumption is one of the fundamental problems faced by engineers and users of mining machinery. Reducing energy consumption while increasing operational safety is the main task of constructors at the stage of developing new assumptions and modernizing existing machines. To this end, identification was made in the scope of electricity consumption of the Roadheading machine (fig. 1).



Figure 1. BH 3000 Roadheading machine

The measurements were made on a three-phase outflow of mine contactor switch type OW-0208M, supplying directly to the Roadheading machine. The voltage (U), current (I) and power (P) waveforms were recorded. The measurements were carried out at the rated pressure in the hydraulic

system and for the increased pressure up to the value simulating the operation at the maximum load. Table 1 presents the results of electrical parameters recorded during the tests.

Table 1. *Energy consumptions results.*

Operation conditions	I	P	Time
	A	kW	hh:mm:ss
Rated pressure	37	30	01:24:15
Maximum pressure	71	4	00:08:01

Based on the experience of designing machines equipped with their own power source, and based on the information obtained from the manufacturer regarding the work pattern performed by the working Roadheading machines in mines, it was assumed that for a machine powered by battery cells, the energy value should be 75kWh, which will allow the machine to work during one work shift.

Stand tests of the innovative power supply system.

The LiFePO₄ cell tests included:

- measurements of voltage, current and temperature during the 20 Ah cell discharge process,
- measurement of current and temperature during a short-circuit test of 20 Ah,
- measurement of voltage, current, temperature and gas emissions during the 20 Ah cells overcharge test to the state of destruction.
- The aim of the research was:
- determination of the chemical composition of cell, as it is to be expected that the cell will leak and the gases will escape in case of a longer lasting emergency condition.
- checking the behavior of the cells in emergency conditions such as short-circuiting on the terminals, overcharging and deep discharge.

Figure 2 shows the time waveforms of voltage, current and temperature recorded during the attempt to discharge the LiFePO₄ cell. Figure 3 shows the cell view after short circuit on the terminals.

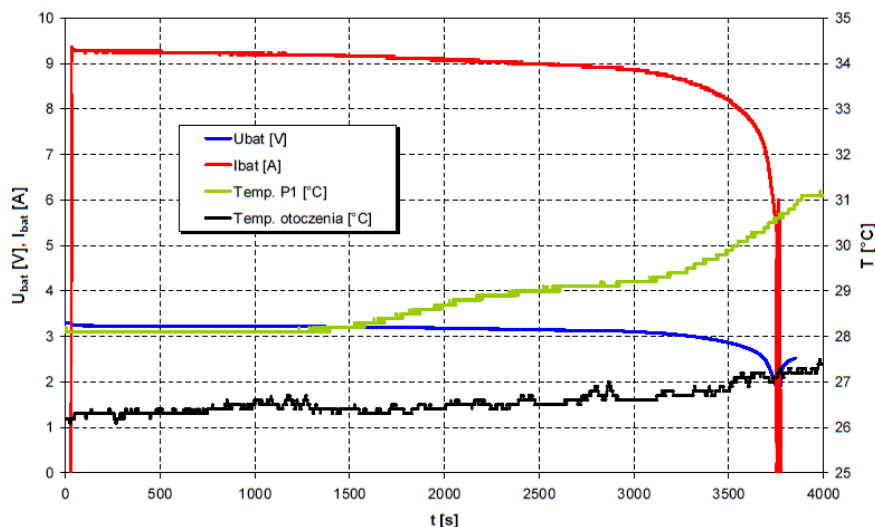


Figure 2. Time waveforms of voltage, current and temperature recorded during the attempt to discharge the LiFePO_4 cell



Figure 3. Cell view after short circuit on the terminals

The test results of LiFePO_4 cells with a capacity of 20 Ah in terms of their resistance to deep discharge, short-circuits on the terminals and overcharging, allow the following statement:

1. Cells subjected to deep discharge do not cause side effects affecting explosion safety and do not pose a threat to the service and service. They can only affect the cell's service life.
2. A short circuit directly at the terminals of the cell is not a hazard. The short-circuit current causes one pole of the cell to be burned or lasts for a period of 10s, after which the current decreases, and the temperature reaches a maximum value of 88 °
3. During the conducted tests, no open fire or explosion occurred.
4. Laboratory tests of lithium-iron-phosphate cells confirmed the possibility of their safe use in potentially methane explosive atmospheres and coal dust.

The developed and made model of the innovative power-supply module after combining in the ITG KOMAG station (fig. 4) has been subjected to functional correctness tests. During the tests, the correct operation of the battery charging and discharging module as well as the control and safety system was checked. As a result of the tests, no irregularities were found. Current when charging cell batteries it is 30A, this allows you to charge the battery in about 3 hours, which is the

fulfillment of the technical and technological assumptions. In addition, the cooling system used allows the continuous operation of the charging module without interrupting the work. The combined control and safety system works properly, and consequently every irregularity was created in the power module model it is detected and blocked by the developed security system.



Figure 4. Innovative power-supply module during the tests

Summary

The results of research on the electric energy demand of the selected stoker were presented, on the basis of which the amount of energy (75 kWh) to be determined by the cell battery intended for feeding the new power supply and control system of the mining Roadheading machine was determined. The concept of an innovative power supply and control system of the new machine is described, focusing on the main elements of electrical equipment: power source - inverter - control system. The conducted research on the possibilities of safe use of LiFePO_4 cells and the correct functioning of the innovative power module were discussed. Introduction of electro mobility elements in the underground mines is in line with the adopted direction of zero-emission drives development.

Static pressure measurement within a flow measurement and mapping chamber

R. Bayer^a

^a Department of Electrical and Electronic Technology, Brno University of Technology, Technická 10, 616 00 Brno, Czech Republic

Abstract

Within a flow measurement and mapping chamber there is an extreme static pressure stability required to maintain static environmental conditions around the main center axis where all dynamic measurements and mapping take place. To be able to achieve such accurate pressure control a very accurate pressure measurement is required. This article aims at the use of a strain gauge for precise static pressure measurement within a flow measurement and mapping chamber.

Introduction

Because of a high pressure difference between the gas flow at the flow measurement chamber input (2 kPa) and its main chamber (30 Pa) and because of maintaining the accuracy of the measurement it is crucial to measure the pressure within the chamber as much precisely as possible. One of the most precise way to measure a pressure is using a strain gauge.

A strain gauge is a device that most commonly consists of a supporting insulating foil with a thin conductive foil with a fine zig-zag or double comb-like pattern as seen on Figure 1. The strain gauge is attached to a measured object using an adhesive with great shape stability, such as cyanoacrylate. As the measured object deforms the cross-section and length of the conductive pattern changes thus its resistance changes based on the extent and direction of the deformation the object under the strain gauge.

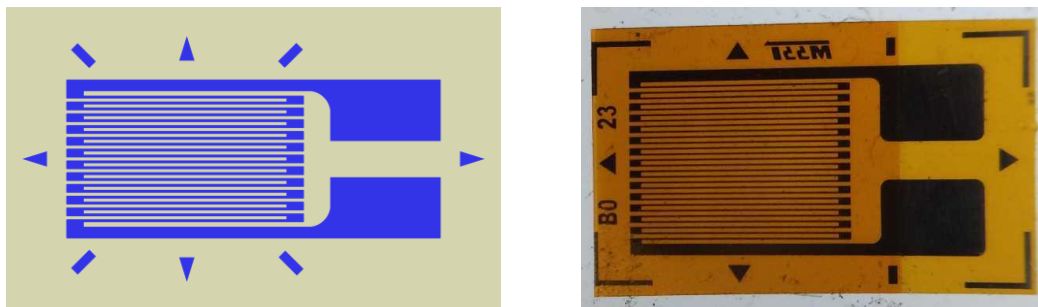


Figure 1. Strain gauge with zig-zag (left) and comb-like (right) pattern

The flow measurement chamber is a low-pressurized chamber designed for supersonic shockwave analysis. Figure 2 shows the chamber that has a cylinder shape with flat inner plate. In the center of the plate there is an inlet nozzle above which a supersonic gas flow forms a shockwave.

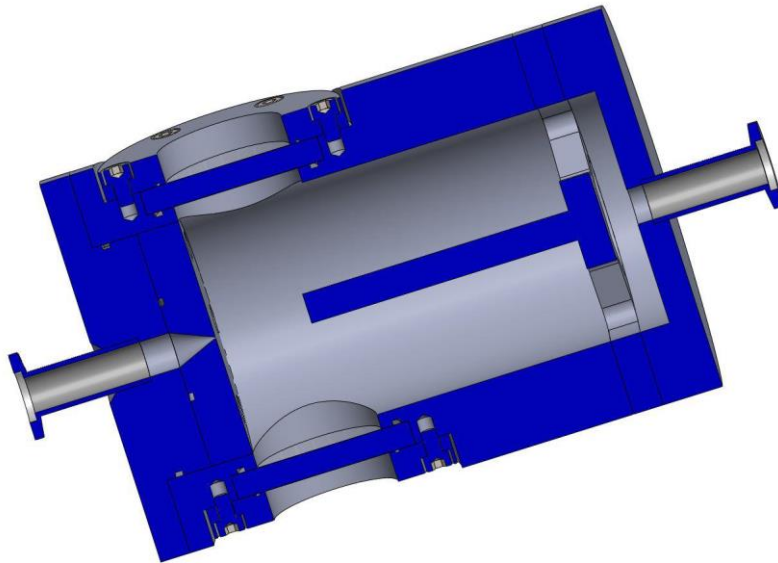


Figure 2. Simplified design of the flow measurement chamber

Next to the inlet nozzle there is a shaft leading under the bottom plate and into the gas inlet of the chamber at at which end a thin steel membrane is attached carrying a strain gauge.

The thickness of the membrane depends on the material used, its diameter, pressure difference between both sides of it and the maximum prolongation the strain gauge can withstand. For example when using steel membrane with 20 mm diameter, pressure difference 2 kPa and strain gauge with maximum prolongation of 2,5 % (meaning 25 μm per 10 mm long strain gauge) the thickness of the membrane is calculated to 0,3 mm.

Results and discussions

Figure 3 shows the results of a structural deformation simulation of the steel membrane. It is the maximum deformation calculated for the strain gauge that will be used.

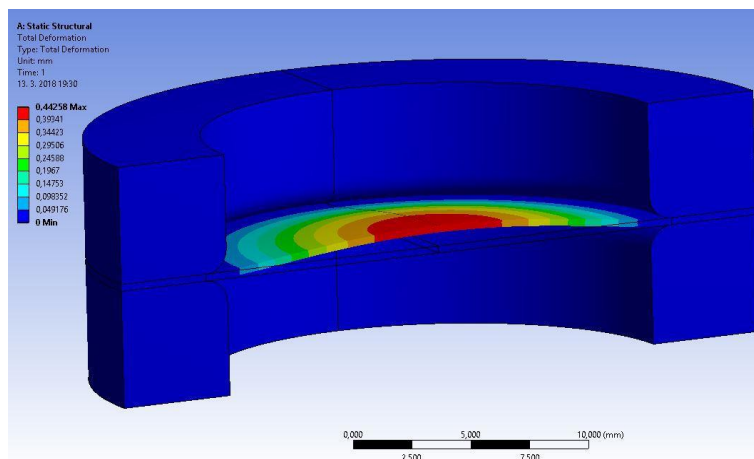


Figure 3. Steel membrane deformation calculation results

Using a strain gauge on a steel membrane as a pressure measuring tool can show us precisely how much and at what distance deflected shockwaves affect the pressure measurement on low-pressurized closed areas.

Acknowledgments

This research has been carried out in the Centre for Research and Utilization of Renewable Energy (CVVOZE). Authors gratefully acknowledge the financial support from the Ministry of Education, Youth and Sports of the Czech Republic under NPU I programme (project No. LO1210) and BUT specific research programme (project No. FEKT-S-17-4595).

References

1. Vyroubal, P. ; Maxa, J. ; Neděla, Vilém ; Jiráček, Josef ; Hladká, K. *Apertures with Laval Nozzle and Circular Orifice in Secondary Electron Detector for Environmental Scanning Electron Microscope*. Advances in Military Technology. 2013, roč. 8, č. 1, s. 59-69. ISSN 1802-2308.
2. Maxa, J. ; Neděla, Vilém. *The Impact of Critical Flow on the Primary Electron Beam Passage through Differentially Pumped Chamber*. Advances in Military Technology. 2011, roč. 6, č. 1, s. 39-46. ISSN 1802-2308.
3. Maxa, J. ; Neděla, Vilém ; Jiráček, Josef. ; Vyroubal, P. ; Hladká, K. *Analysis of gas flow in a secondary electron scintillation detector for ESEM with a new system of pressure limiting apertures*. Advances in Military Technology. 2012, roč. 7, č. 2, s. 39-44. ISSN 1802-2308.
4. Neděla, Vilém; Tihlaříková, Eva; Runštuk, Jiří; Hudec, Jiří. *High-efficiency detector of secondary and backscattered electrons for low-dose imaging in the ESEM*, Ultramicroscopy. 2018, 184, s. 1-11. ISSN 0304-3991, doi:10.1016/j.ultramic.2017.08.003.
5. Neděla, Vilém ; Konvalina, Ivo ; Oral, Martin ; Hudec, Jiří. *The Simulation of Energy Distribution of Electrons Detected by Segmental Ionization Detector in High Pressure Conditions of ESEM*. Microscopy and Microanalysis, 21 (Suppl. 4) , s. 264-269. doi:10.1017/S1431927615013483.
6. Neděla, Vilém ; Hříb, J. ; Havel, L. ; Hudec, Jiří ; Runštuk, Jiří. *Imaging of Norway spruce early somatic embryos with the ESEM, Cryo-SEM and laser scanning microscope*. Micron. 2016, č. 84, s. 67-71. ISSN 0968-4328.

Analysis of the Impact of the Baffle Placement in the Supersonic Flow in the Differentially Pumped Chamber

M. Bílek^a, P. Hlavatá^a, J. Maxa^a,

^a Dept. of Electrotechnology The Faculty of Electrical Engineering and Communication, University of Technology, Technická 3058/10, 616 00 Brno, Czech Republic

The thesis follows to the work of G.D. Danilatos occupy Differential Pumping System with fast stopper focusing on dew design for environmental scanning electron microscope [1]. Thesis concern divider located in the chamber differential pumping and its influence on the nature of the flow. Simulation of individual variants was evaluated using the program Ansys Fluent [2, 3], which calculates with the method final volumes as opposed to calculations performed by G. D. Danilatos which uses the statistical method Monte Carlo.

Ejector Assisted Differential Pumping

Upper part PLA1 near the edge aperture creates a low point (low area) pressure, causing the nozzle, which works as a diffusion pump and carries molecules from the vicinity of the low-pressure area [4, 5]. Redirecting the nozzle flow with use divider it is possible pumping activity stream to create by area with low density at the entrance PLA2. On Fig. 1 [1] is shown field flow with cone PLA2 near the optimal position $a=2,6\text{mm}$, including divider of defector, which is introduced with the tip in the distance $z=1,4\text{mm}$.

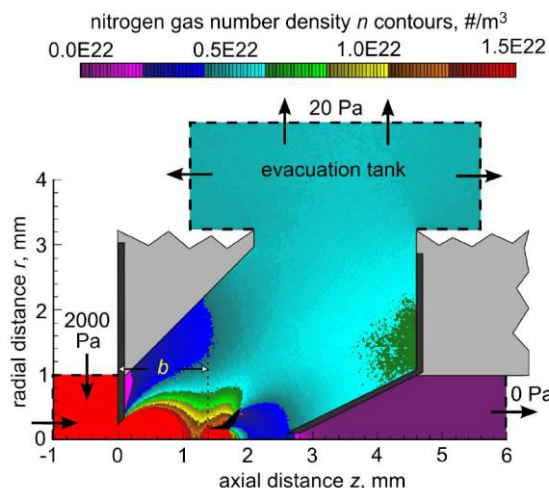


Figure 1. Optimum flow field with conical geometry and divider (system EAPD) [1]

Evaluated variants

In this work, three different variants have been proposed:

- Divider without displacement with larger diameter
- Shifted divider with the original diameter
- Shifted divider with larger diameter

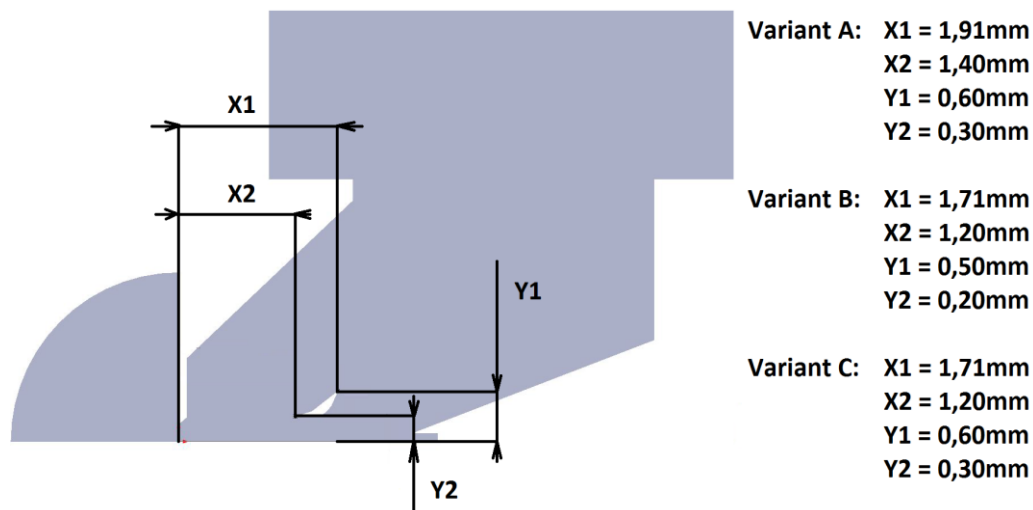


Figure 2. Dimensions of the divider for different variants

Results

It was evaluated four quantity Output – mass flow pumping own differential chamber, which characterizes the quality of regulation flow but on the scattering of the primary beam has a secondary effect Fig.3

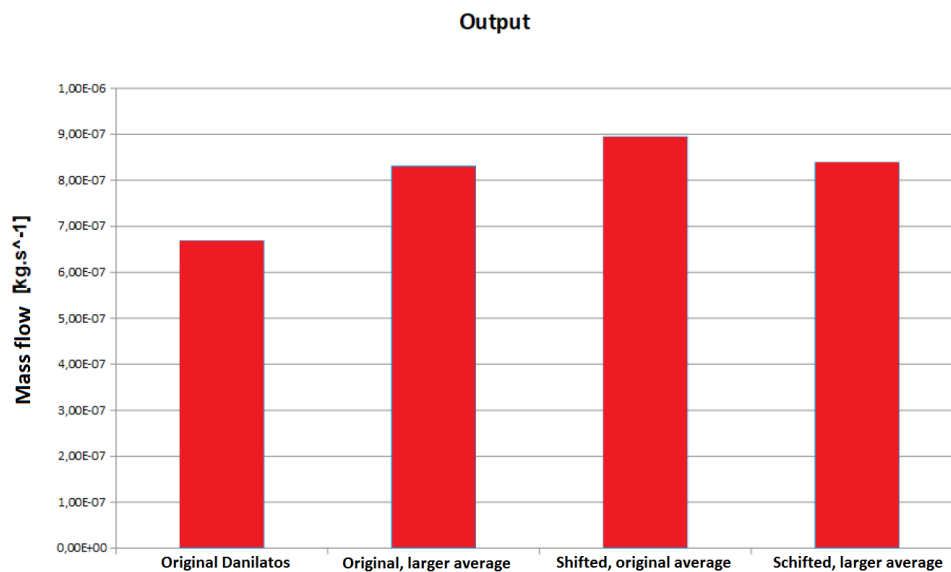


Figure 3. Comparison of the size variants of the divider and their mass flow at the output.

Tubus – mass flow characterizing the amount of flowing gas through the aperture PLA2 to the column. It has a big effect on scattering primary beam still in column above the aperture PLA 2.

Comparison of all variants of mass flow in the column is show on Fig.4.

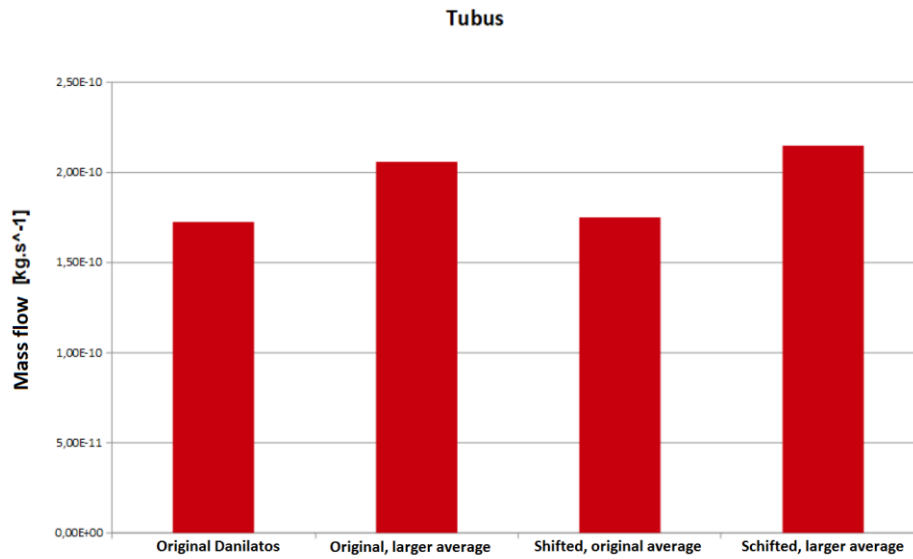


Figure 4. Comparison of size variants of the divider and their mass flows in the column

Average pressure – Average pressure on the line primary beam. It is fact, that more higher average pressure the more higher probability of collision flying electron with gas molecules in a differential pumped chamber. Graphic dependence of average of average pressures for individual size variants of the divider is shown on Fig. 5.

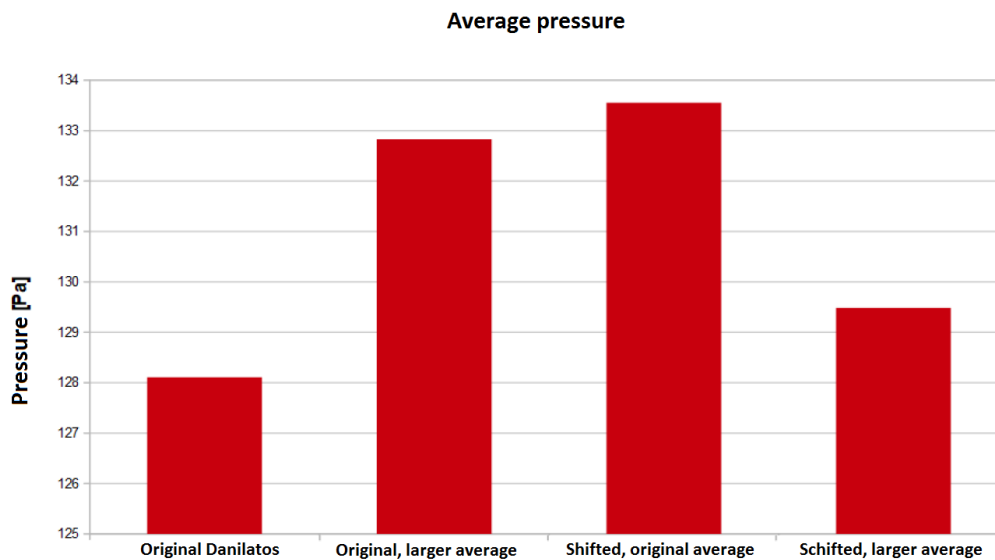


Figure 5. Comparison of size variants of the divider and their average pressure

Probability of scattering – according to the literature is electron scattering is proportional to the multiple pressure and distance which in this pressure the electron fly through [6, 7]. Due to the strong initial pressure dependence $p(x)$ to distances (coordinates x) from PLA 1 best describes the situation integral [8, 9]:

$$Pd = \int_{0=PLA1}^d p(x) dx \quad (2)$$

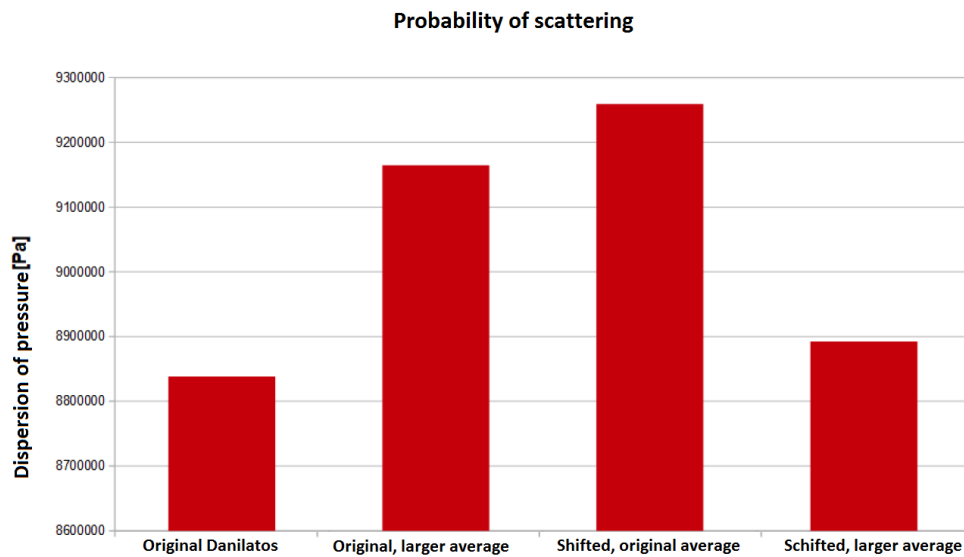


Figure 6. Comparison of size variants of the divider and their probability of scattering

Conclusions

The results show that the shift and change of the diameter divider has a significant effect on three basic variables affecting the primary beam scattering. It is average pressure on the path primary beam, dependence of the scattering on the own path and mass flow of gas passing through the aperture PLA2. The best results are presented by original variant where all comparisons variables are the lowest. Also variant with a shift and larger diameter is worth considering which average pressure and scattering on the path primary beam don't have much larger than the original variant. But the fact that it is a aperture with larger diameter this aperture represents a smaller obstacle passing electrons. The worst is that the larger average in divider causes a worsening mass flow indicator to aperture PLA 2.

Acknowledgments

This research has been carried out in the Centre for Research and Utilization of Renewable Energy (CVVOZE). Authors gratefully acknowledge the financial support from the Ministry of Education, Youth and Sports of the Czech Republic under NPU I programme (project No. LO1210) and BUT specific research programme (project No. FEKT-S-14-2293).

References

1. GD. Danilatos, Velocity and ejector-jet assisted differential pumping: Novel design stages for environmental SEM., Micron, 2012, vol. 43, no. 5, p. 600-611.
2. J. Maxa; M. Bílek; P. Hlavatá; P. Vyroubal and K. Lepřtová, Comparisons Using Methods of Continuum Mechanics and Monte Carlo at Differentially Pumped Chamber. Advances in Military Technology, vol. 11, no. 2, p. 143-150. ISSN: 1802-2308. (2016).
3. P. Vyroubal; J. Maxa; V. Neděla; J. Jiráček and K. Hladká, Apertures with Laval Nozzle and Circular Orifice in Secondary Electron Detector for Environmental Scanning Electron Microscope, Advances in Military Technology, vol. 8, no. 1, p. 59-69, (2013).

4. J. Maxa and V. Neděla, The Impact of Critical Flow on the Primary Electron Beam Passage through Differentially Pumped Chamber. *Advances in Military Technology*, , vol. 6, no. 1, p. 39-46. ISSN 1802-2308, (2011).
5. J. Maxa; V. Neděla; J. Jiráček; P. Vyroubal and K. Hladká, Analysis of gas flow in a secondary electron scintillation detector for ESEM with a new system of pressure limiting apertures. *Advances in Military Technology*, vol. 7, no.2, p.39-44, (2012).
6. V. Neděla; E. Tihlaříková; J. Runštuk; J. Hudec, High-efficiency detector of secondary and backscattered electrons for low-dose imaging in the ESEM. *Ultramicroscopy*, p. 1-11. ISSN 0304-3991, (2018).
7. V. Neděla; I. Konvalina; M. Oral; J. Hudec. The Simulation of Energy Distribution of Electrons Detected by Segmental Ionization Detector in High Pressure Conditions of ESEM. *Microscopy and Microanalysis*, p. 264-269.
8. Neděla, V. Controlled dehydration of a biological sample using an alternative form of environmental SEM. *Journal of Microscopy*. 2010, 237 (1), p. 7-11. ISSN 0022-2720.
9. V. Neděla; J. Hříb; L. Havel; J. Hudec and J. Runštuk, Imaging of Norway spruce early somatic embryos with the ESEM, Cryo-SEM and laser scanning microscope. *Micron*, no. 84, p. 67-71. ISSN 0968-4328, (2016).
10. M. Daněk, *Aerodynamika a mechanika letu*, p. 83, VVLŠ SNP, Košice (1990).

High-Frequency Model of Alkaline Battery in Form of Transfer Function

R. Cipin, M. Toman, P. Prochazka, and I. Pazdera

Department of Power Electrical and Electronic Engineering, Brno University of Technology, Brno,
Technicka 12 6161 00, Czech Republic

This paper deals with a measurement of alkaline battery impedance in wide-range frequency from about one Hz to a few hundred kHz. Measured battery admittance is used for the construction of battery transfer function, i.e., the dependence of admittance on frequency. Comparison of transfer functions for different battery types (alkaline and Li-ion) is shown. And it is shown that transfer functions for both types have the same form.

Introduction

For battery characteristic description, equivalent circuits consisted of combinations of resistances (R) and capacitances (C) are usually used, see [1]. Generally, any battery is a highly nonlinear system and description of its properties with only constant parameters R and C is somehow misleading. For this reason, it is used for battery description a transfer function (TF) for battery admittance.

Battery admittance Y can be very simply calculated from voltage V applied to battery with given angular frequency ω , measured battery current I , and measured phase shift between voltage and current φ .

$$Y(\omega) = \frac{I}{V} e^{-j\varphi}, \quad (1)$$

where j is imaginary unit.

Construction of Admittance Transfer Function

Any transfer function of arbitrary linear or nonlinear system, see Figure 1, can be basically decomposed into elementary transfer functions of two types, see Figure 2.

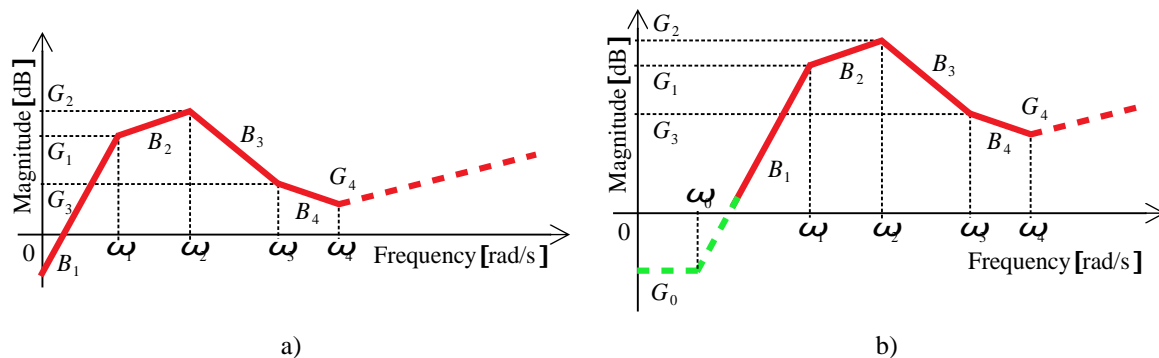


Figure 1. Asymptotic magnitude Bode plots for arbitrary transfer functions.

The first elementary transfer function with a unit gain has a form

$$F(s) = s^q, \quad (2)$$

where s is dummy variable of Laplace transform and q is arbitrary real number ($q \in \mathbf{R}$). For a system consisting only of resistances and capacitances, the number q can only be an integer ($q = \pm 1, \pm 2, \dots$).

The second elementary transfer function with a unit gain has a form

$$F(s) = \frac{(s + \omega)^q}{\omega^q}, \quad (3)$$

where ω is arbitrary angular frequency ($\omega > 0$).

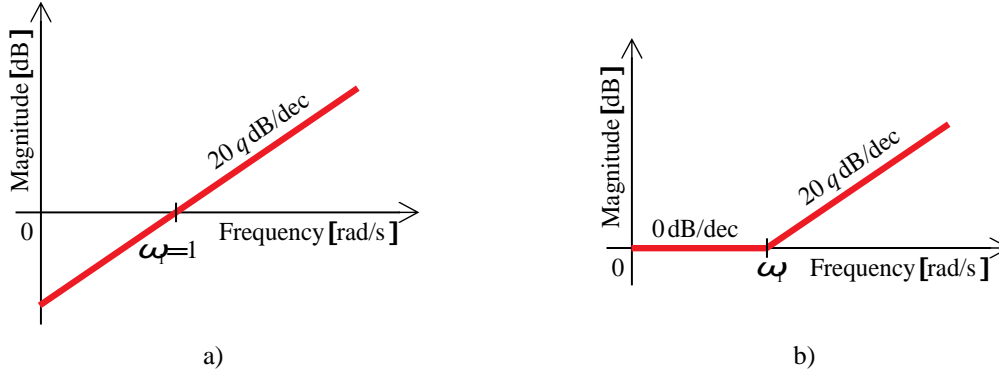


Figure 2. Asymptotic magnitude Bode plots for elementary transfer functions.

Arbitrary TF shown in Figure 1 a) constructed with help of (2) and (3) has a form

$$F(s) = G s^{q_1} \prod_{i=2,3,K} \frac{(s + \omega_i)^{q_i}}{\omega_i^{q_i}}, \quad (4)$$

where G is gain of TF and subscript i stands for position of given variable, see Figure 1.

For a mathematical description of any TF it is important a knowledge of the precise position of ω_i cutoff frequencies and G_i gains at those frequencies. Another, equally important variable is a slope B_i , which can be calculated from known frequencies and gains as follows

$$B_i = \frac{G_i - G_{i-1}}{\log_{10} \omega_i - \log_{10} \omega_{i-1}}. \quad (5)$$

There is important to note that slope B_i can be also calculated from any points on the asymptotic curve not only from edge points.

The individual unknown variables G and q_i in (4) can be very simple calculated from variables ω_i , G_i , and B_i as follows:

- number q_1 $q_1 = \frac{B_1}{20}, \quad (6)$

- gain $G = \frac{10^{\frac{G_1}{20}}}{\omega_1^{q_1}}, \quad (7)$

- number q_i for $i = 2, 3, \dots$ $q_i = \frac{B_i - B_{i-1}}{20}. \quad (8)$

Results of Measurements

Figure 3 shows measured and calculated Bode plot for alkaline battery (Westinghouse Dynamo Alkaline AA batteries Zn/MnO₂). The figure shows a very good agreement between measured and calculated values of battery admittance. The used TF (4) is only the third-order.

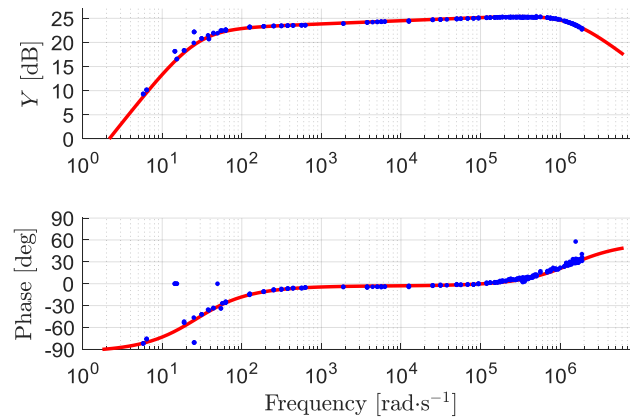


Figure 3. Measured (blue dots) and calculated Bode plot for alkaline battery.

The Table I. shows a comparison of slopes and cutoff frequencies for alkaline and Li-ion battery (Panasonic NCR18650A). From individual values, both battery types can be approximated using the same third-order transfer function.

TABLE I. Calculated slopes and cutoff frequencies for different batteries.

Parameters	[dB]	[dB/dec]			[rad/s]	
	G	B_1	B_2	B_3	ω_1	ω_2
Alkaline battery	0.450	20.86	0.66	-12.75	26.7	1400000
Li-ion battery	0.965	20.59	1.64	-13.64	22.0	4342

Conclusions

The paper deals with a construction of admittance transfer function for the alkaline battery. The battery admittance is calculated from measured values of voltages and currents. A simple way how to get individual parameters for mathematical construction of the transfer function is introduced. Presented theory is applied to alkaline and Li-ion battery.

Acknowledgments

This research work has been carried out in the Centre for Research and Utilization of Renewable Energy (CVVOZE). Authors gratefully acknowledge financial support from the Ministry of Education, Youth and Sports of the Czech Republic under NPU I programme (project No. LO1210).

References

1. X. Zhang, W. Zhang, and G. Lei, *Transactions on Electrical and Electronic Materials*, **17** (6), 2307 (2016). DOI: 10.4313/TEEM.2016.17.6.311.

Change of surface texture parameters of grinded surfaces after application of hard and abrasion resistant layers

D. Dobrocký^a, Z. Pokorný^a, Z. Studený^a

^a Department of Mechanical Engineering, University of Defence in Brno, Kounicova 65, 602 00 Brno, Czech Republic

Continuous technology development builds to the foreground the solution of the quantification of roughness, respectively the surface texture. The surface roughness of the functional surfaces affects the durability and the reliability of the components. The surface roughness has an impact on the accuracy of machine parts running, noise, run-in time, friction loss, electrical resistance, heat transfer, fatigue strength, wear resistance and corrosion resistance (1). Grinding has still the largest share in finishing methods of functional surfaces not only in engineering, but is also used in electrical engineering. At present, the trend is to increase the functional properties of functional surfaces by applying coatings and layers. This is also related to the change in surface texture parameters, which is caused by the creation of a new surface on the original machined surface. The paper deals with the change of selected 3D parameters of the surface texture of grinded steels after application of diffusion technologies. The steel CSN 41 2050 and 34CrNiMo6 after nitriding and ferritic nitrocarburizing in gas and plasma were evaluated. Selected 3D surface texture parameters were measured by the coherence correlation interferometer Talysurf CCI Lite. The change in surface texture parameters is influenced by the preparation of the substrate, i.e. the grinding parameters and the used diffusion technology, as well as the chemical composition of the used steels (2). The steels were grinded with SiC abrasive papers with grain sizes of 120, 220, 600 and 1000 according to FEPA. Steel CSN 41 2050 showed the reduction of the observed surface texture parameters almost all types of surface treatments - roughness decreased. Only in the case of ferritic nitrocarburizing in gas occurred to the deterioration of surface roughness. Similar results were achieved at 34CrNiMo6 steel - ferritic nitrocarburizing in gas led to an increase of surface roughness. For other surface treatments the roughness decreased. Applied diffusion technologies increase the hardness of functional surfaces, corrosion resistance, fatigue strength, wear resistance and reduce coefficient of friction (3). The above-mentioned advantages of applied diffusion layers along with the reduction in surface roughness can contribute to wider use of these technologies in technical practice.

Corrosion Resistance of High Temperature Plasma Nitrided X12CrMoWVNbN10-1-1 martensitic stainless steel

P. Faltejsek, D. Kusmič^a

^a University of Defence, Department of Mechanical Engineering, Brno, Czech Republic, EU

The X12CrMoWVNbN10-1-1 martensitic stainless steel was subjected to plasma nitriding at an increased temperature of 550 °C for 15 h and compared to untreated one. The microstructure and microhardness of the untreated and nitrided stainless steel were evaluated. The corrosion properties of the untreated and plasma nitrided steel samples were evaluated using the anodic polarization tests in neutral 2.5% NaCl deaerated solution. The results showed that plasma nitriding process on the X12CrMoWVNbN10-1-1 stainless steel produced a nitride layer consisting of compound layer and a nitrogen rich diffusion layer. Plasma nitriding process significantly increased the surface hardness of the martensitic stainless steel but also decreased the corrosion resistance of the X12CrMoWVNbN10-1-1 stainless steel. The pitting was evaluated, and the pitting coefficient was calculated. During electrochemical corrosion tests, the nitrided steel showed lower (more negative) corrosion potentials, higher current densities and greatly increased corrosion rates and pitting.

Introduction

Plasma nitriding (ion nitriding) process is chemical-heat treatment process, usually between temperature 450 ÷ 550 °C, used to improve the mechanical properties of construction steels such as surface hardness, tribological properties and fatigue strength [1, 2], Nevertheless, the notch toughness is reduced [3].

In the case of construction steels, increase of corrosion resistance may occur under certain conditions [4]. But the corrosion resistance of nitrided stainless steels is directly dependent on the nitriding process parameters like duration, nitriding atmosphere composition and the process temperature. The authors state that the corrosion resistance of stainless steels is reduced at a plasma nitridation temperature above 450 °C [5], 460 °C for AISI 304 stainless steel [6], 475 °C [7] and 480 °C [8, 9]. Above this temperature occurs of iron and chromium nitrides precipitation (CrN) [8].

With increased temperature of plasma nitriding process the iron nitrides appeared in nitride layer. At temperature of 500 °C the nitride layer consists of CrN, Fe₃N and Fe₄N phases for AISI 304 steel and the pitting was observed. For samples nitrided below temperature of 450 °C no pits were observed [6].

Experimental and Results

Martensitic Stainless steel X12CrMoWVNbN10-1-1 (EN 10204/3.1) was studied in this paper. Following chemical composition (in wt.%): 0.1 C, 0.11 Si, 0.46 Mn, 0.009 P, 0.007 S, 10.60 Cr, 0.83 Ni, 1.03 Mo, 0.2 V, 0.08 Cu, 0.95 W, 0.008 Al, 0.05 Nb, 0.043 N₂, 0.009 As, 0.003 Sb and 0.007 Sn comes from inspection certificate. Blocks of steel were hardened (1080°C/2h/oil), tempered

(740°C/4h/air), stress-free annealed (700°C/3h/air) to $241 \div 255$ HBW5, J factor 91.2. Blocks of steel were cut into samples with diameter of 13 mm and approximately 1 cm thickness, finally grinded to $R_a = 0,4\mu\text{m}$ and degreased in ethanol prior plasma nitriding process and before every measurements. Prepared samples were subjected to plasma nitriding under nitriding atmosphere $3\text{H}_2:1\text{N}_2$ (l/h) gas ratio for 15 hours, in 550°C in the RUBIG PN 60/60 device.

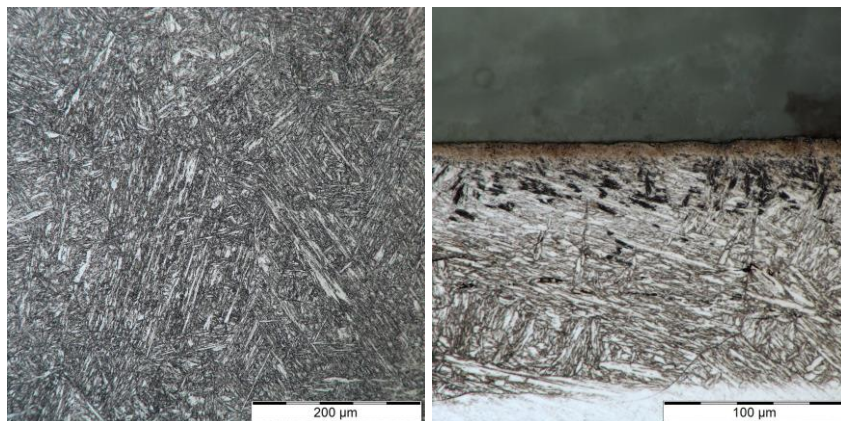


Figure 1. a, b) Microstructure of untreated and plasma nitrided steel with visible compound and diffusion layer (5% Nital)

Samples were studied by optical microscopy, see Figure 1. After plasma nitriding the surface hardness increased to 1124 HV, from original value of 295 HV. Thanks to etching by 5% Nital is the diffusion layer visible, as well the porosity of 8,96 μm thick compound layer is evident. The whole depth of case layer reached 0,191 mm (evaluated by microhardness measuring using LECO LM247 AT, DIN 50190).

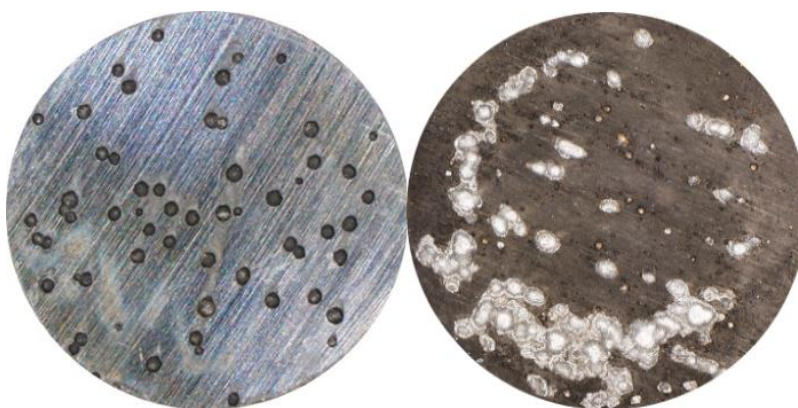


Figure 2. Pitting on the X12CrMoWVNbN10-1-1 steel after potentiodynamic tests (a) untreated, (b) plasma nitride

Plasma nitrided steel surfaces were documented by the optical microscopy (OLYMPUS DSX 100) before and after potentiodynamic electrochemical tests (Figure 2). After potentiodynamic tests pitting was evaluated using the laser confocal microscopy (OLYMPUS OLS 3000) and the pitting factor (PF) was calculated according to ISO 11463 standard, as ratio of deepest penetration to the average of 10 measured penetrations. For plasma nitrided steel sample was PF 1.222 and for untreated sample 1.27. Additionally, width and depth of pits was measured. For plasma nitrided sample average of width of pits was 693.5 μm and for untreated sample 340 μm .

On the untreated and plasma nitrided steels electrochemical tests were carried out using the Biologic SP 150 and software EC-Lab V11.10. As measuring technique was chosen Cyclic

Potentiodynamic Polarization (ASTM-61) with following parameters: $dE/dt = 0,166$ mV/s, $E_i = -0.25$ V, $E_L = 2$ V, $I_p = 25$ mA, E range (-2 V; 2 V). Measured surface of steel sample was 0.865 cm². Samples were exposed to deaerated 2.5% NaCl solution. Potentiodynamic curves of untreated and plasma nitrided X12CrMoWVNbN10-1-1 steel samples were obtained (see Figure 3.). Potentiodynamic polarization tests were evaluated by Tafel extrapolation method of corrosion rate. Measured and calculated results are summarized in Table 1.

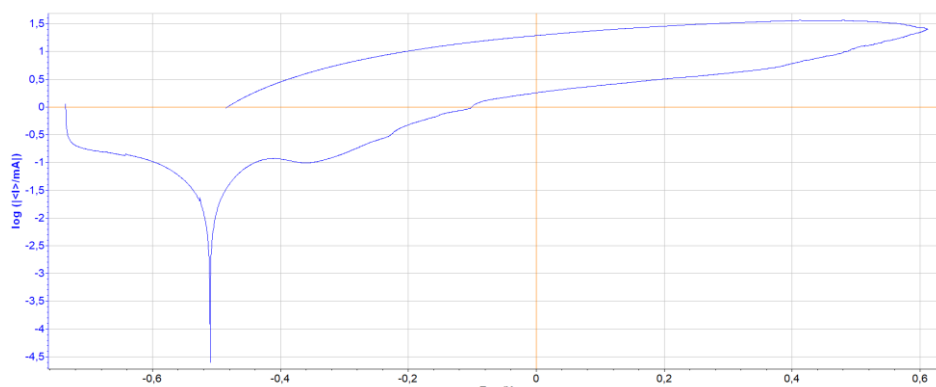


Figure 3. Potentiodynamic curve of plasma nitrided X12CrMoWVNbN10-1-1 steel (550°C) in deaerated 2.5% NaCl solution.

TABLE I. Results of potentiodynamic electrochemical tests on X12CrMoWVNbN10-1-1

	v_{corr} (mm/a ⁻¹)	E_{corr} (mV)	I_{corr} (μA)	β_c (mV)	β_a (mV)
ϕ (nitrided)	1,076	-503,973	80,710	475,300	430,933
σ (nitrided)	0,448	115,961	33,575	168,059	229,936
ϕ (untreated)	0,198	-384,900	14,820	298,625	125,575
σ (untreated)	0,053	15,533	3,447	49,611	35,006

Conclusion

This paper describes corrosion resistance of plasma nitrided X12CrMoWVNbN10-1-1 martensitic stainless steel in deaerated 2.5 % NaCl solution compared to untreated sample. Increase of current density and corrosion rate and shift of corrosion potential to more negative values was observed for plasma nitrided samples. Calculated PF was similar for untreated and plasma nitrided samples. Average width of pits for nitrided sample was doubled compared to untreated one. Summary is that corrosion resistance for plasma nitrided X12CrMoWVNbN10-1-1 steel in comparison to untreated one is decreased.

References

1. Z. Studeny, *Manufacturing Technology*, 15(1), (2015)
2. P. Pokorný, V. Hruby, et al., *Kovove materialy – Metallic materials*, 50(3), (2012)
3. D. Dobrocký, Z. Studeny, Z. Pokorný et al., in *Metal 2016*, Brno (2016)
4. D. Kusmík, O. Čech, P. Faltejsek in *Metal 2016*, Brno (2016)
5. W.J. Yang, M. Zhang, Y. H. Zhao, *Surface and Coatings Technology*, 298 (2016)
6. W. Liang, *Applied Surface Science*, 211(1-4) (2003)
7. E. Menthe, K.-T. Rie, *Surface and Coatings Technology*, 116-119 (1999)
8. L. Yang, Z. Wang, L. Wang, *Applied Surface Science*, 298 (2014)
9. X.Y. Li, *Surface Engineering*, 17(2), (2013)

Battery-powered Soldering Gun

J. Martis^a, P. Vorel^a and D. Cervinka^a

^a Department of Power Electrical and Electronic Engineering, Brno University of Technology, Brno 61600, Czech Republic

Introduction

The classic transformer-powered soldering gun has many advantages. It heats up quickly, has enough power for soldering larger conductors and is convenient for soldering e.g. two wires together (no need for a third hand, the solder on the tip doesn't overheat). The disadvantages are a requirement of mains power and a relatively large weight because of the transformer.

The soldering gun requires a relatively large power (around 70-100 W). Until recently, common batteries were unable to supply such power for longer time and with the required size and weight. Moreover, the current required for the soldering tip is in the range of 80-250 Amps (depending on the tip material), semiconductors able to handle such currents with low losses in small packages have only recently been made available. These are probably the reasons why high-power cordless soldering guns are not being sold at all today. There are only low power battery-powered soldering irons on the market, which reach a maximum power of around 12-16 watts [1].

As will be shown in this contribution, lithium-ion battery technology together with modern semiconductors makes it possible to construct a convenient and light-weight battery-powered soldering gun. A power control feature has also been added, which allows for more variability during soldering.

Battery selection

The required power supplied from the battery is around 80 W. A standard 18650 Li-Ion cell has an energy capacity of around 10 Wh and is able to supply 20 W continuously. Four common Li-Ion cells will fit inside the soldering gun housing, have the required power handling capability and allow for 30 minutes of continuous operation. However, the soldering gun is not operated continuously, so the practical operational time will be much longer (over 1 hour).

Voltage conversion

It has been measured that a standard copper wire soldering gun tip requires around 0.3 Volts and 250 Amps with cold tip (resistance of 1.2 m Ω). Some types of soldering guns are designed for a different tip material, which has a higher resistivity and requires around 0.6 Volts and 100 Amps (resistance of 6 m Ω). Thus, the soldering tip cannot be connected directly to the cells with voltage of around 3.7 V.

Therefore, a voltage converter must be used. It has been measured, that the inductance of the current-carrying path of the soldering gun is around 150 nH, which means reactance of around 50 m Ω at a practical converter switching frequency of 50 kHz. If an unrectified HF-transformer was used to supply the soldering tip, the converter would need to supply the large apparent power, resulting from large ratio of inductive reactance to tip resistance. Also, the transformer would

increase the weight and size of the device. Rectified transformer is impractical because of the losses on the rectifier at high current.

It can be shown that a simple synchronous buck converter can be used to power the soldering tip directly from the cell voltage of 3.7 V. A higher voltage is not practical, because the switching losses would be increased. A single series cell configuration also simplifies the required battery monitoring circuits. For this circuit, a higher voltage on the soldering tip and lower current is desirable, so the higher resistivity soldering tip was selected and thus the required parameters of the converter are around 100 A and 0.6 V. The transistors must be able to

A schematic of the power part of the converter is shown in Figure 1. A synchronous configuration of the buck converter is highly desirable, because it greatly decreases conduction losses on the lower diode (replaced by MOSFET Q2). With modern MOSFETs with ON-resistance below 1 m Ω and with small surface-mount packages, the converter can be realized on a small space. Parallel connection of transistors is used.

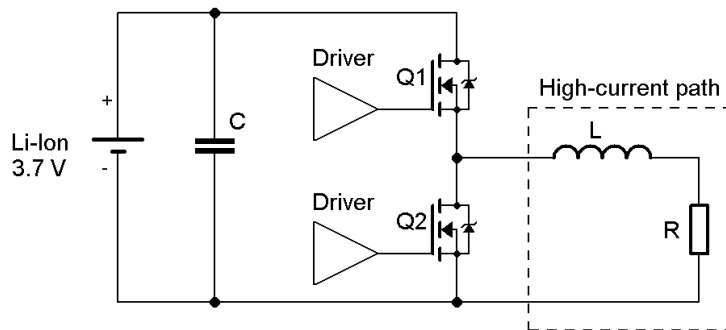


Figure 1. Power circuit of the battery-powered soldering gun.

A large advantage of this configuration is that it does not require any additional magnetic components. It can be shown that the inductance of the high-current path of around 150 nH (soldering tip and tip holders) is sufficient as the filtering inductance of the buck converter. Also, no output filtering capacitor is required, because voltage ripple on the soldering tip does not cause problems.

Prototype

A circuit board of the converter can be seen in Figure 2. Dimensions of the board are 90x33 mm. The board is realized as four-layer with each layer thickness of 70 μm . This is required because of the large currents and small needed dimensions of the board. The power transistors used are type BSC010NE2LSATMA1 from Infineon (25 V; 0.8 m Ω ; 100 A max.). Two in parallel are used for the high-side switch (Q1 in Figure 1) and six in parallel are used for the low-side switch (Q2 in Figure 1). The converter board also includes the required control circuits and gate drivers. Control is open-loop, with duty cycle user-adjustable by external potentiometer (adjusts the output power).

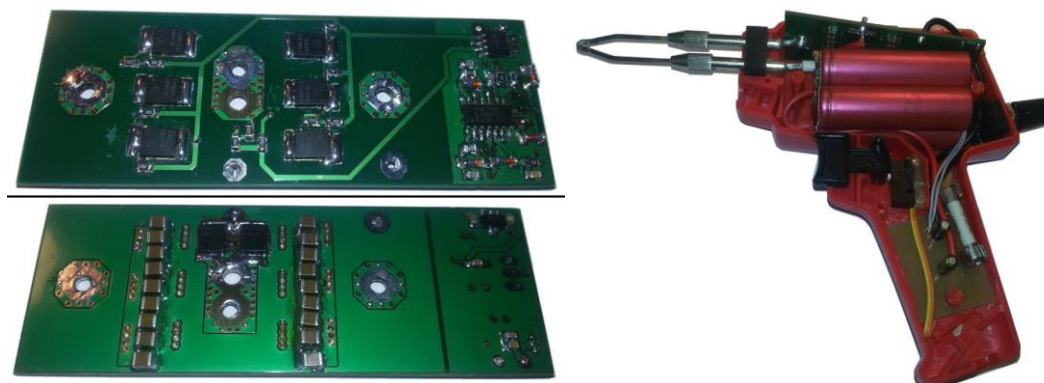


Figure 2. Voltage converter board (left) and a finished prototype (right).

A finished prototype can be seen in Figure 2. The electronics have been built into a housing taken from a transformer-powered soldering gun. The converter board is on the top, while the smaller board on the bottom includes battery management and an auxiliary DC-DC converter, which provides the required 15 Volts for the control circuits and gate drivers from the 3.7 V on the battery (circuits are SMT on the other side of the board). A power control potentiometer, which adjusts the duty cycle, is on the back. The weight of the prototype is 0.37 kg.

Conclusion

The transformer-powered soldering gun is a specific and irreplaceable piece of equipment. A cordless battery-operated modification has been designed, constructed and successfully tested. The combination of Li-Ion cells and modern semiconductors allows for light weight (0.37 kg), long operation time (over 1 hour) and adjustable power.

Acknowledgment

This research work has been carried out in the Centre for Research and Utilization of Renewable Energy (CVVOZE). Authors gratefully acknowledge financial support from the Ministry of Education, Youth and Sports of the Czech Republic under NPU I programme (project No. LO1210).

References

1. Weller BL60MP Soldering iron. <http://www.newark.com/weller/bl60mp/battery-soldering-iron-12w-510deg/dp/43AC8204>

Separation of Chromium from Tanning Wastewater by Electrochemical Method

Falah K. Matloub, Muataz Mohammed Sulaiman, Zaid Nidhal Shareef

Abstract

The removal of the chromium from spent tannery solution was carried out by electrochemical technique in order to minimize the pollution problem of tanning process activity using platinum as anodic electrode and iron, aluminum, nickel and copper as cathodic electrode.

The volume of cell was 250 cm³. A treated synthetic bath solution contains 12.87g/l of Cr(OH)SO₄. The current density range was (1.5 - 3.5) A.dm⁻² and the temperature (25 – 45) °C. Three organic acids (formic acid, citric acid and acetic acid) were used as additives to improve electrodeposition.

The removal percent is determined by using atomic absorption Spectrophotometer. The best removal of chromium is 97.11% after four hours, the best temperature is 35 °C and the best current is 3.5 A.dm⁻². The powder obtained from the deposits on the cathode was analyzed by X-Ray Diffractometer, Differential Scanning Calorimetry and Fourier Transform Infrared. They were shown that the powder was composed of Cr₂O₃ after heating. The chromium electro-deposition takes place because of the formation of active chromium–carbamid complexes. The complex compounds were expected as formate, citrate and acetate of chromium.

Design of the conic static probe tip of the Pitot's tube in experimental chamber

P. Hlavatá^a, J. Maxa^a, P. Vyrubal^a

^a Department of Electrical and Electronic Technology, Brno University of Technology, Technická 10, 616 00 Brno, Czech Republic

This article comes out from the series of articles devoted to the issue of pumping in the differentially pumped chamber. This article is based on a study of Dr. Danilatos, where pumping of the differential pumped chamber is solved using the Monte Carlo statistical method. To solve the problem we use the mechanics of continuum with experimental verification. The article deals with a construction of the conic tip of the static probe.

Introduction

This article is based on a study written by Dr. Danilatos [1], which deals with the pumping of the differential pumped chamber in an environmental scanning electron microscope using the Monte Carlo statistical method [2]. Based on these articles, a comparative study [3] was produced, where comparable results were obtained by Mechanics of continuum using the Ansys Fluent method, finite volume method [4, 5, 6]. Based on this theory the experimental chamber is being created for the evaluation of the flow velocity on the primary electron beam path using Pitot's tube.

Insomuch as calculation is assumed the character of the supersonic flow (Fig. 1), is necessary to construct the static probe tips with the head tip, avoiding of the formation of the torn shock wave, for which arises big pressure loss distorting the results obtained using probe. It is need, using suitable cone, to achieve oblique shock wave [7, 8, 9].

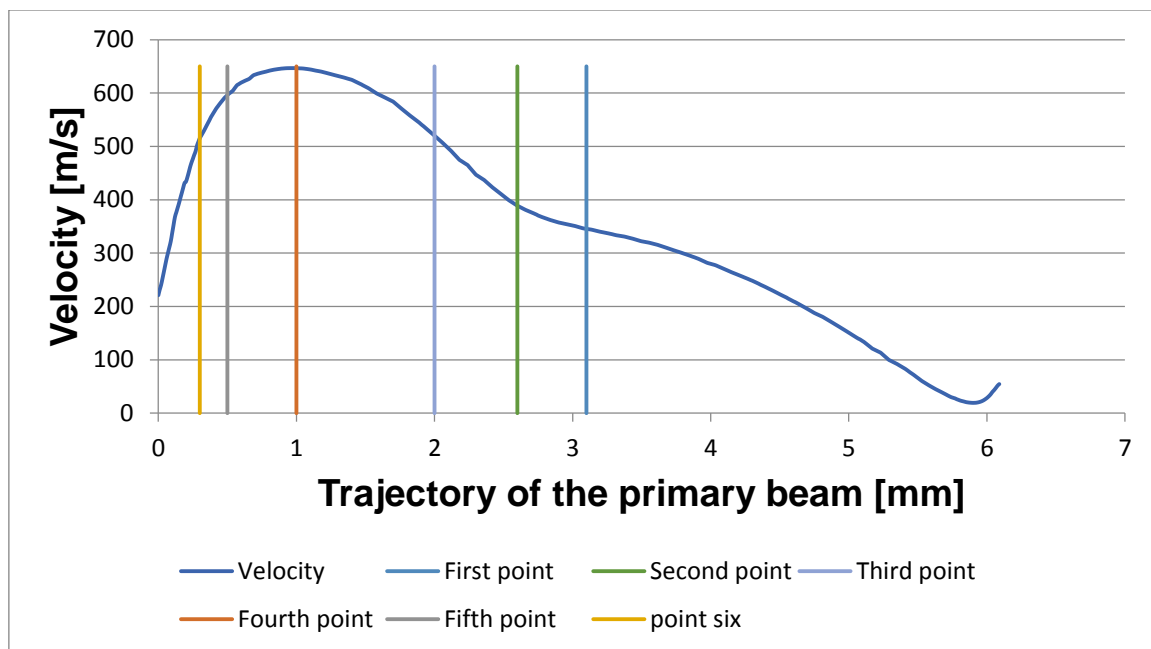


Figure 1. Velocity running on the primary electron beam path

Taylor Maccoll Analysis

According to Taylor- Maccoll theory¹, the ratio of Mach number to static probe tip's angle has impact to a shape of the shock wave (Fig. 2). Given flow velocity ratio and probe tip's angle comes out from the relationship (1):

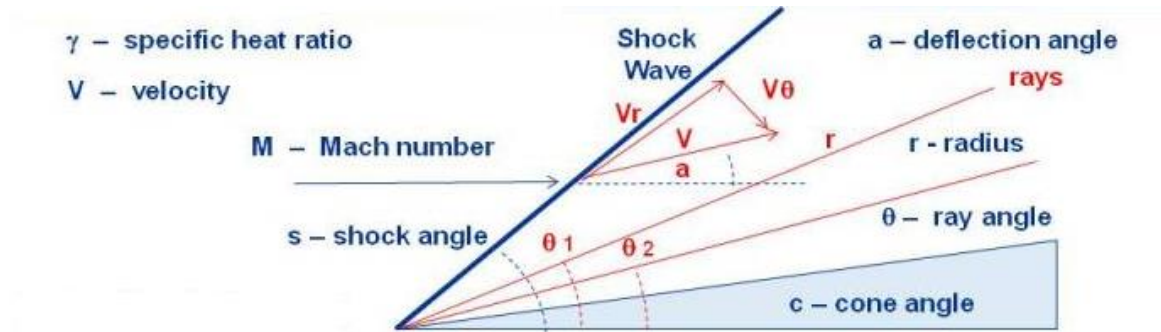


Figure 2. Taylor – Maccoll theory

$$\frac{\gamma-1}{2} \left[1 - v_r^2 - \left(\frac{dv_r}{d\theta} \right)^2 \right] \left[2v_r + \cot \theta \frac{dv_r}{d\theta} + \frac{d^2 v_r}{d\theta^2} \right] - \frac{dv_r}{d\theta} \left[v_r \frac{dv_r}{d\theta} + \frac{dv_r}{d\theta} \frac{d^2 v_r}{d\theta^2} \right] = 0 \quad (1)$$

$$v_\theta = \frac{dv_r}{d\theta} \quad (2)$$

Given dependence is placed to a graphic and has form that is pictured in Fig. 3. In the area above the curve the torn shock wave is created, in opposite, below the curve the oblique shock wave is created [10].

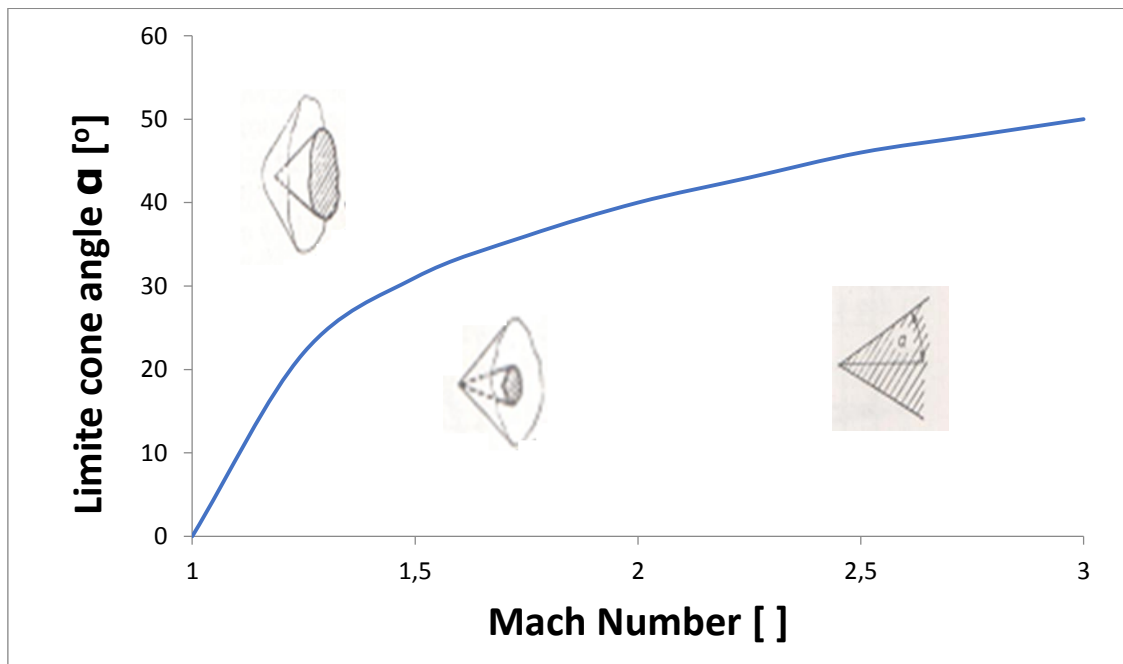


Figure 3. Dependence of cone angle to Mach number.

¹ <https://www.grc.nasa.gov/WWW/k-12/airplane/coneflow.html>

Results and discussions

On the primary electron beam path was selected six points in which will be measured the velocity using Pitot's tube (Fig. 1). From mentioned Taylor- Maccoll theory were derived maximal cone angles of the static probe for given measured points (TAB I.).

TABLE I. Resulting probe angles.

	Velocity [m/s]	Mach [-]	Theoretical angle [°]
POINT 1	345	1,04	7
POINT 2	387	1,17	12
POINT 3	520	1,57	33
POINT 4	650	1,96	38
POINT 5	600	1,81	35
POINT 6	515	1,55	32

For individual variants the probe shapes in practice in 3D solid model are pictured in Fig. 4.

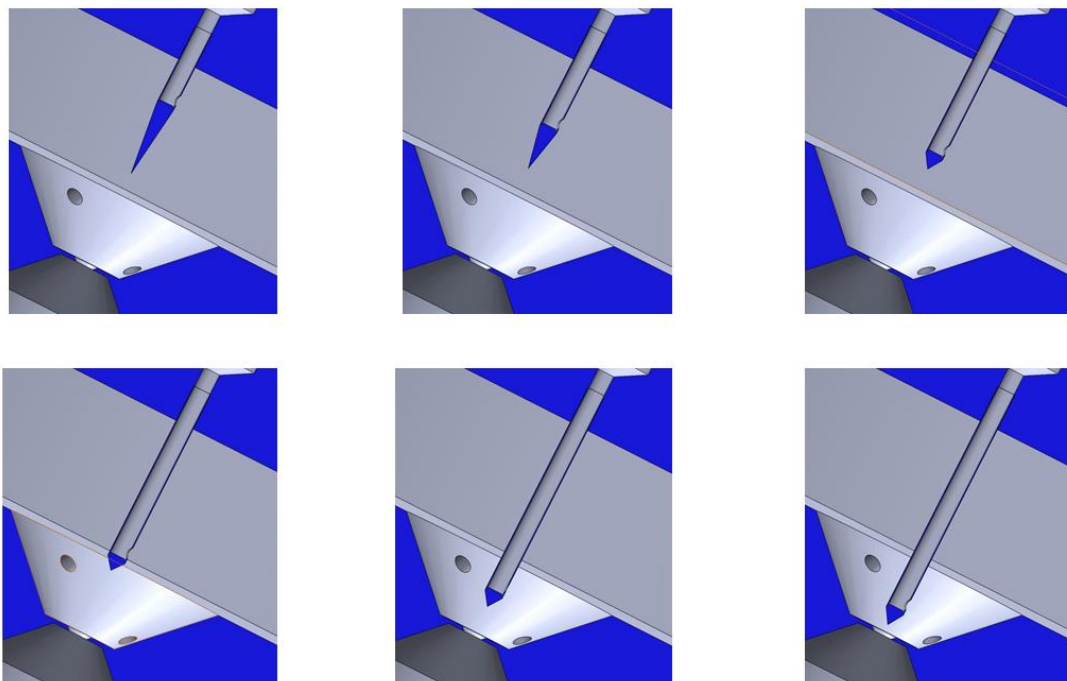


Figure 4. Probe cone shapes for individual measured points.

Acknowledgments

This research has been carried out in the Centre for Research and Utilization of Renewable Energy (CVVOZE). Authors gratefully acknowledge the financial support from the Ministry of Education, Youth and Sports of the Czech Republic under NPU I programme (project No. LO1210) and BUT specific research programme (project No. FEKT-S-17-4595).

References

1. GD. Danilatos, Velocity and ejector-jet assisted differential pumping: Novel design stages for environmental SEM. *Micron*, vol. 43, no. 5, p. 600-611, (2012).
2. V. Neděla, Controlled dehydration of a biological sample using an alternative form of environmental SEM. *Journal of Microscopy*. **237** (1), p. 7-11. ISSN 0022-2720. (2010).
3. J. Maxa; M. Bílek; P. Hlavatá; P. Vyroubal and K. Lepltová, Comparisons Using Methods of Continuum Mechanics and Monte Carlo at Differentially Pumped Chamber. *Advances in Military Technology*, vol. 11, no. 2, p. 143-150. ISSN: 1802-2308. (2016).
4. P. Vyroubal; J. Maxa; V. Neděla; J. Jiráček and K. Hladká, Apertures with Laval Nozzle and Circular Orifice in Secondary Electron Detector for Environmental Scanning Electron Microscope, *Advances in Military Technology*, vol. 8, no. 1, p. 59-69, (2013).
5. J. Maxa and V. Neděla, The Impact of Critical Flow on the Primary Electron Beam Passage through Differentially Pumped Chamber. *Advances in Military Technology*, , vol. 6, no. 1, p. 39-46. ISSN 1802-2308, (2011).
6. J. Maxa; V. Neděla; J. Jiráček; P. Vyroubal and K. Hladká, Analysis of gas flow in a secondary electron scintillation detector for ESEM with a new system of pressure limiting apertures. *Advances in Military Technology*, vol. 7, no.2, p.39-44, (2012).
7. V. Neděla; E. Tihlaříková; J. Runštuk; J. Hudec, High-efficiency detector of secondary and backscattered electrons for low-dose imaging in the ESEM. *Ultramicroscopy*, p. 1-11. ISSN 0304-3991, (2018).
8. V. Neděla; I. Konvalina; M. Oral; J. Hudec. The Simulation of Energy Distribution of Electrons Detected by Segmental Ionization Detector in High Pressure Conditions of ESEM. *Microscopy and Microanalysis*, p. 264-269.
9. V. Neděla; J. Hříb; L. Havel; J. Hudec and J. Runštuk, Imaging of Norway spruce early somatic embryos with the ESEM, Cryo-SEM and laser scanning microscope. *Micron*, no. 84, p. 67-71. ISSN 0968-4328, (2016).
10. M. Daněk, *Aerodynamika a mechanika letu*, p. 83, VVLŠ SNP, Košice (1990).

Comparative analysis of ideal and real gas in pumping of the experimental chamber

J. Maxa^a, P. Hlavatá^a, P. Vyroubal^a

^a Department of Electrical and Electronic Technology, Brno University of Technology, Technická 10, 616 00 Brno, Czech Republic

This article comes out from the series of articles devoted to the issue of pumping in the differentially pumped chamber. This article is based on a study of Dr. Danilatos, where pumping of the differential pumped chamber is solved using the Monte Carlo statistical method. To solve the problem we use the mechanics of continuum with experimental verification. The article deals with a construction of the conic tip of the static probe.

Introduction

This article is based on a study written by Dr. Danilatos [1], which deals with the pumping of the differential pumping chamber in an environmental scanning electron microscope using the Monte Carlo statistical method [2]. Based on these articles, a comparative study [3] was produced, where comparable results were obtained by Mechanics of continuum using the Ansys Fluent method, finite volume method [4, 5, 6]. Based on this theory the experimental chamber is being created for the evaluation of the flow.

In the CFX simulation settings is usually choose for the calculation gas as an ideal gas. Ideal gas is perfectly compressible without inertial friction unlike the real gas. The particles have to fulfill the following conditions:

Diameters of the particles are negligible with respect to distances in between them (ideal gas particles are possible to consider as material points),

Except the collisions the particles do not act on themselves,

Total kinetic particles energy does not change in mutual collisions, it means, particle collisions are perfectly flexible.

Consequence of these conditions is perfect flexibility and perfect fluidity of the ideal gas.

Real gas almost suits to the conditions of the ideal gas in limited scope around the temperature of 0 °C and pressure of 101 325 Pa (in normal conditions). Real gases getting closer to properties of the ideal gas in satisfactorily high temperature and low pressure.

Ideal gas

Ideal gases are used for easier exploration of the properties and behavior of the gases in mechanical and thermodynamic processes. For thermodynamic processes in the gases the state equation applies:

$$pV = nRT = \frac{m}{M}RT$$

;where p – gas pressure, V – volume, n – substance amount, T – thermodynamic temperature, R – universal gas constant, m – gas mass.

Real gas

Real gas differs from the ideal gas. The real gas particle (molecules) have finite volume and act to each other with cohesive (attractive) forces. For this reason is imperfectly compressible and it has inertial frictions.

For the description of the real gases the van der Waals state equation applies

$$\left(p + \frac{an^2}{V^2}\right)(V - nb) = nRT$$

where a and b are constants of van der Waals equation.

The real gas pressure caused with the collisions of the molecules to the wall is lower than the ideal gas pressure by the correction value for the interaction of molecules:

$$\frac{an^2}{V^2}$$

It is because of the damping of the molecules collision acting the intermolecular attractive forces.

From the value of total volume V is subtracted the excluded volume of the molecules as a part of the total volume, which the molecules occupy by themselves. This is provided by the correction term:

$$nb$$

The simplified shape of the van der Waals state equation:

$$pV = n \left[RT + p \left(b - \frac{a}{RT} \right) \right]$$

Redlich-Kwong equation

In mathematical- physics mapping of the gas flowing in experimental chamber was considered the impact of the simplification in the choosing of the ideal gas [7, 8, 9].

The comparing calculation of the flowing in the experimental chamber was made with the setting of the braking of the supersonic flow and with the heat transfer.

The calculation with the ideal gas sets was compared to the calculation with the real gas sets. It was chosen for the real gas, the setting of the Redlich-Kwong equation (10). It is two-dimensional equation which is modified form of the van der Waals equation. It obtains dependency of the constant of the attractive forces impact on the temperature and modified volume dependency, where pressure p is expressed by relationship

$$p = \frac{RT}{V_m - d} - \frac{c}{\sqrt{T}V_m(V_m + d)}$$

c , d are constants and for given problem of nitrogen used have value: $c = 1,5554 \text{ [dm}^6 \text{ Mpa.K}^{1/2} \text{ mol}^{-2} \text{]}$

$$d = 0,026738 \text{ [dm}^6 \text{ Mpa.K}^{1/2} \text{ mol}^{-2} \text{]}$$

Results and discussions

It was made comparing time-changing calculation of the flow through the nozzle with subsequent flow braking by artificial flow throttling.

The values of pressure, velocity and temperature are identical during the whole time running. In Fig. 1 and 2 are pictured the vales of the temperature ratio in time of 318 sec.

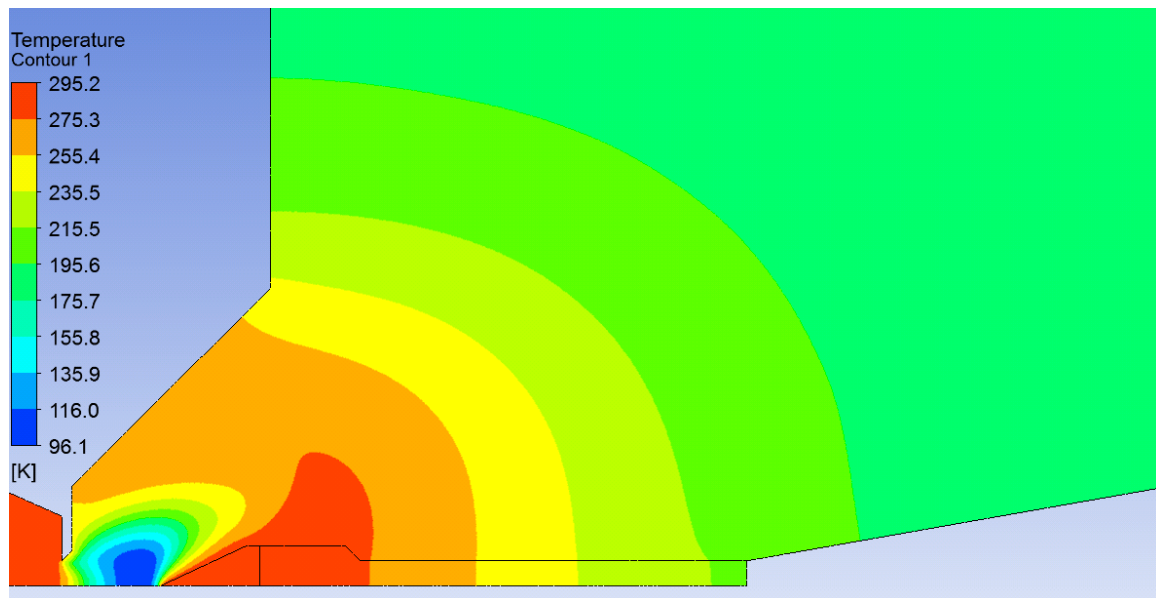


Figure 1. Temperature ratio for ideal gas setting.

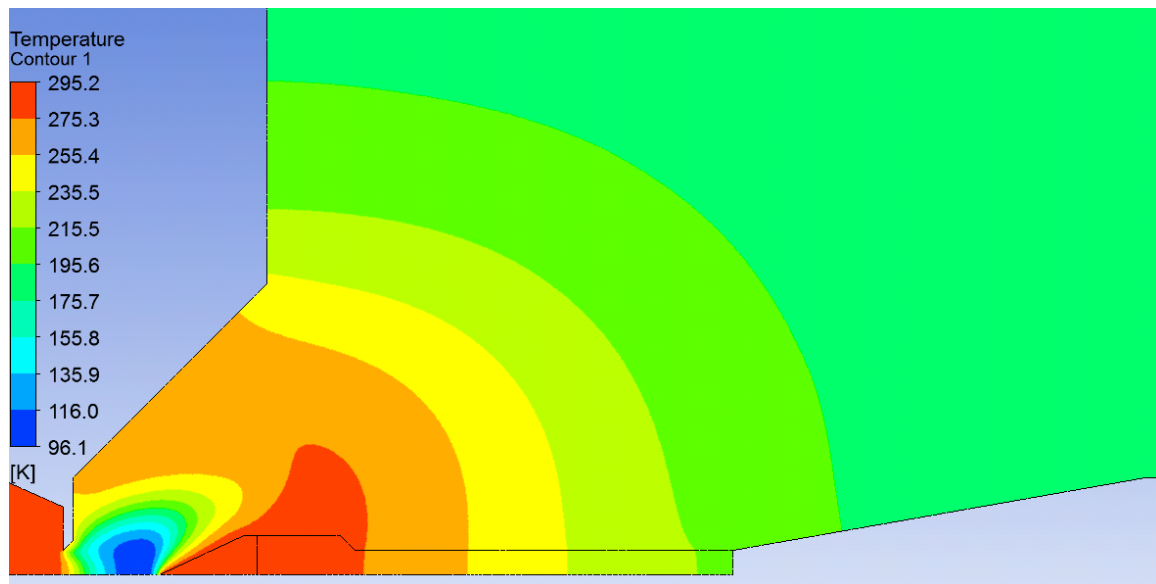


Figure 2. Temperature ratio for real gas setting.

Acknowledgments

This research has been carried out in the Centre for Research and Utilization of Renewable Energy (CVVOZE). Authors gratefully acknowledge the financial support from the Ministry of Education, Youth and Sports of the Czech Republic under NPU I programme (project No. LO1210) and BUT specific research programme (project No. FEKT-S-17-4595).

References

1. GD. Danilatos, Velocity and ejector-jet assisted differential pumping: Novel design stages for environmental SEM. *Micron*, vol. 43, no. **5**, p. 600-611, (2012).
2. V. Neděla, Controlled dehydration of a biological sample using an alternative form of environmental SEM. *Journal of Microscopy*. **237** (1), p. 7-11. ISSN 0022-2720. (2010).
3. J. Maxa; M. Bílek; P. Hlavatá; P. Vyroubal and K. Lepřtová, Comparisons Using Methods of Continuum Mechanics and Monte Carlo at Differentially Pumped Chamber. *Advances in Military Technology*, vol. 11, no. **2**, p. 143-150. ISSN: 1802-2308. (2016).
4. P. Vyroubal; J. Maxa; V. Neděla; J. Jiráček and K. Hladká, Apertures with Laval Nozzle and Circular Orifice in Secondary Electron Detector for Environmental Scanning Electron Microscope, *Advances in Military Technology*, vol. 8, no. **1**, p. 59-69, (2013).
5. J. Maxa and V. Neděla, The Impact of Critical Flow on the Primary Electron Beam Passage through Differentially Pumped Chamber. *Advances in Military Technology*, , vol. 6, no. **1**, p. 39-46. ISSN 1802-2308, (2011).
6. J. Maxa; V. Neděla; J. Jiráček; P. Vyroubal and K. Hladká, Analysis of gas flow in a secondary electron scintillation detector for ESEM with a new system of pressure limiting apertures. *Advances in Military Technology*, vol. 7, no.**2**, p.39-44, (2012).
7. V. Neděla; E. Tihlaříková; J. Runštuk; J. Hudec, High-efficiency detector of secondary and backscattered electrons for low-dose imaging in the ESEM. *Ultramicroscopy*, p. 1-11. ISSN 0304-3991, (2018).
- 8.** V. Neděla; I. Konvalina; M. Oral; J. Hudec. The Simulation of Energy Distribution of Electrons Detected by Segmental Ionization Detector in High Pressure Conditions of ESEM. *Microscopy and Microanalysis*, p. 264-269.
9. V. Neděla; J. Hříb; L. Havel; J. Hudec and J. Runštuk, Imaging of Norway spruce early somatic embryos with the ESEM, Cryo-SEM and laser scanning microscope. *Micron*, no. **84**, p. 67-71. ISSN 0968-4328, (2016).
10. M. Řehák, Popis stavového chování plynu, p.273, ZU, Plzeň (2013).

The influence of alloying elements on surface hardness of ferritic nitrocarburizing layers of ball screws

Z. Pokorný, D. Dobrocký, P. Faltejsek

Department of Mechanical Engineering, University of Defence, Brno, Czech Republic

The article deals with a chemical composition of saturated layers after ferritic nitrocarburizing process. Experiments are focused on using of gas ferritic nitrocarburizing processes for surface treatment due to increasing of surface hardness with low influence on the dimensional accuracy. Ferritic nitrocarburizing processes were applied to steels C 35 (sample A1), 37Cr4 (sample A2) and 42CrMo4 (sample A4) used for ball screw manufacturing, which were subsequently evaluated by electron microscopy, GDOES and microhardness methods. The results of measurement showed high influence of alloying elements on surface hardness of created carbide-nitride layer after chemical-heat treatment process. Main task was to compare microhardness after ferritic nitrocarburizing in accordance with chemical composition.

Introduction

The aim of this paper is to achieve an enhanced of surface hardness, better wear resistance and reduced friction coefficient connected to specific surface morphology. During chemical heat-treatment process primarily the interstitial phases of nitrides and carbides of iron are created. The initial nitrides and carbides phases are created in grain boundaries, in biggest defects well known as an area defects. Generally, these type of nitrides and carbides caused only low increasing of microhardness. The surface hardness after chemical heat treatment depends on two fundamental phenomenon. The surface hardness of created carbide and nitride phases depends on microstructure and finally on content of suitable alloying elements in steel. Generally, the fundamental elements caused increasing of mechanical properties are alloying elements as molybdenum, vanadium, aluminum or chrome. The mechanical properties of layer are dependent on the proportion of created individual phases in steel. The created compound layer has been very hard and brittle with good friction and anticorrosion properties. The thickness and hardness of γ' -Fe₄N (diffusion layer) depends on quantity and suitability of alloying elements for mentioned treatment process. Therefore, this paper demonstrates the influence of selected alloying elements on increasing of surface hardness. This optimized used technology called ferritic nitrocarburizing. After chemical heat treatment application, special semi-diffusion area (part) of heterogeneous layers are created in the surface. This part of created layer has another different characteristics than layer established after standard nitriding processes. For comparison with standard nitriding process chemical composition of steel was verified by GDOES/Bulk method on LECO SA 2000 spectrometer and local measurement of composition was carried out on SEM microscope Hitachi Tabletop 3000 equipped by XRD Oxford Instruments Stream-2. Microstructure was evaluated by using SEM method on Hitachi Tabletop 3000. Thickness and microhardness of nitrated layers were measured by microhardness method in accordance with DIN 50190 standard on automatic microhardness tester LECO LM 247 AT. Thickness of compound layer was evaluated by electron microscopy. The evaluation of influence of alloying elements on depth and surface hardness was performed by using microhardness indentation test.

Battery powered mini-excavator

P. Prochazka, I. Pazdera, R. Cipin, P. Vorel, J. Knobloch

^a Department of Power Electrical and Electronic Engineering, Brno University of Technology, Technicka 12, Brno, 616 00, Czech Republic

Introduction

Electric machines are already commonly utilized in application with working machines (1), (2) a (3). This paper describes electric drive of 2t mini excavator. There are several reasons why to utilize electric machines in such application. Especially in closed space where the exhausted gasses cause problems for machine operators and other working staff in case of excavators with combustion machine. There are also another benefits in case of electric machine in comparison with combustions machine in mini-excavator application. Diesel engine has to operate in idle speed even if the excavator does not operate, which makes its operation inefficient in terms of fuel consumption. It is possible to significantly reduce energy consumption if we use electric machine because the electric motor is able to operate with significantly lower speed or can immediately stop and is ready to start with higher dynamic then combustion machines. The Mini-excavator often stays in such idle state during every day working cycle.



Figure 1. Excavator E19 during digging test.

Electric drive concept

Electric drive concept of two-ton excavator is shown in Figure 2. It is similar topology used in many traction applications. Permanent magnet synchronous motor (PMSM) is used as main drive unit. This kind of motor has excellent power to volume ratio with high efficiency especially at lower speed. Furthermore, the salient type of PMSM was choose to improve its behavior at higher speed where the field weakening strategy can be employed. PMSM has to operate with three-phase inverter to achieve excellent dynamic and stability in comparison with combustion engine. The

stability and dynamic is achieved with appropriate control strategy which in case of PMSM is usually field oriented control strategy (FOC).

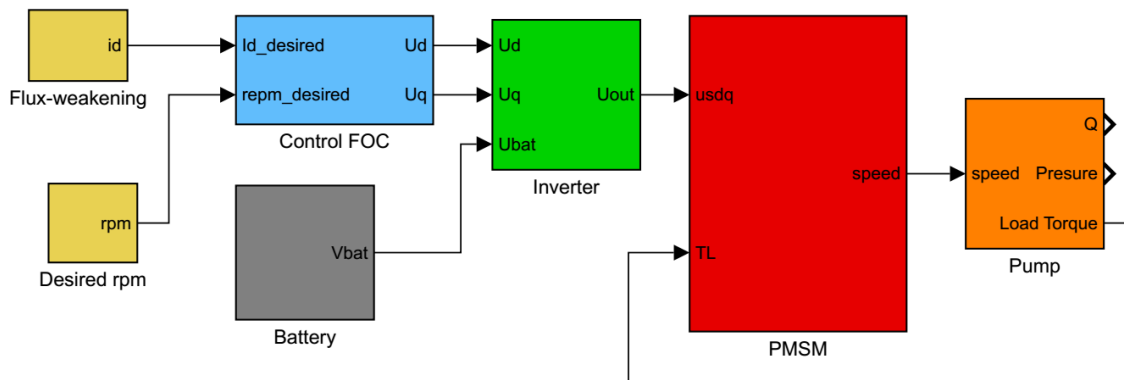


Figure 2. Basic concept of electric drive for Excavator E19.

The most important part of electric drive is Lithium based accumulator as an energy source. The battery capacity and battery voltage was considered as a critical parameter. Battery voltage was chosen with respect to safety of operators and working staff. Moreover, if we assume condition in which working machines have to operate. The battery voltage was set to operate at 50 V. There are also a lot of commercial product (inverters, motors) at such voltage range. Lower voltage level is limiting in terms of total battery current at assumed maximal drive power.

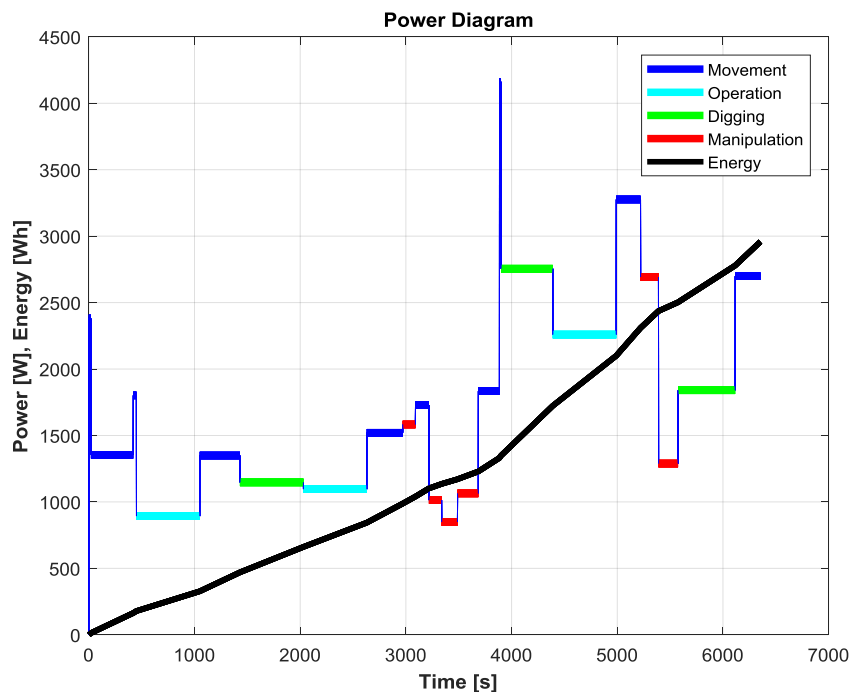


Figure 3. Desired power and consumed energy during Excavator E19 working cycle.

The most important parameter of the battery is its capacity. It was considered that the total battery energy has to be sufficient for defined working profile, see Figure 3. This profile was derived from known typical profile of excavator with combustion engine. To obtain such profile is

quiet simple task, because there are lot of data and experience with excavator operation (4). The working cycle form Figure 3 defines averages power desired for defined time at typical kind of operation. The working cycle takes about two hours but in real application it is not assumed that the excavator operates continuously without breaks. Therefore, according to Figure 3 the total consumed energy (3kWh) during one working cycle should be sufficient for ca four-hour operation. The total battery capacity was then finally set to 3,6kWh. This amount of energy should be sufficient even if the total efficiency of inverter, motor and battery itself is considered about 80 %. In fact, the total consumed energy according to Figure 3. is derived for combustion engine. But if we consider dynamically controlled electric drive of excavator, then is should be consumed less energy. Improved electric drive performance has positive impact on efficiency of excavator hydraulic components.

Conclusion

This paper summarizes basic information of two-ton mini-excavator including basic description of electric drive design. Electric motor drives main oil pump which supply all hydraulic components in excavator (hydraulic components for working arm, cabin rotation and). The desired battery capacity (3,6 kWh) is calculated with respect of typical excavator operational cycle. The full paper gives more information about design procedures and simulations of battery powered electric drive in mini-excavator application.

Acknowledgments

This research work has been carried out in the Centre for Research and Utilization of Renewable Energy (CVVOZE). Authors gratefully acknowledge financial support from the Ministry of Education, Youth and Sports of the Czech Republic under NPU I programme (project No. LO1210).

References

1. S. Cho, S. Yoo and C. G. Park, 2013 World Electric Vehicle Symposium and Exhibition (EVS27), Barcelona, 2013, pp. 1-8.
2. S. Lee, J. Lee, H. Lee and S. H. Lee, IECON 2013 - 39th Annual Conference of the IEEE Industrial Electronics Society, Vienna, 2013, pp. 4653-4659.
3. J. I. Yoon, A. K. Kwan and D. Q. Truong, 2009 ICCAS-SICE, Fukuoka, 2009, pp. 3825-3830.
4. J. Nevrlý, Z. Nemec, I. Pazdera, M. Nozka, 24th International Conference ENGINEERING MECHANICS 2018, Svratka, Czech Republic, 14 – 17 May 2018. ISBN 978-80-214-5497-2.

Study of the Current Value Influence on the Internal Resistance Value

T. Reichl^a, P. Hrzina^a

^a Czech Technical University in Prague, Faculty of Electrical Engineering, Department of Electrotechnology

Abstract

Lithium-ion batteries are a complex energy storage device that is characterized by a complex degradation behavior that affects both its capacity and internal resistance. There are currently a number of impulse methods for evaluating the internal resistance of cells and batteries. This work deals with the analysis of the chosen method for calculating the internal resistance of the cell in dependence on the different C-Rates of the current.

Introduction

Capacity and internal resistance are two essential parameters for power and state of batteries determination [1]. It is necessary to take into account the fact that the great extension of batteries into different applications brought also the change in the discharging current course with. Most of today's modern applications require a high discharge current.

The question is what the current value is correct for determining the internal resistance parameter. There are some limitations here. An example is the state of charge or the Tafel equation [4]. This is the subject of exploring this work if these constraints are reflected in large capacitive electrochemical sources.

Impulse method

Known impulse methods are facing the following problems. Usual time for measurement of the internal resistance is too long to provide precise results. The first method of measurement duration shortening is the reducing of the current. But if the amplitude of the pulse is reduced, the voltage response is also reduced. Since the internal resistance is calculated by the difference of two voltages, it results to a strong increase of measurement uncertainty. The second possibility is reducing the amount of charge change by reducing the pulse duration – using impulse test method [1].

Another problem arises from the ambiguity of internal resistance determination. If it is determined in a state where the load is disconnected (open circuit voltage state) or when the load is connected. During each measurement the internal resistance of the LFP battery cells was measured at 25°C using the current pulse. The internal resistance was measured for both charging and discharging current pulses and for four C-rates (4C, 2C, 1C, 0.5C), since the value of the resistance changes significantly with the amplitude of the load current. Each current pulse was applied for 18 seconds [2], while prior to the pulse a 15 minutes relaxation period was imposed in order to allow the LFP cell to reach thermodynamic stability [3].

Therefore, this work deals with how the value of internal resistance will change if the C-Rates pulses are reduced, figure 2. If the cell about large capacity values like 100Ah is tested, the impulse outputs of about 500W or more can be got.

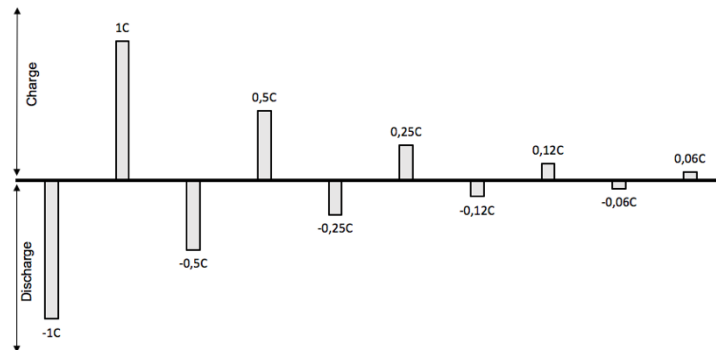


Figure 1. Example of the test pulses

Experiment

Measurement was done on charge and discharge stations I-TECH. On this device, parameters for charging and discharging currents were set according to the cell (TABLE I). The values of current, voltage, capacitance and temperature were recorded at regular intervals for later evaluation.

Graphs and results

TABLE I. Internal resistance

SOC 80%		SOC 50%		SOC 20%	
Charge impulse [mΩ]	Discharge impulse [mΩ]	Charge impulse [mΩ]	Discharge impulse [mΩ]	Charge impulse [mΩ]	Discharge impulse [mΩ]
PULZ 1C		PULZ 1C		PULZ 1C	
1.14	2.70	1.19	2.63	1.47	2.86
PULZ 0.5C		PULZ 0.5C		PULZ 0.5C	
1.20	2.95	1.90	2.70	2.78	2.88
PULZ 0.25C		PULZ 0.25C		PULZ 0.25C	
2.90	3.05	2.74	2.70	2.80	2.88
PULZ 0.12C		PULZ 0.12C		PULZ 0.12C	
2.95	3.10	2.75	2.90	2.89	2.89
PULZ 0.06C		PULZ 0.06C		PULZ 0.06C	
3.20	3.20	3.10	3.00	3.00	3.00

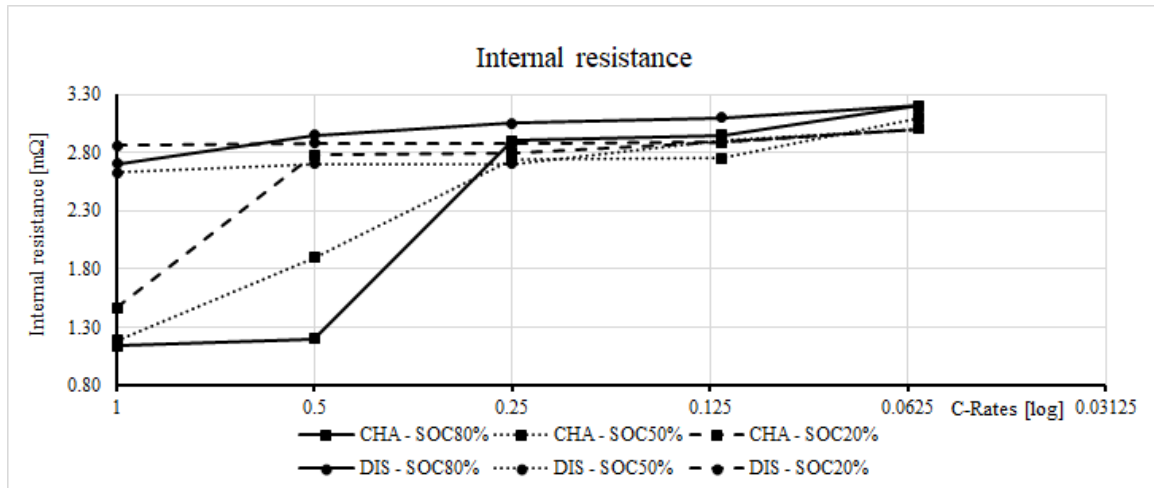


Figure 2. The results in the graph

Conclusion

The results show that there is a dependence of the internal resistance value on the pulse value. It can be seen that if large impulse is applied, particularly the charging one, the value of the internal resistance is less than the average for the rest of the pulses. Another phenomenon has been observed when the small impulses have been applied; there is no observable SOC dependence on internal resistance. These phenomena can be caused by the Tafel law.

The results summarized in this work are the first results and the work will be further extended.

Acknowledgments

This work has been supported by SGC grant CTU, number SGS18/071/OHK3/1T/13 and SGS18/068/OHK3/1T/13 and Department of Energy Technology, Aalborg University, Denmark.

References

1. SCHWEIGER, Hans-Georg, Ossama OBEIDI, Oliver KOMESKER, et al. Comparison of Several Methods for Determining the Internal Resistance of Lithium Ion Cells. *Sensors*. 2010, 10(6), 5604-5625. DOI: 10.3390/s100605604. ISSN 1424-8220.
2. ISO 12405-1 Electrically propelled road vehicles – Test specification for lithium-ion traction battery packs and systems – Part 1: High-power applications, 2011.
3. STROE, Daniel-Ioan, Maciej SWIERCZYNSKI, Soren Knudsen KAR a Remus TEODORESCU. A comprehensive study on the degradation of lithium-ion batteries during calendar ageing: The internal resistance increase. 2016 IEEE Energy Conversion Congress and Exposition (ECCE). IEEE, 2016, 2016, , 1-7. DOI: 10.1109/ECCE.2016.7854664. ISBN 978-1-5090-0737-0.
4. REDDY, Thomas B a David LINDEN. *Linden's handbook of batteries*. 4th ed. New York: McGraw-Hill, c2011, 1 v. (various pagings). ISBN 9780071624213.

Preparation and corrosion of biodegradable iron based porous materials

M. Sedlaříková, J. Vondrák*, A. Košíček and M. Hávová

*correspondence author: vondrakj@feec.vutbr.cz

Faculty of Electrical Engineering and Communications, BUT, Czech Republic

Abstract

A new iron based porous materials were suggested. They were prepared by loading of a polyurethane foam by mixture of iron and other metal powders (Ag, Mg and Si) and by annealing of the samples in nitrogen atmosphere. Their fundamental behaviour in physiologic solutions, their modifications and in blood plasma was tested. Usually, the increase of doping level yielded in increased corrosion rate and in partial passivation. Addition of hydrogen peroxide increased corrosion rate.

Thousands of people have been suffering by defect of skeletal systems either as a result of an accident or originating from some disease. Either titanium or chromium – iron alloys are most frequently used for their surgical reparation. Usually, they will remain in the patient's body for life or for a long time. The possibility of implants which would vanish from the body in a way synchronous to regeneration of damaged skeleton tissues seems attractive. It would be very good to tailor the properties of the implant to the surrounding tissue from the viewpoints of elasticity, hardness and rate of dissolution followed by sorption of the product in the tissue.

This work was started on basis of papers (1,2).

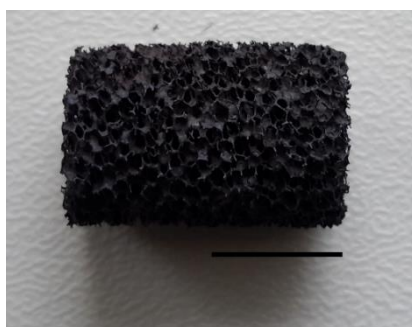


Figure 1. Example of an annealed sample.

Fig1 gives view on the sample prepared by heat procedure described above; the mass is composed from 100% Fe.

Metal powder was mixed thoroughly and then water was added. After another mixing, the sample of polyurethane was soaked by the suspension of metal powder and dried. Finally, it was annealed on a ceramic boat in a furnace filled by nitrogen. First, the temperature 450 °C was kept and it was followed by annealing at 1150 °C; metals Ag, Si or Mg added to Fe were used. The magnesium samples suffered for insufficient coherence and only admixtures to 2.5% Mg was used therefore.

Table 1 shows as an example the starting composition of sample containing 1.5 % Mg.

The view on an example (pure iron) is in Fig. 1 XRD analysis of 100% Fe containing sample indicated the presence of magnetite after annealing.

Corrosion in selected solutions was investigated by two means. First, standard corrosion diagram was recorded and described by a potentiostat μ AUTOLAB. Further, a long-term exposition to test solutions was performed and the change of mass was elucidated by gravimetrically.

Following liquids have been used as the solutions for immersing samples:

The choice of test liquids was governed by the aim to simulate conditions in a livid tissue. The tartrates should act as chelating agent and hydrogen peroxide as a oxidative substance in blood saturated by oxygen solution. 0.9 % NaCl and Ringer solution (both standard physiologic solutions, solution of NaCl + 0.3 ml/ml H₂O₂ and NaCl containing 1,5 g of tartaric acid and pH adjusted to 3.5 and blood plasma without insoluble parts were used.

The appearance is strongly dependent by the morphology of polyurethane substrate even after its burning-out. after annealing

As an example, the EDX spectrum of a Fe-Si sample after annealing is shown in Fig. 2. Further, the quantified results of EDX analysis of a sample doped by 1.5 % Mg is listed in Tab. 1. The results coincide with expected composition of initial blend of Fe and Mg.

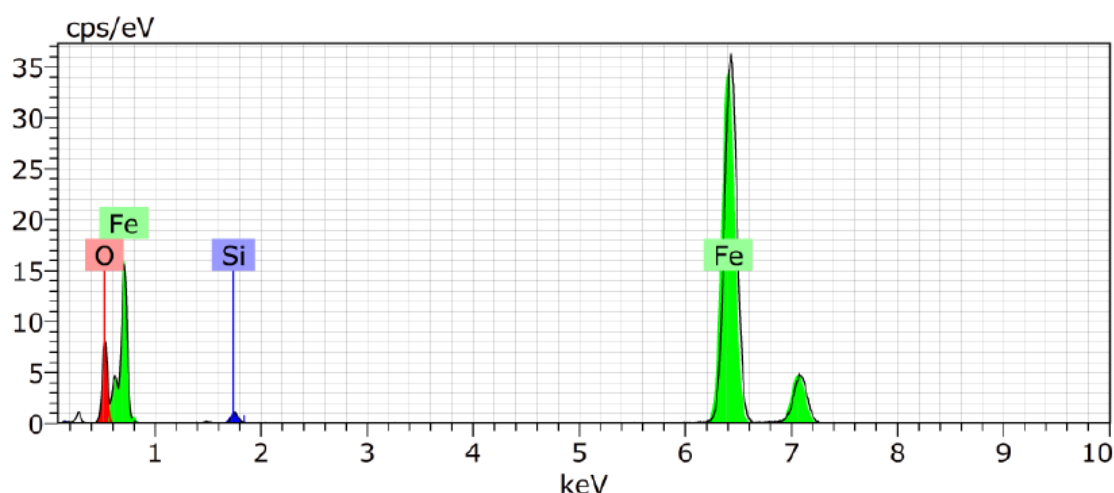


Figure 2. Example of EDX spectrum obtained on sample containing Fe and Si.

Table 1. Analysis of sample with initial composition 1,5 % of Mg (obtained by EDX analysis)

Element	Atomic number	% by weight	Atomic %
Carbon	6	4.18	14.33
Oxygen	8	7.41	19.24
Magnesium	12	1.33	8.86
Iron	26	87.02	64.18

Following Fig. 3 gives an example the corrosion curves and their changes in the course of time. Investigated material was Fe doped by 2.5 % of Mg; higher degree of doping did not yield any compact sample.

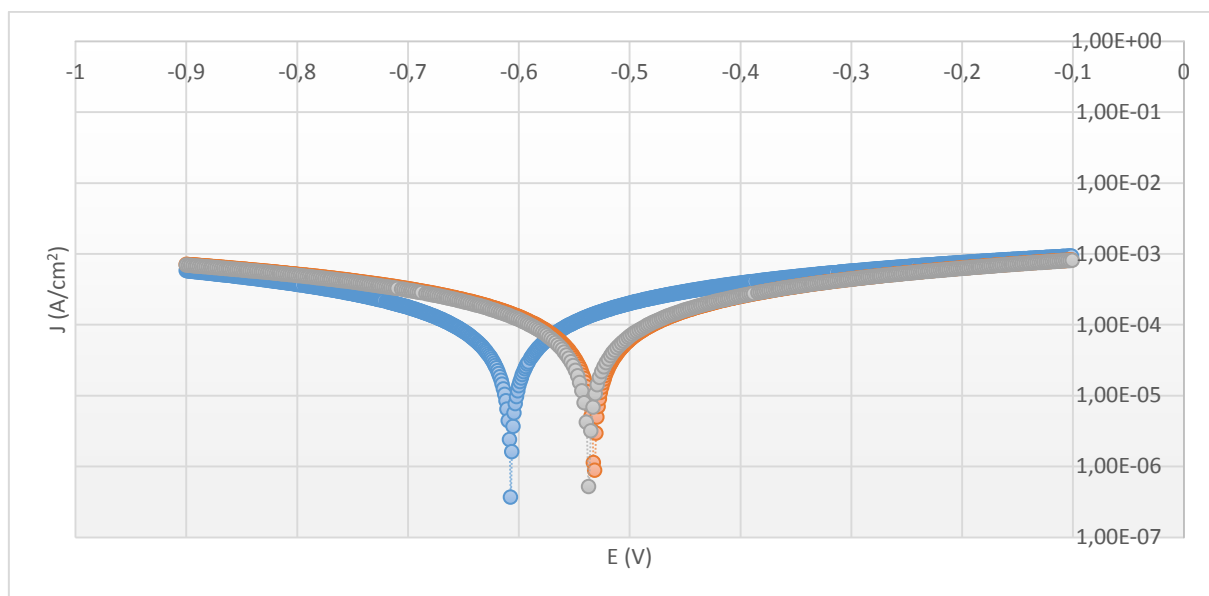


Figure 3. Corrosion curves of iron doped by 2.5 % Mg in Ringer solution presented as current – potential .. Colours: 1st day blue, 8th day orange, 15th day grey.

The samples of iron doped by Mg were exposed to blood plasma. After several weeks, they became covered by a deposit of coagulation products, which slowed down the corrosion markedly.

Undoubtedly, 100% Fe in contact with physiologic solution is rather simple and regular. On contrary, passivation effects were observed on other materials.

Most extended observation was performed on system of Fe doped by silicon. It should be noted, that the mass of the sample being immersed for some time in Ringer solution depends strongly on the amount of dopant. For lowest silicon content, the mass change corresponds to mass increase, probably due to formation of some passivation layer. Following Fig. 4 shows the mass changes of a Si doped samples of various amounts of Si in Ringer solution

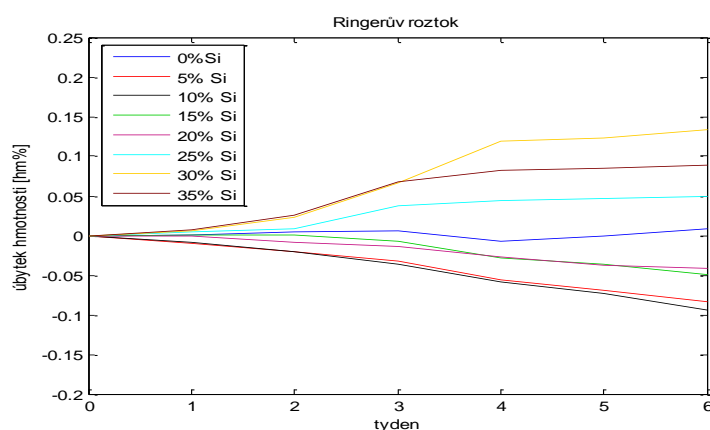


Figure 4. Corrosion of various Fe samples doped by SI

The highly doped samples decomposed rather strongly, probably due to instability of silicon particles

Such a behaviour was observed even on samples doped by other metals. Somewhat different picture was observed on Ag doped samples. The corrosion rate is increased by silver doping in comparison with pure Fe alloy even if the amount of silver was the lowest.

Generally spoken, the presence of hydrogen peroxide accelerated the corrosion, most clearly in first days of exposition. On the other hand, phosphate containing solution produced marked passivation of material surface.

For observation the effect in blood plasma it is recommended to apply substances used in medicine for prevention of solid precipitation on the surface of metals.

In future, the composition of residua generated at deep corrosion will be important for judging the suitability of investigated metals in surgery as self-decomposing implants.

Acknowledgement

This research work has been carried out in the Centre for Research and Utilization of Renewable Energy (CVVOZE). Authors gratefully acknowledge financial support from the Ministry of Education, Youth and Sports of the Czech Republic under NPU I programme (project No. LO1210)

References

1. Orinakova, Renata; Orinak, Andrej; Giretova, Maria; et al., *J. Biomat. Appl.* **30**, (2016),1764
2. Dudrova, Eva; Kabatova, Margita; Orinakova, Renata; et al., *Int. Journal of Electrochem. Sci.*, **11** (2016),1751

Chemical corrosion of porous iron alloys prepared pyrolytically

M. Sedlaříková¹, J. Vondrák¹, Z. Galanova¹, P. Čudek¹, T. Binar²

¹FEEC, BUT, Department of Electrical and Electronic Technology

²University of Defense, Brno, Czech Republic

Porous iron-based materials can be prepared by pyrolysis of metal powders deposited onto polyurethane foam BULPREN and subsequent annealing in an inert atmosphere ^{1, 2}. The aim of this paper is to investigate details of their slow decomposition with the prospective of using them as biodegradable metallic components for various purposes. Systems to be investigated were: pure Fe, pure Zn, Fe + Mn, Fe+ P, Fe+ Zn and Zn + Mg. Moreover, one sample containing Fe, Mg, Zn, and Ag was studied. Emphasis will be laid on the chemistry and mechanic properties of their corrosion. The main idea of pyrolytic preparation originated in papers ^{3, 4}.

Fundamental composition of materials used for investigations was Fe composites with various added metals. At first place, gravimetric estimation of corrosion rate was performed. As the liquids for corrosion studies, the standard physiologic solution, the commercial Ringers solution and synthetic body liquid (marked as SBL) according to ⁵; this solution is composed of sodium, potassium and calcium halides, further hydrogen carbonate and monohydrogen phosphate as regulators of pH and finally, tris(hydroxymethyl) methyl amine in amount 6.057 g/l as a complexing agent the role of which is to keep corrosion products of metals in solution. For example, the value of pH in contact with %100 Fe containing sample after 124 days from neutral value 7.15 to 9.45 in solution of NaCl, but from 7.19 to 7.23 in SBF after 15 days.

Microscopic observation including EDX observations and. X-Ray diffraction analysis was performed. Hardness according to Vickers was also studied.

The morphology of 100% Fe sample is shown in Fig. 1. Apparently, the foamy structure of the polyurethane matrix is pertained after the annealing. On contrary, the Fe - Mg - Zn - Ag composite was fairly heterogenous and crystallites can be seen on it surface.

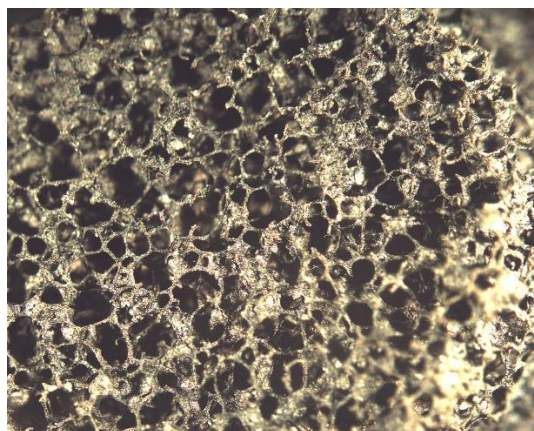


Figure 1. 100 % Fe deposited on polyurethane. Magnification: 20 times,

Fresh iron samples and samples exposed to the SBL were analysed by EDX method. The results are shown in following table 1.

From the date it seems evident than the content of pure iron decreased. On contrary, the oxide detected on XRD as oxide FeO remained almost unchanged and its relative content increased in comparison with fresh material. This is analogous to the method used for separation of iron compounds in iron alloys and based on different solubilities in etchants.

Table 1. EDX analysis of a 100% sample of Fe etched by SBF.

Element	Amount of the element in sample as prepared [%]	Amount of the element after 54 days in SBF solution [%]
Iron	80.64	63.35
Oxygen	17.64	29.07
Carbon	1.33	5.91
Sulphur	0.38	-
Chlorine	-	1.67

Table 2. EDX analysis of fresh and etched of sample containing 90 % Fe and 10 % Mn in SBF.

Element	etched	Amount of the element after 120 days in solution [%]
Iron	81.14	58.54
Manganese	4.59	1.20
Oxygen	12.46	30.57
Carbon	1.11	7.24
Sulphur	0.71	-

The elution of metallic Fe and Mn and evidence of metal oxides is even more seen.

The texture of Fe-P composite is different. Even visually, this composite is of different mechanic properties. The morphology is displayed in following figures. (see Fig. 2).

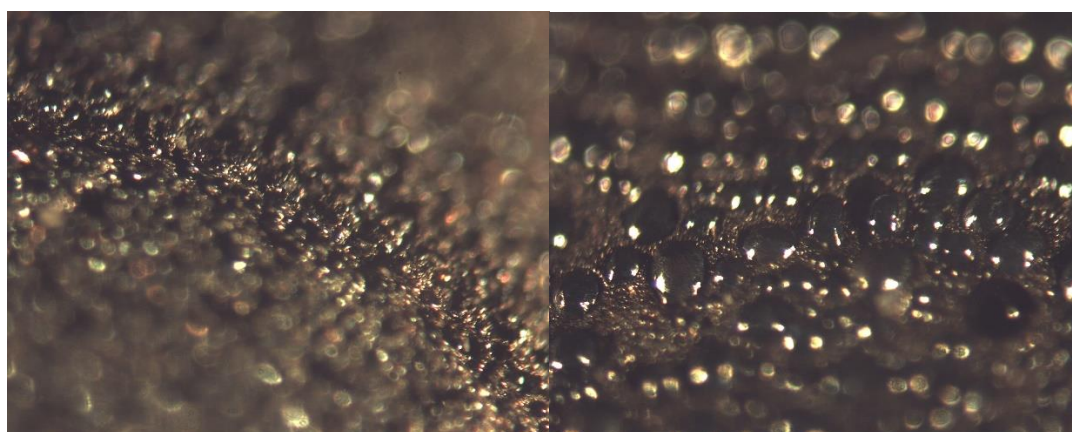


Figure 2. 90 % Fe – 10 % P sample, amplification of the picture is 20x (left) and 100x (right)

The heterogeneity of phosphorus distribution in the sample is apparent.

Further studied phenomenon was the change of corrosion current and potential. An example of results is given in following Tab. For several samples. It seems clear that the corrosion potentials

of samples rich on zinc is fairly negative in comparison with samples with prevailing iron; this may be explained by strong passivation of iron in the electrolyte.

Table 3. *corrosion of various samples in 3 weeks*

Sample	Corrosion current			Corrosion potential		
	1 week	2 weeks	3 weeks	1 week	2 weeks	3 weeks
80% Zn - 20% Mg	-0.5	-0.728	-0.411	$2.514 \cdot 10^{-6}$	$7.150 \cdot 10^{-6}$	$1.56 \cdot 10^{-6}$
60% Zn - 40% Mg	-0.411	-0.409	-0.359	$1.895 \cdot 10^{-6}$	$1.909 \cdot 10^{-6}$	$1.791 \cdot 10^{-6}$
90% Zn - 10% Mg	-0.57	-0.352	-0.399	$1.857 \cdot 10^{-6}$	$1.758 \cdot 10^{-6}$	$3.952 \cdot 10^{-6}$
90% Fe - 10% P	-0.604	-0.675	-0.596	$1.149 \cdot 10^{-5}$	$7.572 \cdot 10^{-6}$	$1.192 \cdot 10^{-5}$
95% Fe - 5% P	-0.777	-0.449	-0.699	$1.437 \cdot 10^{-5}$	$5.291 \cdot 10^{-6}$	$2.496 \cdot 10^{-5}$
60% Fe - 40% Zn	-1.157	-0.864	-0.565	$2.269 \cdot 10^{-5}$	$1.350 \cdot 10^{-5}$	$1.007 \cdot 10^{-5}$
100% Zn	-1.118	-1.068	-1.055	$7.346 \cdot 10^{-5}$	$5.417 \cdot 10^{-5}$	$1.057 \cdot 10^{-4}$
80% Fe - 20% Zn	-1.095	-0.777	-0.566	$3.448 \cdot 10^{-5}$	$1.092 \cdot 10^{-5}$	$6.042 \cdot 10^{-6}$

Finally, we investigated fresh prepared samples by measuring of hardness according to Vickers. We see again that soft metals do not contribute to hardness of the material (see Table 4)..

Table 4. *Microhardness of 100 % Fe and various composites based on zinc*

Sample	Microhardness HV 0.02			
	Min.	Max.	Medium value	Standard deviation
Fe	41.4	87.4	72.9	± 14.2
80 % Zn – 20 % Mg	19.9	42.8	31.5	± 8.2
60 % Zn – 40 % Mg	19.5	66.9	34.2	± 13.6
90 % Zn – 10 % Mg	22.9	33.3	27.3	± 3.6
100 % Zn	18.2	57.0	35.8	± 12.0

Conclusions

First, the use of SBF for corrosion testing might be useful mainly if we will be interested into the stadium of full decomposition of our materials in electrolytes. Further, high content of zinc resulted in material with rather low hardness and strongly negative corrosion potential, most likely, due to strong electropositivity of Zn. The additive of phosphorus did not show any useful properties.

Acknowledgement

This research work has been carried out in the Centre for Research and Utilization of Renewable Energy (CVVOZE). Authors gratefully acknowledge financial support from the Ministry of Education, Youth and Sports of the Czech Republic under NPU I programme (project No. LO1210)

References

1. Sedlaříková Marie, Vondrák, Jiří et al, ECS Trans. 2017 81(1): 297-304
2. Sedlaříková Marie, Vondrák, Jiří et al, meeting ABAF – 19, to be published
3. Orinakova, Renata; Orinak, Andrej; Giretova, Maria; et al., *J. Biomat. Appl.* **30**, (2016),1764
4. Dudrova, Eva; Kabatova, Margita; Orinakova, Renata; et al., *Int. Journal of Electrochem. Sci.*, **11** (2016),1751
5. Li J. Y. et al., *Journal of Alloys and Compounds* 728 , pages 37 to 42

Thermal Model of Cylindrical Battery Cell

M. Toman^a, R. Cipin^a, P. Vorel^a

^a Department of Power Electrical and Electronic Engineering, Brno University of Technology, Technicka 12, Brno 616 00, Czech Republic

This article deals with the calculation of temperature of a cylindrical battery cell using thermal network. The cell is modeled as a cylindrical body with differential conductivity in the radial and axial direction. The considered thermal network requires a calculation of only one node temperature that represents the mean temperature of the whole cell. The results of the calculations were compared using a finite element method and a very good match was achieved.

Introduction

Thermal calculation is one of the partial steps in designing battery packs for power applications. Nowadays, these calculations are performed in most cases using the finite element method. This method undoubtedly has many advantages, especially when dealing with complex geometrical shapes. However, in some aspects, this method may still have a number of disadvantages. For example, computing hardware requirements, long calculation time, or the impossibility of implementation such model into an algorithm in a microprocessor that would estimate the battery pack temperature. Therefore, in many cases, it may be advantageous to use a thermal model based on a thermal network. The basic part of an arbitrarily complex thermal network of a battery pack is the thermal network of one battery cell. An analysis of a thermal network of a cylindrical-shape battery cell is the subject of this article.

Calculation of Battery Cell Temperature Using Thermal Network

The considered thermal network of a cylindrical battery cell is shown in Fig. 1. In this figure, all parameters related to the radial direction are indicated by “r” in the subscript and the parameters related to the axial direction are indicated by “a”.

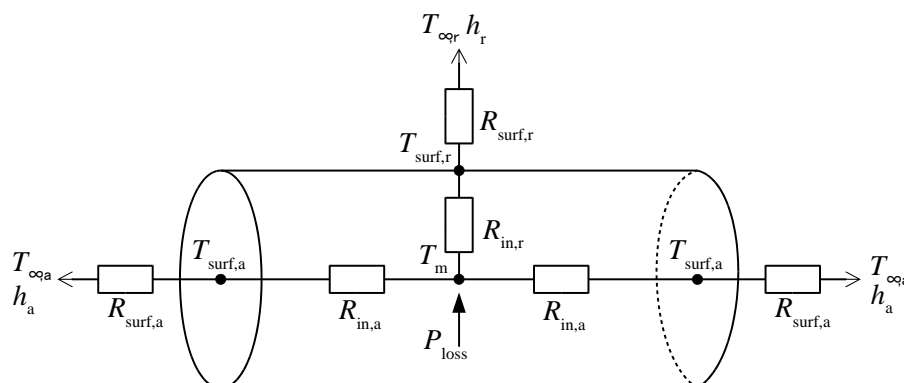


Figure 1. The considered thermal network of a cylindrical battery cell.

The analysis is performed under the following assumptions:

- Power losses P_{loss} are generated in the battery. These losses are uniformly distributed throughout the whole volume and they are transferred to the ambient by convection.
- The temperature distribution in the radial and axial direction is parabolic.
- The ambient temperature in the axial direction $T_{\infty,a}$ has the same value on both sides of the battery as well as the heat transfer coefficient h_a . Thus, the temperature distribution is symmetrical relative to the battery center.
- The thermal conductivity in the radial direction k_r has a different value than the thermal conductivity in the axial direction k_a .

In the following section, the relationships for the individual thermal resistances and nodal temperatures shown in the Fig. 1 are given. Surface thermal resistances $R_{\text{surf},r}$ and $R_{\text{surf},a}$ are classically determined as a thermal resistance by convection:

$$R_{\text{surf},r} = \frac{1}{h_r A_r} \quad (1)$$

$$R_{\text{surf},a} = \frac{1}{h_a A_a} \quad (2)$$

where h_r , h_a are heat transfer coefficients in radial and axial direction respectively and A_r , A_a are cell surface areas in radial and axial direction respectively.

Under the above assumption that the temperature distribution is parabolic in the axial and radial directions, the internal resistances are calculated according to equations:

$$R_{\text{in},r} = \frac{1}{6\pi L k_r} \quad (3)$$

$$R_{\text{in},a} = \frac{L}{6k_a A_a} \quad (4)$$

where L is the length of the battery. The assumption that the temperature distribution in one direction is parabolic is true in fact only when a heat flow is zero in the other direction. This means that the temperature distribution in the radial direction is purely parabolic only when the axial heat flow is zero, ie when h_a is zero and vice versa. Furthermore, it will be shown that the simplifying assumption that temperature distribution is parabolic in both directions if both flows are non-zero, provides sufficiently accurate results.

From the previous equations, it is possible to express the total resistances in individual directions as:

$$R_{\text{total},r} = R_{\text{in},r} + R_{\text{surf},r} \quad (5)$$

$$R_{\text{total},a} = R_{\text{in},a} + R_{\text{surf},a} \quad (6)$$

Unknown nodal temperatures can now be determined by the following equations:

$$T_m = \frac{P_{\text{loss}} + T_{\infty,r} \frac{1}{R_{\text{total},r}} + T_{\infty,a} \frac{2}{R_{\text{total},a}}}{\frac{1}{R_{\text{total},r}} + \frac{2}{R_{\text{total},a}}} \quad (7)$$

$$T_{\text{surf},r} = T_{\infty,r} + \frac{R_{\text{surf},r}(T_m - T_{\infty,r})}{R_{\text{total},r}} \quad (8)$$

$$T_{\text{surf},a} = T_{\infty,a} + \frac{R_{\text{surf},a}(T_m - T_{\infty,a})}{R_{\text{total},a}} \quad (9)$$

where T_m is the mean temperature of the battery, $T_{\text{surf},r}$ is the mean cell surface temperature in the radial direction and $T_{\text{surf},a}$ is the mean cell surface temperature in the axial direction. The maximum temperature T_{max} is at the center of the battery and is calculated according to the equation:

$$T_{\text{max}} = T_{\text{surf},r} + \frac{h_r D (T_{\text{surf},r} - T_{\infty,r})}{4k_r} \quad (10)$$

where D is the diameter of the cell.

Results

By using the mentioned equations, temperatures of Li-Ion 18650 cell with diameter of 18.4 mm and length of 65 mm were calculated. The thermal conductivities of the cell are $k_r = 0.2 \text{ W}\cdot\text{m}^{-1}\cdot\text{K}^{-1}$ and $k_a = 30 \text{ W}\cdot\text{m}^{-1}\cdot\text{K}^{-1}$. Power losses are $P_{\text{loss}} = 1 \text{ W}$. Ambient temperatures are $T_{\infty,r} = T_{\infty,a} = 20 \text{ }^\circ\text{C}$. Three solutions with different combinations of heat transfer coefficients were performed, see table I. To validate the results, the solution was also done using the finite element method in Ansys. It can be seen that the results have a very good match.

TABLE I. Comparison of the results obtained by the thermal network and by solution in Ansys.

	$h_r = 20, h_a = 0 [\text{W}\cdot\text{m}^{-2}\cdot\text{K}^{-1}]$			$h_r = 1, h_a = 20 [\text{W}\cdot\text{m}^{-2}\cdot\text{K}^{-1}]$			$h_r = h_a = 20 [\text{W}\cdot\text{m}^{-2}\cdot\text{K}^{-1}]$		
	T_m	T_{max} [$^\circ\text{C}$]	$T_{r,\text{surf}}$	T_m	T_{max} [$^\circ\text{C}$]	$T_{r,\text{surf}}$	T_m	T_{max} [$^\circ\text{C}$]	$T_{r,\text{surf}}$
Thermal network	41.8	43.9	37.7	105.9	106.6	104.7	38.6	40.3	35.1
Ansys	41.8	43.9	37.7	106.4	107.0	105.1	38.7	40.5	35.3

Conclusion

The paper dealt with the thermal model of battery cell based on use of a thermal network. In the used network, the battery temperature calculation is based on calculation of only one mean temperature of the whole cell. From this temperature, it is possible to calculate the cell surface temperatures and also the maximum cell temperature. The verification of the results was performed using the finite element method in Ansys and a very good match was obtained. In the full paper, more complex thermal networks will be discussed and thermal capacitances will be added so it will be possible to solve the transient state. Also the references will be included in the full paper.

Acknowledgment

This research work has been carried out in the Centre for Research and Utilization of Renewable Energy (CVVOZE). Authors gratefully acknowledge financial support from the Ministry of Education, Youth and Sports of the Czech Republic under NPU I programme (project No. LO1210).

Electrical conductivities of reduced graphene oxide thin-film layers

J. Vanek¹, and R. Mach²

¹ Centrum výzkumu a využití obnovitelných zdrojů energie, Vysoké učení technické v Brně, Technická 10, 612 00 Brno

² Fakulta elektrotechniky a komunikačních technologií, Vysoké učení technické v Brně, Technická 10, 612 00 Brno

Introduction

Since its discovery in 2004, graphene, a two-dimensional, entirely sp^2 -hybridized, single-layered form of carbon has been the focus of intense fundamental and applied research due to its unique electronic, optical, and mechanical properties. [1,2]

Graphene oxide (GO) is an excellent candidate for dispersion in aqueous environments due to its hydrophilic nature. GO is a possible intermediate for the production of graphene and is a compound of carbon, oxygen, and hydrogen in variable ratios. The maximally oxidized bulk product is a yellow solid that retains the layer structure of graphite but with much larger and more irregular spacing. [3] The oxidized moieties of GO can be compatible with various substrates and are able to interact with different inorganic, organic or biomaterials. Thus, GO is not only a precursor material of graphene but also a polymeric material with its own properties. GO has been used in polymer composites, [4] dielectric layers in electronic devices, [5] solar cells, [6] and various biological systems [7] such as DNA analysis. [8] Unlike graphene, GO is an electrically insulating material. Many defect sites can be generated on the surface of GO due to the disruption of the sp^2 bonding network of graphene by the oxidized portion of GO. These defects may be reduced by means of thermal reduction or chemical processes through the preparation of reduced graphene oxide, and the electrical properties of graphene can be restored. [9–11]

Conductivity of RGO

As it is shown in papers [12–16], in the range of temperatures below 200 K the dependence of electrical conductivity on the temperature in the RGO is in good agreement with the hopping mechanism of conductivity with the variable range hopping. This type of transport of charge is described by an equation [17, 18]

$$R = R_0 \exp\left(\frac{T_0}{T}\right)^m, \quad (1)$$

where T is the temperature, T_0 is a characteristic temperature, m depends on a system dimension and takes on values $1/3$ or $1/4$ – two-dimensional [9, 10] and three-dimensional [11] structures, respectively. A similar dependence with a power $m = 1/2$ is observed for the Efros-Shklovskii mechanism [10, 16]. At higher temperatures the dependence of resistance has an activation character and is described by an exponential dependence [12]

$$R = R_0 \exp\left(\frac{E_a}{k_B T}\right), \quad (2)$$

where E_a is the activation energy and k_B is the Boltzmann constant.

When electronic devices on the basis of RGO are created, it is necessary to know influence of external factors on properties of material.

One of main parameters of many devices is the electrical conductivity. The aim of this work was the study of effect of temperature on the electrical conductivity of thermally reduced GO.

Sample preparation

Two different graphite oxide material and dispersions were prepared:

1. The 1 mg of the prepared graphete oxide material GOPAZ was dispersed in 30 ml NMP (N-methylpyrrolidon) with the aid of bath ultrasonication, and then the dispersions was as a thin layer applied on the substrate.
2. The 10 mg of the prepared graphene oxide material SIGMA ALDRICH was dispersed in solution of 10 ml water H₂O and 2,5 ml ethanol with the aid of bath ultrasonication, and then the dispersions was as a thin layer applied on the substrate.

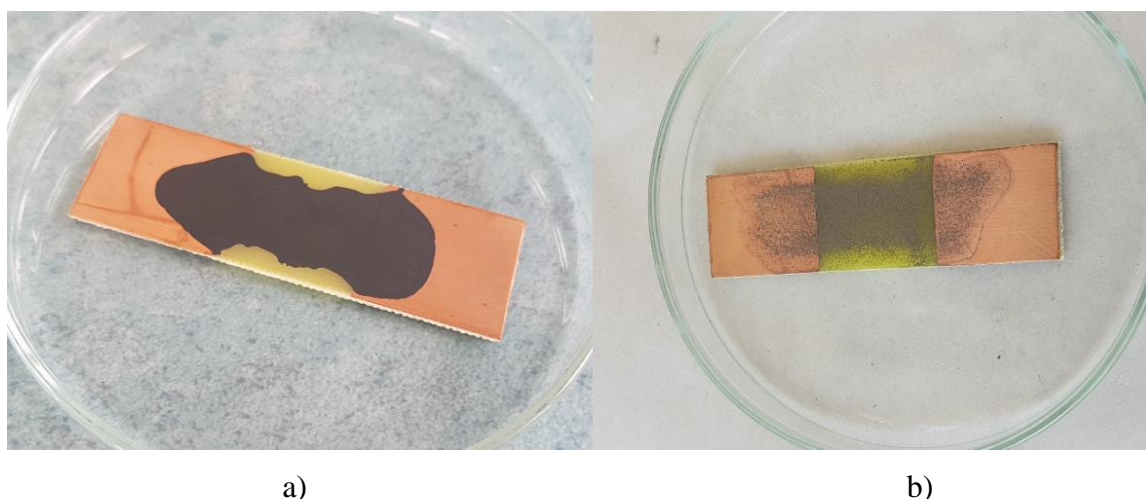


Figure 1. a) GO SIGMA ALDRICH and b) GO GOPAZ layers on substrate

Measurement of electrical and photoelectric properties

Conductivity measurements were performed on four samples. The multimeter LINI-T UT71A was used in all cases to measure the resistance of the samples.

In the first step, the dimensions of the deposited thin layers were determined. From the ellipsometric measurements based on the fitting model used, the thickness of the deposited layers was determined at 49 nm. The measurements were carried out on different samples with different substrates, the application on all substrates was identical. Therefore, it can be assumed that the thickness of the layers will be similar.

Table1. Measured basic parameters of graphen oxides layers

	R [kΩ]	L [mm]	w [mm]	d [nm]	σ [S.m ⁻¹]	ρ [Ω.m]
K1RGO	3.848	18.0	9	49	10610	9.4276E-05
K2RGO	2.477	34.5	19	49	14960	6.6843E-05
K3RGO	2.597	42.8	20	49	16820	5.9464E-05
K4RGO	2.537	52.0	21	49	19920	5.0203E-05

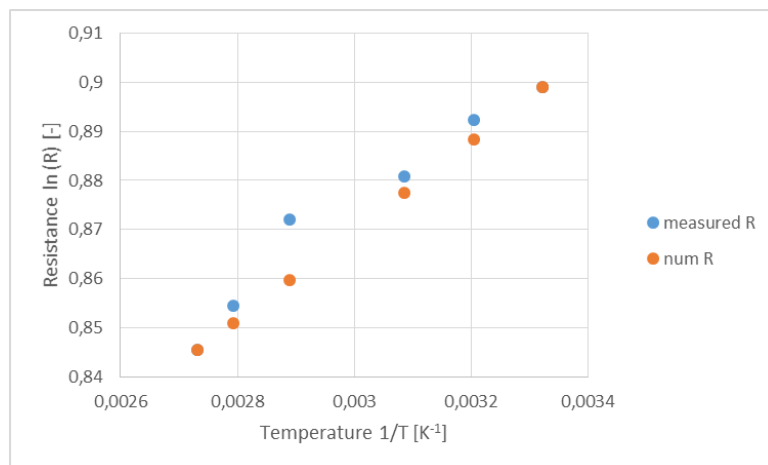


Figure 2: Dependence of resistance of GO thin layer K2RGO on temperature.

Blue points are measured data and red points are calculated value for $E_a = 0.0083$ eV and $R_0 = 1.79 \Omega$

With the help of formula (2) the activation energies E_a are calculated in the high temperature part of dependence of resistance on the temperature. The found values of activation energy are in a range of 0.0032 to 0.0124 eV. The example for sample K2RGO is corresponding to equation:

$$R = 1.79 \exp\left(\frac{1.33 \cdot 10^{-21}}{k_B T}\right)$$

Conclusion

From the obtained results, the mechanism of conductivity in graphene oxide obtained by the chemical method and thermally reduced in the high temperature depends on the activation energy E_a . In the temperature range of 290 - 390 K there are shown the Efros-Shklovskii mechanism in the samples with a higher degree of reduction (longer treatments and a higher temperature of reduction).

Acknowledgments

This research work has been carried out in the Centre for Research and Utilization of Renewable Energy (CVVOZE). Authors gratefully acknowledge financial support from the Ministry of Education, Youth and Sports of the Czech Republic under NPU I programme (project No. LO1210).

References

1. Novoselov, K. S.; Geim, A. K.; Morozov, S. V.; Jiang, D.; Zhang, Y.; Dubonos, S. V.; Grigoreiva, I. V.; Firsov, A. A. Electric Field Effect in Atomically Thin Carbon Films. *Science* 2004, 306, 666–669.
2. Huang, X.; Qi, X.; Boey, F.; Zhang, H. Graphene-Based Composites. *Chem. Soc. Rev.* 2012, 41, 666–686.
3. Hummers, W. S.; Offeman, R. E. Preparation of Graphitic Oxide. *J. Am. Chem. Soc.* 1958, 80, 1339–1339.

4. Stankovich, S.; Dikin, D. A.; Dommett, G. H. B.; Kohlhaas, K. M.; Zimney, E. J.; Stach, E. A.; Piner, R. A.; Nguyen, S. T.; Ruoff, R. S. Graphene-Based Composite Materials. *Nature* 2006, 442, 282–286.
5. Myung, S.; Park, J.; Lee, H.; Kim, K. S.; Hong, S. Ambipolar Memory Devices Based on Reduced Graphene Oxide and Nanoparticles. *Adv. Mater.* 2010, 22, 2045–2049.
6. Yin, Z.; Wu, S.; Zhou, X.; Huang, X.; Zhang, Q.; Boey, F.; Zhang, H. Electrochemical Deposition of ZnO Nanorods on Transparent Reduced Graphene Oxide Electrodes for Hybrid Solar Cells. *Small* 2010, 6, 307–312.
7. Sun, X.; Liu, Z.; Welscher, K.; Robinson, J. T.; Goodwin, A.; Zaric, S.; Dai, H. Nano-Graphene Oxide for Cellular Imaging and Drug Delivery. *Nano Res.* 2008, 1, 203–212.
8. He, S.; Song, B.; Li, D.; Zhu, C.; Qi, W.; Wen, Y.; Wang, L.; Song, S.; Fang, H.; Fan, C. A Graphene Nanoprobe for Rapid, Sensitive, and Multicolor Fluorescent DNA Analysis. *Adv. Funct. Mater.* 2010, 20, 453–459.
9. Wang, R.; Wang, S.; Zhang, D.; Li, Z.; Fang, Y.; Qiu, X. Control of Carrier Type and Density in Exfoliated Graphene by Interface Engineering. *ACS Nano* 2011, 5, 408–412.
10. Rana, U.; Malik, S. Graphene Oxide/Polyaniline Nanostructures: Transformation of 2D Sheet to 1D Nanotube and in situ Reduction. *Chem. Commun.* 2012, 48, 10862–10864.
11. Zhang, K.; Zhang, L. L.; Zhao, X. S.; Wu, J. Graphene/Polyaniline Nanofiber Composites as Supercapacitor Electrodes. *Chem. Mater.* 2010, 22, 1392–1401.
12. Muchharla B, Narayanan TN., Balakrishnan K, Ajayan PM, Talapatra S. Temperature dependent electrical transport of disordered reduced graphene oxide. *2D Materials*, 2014, 1:011008(1-5).
13. Joung D, Khondaker SI. Efros-Shklovskii variable-range hopping in reduced graphene oxide sheets of varying carbon sp² fraction. *Physical Review D*, 2012, 86:235423 (1-8).
14. Eda G, Mattevi C, Yamaguchi H, Kim HK, Chhowalla M. Insulator to Semimetal Transition in Graphene Oxide. *J. Phys. Chem. C*, 2009, 113:15768-15771.
15. Kaiser AB, Gómez-Navarro C, Sundaram RS, Burghard M, Kern K. Electrical Conduction Mechanism in Chemically Derived Graphene Monolayers. *Nano Letters*, 2009, 9(5):1787-1792.
16. Venugopal G, Krishnamoorthya K, Mohanc R, Kim SJ. An investigation of the electrical transport properties of graphene-oxide thin films. *Materials Chemistry and Physics*, 2012, 132:29-33.
17. Shklovskii BI, Efros AL. *Elektronnye svoystva legirovannyh poluprovodnikov*. [Electronic properties of doped semiconductors]. Moscow, Nauka Publ., 1979, 416 p.
18. Mott N, Devis Je. *Elektronnye processy v nekristallicheskih veshhestvah*. [Electronic processes in non-crystalline materials] Moscow, Mir Publ., 1982, t.1, 368 p.

FEA Methods for Lithium Ion Battery Simulation

P. Vyroubal^a, T. Kazda^a

^a Department of Electrical and Electronic Technology, Brno University of Technology, Technická 10, 616 00 Brno, Czech Republic

This article deals with simulation methods in electrochemistry of lithium ion battery. There are several methods to simulate lithium ion battery using the FEA method. It is possible to use a classic FEM approach, a system approach or an equivalent circuit.

Introduction

Numerical modelling is the method by virtually testing and verifying the functionality of a specific product or component. The primary goal is to get approximate results of how the system behaves in a given time and environment.

This paper deals with a possibility of the use the numerical simulation for system simulation in the unconventional power sources of electrical energy. This method is useful in application where the complex environment is necessary to use, e.g. electro-mobility, solar power station, etc. It is possible to simulate electro-chemical reactions, current fields, temperature fields, electric potentials, concentrations, charging and discharging cycle, electromagnetism, etc. In this case, it will be presented the multiphysical approach of system simulation of short circuit in the lithium ion battery.

When performing system simulations, we first need to simulate a suitable battery for a given process to obtain discharge curves at a given battery load. There are several ways to do this:

- Use an external solver (Matlab, etc.)
- Use the integrated solver (Ansys, Comsol, etc.)
- Do not use any, just determine the discharging current

Using Matlab Simulink

The Battery block implements a generic dynamic model parameterized to represent the most popular types of rechargeable batteries, for example, lithium ion, lead acid, nickel-cadmium, etc.

For lithium ion battery, the general model for charge and discharge is in this form:

$$\nabla \cdot (\sigma_- \nabla \varphi_-) = (j_{ECh} - j_{short}) \quad (1)$$

And

$$E_{discharge} = f_2(it, i^*, Exp, BattType) \quad (2)$$

where E_{charge} and $E_{discharge}$ are the functions of it (Extracted capacity (Ah)), i^* (Low frequency current dynamics (A)), Exp (Exponential zone dynamics (V)) and $BattType$ (type of the battery).

Using ANSYS system

The MSMD model (Multi-Scale Multi-Domain), which comprises for each layers different physical properties was used. Battery thermal and electrical fields are solved in the CFD domain at the battery cell's scale using the following differential equations:

$$\frac{\partial \rho C_p T}{\partial t} - \nabla \cdot (k \nabla T) = q \quad (5)$$

resp.

$$\frac{\partial \rho C_p T}{\partial t} - \nabla \cdot (k \nabla T) = \sigma_+ |\nabla \Phi_+|^2 + \sigma_- |\nabla \Phi_-|^2 + \dot{q}_{ECh} + \dot{q}_{short} \quad (6)$$

and

$$\nabla \cdot (\sigma_+ \nabla \varphi_+) = -j \quad (7)$$

resp.

$$\nabla \cdot (\sigma_+ \nabla \varphi_+) = -(j_{ECh} - j_{short}) \quad (8)$$

and

$$\nabla \cdot (\sigma_+ \nabla \varphi_+) = j \quad (9)$$

resp.

$$\nabla \cdot (\sigma_- \nabla \varphi_-) = (j_{ECh} - j_{short}) \quad (10)$$

where σ_+ a σ_- are conductivities of positive and negative electrode, φ_+ a φ_- are potentials of positive and negative electrode, j_{ECh} a \dot{q}_{ECh} volumetric current and heat generated by electrochemical reactions, respective j_{short} a \dot{q}_{short} volumetric current and heat generated by internal short circuit (in normal conditions are these variable zero values). Electrochemical sub-models relate the local current density to the potential. The cell model couples sub-models to thermal and electrical fields within the cell, integrates over multiple electrode-pairs [13].

Results and discussions

a) Using Matlab Simulink

Charging current for the second measurement was set to 0.5C (1500 mA) and the maximum charging potential was set to 4.2V. This was followed by CV charging until current dropped to 0.05C (150mA). After that discharging by current 0.5C (1500 mA) was used. Cut-off potential was set to 2.75V.

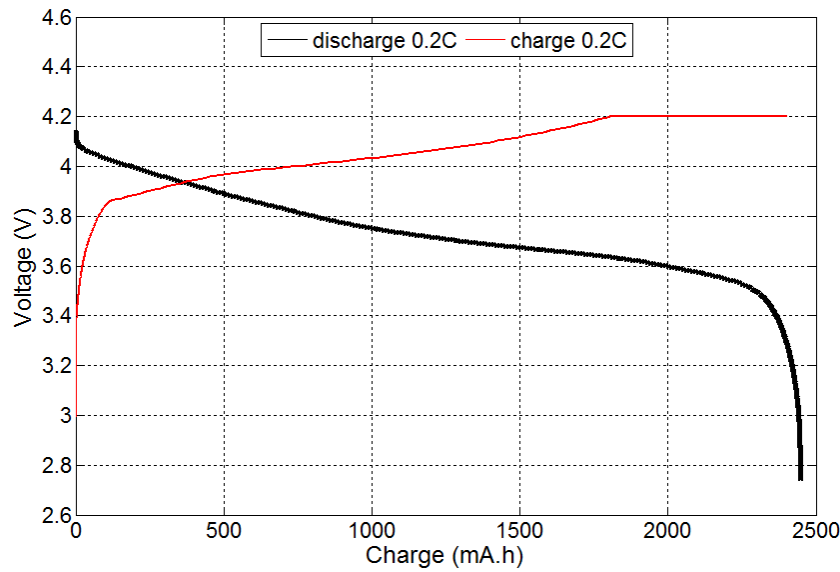


Figure 1. Charging and discharging characteristics of lithium ion battery for 0.2C.

b) Using ANSYS system

KOKAM battery with a reported capacity of 4000 mAh was connected to a potentiostat BioLogic - VMP3 to test its electrochemical characteristics and detection of temperature changes that occur when higher discharge currents are included. The battery was charged at 0.2 C, a current 800 mA. For the charging, was CCCV charging mode selected, while achieving voltage of 4.2 V CC mode was switched to the CV until the current does not fall below 200 mA. As the discharge current was selected current 4 A and thus discharging was terminated after reaching 3 V.

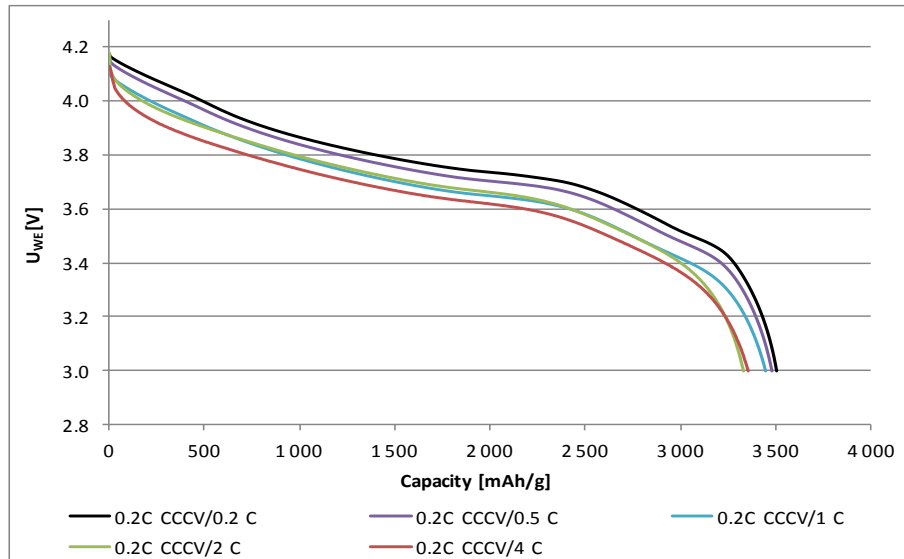


Figure 2. Comparison of discharge curves by real tested battery KOKAM with different C rate.

Acknowledgments

This research work has been carried out in the Centre for Research and Utilization of Renewable Energy (CVVOZE). Authors gratefully acknowledge financial support from the Ministry of Education, Youth and Sports of the Czech Republic under NPU I programme (project No. LO1210) and BUT specific research programme (project No. FEKT-S-17-4595).

References

1. L. Cai and R. E. White, *J. of Power Sources*, **196** (2011).
2. O. Tremblay, *World Electric Vehicle Journal*, **3**, 3 (2009).
3. D. Linden and T. B. Reddy, *Handbook of batteries*, p. 1454, McGraw-Hill, New York (2002).
4. P. Vyroubal and J. Maxa, *ECS Trans.*, **48**(1) (2014).
5. R. Spotnitz and J. Franklin, *J. of Power Sources*, **113**(1) (2003).
6. A. M. Colclasure, *Electrochimica Acta*, **113**(1) (2010).

FEM Analysis of LiIon Battery Nail Test

P. Vyroubal^a, T. Kazda^a

^a Department of Electrical and Electronic Technology, Brno University of Technology, Technická 10, 616 00 Brno, Czech Republic

Internal short-circuit is the most dangerous abusive condition for Li-ion batteries and has been the root cause for several catastrophic accidents involving Li-ion batteries in recent years. Large-format Li-ion batteries are particularly vulnerable to internal short-circuits because of high energy content. Nail penetration test is commonly used to study the internal short-circuits, but the test results usually have poor reproducibility and offer limited insight. This paper deals with a possibility of numerical simulation of internal short circuit test using FEM.

Introduction

The issue of numerical modeling of lithium-ion batteries lies in the geometric model, where is necessary to define each layer structures as they go behind [1]. These structures are sandwich type and very thin and moreover act in several layers, which implies problematic formation of computational mesh in 3D. Furthermore, these domains are multiphysical character, i.e., that the solution comprises the association of several types of properties (e.g. conductivity, heat capacity, thermal conductivity, mechanical properties, etc.), which greatly complicates the problem by [2] and [3].

The short-circuit intensity can be described by a fundamental variable-volumetric contact resistance, which could be computed as rc/a , where rc is the contact resistance of the electrode sheet in the unit of Ωm^2 , and a is the specific area of the electrode sheet in the battery volume in units of $1/m$. The transfer short current density j_{short} , in equation 4 and 5, and extra heat generated due to the short are computed as [4]:

$$j_{short} = a j'_{short} = a(\Phi_+ - \Phi_-)/r_c \quad (1)$$

and

$$\dot{q}_{short} = a(\Phi_+ - \Phi_-)^2/r_c \quad (2)$$

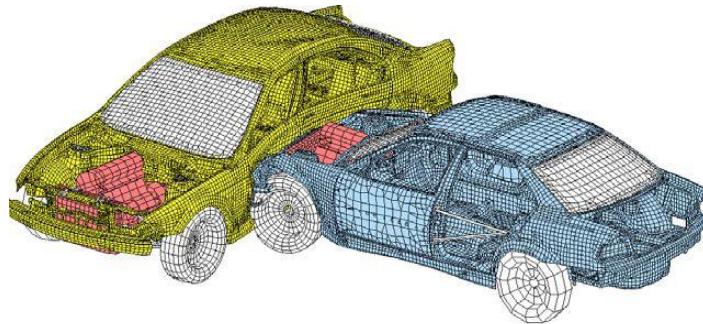


Figure 1. The FEM illustration of electric vehicle crash [5].

Results and discussions

The following figure shows the discharge temperature comparison for each C and "nail" test. It is clear from the picture that the larger the discharging current the battery discharges, the more the battery heats up. Warming up the "nail" test is only shown at a certain point in time. The temperature is still rising steadily.

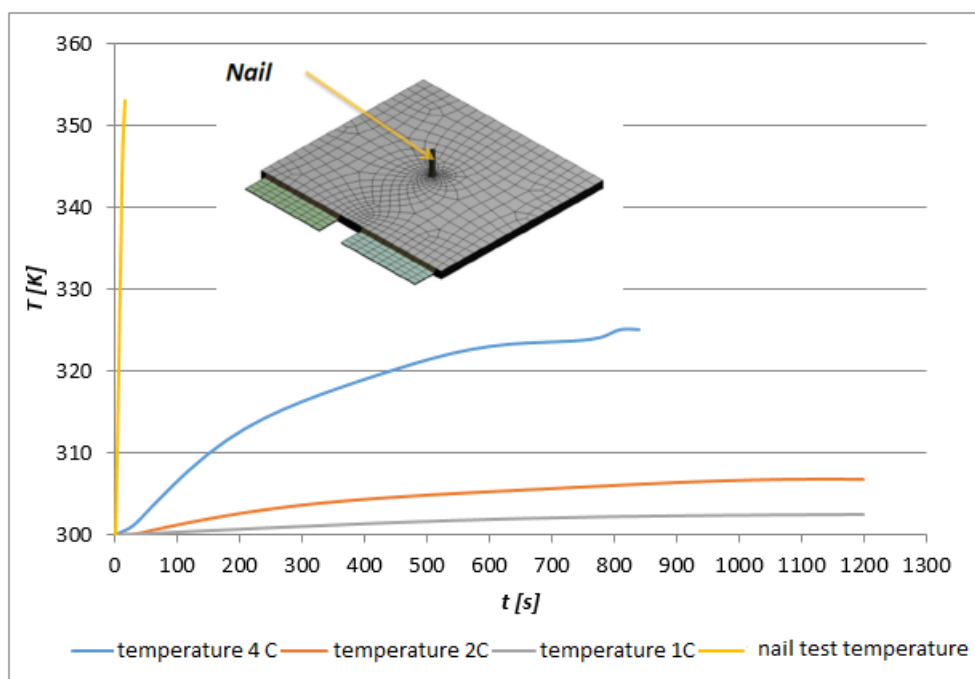


Figure 2. 1C discharging (real vs MSMD model - left) and temperature distribution (right).

Acknowledgments

This research work has been carried out in the Centre for Research and Utilization of Renewable Energy (CVVOZE). Authors gratefully acknowledge financial support from the Ministry of Education, Youth and Sports of the Czech Republic under NPU I programme (project No. LO1210) and BUT specific research programme (project No. FEKT-S-17-4595).

References

1. P. Vyroubal, J. Maxa and T. Kazda, *ECS Trans.*, **48**(1), 7 (2014).
2. B. Scrosati, J. Hassoun and Y. Sun, *Energy & Environmental Science*, 4 (2011).
3. D. Linden and T. B. Reddy, *Handbook of Batteries*, McGraw-Hill, Michigan (2002).
4. N. Nitta, F. Wu, J. T. Lee, G. Yushin, *Materials Today*, 18 (2015) 252.
5. W. Zhao, G. Luo, *Journal of Electrochemical Society*, 1 (2015) 162.

Thermal Simulation of Thermo-photovoltaic Emitter

P. Vyroubal,¹ L. Šimonová¹

¹Department of Electrical and Electronic Technology, Brno University of Technology, Technická 10, 616 00 Brno, Czech Republic

Thermophotovoltaic (TPV) belongs to the third generation of photovoltaics. This technique works on the principle of an effect of use as much of the radiation spectrum for optimal system operation. Traditional photovoltaic solar cells have an inherent limit on the efficiency at which they can convert sunlight into energy. This article deals with the simulation of temperature conditions in thermos-photovoltaic system

Introduction

Conventional solar cells are able to operate in the visible to near-infrared region of the spectrum. This limit, based on the band gap of the material, used and known as the Shockley-Queisser limit is about 33.7 percent for standard solar cells [1].

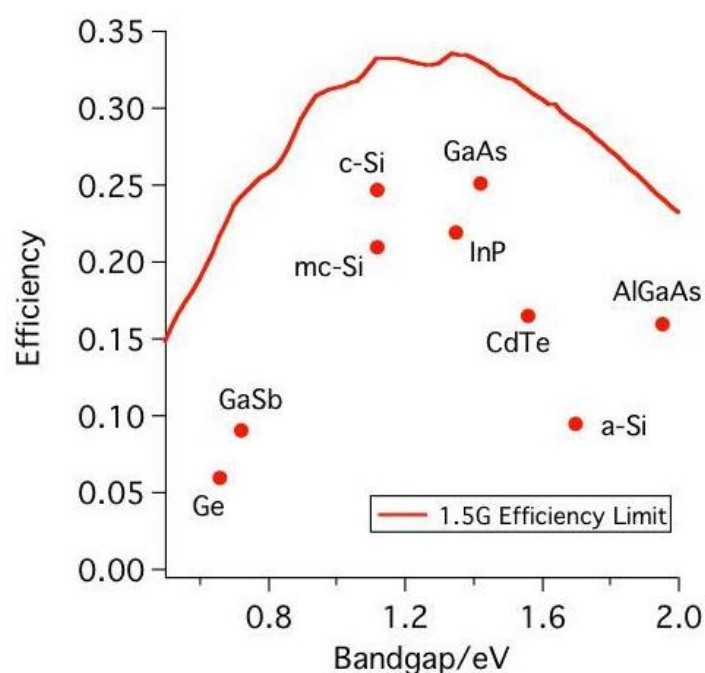


Figure 1. Band gap and efficiency [1].

Thermophotovoltaic systems have great potential application in commerce, military and aerospace industry. At present, the research on TPV primarily focuses on the spectral control technology and system construction.

To achieve the maximum efficiency, all photons should be converted. A process often termed photon recycling can be used to approach this. Here reflectors are placed behind the converter and anywhere else in the system that photons might not be efficiently directed to the collector. These

photons are directed back to the concentrator where they can be converted, or back to the emitter, where they can be reabsorbed to generate heat and additional photons. An idealized TPV system would use photon recycling and selective emission to convert all photons into electricity.

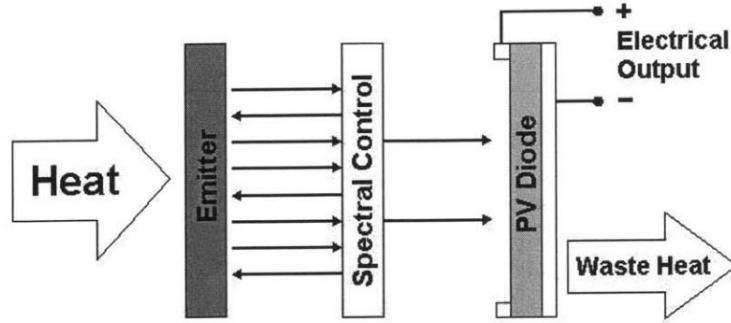


Figure 2. The efficient TPV system [2].

For the emitter, deviations from perfect absorbing and perfect blackbody behavior lead to light losses. For the case of selective emitters, any light emitted at wavelengths not matched to the band gap energy of the PV may not be efficiently converted (for reasons discussed above) and leads to reduced efficiency. In particular, emissions associated with phonon resonances are difficult to avoid for wavelengths in the deep IR, which cannot be practically converted. Ideally, an emitter will not emit in this range, and energy will only be converted at wavelengths that are easily converted. Examples of material with varying indices that results in selective emission for TPV applications are rare-earth oxides, such as holmium (Ho) or erbium (Er) oxide, and transition metals, such as hafnium (Hf) or tungsten (W) [2].

For blackbody emitters or imperfect selective emitters, filters are needed to reflect non-ideal wavelengths back to the emitter. In practice, these filters are rarely perfect. Any light that is absorbed or scattered and not redirected to the emitter or the converter is lost. Additionally, practical filters often reflect a small percentage of light in desired wavelength ranges or transmit light of non-ideal wavelengths. Both can lead to inefficiencies.

Even for systems where only light of optimal wavelengths is passed to the converter, inefficiencies associated with non-radiative recombination and ohmic losses exist. Since these losses can depend on the intensity of light incident on the cell, real systems must consider the intensity produced by a given set of conditions (emitter material, filter, operating temperature) [3].

The mathematical model includes the laws of conservation of momentum (represented by the full Navier-Stokes equation), mass and energy. The energy equation is in the form:

$$\frac{\partial(\rho E)}{\partial t} + \frac{\partial}{\partial x_k} [u_k(\rho E + p)] = \frac{\partial}{\partial x_k} \left(k \frac{\partial T}{\partial x_k} - \sum_{j'} h_{j'} J_{j'} + u_j \tau_{ij} \right) + S_h$$

where S_h is absorbed/emitted radiative energy defined as:

$$\frac{dI(\vec{r}, \vec{s})}{ds} + (a + \sigma_s)I(\vec{r}, \vec{s}) = an^2 \frac{\sigma T^4}{\pi} + \frac{\sigma_s}{4\pi} \int_0^{4\pi} I(\vec{r}, \vec{s}') \Phi(\vec{s} \cdot \vec{s}') d\Omega'$$

Where I is radiation intensity, which depends on position and direction, \vec{r} position vector, \vec{s} direction vector, a absorption coefficient, σ_s scattering coefficient, n refractive index, T local

temperature, σ Stefan-Boltzmann constant ($5.672 \cdot 10^{-8} \text{ Wm}^{-2}\text{K}^{-4}$), Φ phase function, \vec{s}' scattering direction vector, Ω' solid angle.

Results and discussions

The potential efficiency of such a system is much larger than expected performance of conventional photovoltaic system. Real experiments are much worse. In the TPV are mainly very expensive materials [4]. Production of such a system is a lengthy, time-consuming and costly, and the resulting efficiency is around 0% to 2% in laboratory conditions. Therefore, it is more efficient to perform a first simulation that can at least partially approximate the properties of the system.

Acknowledgments

This research work has been carried out in the Centre for Research and Utilization of Renewable Energy (CVVOZE). Authors gratefully acknowledge financial support from the Ministry of Education, Youth and Sports of the Czech Republic under NPU I programme (project No. LO1210) and BUT specific research programme (project No. FEKT-S-17-4595).

References

1. BORELAND, M., Ch., DEY, N., EKINS-DAUKES and Y., YIN. The Solar Energy Group: Photovoltaics Research. [online]. The University of Sydney [cit. 2014-07-31]. Available from: <http://www.physics.usyd.edu.au/app/solar/research/pv.html>
2. LIN, S. Y., J. MORENO and J. G. FLEMING. Three-dimensional photonic-crystal emitter for thermal photovoltaic power generation [online]. [cit. 2014-07-31]. ISBN <http://dx.doi.org/10.1063/1.1592614>.
3. COUTTS, T., J. An overview of thermophotovoltaic generation of electricity. Solar Energy Materials and Solar Cells. 2001, roč. 66, 1-4, s. 443-452. ISSN 09270248.
4. GREEN, M., A. Third generation photovoltaics: advanced solar energy conversion. New York: Springer, 2006, xi, 160 p. Springer series in photonics, v 12. ISBN 35-404-0137-7.



plynová chromatografie ICP-OES příprava vzorku
elementární ANALÝZA elektrochemie SEA
analýza povrchů **separační** techniky
DVS REOLOGIE ATOMOVÁ spektroskopie
GC temperace kapalinová chromatografie
UV-VIS spektrometrie GC-MS lyofilizátory
konfokál B.E.T. LIMS MIKROSKOPIE koncentrátory
CHNSO analýza AAS analýza částic HPLC
hmotnostní SPEKTROMETRIE centrifugy EXTRUZE
ICP-MS **SERVIS** termická analýza AIR monitoring
XPS widefield TEXTURA spotřební materiál NMR
DLS automatické dávkování iGC TOC analýza RVC



COMPANY ACTIVITIES, PRODUCTS AND SERVICES:

SVOS spol. s r.o. (Ltd.) belongs to the leading manufacturers of special armoured vehicles in Europe and during its history gained a secure position, not only on the European market but due to its high quality **SVOS** vehicles are exported all over the world. The company has been established in 1992 and has continued the tradition of special vehicles production for defence use in the region (since 1918).

Most sophisticated and up-to-date methods sourced from **SVOS** research and development activities together with **SVOS** long-time experience, precise craftsmanship and most resistant materials – ballistic steel and composite elements and bullet-resistant glass are applied in the construction process and creating unique and high-quality armoured vehicles.

Clients can select the level of the ballistic protection conforming to European, US, NATO or any other national standards. The high quality standard of **SVOS** vehicles is proven by repeatable and continuous cooperation with most reputable customers as well as by **SVOS** certification of quality system according to civilian standard ISO 9001 as well as military standard AQAP 2110.

SVOS production portfolio covers armoured vehicles for civilian use (armoured limousines, armoured SUVs, armoured busses, cash-in-transit vehicles and armoured trucks) as well as for military and police use (armoured personnel carriers, multi-purpose armoured vehicles, armoured ambulances, armoured combat vehicles, light armoured patrol vehicles, armoured trucks, armoured heavy-duty cross-country vehicles, riot control vehicles etc.)

The **SVOS** products are in service at various governments, armies, aid organisations as well as high-ranking VIP globally.



General sponsor



Other sponsors



Title: Advanced Batteries Accumulators and Fuel Cells – 19th ABAF

Edited: Jiří Vondrák
Marie Sedlaříková
Vítězslav Novák
Petr Bača

Publishing Office: Jiří Vondrák
Marie Sedlaříková
Vítězslav Novák
Petr Bača

Deadline: August 1st 2018

Publisher: Brno University of Technology
Faculty of Electrical Engineering and Communication
Department of Electrical and Electronic Technology

Year: 2018

The authors are fully responsible for the content and language of their contribution

ISBN 978-80-214-5651-8